## *The aerodynamic characteristics of an exposed racing car wheel*

Mears, Andrew Paul

# The Aerodynamic Characteristics of an Exposed Racing Car Wheel

Andrew Paul Mears



A Thesis presented for the degree of
Doctor of Philosophy

Centre for Automotive Research
School of Engineering
University of Durham
England

September 2004



To Georgina and Rachel

# The Aerodynamic Characteristics of an Exposed Racing Car Wheel

**Andrew Paul Mears**

Submitted for the degree of Doctor of Philosophy
September 2004

## Abstract

The aerodynamics of an exposed racing car wheel have been analysed using experimental and computational (CFD) techniques. A 40% full-scale pneumatic tyre/wheel assembly was used for the experimental investigations and the exact geometry was replicated in the CFD model. The wheel had an aspect ratio of 0.53 and the tests were conducted at a Reynolds number, based on the wheel diameter, of $2.5 \times 10^5$. Both rotating and stationary wheels were tested with moving and fixed ground-planes, respectively.

The experiments were conducted using new and existing methods of data acquisition and analysis. A non-intrusive radio telemetry system was successfully designed and developed that enabled surface static pressure data to be transmitted from a rotating wheel to a local PC. Other experimental techniques included the use of particle image velocimetry (PIV) and a pneumatic non-embedded five-hole pressure probe to investigate the flow-field about the wheel.

The early flow separation, which is a characteristic of the rotating wheel, was observed in the surface static pressure distributions and PIV velocity fields. Lift and drag forces were found to decrease as a result of wheel rotation, which agreed with the work of other investigators, and the mechanisms responsible for such force reductions are postulated. The wake structures were investigated and showed weaker streamwise vorticity for the rotating wheel compared to the stationary wheel.

The most important and remarkable aspect of this work was the experimental observation and subsequent CFD prediction of the rear jetting flow mechanism whose existence was previously theoretically predicted by another investigator. The PIV velocity fields clearly show the rear jetting phenomenon and this is further corroborated by a negative pressure peak in the surface pressure distributions on the wheel centreline. The effects the rear jetting phenomenon has on the wake mechanics, and hence the forces acting on the rotating wheel, are postulated.

# Declaration

The work in this thesis is based on research carried out at the Centre for Automotive Research, School of Engineering, University of Durham, England. No part of this thesis has been submitted elsewhere for any other degree or qualification and it is all my own work unless referenced to the contrary in the text.

# Acknowledgements

First and foremost, I would like to express my deepest thanks to my supervisor, Dr. Rob Dominy, for the continued support, guidance and encouraging words he has offered me throughout the course of this work.

My thanks must extend to the staff in the School of Engineering, in particular Mr. Ian Hutchinson (Electronics Workshop) for manufacturing the radio telemetry system and Mr. Roger Little for his sterling efforts in the manufacture of the wheel rim assembly.

I must also thank my fellow research students for the countless discussions and chats that made my time at Durham most enjoyable. To name but a few of you: Mr. Andy Lawson, Mr. Craig Robinson, Dr. Hui Yang, Dr. Grant Ingram and Dr. Tom Joyce.

I am extremely grateful to the University of Durham Ph.D. studentship fund for providing the funding that enabled this work to happen.

Thanks must go to my wife, Georgina, for her love and support throughout the course of this research and for encouraging me to pursue my aspirations.

Finally, a very special thanks to my little daughter, Rachel, for her abilities to make me laugh and smile.

# Contents

# List of Figures

# List of Tables

# Nomenclature

$A_e$ ..... Element Area ($m^2$)

$A_t$ ..... Cross-sectional Area of the Wind Tunnel ($m^2$)

$A_w$ ..... Frontal Area of the Wheel ($m^2$)

$C_{Dw}$ ..... Wheel Drag Coefficient

$C_{Lw}$ ..... Wheel Lift Coefficient

$Cp$ ..... Surface Static Pressure Coefficient

$C_{Pitch}$ ..... Pitch Coefficient

$C_S$ ..... Static Pressure Coefficient

$C_T$ ..... Total Pressure Coefficient

$Cv_i$ ..... Velocity Coefficient

$C_{Yaw}$ ..... Yaw Coefficient

$D$ ..... Wheel Diameter (m)

$f_{rot}$ ..... Wheel Rotational Frequency (Hz)

$f_S$ ..... Sampling Frequency (Hz)

$F_{De}$ ..... Drag Force Acting on Element (N)

$F_{Dw}$ ..... Drag Force (N)

$F_{Lw}$ ..... Lift Force (N)

$n$ ..... Vortex Shedding Frequency

$P_1$ ..... Pressure at Hole 1 (5-hole probe)

$P_2$ ..... Pressure at Hole 2 (5-hole probe)

$P_3$ ..... Pressure at Hole 3 (5-hole probe)

$P_4$ ..... Pressure at Hole 4 (5-hole probe)

$P_5$ ..... Pressure at Hole 5 (5-hole probe)

$P_{atm}$ ..... Atmospheric Pressure (Pa)

$P_{Av}$ ..... Mean Pressure from Holes 2-5 (5-hole probe)

$P_{dyn\_ref}$ ..... Reference Dynamic Pressure (Pa)

$P_M$ ..... Measured Pressure at Transducer (Pa)

$P_O$ ..... Total Pressure (Pa)

$P_{O\_ref}$ ..... Reference Total Pressure (Pa)

$P_S$ ..... Static Pressure at Surface of Wheel (Pa)

$P_{S\_ref}$ ..... Reference Static Pressure (Pa)

$Re$ ..... Reynolds Number

$r_M$ ..... Radial Position of Pressure Scanner (m)

$r_S$ ..... Radial Position of Pressure Tapping (m)

$r_W$ ..... Wheel Radius (m)

$St$ ..... Strouhal Number

$t$ ..... Time (s)

$T_{atm}$ ..... Atmospheric Temperature (deg C)

$u$ ..... Horizontal Velocity Component Normal to Streamwise Component (m/s)

$v$ ..... Vertical Velocity Component Normal to Streamwise Component (m/s)

$V_B$ ..... Moving Groundplane Velocity (m/s)

$V_C$ ..... Wheel Circumferential Velocity (m/s)

$V_{D/A}$ ..... Voltage Output from D/A

$V_{POT}$ ..... Potentiometer Voltage (V)

$V_{ref}$ ..... Freestream Velocity (m/s)

$V_{LC}$ ..... Load Cell Voltage (V)

$w$ ..... Streamwise (Axial) Velocity Component (m/s)

$W$ ..... Wheel Width (m)

*Greek Letters*

$\beta$ ..... Yaw Angle (deg)

$\zeta$ ..... Spanwise Vorticity

$\theta$ ..... Wheel Angular Position ($deg$)

$\theta_{PHASE(OFFSET)}$ ..... Phase Angle Offset (deg)

$\mu$ ..... Fluid Dynamic Viscosity [Air] ($Ns/m^2$)

$\xi$ ..... Streamwise Vorticity

$\rho$ ..... Fluid Density [Air] ($kg/m^3$)

$\rho_{x,y}$ ..... Correlation Coefficient

$\tau$ ..... Telemetry Transfer Time Lag (s)

$\phi$ ..... Tapping Angle Relative Normal to Tread Region

$\omega$ ..... Angular Velocity (rad/s)

*Abbreviations*

A/D ..... Analogue-to-Digital Converter

AR ..... Aspect Ratio (Wheel Width/Diameter)

CFD ..... Computational Fluid Dynamics

CMM ..... Coordinate Measuring Machine

D/A ..... Digital-to-Analogue Converter

FFT ..... Fast Fourier Transform

LC ..... Load Cell

LDA ..... Laser Doppler Anemometry

MGP ..... Moving Groundplane

N-S ..... Navier-Stokes Equations

PIV ..... Particle Image Velocimetry

PRESTO! ..... PREssure STaggering Option

PSD ..... Power Spectral Density (Power Spectra)

RANS ..... Reynolds Averaged Navier-Stokes

SF ..... Velocity Scaling Factor (PIV)

SPD ..... Surface Pressure Distribution

TTFC ..... Tubing Transfer Function Correction

WI ..... Wake Integral

# Chapter 1

# Introduction

This thesis investigates the aerodynamics of exposed racing car wheels. The majority of the work focuses on the time-averaged aerodynamic flow-field although references are made to the unsteady flow structures exhibited in the highly three-dimensional, inherently unsteady wheel wake. A key element to this work was the development of experimental instrumentation techniques and methods of analysis that make it possible to investigate the aerodynamic characteristics of wheels. It is hoped that these techniques may prove beneficial far beyond the scope of the investigations conducted in the present work.

This chapter gives a brief introduction into wheel aerodynamics and the research that has been conducted in this investigation. The main research objectives are highlighted and an overview of the thesis structure is stated. This introductory chapter is not intended to provide an exhaustive account of wheel aerodynamics but merely set the scene in the context of this investigation and give an insight into subsequent chapters and their contents.

## 1.1 Overview of Wheel Aerodynamics

The aerodynamic characteristics of rotating exposed wheels have received growing attention in recent years both experimentally (Hinson [22]; Mears et al [39], [40] and [38]; Skea et al [61] and [62]; Knowles et al [31]) and computationally (Axon [5];

Axon et al [6] and [7]; Kellar et al [28]; Skea et al [61] and [62]; Knowles et al [31] and [30]). However, unanswered questions still remain with respect to the flow physics of the isolated wheel. Understanding how the wheels interact with the bodywork of a racing car is a much greater challenge, and perhaps one which cannot be fully resolved until the isolated wheel flows are fully understood.

Historically the air flow about exposed racing wheels has received relatively little attention and this is primarily due to the technical difficulties associated with a wheel rotating in contact with a moving groundplane, which has usually allowed only a superficial analysis of the flow-field. The flow-field is extremely complex, dominated by three-dimensionality and inherent flow unsteadiness in the separated region.

Exposed wheels contribute significantly in terms of wheel drag and it has been reported by Dominy [16] that for an open-wheeled Grand Prix car the wheel drag, as a percentage of the overall vehicle drag, can be between 35 and 50 percent. The drag force acting on the wheel is relatively straightforward to measure using a conventional load cell, although inconsistencies exist between published data (see Chapter 2). However, the quantification of the lift force is far more difficult since separating the aerodynamic lift force from the varying wheel-to-ground reaction force is a difficult task. Quantifying the wheel lift force is of major importance in the context of racing cars where the magnitudes of the aerodynamic forces are proportionately higher compared to those of passenger cars, and any source of confusion in the experimental assessment of the overall lift force magnitude and front-to-rear lift force distribution could have serious affects on the vehicle dynamics and indeed the overall performance of the racing car.

It has been widely accepted since the work of Fackrell [19] and Fackrell and Harvey [20], [21] that an isolated stationary wheel in contact with the ground generates positive time-averaged lift and drag forces, and these forces decrease due to wheel rotation. The current understanding of the exact mechanisms responsible for such force reductions remain fairly limited and are discussed throughout this thesis.

The racing car wheel is essentially a low aspect ratio circular cylinder that rotates in contact with the ground. The majority of research involving cylinder flows has focused on an "infinite" cylinder which spans the working section positioned normal to the free stream, far away from any plane boundary; these types of investigation have been well documented by many fluid dynamicists (such as Zdravkovich [69] and Norberg [45]). The flow about the cylinders usually being quasi-two-dimensional with minimal effects from any cross flow (cross component of free stream velocity). Caution should therefore be taken when trying to draw any meaningful conclusions and correlations between a predominantly two-dimensional flow-field and that of three-dimensional flow. However, a number of investigations have been conducted looking at free-end effects for low aspect ratio circular cylinders (such as Park and Lee [47], [48]), where the cylinder was positioned with one end fixed to the wind tunnel floor and the opposite end located in the free stream away from any wall. The influence of ground effect on circular cylinder flows has also been investigated (such as Bearman and Zdravkovich [10]), where the ground clearance of the cylinder was reduced until the cylinder was in contact with the ground. The relevant details of these investigations are given in Chapter 2.

The aerodynamics of the complete F1 racing car are highly complex with most parts of the car being largely influenced by interactions with other parts of the car. Therefore, ideally it is important to experimentally assess the complete vehicle. For the wheel flows, where the current knowledge is relatively limited, it is important to fully understand the wheel in isolation from the rest of the car before any attempt is made to analyse the wheel-bodywork interaction. Therefore, the motivation for this work is to further the current understanding of wheel aerodynamics, which will lead to routine integration of the wheels into the experimental assessment of the aerodynamics of the complete F1 racing car, and thus ultimately help racing car aerodynamicists in the design and set-up of their cars.

## 1.2 Scope and Objectives of this Investigation

### 1.2.1 Scope of this Investigation

This work will investigate the aerodynamic characteristics of an exposed racing wheel. The work will be confined to the investigation of an isolated/exposed wheel without camber effects, since a more comprehensive understanding of this relatively "simpler" case will provide the necessary building blocks for future work that could encompass such details as vehicle bodywork (i.e. front wing, suspension, brake ducts, etc.), or in the context of passenger cars, wheelhouse cavities. Suffice to say our current understanding of wheel flows is not at such an advanced state to permit a complete analysis of how the wheel flows interact with other vehicle systems or components. Although this investigation is primarily aimed at racing car wheel aerodynamics, the scope of the work could easily be adapted to passenger vehicle wheel aerodynamics.

### 1.2.2 Objectives of this Investigation

The main objectives of this work were derived having conducted the extensive literature review, which is presented in the next chapter. They can be summarised as follows: -

- To develop the necessary experimental techniques and methods of analysis to allow a detailed analysis of the wheel flows. Namely, to develop a non-intrusive radio telemetry system enabling surface static pressure data to be transmitted from a rotating or stationary (non-rotating) wheel to a local laboratory computer for data analyses.

- To further advance the current understanding with respect to the flow physics associated with exposed racing wheels and highlight any pertinent flow features. This will be achieved by using a combination of new and existing experimental and computational tools and techniques.

- To investigate the use of computational fluid dynamics (CFD) at predicting the flow-field about exposed racing wheels, both in terms of quantitative and

qualitative results accuracy, using a commercial CFD code and relatively limited hardware resources.

## 1.3 Thesis Structure

Chapter 2 addresses and critically appraises the current literature within the field of wheel aerodynamics, both experimentally and computationally. Cylinder flows are also reviewed in an attempt to assist and further develop the understanding of the flow physics associated with exposed wheels. Chapter 3 concentrates on the design of the experimental multi-element wheel. Design descriptions and the motivating factors behind them are discussed. Chapter 4 presents the experimental details regarding the design, development and commissioning of the pressure measurement instrumentation, namely the Durham University Radio Telemetry System. System specifications, software development, analysis procedures and validation are discussed. Chapter 5 focuses on the experimental flow-field investigation techniques. Experimental configurations are presented and discussed for both pneumatic pressure probe and particle image velocimetry (PIV) methods. Chapter 6 deals with all aspects of the 3D computational modelling using the commercially available Fluent 6.0 CFD package and relatively limited computational resources. Chapter 7 shows details of the experimental and computational investigations that were conducted using the instrumentation and CFD techniques previously described. Chapter 8 presents the experimental results acquired using the various instrumentation techniques. Chapter 9 presents the CFD results obtained through the numerical modelling. Chapter 10 discusses the experimental and computational results, and aims to link together the various results obtained in this work and those of other investigators. The "special" flow features of the wheel are discussed. Chapter 11 states the main conclusions of the research and gives some recommendations for future work.

# Chapter 2

# Literature Review

The aims of this chapter are to critically review the literature and current level of understanding of wheel aerodynamics from an experimental and computational standpoint. A comprehensive and thorough critical appraisal of the relevant literature is presented, mainly for isolated wheels, although wheels housed within wheelhouse cavities are discussed where appropriate. A brief review highlighting the relevance of circular cylinder flows has been conducted in an attempt to assist in the understanding of the physics of the flow about an isolated wheel. The wheel aerodynamic literature review takes the format of reviewing the work of each investigator in chronological order before the results and current understanding are summarised.

## 2.1 The Relevance of Bluff Body Flows

A bluff body is categorised as a body of any shape which experiences complete boundary layer separation before the trailing edge. The overall drag force acting on the body is dominated by pressure drag. The racing car wheel is a bluff body and therefore a review of bluff body flows, such as two-dimensional flow about high aspect ratio cylinders or flows about axisymmetric bodies such as spheres, could assist in the analysis of the wheel flows. However, certain distinguishing features of the wheel and the conditions of its operation complicate the flow-field making the analysis more difficult. Namely, the wheel has a low aspect ratio, typically

of less than unity, and it rotates in contact with a moving groundplane. These conditions are not new to the world of fluid mechanics and a number of investigations have been carried out for each condition (whether low aspect ratio, rotation, etc.), however it is difficult to find an investigation in the literature of circular cylinder flows that encompasses all of these factors in a single experiment. The analysis of such literature that investigates each constituent factor of the wheel flows, however, can still be useful in further understanding the aerodynamics of the wheel.

### 2.1.1 Effects of Low Aspect Ratio

End effects play an important part in determining the wake structure of the wheel. The low aspect ratio (AR) of a racing car wheel (typically AR = 0.5) causes extrinsic three-dimensional flow effects as well as intrinsic flow three-dimensionality caused by natural instabilities in quasi-two-dimensional flow. Roshko [52] states that intrinsic three-dimensional effects first appear at Reynolds numbers above 180 and contribute to the turbulent nature of the flow at higher Reynolds numbers. For a bluff body positioned in a freestream with no ground and with an aspect ratio of 0.5 the spanwise coherent vortex shedding structures would be significantly weakened by the flow at the ends of the body. Park and Lee [47] conducted an experimental study into the wake structure of finite cylinders using hot-wire anemometry. Cylinders of varying aspect ratio were positioned vertically in the working section with one end secured on a fixed groundplane and the other end was free with no boundary. The power spectra of the streamwise velocity component in the wake of the cylinders were presented and the clear peak seen for high aspect ratio bodies was observed at a Strouhal number (St) of around 0.2, which is typical for two-dimensional flow about cylinders. As the aspect ratio of the cylinders was decreased the shedding frequency decreased (lower Strouhal number (around St = 0.15)) until at an aspect ratio of 6.0 (which is much larger than a racing car wheel) the power spectra did not show any signs of vortex shedding. Moreover, the regular vortex shedding disappeared towards the free end of the cylinder for the cylinder of aspect ratio 10.0. Two counter-rotating longitudinal vortices were observed by Park and Lee [47] at the free end of the cylinder. It therefore seems, and will indeed be

shown and discussed throughout this thesis, that the wake structure for a wheel with an aspect ratio of 0.5 would be completely different to that of a two-dimensional cylinder although the centreline, or midspan, of the wheel could exhibit some two-dimensionality but not any spanwise coherent vortex shedding. In a recent study by Park and Lee [48], a cylinder was fitted with different end profile geometries (flat, hemispherical, radiussed and bevelled geometries) to establish the effects of such geometrical features on the wake structures. The vortex shedding was seen to be influenced by the end profile geometry, as indeed should be the case since this geometry would influence the generation of the counter-rotating vortices at the free end of the cylinder and hence influence the secondary flow and three-dimensionality. Therefore, two-dimensional flows, such as high aspect ratio cylinders, have limited relevance in the context of the wheel flows. Moreover, according to Bearman [8] the drag generation for three-dimensional bodies is not dominated by the regular shedding of intense vortices.

### 2.1.2 Effects of Ground Contact

The effects of ground contact also eliminate regular vortex shedding even for high aspect ratio cylinders and have been the subject of a number of investigations. Bearman and Zdravkovich [10] showed these effects for a cylinder that spanned the working section thus eliminating any extrinsic three-dimensionality. The cylinder-to-ground clearance ratio was varied and a hot-wire probe was placed downstream of the cylinder. Power spectral density plots of the hot-wire streamwise velocity component showed regular vortex shedding when the cylinder-to-ground gap was large. At small clearance ratios the power spectra showed a small peak corresponding to weakened vortex shedding, although these data were for the upper region of the cylinder wake. At the lower region of the wake (next to the groundplane) there were no signs of vortex shedding and this will be due to the suppression of the separated shear layer on the underside of the cylinder. This has been corroborated recently by Lei et al [35] who presented similar data and also observed that the suppression of the vortex shedding was dependent on the boundary layer thickness at the cylinder position. For zero ground clearances both investigators found no regular vortex

shedding. Similar conclusions were drawn in an investigation by Kim et al [29] for flow about a square cylinder at various cylinder-to-ground gap ratios. For a wheel, at least a stationary wheel with fixed groundplane, the presence of the groundplane and low aspect ratio will change the flow structure vastly as will be shown further on in this thesis. Additionally, ground contact prevents direct lift force measurement using a force balance due to the varying wheel-ground reaction force.

### 2.1.3 Effects of Wheel Rotation

Wheel rotation complicates the flow field still further. The well known Magnus effect for a high aspect ratio cylinder, if rotated in the same direction as the wheel, would cause a negative lift force. However, when the cylinder is in contact with the groundplane the lift force would change sign into a positive lift force as the Magnus effect no longer has an effect. The circulation of fluid around the complete cylinder periphery no longer exists due to ground contact. There will still, however, be fluid in circulation with the cylinder or wheel because of the no-slip condition at the surface, but ground contact prevents complete circulation of fluid; therefore there will be no accelerated fluid around the lower part of the cylinder / wheel. All of these effects are discussed where relevant throughout this thesis.

The relevance of nominally two-dimensional cylinder flows is therefore limited with regard to further understanding the wheel flows. The free end cylinder flows do however give an insight into the three-dimensional flow structures (e.g. the trailing vortices) in the wake, even though no groundplane was present. Indeed the wheel flows are a combination of low aspect ratio, ground contact and rotation, and therefore all of these factors need to be present in one experiment. This will in fact be shown in the remainder of this chapter, such to correctly analyse the aerodynamics of rotating wheels.

## 2.2 A Review of Wheel Aerodynamics

The total number of research publications within the field of wheel aerodynamics has more than doubled in the past few years, although this still equates to few papers when compared to upper body aerodynamics. The main reasons for such increased interest into wheel aerodynamics are: firstly, moving groundplanes (MGP's) are now commonplace both within academia and industry; secondly, the benefits of fully understanding wheel aerodynamics in the context of racing and passenger cars are better established nowadays; and thirdly CFD plays a more predominant role in the design and evaluation of vehicle aerodynamics. A factor in the increase in CFD research is the advancement in the available computationally intensive hardware, that have the capability of solving unstructured and structured grids with an ever increasing number of cells. Current publications in general vehicle aerodynamics research, such as Singh [60] and Sims-Williams and Duncan [59], quote three-dimensional volume grids of the order of $10^6$ and $10^7$ cells, respectively, and generally employ parallel computing hardware.

Morelli [42] was the first to carry out aerodynamic research specifically aimed at automobile wheels. The research encompassed both isolated and shrouded (faired) wheels. A wheel was mounted in the centre of the wind tunnel working section at the University of Turin; the working section was of circular geometry with a diameter of 3m. A flat plate was mounted in the working section, parallel to the freestream, in order to represent a stationary groundplane. The wheel was inserted a small distance, without any contact, into a cut out in the plate. According to Morelli, this was to simulate the deflection of the wheel onto the ground. He stressed that there was no contact between the wheel and plate under any condition of rotation, and wheel rotation was made possible via a DC motor. A wheel fairing could cover the wheel at various heights and a six-component force balance, connected to the driveshaft, was used to measure the aerodynamic forces and moments. The plate/wheel assembly could be yawed up to a maximum yaw angle of twenty degrees.

The most significant result that Morelli observed was that the wheel lift force was in

fact negative. This result is of opposite sign, compared to subsequent observations where the wheel lift is positive for both stationary and rotating wheels. The reason why he obtained a negative lift force is most likely due to the gap that existed between the wheel and ground causing air to accelerate under the wheel and therefore resulting in a reduction in static pressure. He also discovered that by fitting smooth covers to both sides of the wheel rim the drag was reduced by around 22%. Another observation was that the drag force acting on the wheel increased by around 7-10% from the stationary to the rotating wheel; again contrary to subsequent results. However, all results should be taken with slight caution due to the negative lift force results.

Stapleford and Carr [63] conducted a study into fully exposed rotating wheels when attached to an idealised racing car model. The research was aimed at establishing the importance of having a moving ground surface, wheel rotation and ground clearance on the aerodynamic forces. They identified the need for correct wind tunnel representation of the wheel flows, particularly for racing cars where there are serious consequences if errors exist regarding the experimental evaluation of the aerodynamic forces due to the cars being relatively light weight and travelling at potentially high speeds. Wind tunnels at M.I.R.A. (The Motor Industry Research Association) and Imperial College were used for stationary ground and moving ground work, respectively. The Imperial College 5ft x 4ft tunnel was used at the lower freestream velocity of 46m.p.h., due to belt lift at the higher speed of 70m.p.h. The model consisted of a very slender body with four wheels of typical track and wheelbase proportions. Wheel rotation was enabled by the use of an electric motor mounted inside the model body. Force measurements were taken using a conventional balance, which was mounted under the working section for the stationary groundplane work at M.I.R.A, and mounted overhead in the case of the moving groundplane at Imperial College. Polystyrene wheels of 6 ins. (152.4mm) diameter with square edge profiles were used, giving a wheel diameter based Reynolds number of approximately $2 \times 10^5$. Stapleford and Carr would have preferred a larger Reynolds number, since the wheel was in the critical Reynolds number range, and they therefore thought

repeatability would be poor, but bearing in mind the reduced velocity of the wind tunnel freestream this was not possible. However, they found that the level of repeatability was acceptable, within the limits of $\pm 0.10$ for $C_{Dw}$ and $\pm 0.15$ for $C_{Lw}$, although these levels of repeatability appear proportionately high relative to the values of lift and drag coefficient obtained; $C_{Lw}$ of 0.167 and $C_{Dw}$ of 0.801 for the rotating wheel at the minimum ground clearance of 0.05 inches. For the moving ground simulation the wheel was not allowed to contact the moving belt as this would have caused difficulties in measuring the aerodynamic lift forces. Strips of paper, bridging the gap between the wheels and the belt, were used in an attempt to block the airflow under the wheels at the minimum ground clearance. When the wheel/ground clearance was increased the lift force tended towards zero for the stationary wheel, which is expected since the flow-field becomes more symmetrical as the boundary effects have a diminishing influence the further away the wheel is positioned. For the rotating wheel the Magnus effect was observed as the wheel/ground clearance was increased, although at reduced magnitude when compared to the theoretical value for two-dimensional flow over a rotating circular cylinder. For the wheel, the finite length will reduce the effect due to three-dimensional flow around the sides of the wheel.

Surface pressures were measured using a static pressure probe, with the tapping positioned at the centreline of the wheel as close as possible to the surface. Figure 2.1 shows the apparatus used to measure the static pressures around the wheels. Readings were made at intervals of 30 degrees around the wheel periphery (see Figures 2.4 and 2.5 which show the surface static pressure distributions of Stapleford and Carr [63] for the centreline of the rotating and stationary wheels, respectively (after Fackrell [19])). These results will be discussed alongside those of Fackrell [19] later in this section. The use of a static pressure probe would have prevented the measurement of pressure at the contact patch and this is why pressure coefficients in excess of unity were not observed. Also the probe and support apparatus must have affected the measurements taken due to the intrusive nature of the technique. Drag and lift coefficients were calculated using the force balance. The coefficients

presented were all positive values, and were reduced when the wheels were rotating, which is in agreement with subsequent results.

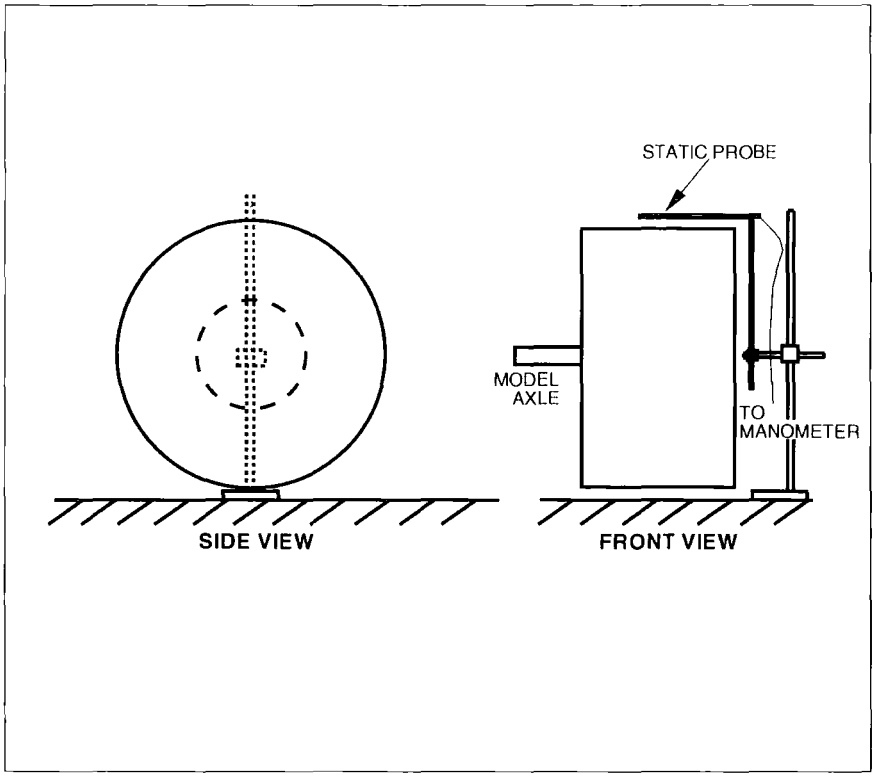


Figure 2.1: Apparatus for Measuring the Static Pressure Distribution around Stationary and Rotating Wheels (after Stapleford and Carr [63]).

Stapleford and Carr [63] also conducted a flow visualisation investigation using wool tufts on a framework that was fixed over the front and rear wheels of the car model on the wheel centreline. Figure 2.2 shows the flow patterns obtained for the stationary and rotating wheels with the gaps sealed. The results show that the flow separated from the upper region of the wheel at an earlier position for the rotating wheel when compared to the stationary wheel. The flow also exhibited flow reversal in the wake. The stationary wheel shows attached flow around the top of the wheel and downwash behind it. This particular method of flow visualisation can provide useful qualitative information, although using a large grid can be intrusive and affect the flow-field.

Figure 2.2: Stationary (left figure) and Rotating (right figure) Flow Patterns using a Wool Tuft Grid (after Stapleford and Carr [63])

Stapleford and Carr [63] found that the moving ground surface did not appear to affect the aerodynamic forces significantly, except where a very small ground clearance was present. The errors that resulted as a consequence of leaving a gap under the wheel were exacerbated for the moving ground work since it merely increased the flow through the gap. An equivalent stationary wheel method was proposed to be used in place of the rotating wheel with moving ground. The idea being that the aerodynamic forces acting on the rotating wheel could be replicated by leaving a small gap of between 0 and 5% of the wheel diameter under the stationary wheel with fixed ground. However, leaving a small gap under the wheel will, admittedly, reduce the lift force acting on the wheel due to a reduction in the local static pressure at the contact patch, at the expense of considerably altering the flow-field, and will not be representative of the true on-road conditions. As will be seen later in this thesis, it is the early separation that is one of the agents causing a reduction in the lift force for the rotating wheel and this cannot be reproduced with a stationary wheel.

The work by Fackrell [19] into isolated wheel aerodynamics is the most well cited. This work is described in Fackrell and Harvey [20], [21], and in more detail in Fackrell [19]. A number of CFD studies have used the results of Fackrell as a means of model validation.

The research carried out by Fackrell involved looking into the flow-field around exposed Grand Prix car wheels. The wheels were representative of Formula One cars

with a diameter of 16.375 ins. The wheels were tested in the Imperial College wind tunnel, equipped with a moving ground, at a freestream velocity of 61ft/sec, which corresponds to a Reynolds number of $5.3 \times 10^5$. Fackrell considered this to be sufficiently high that it would be representative of the real flow of a full-scale racing car wheel, since both flows were in the supercritical flow regime. Six different wheel configurations were tested: two different edge profiles and three different wheel widths. Hence, the effects of edge profile and aspect ratio were analysed. The main geometrical features of Fackrell's wheels are shown in Table 2.1. The experimental configuration was such that the wheel was in contact with the moving ground as depicted in Figure 2.3. The wheel was mounted on steel rods, which were not too dissimilar to the suspension of a racing car. With this configuration Fackrell was led to develop a method that would enable the surface pressures around the wheel to be measured, since a conventional force balance would not allow the lift forces to be measured with the wheel contacting the ground. The system comprised a condenser microphone, with its associated oscillator, which was placed on the axis of rotation. A series of pressure tappings were mounted across the wheel (spanwise) and each one was connected in turn. The signal from the microphone was then taken from the rotating assembly through slip rings and into a reactance converter. The output of the converter was proportional to the pressure acting on the microphone. This system allowed time-averaged surface pressures to be measured and by integrating the pressure data the time-averaged lift and drag forces and coefficients could be calculated. Further details can be found in Fackrell [19].

| Wheel | Diameter (in) | Width (in) | AR |
|---|---|---|---|
| A | 16.375 | 4.25 | 0.26 |
| B | 16.375 | 6.75 | 0.41 |
| C | 16.375 | 9.25 | 0.56 |

Table 2.1: Main Geometrical Features of Fackrell's Wheel.

Surface pressures were measured for both stationary and rotating wheels. Figure 2.4 shows the centreline static pressure distribution around the rotating wheels (after

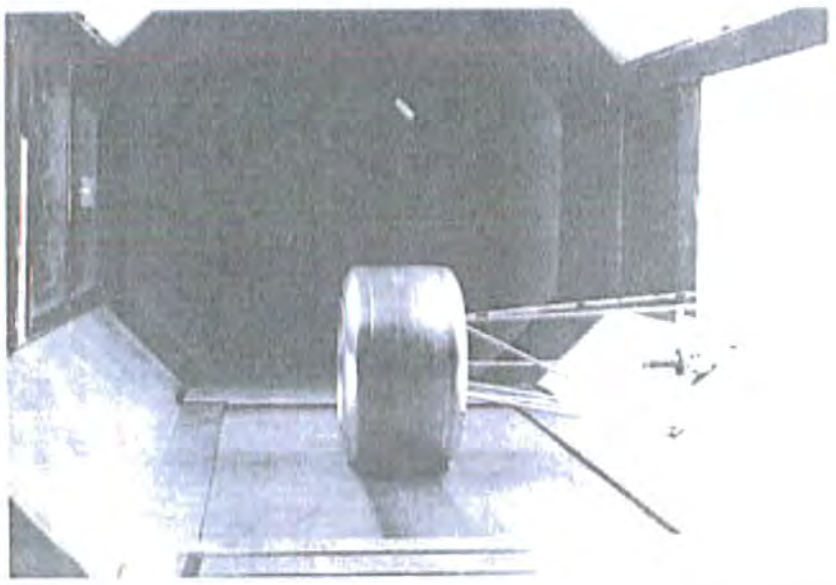

Figure 2.3: Experimental Wheel Configuration (after Fackrell [19]).

Fackrell [19]). Wheel 2 had a much more rounded edge profile than Wheel 1. The results of Stapleford and Carr [63] are also presented in this figure. The pressure distribution of Wheel 1 and Wheel 2 look very similar, although it was only edge profile that was changed; the aspect ratio was kept constant. There was a slight difference in base pressure just behind the wheel, and this will be due to the different edge profile geometry affecting the formation and strength of the trailing vortices and hence base pressure as the flow from the separated region is entrained into the vortical structures. Bearing in mind these results are for the centreline of the wheel, one would expect the pressure distribution to be more affected closer to the wheel edge. At the contact patch (90 degrees) both Wheel 1 and Wheel 2 have pressure coefficient values in excess of unity. Fackrell postulated that this was due to the air being squeezed in the corner between the wheel and the road and referred to it as the "jetting" phenomenon. An interesting point mentioned by Fackrell was that he expected to observe a negative pressure peak behind the line of contact, although he didn't observe it experimentally. However, he did predict the existence of the "jetting" phenomenon after the line of contact. This phenomenon is discussed in great detail throughout the present work. The results of Stapleford and Carr [63] do not show the jetting phenomenon, although it is not surprising bearing in mind the gap that existed between the wheel and ground. Moreover, even if the wheel

had contacted the ground in the investigation conducted by Stapleford and Carr, the pressure at the contact patch would have been impossible to measure using a static pressure probe as demonstrated by Imaizumi and Yoshida [24]. The results of Stapleford and Carr actually show that the pressure near the contact patch is below the stagnation value that would be expected even when neglecting the "jetting" effects, and this is again due to the gap that existed under the wheel. Good agreement between base pressures is apparent between the results of Fackrell and Stapleford and Carr, however these measurements were taken in the separated region where the pressure should be relatively constant and probably less sensitive to the intrusive nature of the static probe. From Figure 2.4 it can be seen that the flow separates at approximately 290 degrees, which is of course in front of the top of the wheel.

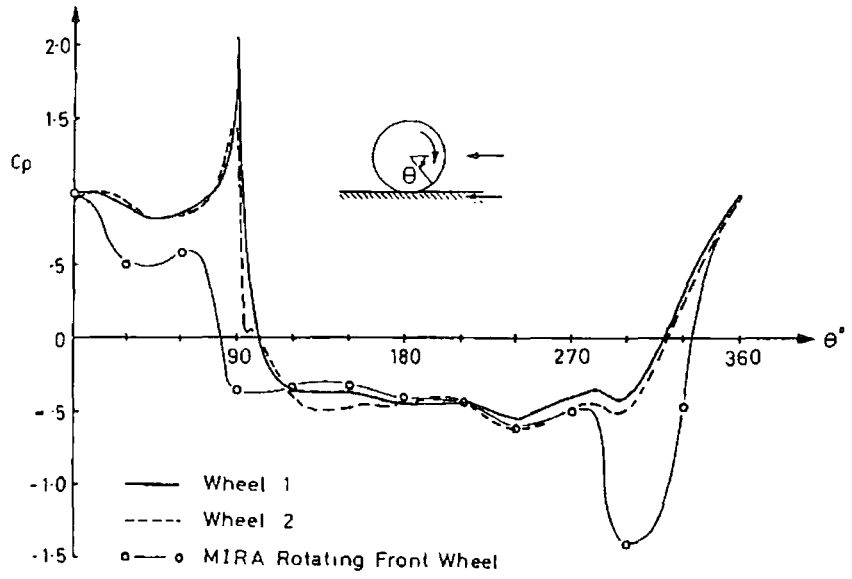


Figure 2.4: Centreline Surface Static Pressure Distribution for a Rotating Wheel (after Fackrell [19]).

Figure 2.5 shows the static pressure distribution around a stationary wheel (after Fackrell [19]). Again, the results of Stapleford and Carr [63] are also presented in this figure. The pressure can be seen to rise to the stagnation value at the contact patch. There is no "jetting" in this case due to the wheel being stationary. The base pressure is of a much lower pressure than the rotating case resulting in higher drag for the stationary wheel. The lift and drag coefficients for the B2 of Fackrell

are presented in Table 2.2. The strong negative pressure over the wheel will contribute to the increase in lift for the stationary wheel and will be due to separation occurring later i.e. at approximately 210 degrees, therefore the flow accelerates over the top of the wheel. The results of Stapleford and Carr show a similar trend, but again the pressures are in error due to the experimental set-up. Once again, the base pressure seems to be in reasonable agreement and this is most likely due to the aforementioned reasons.

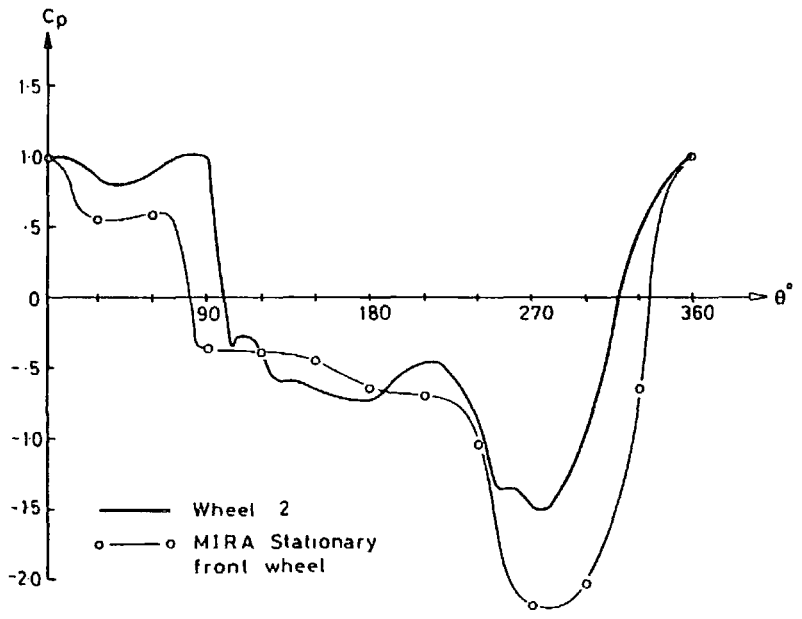


Figure 2.5: Centreline Surface Static Pressure Distribution for a Stationary Wheel (after Fackrell [19]).

| | $C_{Lw}$ | $C_{Dw}$ |
|---|---|---|
| B2 Rotating | 0.44 | 0.58 |
| B2 Stationary | 0.76 | 0.77 |

Table 2.2: Time-Averaged Lift and Drag Coefficients for the B2 Wheels (after Fackrell [19])

Fackrell also carried out an investigation into the flow-field in the wake of the wheel. A Kiel tube, insensitive to yaw up to $\pm$ 35 degrees, was used to measure total head

at four spanwise stations behind the wheel, both for the rotating and stationary wheels. Figure 2.6 shows the total head contours at the four different planes (after Fackrell [19]). In fact the only contour lines acquired and presented are those corresponding to 90% of the freestream value of total pressure. Fackrell stated these contours could be used loosely as the edge of the wake. However, only knowing the bounds of the wake shape has its limitations and no attempts were made to identify the flow structures in the near-wake, or further downstream of the wheel for that matter. No magnitude or direction of the local flow could be calculated since a single hole Kiel tube was used, which has limited use. The use of a multi-hole pressure probe, such as a five hole probe, would have yielded far more useful information into the flow structures in the wake, although by no means does the exclusion of such analyses detract from the relatively exhaustive investigation conducted by Fackrell. The total head contours do, however, provide supporting evidence that separation does occur before the top of the wheel, for the rotating case c.f. pressure distribution for rotating wheels (Figure 2.4).

Cogotti [14] carried out a two-part study into the aerodynamic characteristics of car wheels. Part one related to isolated wheels and part two was concerned with the effects of fitting the wheel to a car body. This review is only concerned with the results of part one. The study was conducted in the Pininfarina wind tunnel. Exposed wheels were fitted with 145SR10 Cinturato Pirelli tyres, which were then fitted to an AC motor. The motor enabled the ground clearance to be adjusted and the wheels were rotated at 1500rpm in order to match the circumferential wheel and freestream velocities, giving a test Reynolds number of $1.1 \times 10^6$ based on wheel diameter. The choice of Reynolds number was largely based on a study, by Cogotti, in which he varied the Reynolds number for an isolated stationary wheel experiment and measured lift and drag coefficients. He found a critical Reynolds number that was similar to cylinders and spheres. The transition range for the Reynolds number of a stationary wheel was found to be in the range $1 \times 10^5$ to $1 \times 10^6$. Figure 2.7 shows the drag and lift coefficients for an isolated stationary wheel contacting the ground at different Reynolds numbers (after Cogotti [14]). The drag and lift coef-

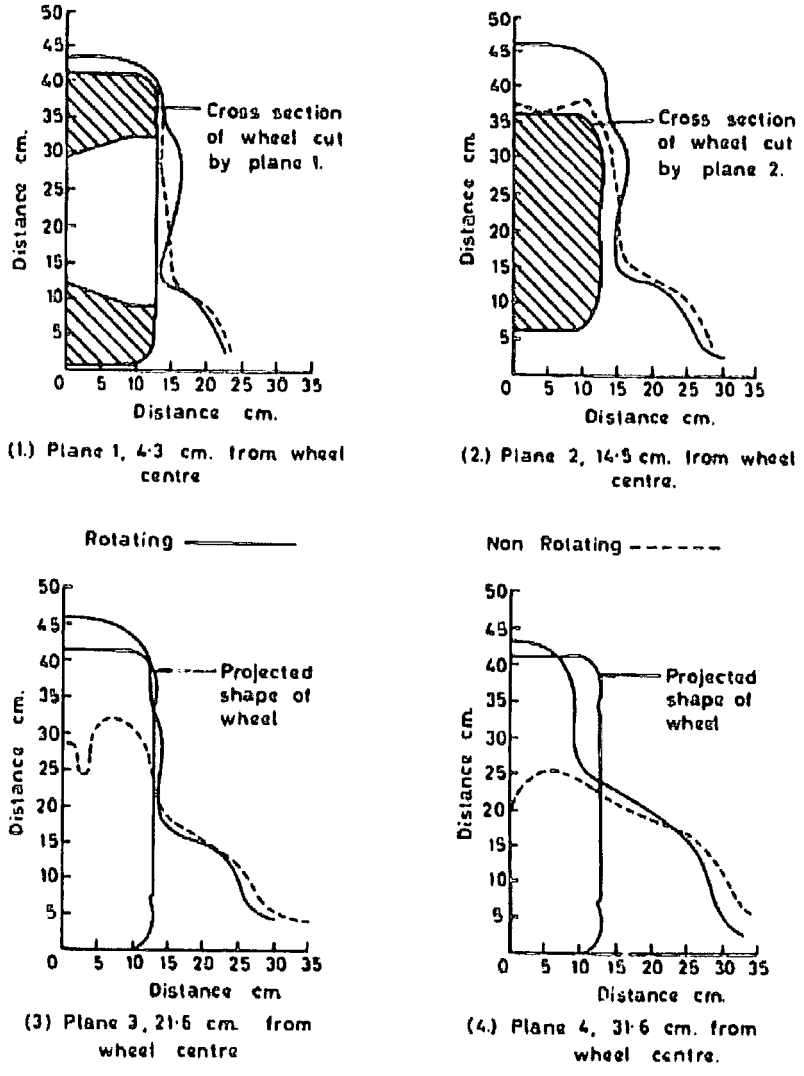


Figure 2.6: Wake Outline Behind Rotating and Stationary Isolated Wheels (after Fackrell [19]).

ficients are, on average, high at low Reynolds numbers and low at high Reynolds numbers, suggesting that the flow has gone through the transition from a sub-critical Reynolds number to a super-critical Reynolds number. This drag reduction from a sub-critical to supercritical regime is confirmed by Zdravkovich [69], who also states that a super-critical flow regime starts in the Reynolds number range of $5 \times 10^5$ to $1 \times 10^6$, which is in good agreement with Fackrell, whose Reynolds number was $5.3 \times 10^5$ i.e. super-critical. Cogotti made no attempt to investigate the Reynolds number effects for the rotating wheel. The Reynolds number for the present study is shown in Chapter 3 and is discussed in Chapter 10.

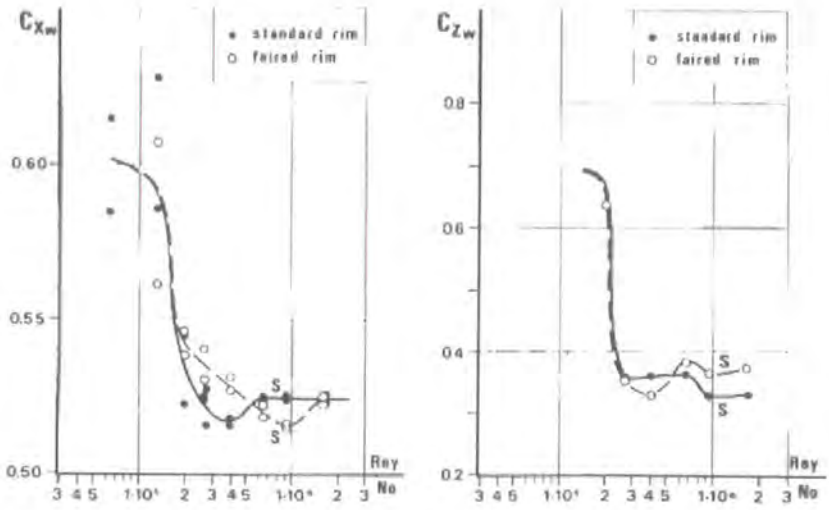


Figure 2.7: Drag and Lift Coefficients at Different Reynolds Numbers (after Cogotti [14]).

Tests were carried out for both stationary and rotating wheels. Whether a fixed groundplane or moving groundplane was used was not stated, although it is thought to be fixed based on the images presented. For the case of zero ground clearance small pads, the size of the wheel-ground contact patch, were inserted between the wheel and the ground to try and prevent air from flowing under the wheel.

The time-averaged lift and drag coefficients, obtained using a conventional force balance, were found to be positive for both stationary and rotating wheels. These values decreased with wheel rotation, which is in agreement with other investigators. Cogotti found that the lift coefficient was highly dependent on the wheel-ground sealing for a rotating wheel. Figure 2.8 shows the pressure distribution under the rotating wheel at different ground clearances. There is a strong negative pressure under the wheel until the wheel contacts the ground; the pressure then suddenly becomes positive. He states that sealing the gap is of critical importance to ensure that correct simulation of the true on-road conditions is met.

Cogotti also noted a marked reduction in wheel drag as a result of using a faired rim, which is in good agreement with Morelli [42]. Wheel drag was also found to

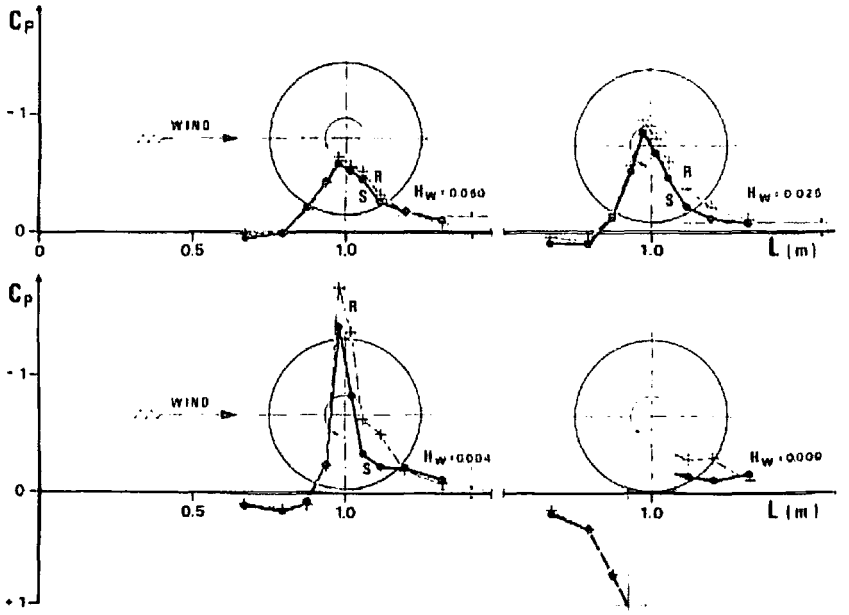


Figure 2.8: Stationary Groundplane Pressure Distributions (after Cogotti [14]).

increase with increased yaw angle. This is particularly important for passenger vehicles, where the localised flow at the wheels can approach at incidence. Wickern et al [68] state the local yaw angle is always approximately 15 degrees due to the flow from the nose of the vehicle, which causes the airflow to approach the front wheels at incidence. The wheels were tested on a production Audi A3 vehicle.

Bearman et al [9] carried out a study into wheel wake structures. The experiment actually used one of the wheels that Fackrell [19] had previously used. The Reynolds number was slightly higher at $5.5 \times 10^5$ c.f. Fackrell [19] of $5.3 \times 10^5$. A nine-hole pressure probe was used, which was located on traverse gear and connected to a local desktop computer to enable automation and data acquisition. Wake measurements were made at discrete points using a grid of points in the spanwise plane. The plane was 2.5 diameters downstream of the centre of the wheel. The data logged at each point were: total pressure, static pressure and flow direction. Flow direction was measured by aligning the probe with the local flow. This method is described in more detail in Bryer and Pankhurst [11]. From the measurements taken, all three components of the time-averaged velocity field and streamwise vorticity were computed. Figure 2.9 shows the contours of constant total pressure for

both stationary wheel, fixed ground and rotating wheel, moving ground. The taller wake is apparent for the rotating case, which agrees with Fackrell's observation. Direct comparison with Fackrell, with respect to total pressure contours in the wake, is difficult due to the axial position of the probes being quite different since the maximum distance Fackrell made measurements was 36.1cm (approximately 0.85 wheel diameters) downstream from the centre of the wheel, compared to 126cm by Bearman et al. The results of Bearman et al are limited in the sense that only one plane was traversed in the wake and were the only published results regarding wake structures behind isolated wheels prior to this work and the work of Knowles at al [31], [30].

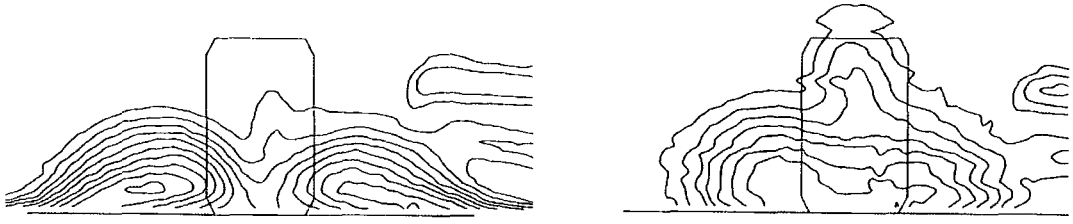

(a) Stationary. (b) Rotating.

Figure 2.9: Time-Averaged Contours of Constant Total Pressure in the Wheel Wake at 2.5D (after Bearman et al [9]).

Imaizumi and Yoshida [24] conducted a study into wheel aerodynamics. A notchback model and an open-wheeled model were used. The wheels were driven by electric motors for the rotating wheel case and the motors were disconnected for the stationary wheel study. A ground clearance of 2mm was chosen to allow for wheel rotation, although whether the gaps were sealed was not stated. Also, the Reynolds number was not stated. A static pressure probe was used to measure the static pressure around the wheel periphery. It was found that the lift and drag coefficients were reduced when the wheels were rotated. Pressure coefficients less than or equal to unity were measured, therefore no "jetting" was observed. This is not surprising due to the contact patch being inaccessible when using a static pressure probe, and the gap that existed under the wheel would not generate the jetting phenomenon. It

is surprising that Imaizumi and Yoshida [24] adopted this approach especially when previous investigations highlighted these problems.

Axon [7] carried out a comprehensive computational (CFD) study into isolated wheel aerodynamics using the commercially available CFD package Fluent. This work is described in Axon et al [6], [5], and in more detail in Axon [7]. An experimental study into wheelhouse cavity flows was also conducted. This was probably the first published CFD study into wheel flows, although Skea et al [61] may have started their research at a similar time.

The wheel modelled by Axon was a very slightly modified version of the wheel used by Fackrell [19]. The width was based on the central hub section of Fackrell's wheel and resulted in a wheel with an aspect ratio of 0.6. Preliminary 2D analyses were conducted to aid in the development of the 3D model. The boundary conditions chosen reflected those of the experiment of Fackrell, hence the Reynolds number was the same ($Re = 5.3 \times 10^5$). An interesting part of the modelling of the wheel was the treatment of contact patch. Vertical support planes were placed at 10 degrees and 350 degrees to represent the contact patch and the wheel was located to sit on these planes, therefore the wheel contacted the groundplane through these small vertical planes. This meant that it would have been easier to mesh this region of the contact patch using hexahedral elements without resulting in highly skewed cells, and as will be discussed later the jetting phenomenon at the front of the contact patch was in fact predicted using this technique. Interestingly other investigators (discussed later in this Chapter) used hexahedral cells with the wheel located directly on the groundplane and the predicted surface pressure field showed almost no signs of jetting. This aided the choice of meshing strategies for the work presented in this thesis significantly.

Purely hexahedral volume mesh structures were used by Axon [7]. The initial volume meshes consisted of 250,000 cells and these were refined gradually using decreased cell height growth rates. By increasing the number of cells within the boundary

layer the effects of using a two-layer wall treatment could be established compared to standard wall functions. A symmetry plane was used on the centreline of the wheel and Axon [7] proved that this had little effect on the predicted lift and drag forces and surface pressure distribution since the solution was steady state. He actually modelled the complete wheel and the predicted results were almost identical to those with the symmetry plane. The final mesh used for all subsequent solutions had 538,350 cells and a symmetry plane. For transient solutions the complete wheel would require modelling. The influence of numerics on the wheel flow solutions were ascertained in terms of turbulence modelling, turbulent closure method and symmetry plane. It was found that the k-$\epsilon$ RNG turbulence model offered increased accuracy over the standard k-$\epsilon$ model and was therefore chosen to analyse the aerodynamics of isolated wheels since it better predicted the separation from the top of the rotating wheel. Second-order upwind discretisation was used for the convective terms to increase solution accuracy.

The additional boundary layer refinement resulted in pressure coefficients of around Cp = 1.9 at the contact patch, which compare well with the data of Fackrell [19]. No negative pressures were present after the line of contact, which is surprising since the front jetting was predicted so well. The outline of the wake was also predicted at the same streamwise stations as those of Fackrell and the results were in good agreement using the k-$\epsilon$ RNG turbulence model with two-layer wall treatment, although the wheel edge profile was slightly different and would affect the wake structure. It would have been useful to see the predicted wake structures rather than just the outline of the wake and to observe the velocity field in the near-wake. The reduction of the lift and drag forces acting on the wheel caused by wheel rotation were predicted. The remainder of the work by Axon [7] was concerned with shrouded wheel flows.

Skea et al [61] modelled a 3D rotating wheel using the CFD package Star-CD. The diameter of the wheel was 0.5m with a width of 0.25m (AR = 0.5). The flow domain modelled was 2m x 2m x 9m and the velocity at inlet to the domain was set

to $20ms^{-1}$ giving a Reynolds number, based on the wheel diameter, of $6.9 \times 10^5$.

Three different hexahedral volume meshes were used each with successively more refinement compared to the initial mesh. The initial mesh consisted of 200,000 cells, the second mesh comprised of 250,000 cells, and finally the third mesh consisted of 360,000 cells. The final grid was refined close to the wheel in order to satisfy the recommendations for the wall treatment such that the velocity distribution near to the wall could be resolved. The y+ values were monitored for each solution to ensure they were in the appropriate range. Wall functions (law-of-the-wall) and the two-layer method were used for the wall treatment.

The standard, RNG and non-linear k-$\epsilon$ turbulence models were used with the default model settings. Three differencing schemes were used for the study to establish the effects of using different schemes; these schemes were upwind, MARS and QUICK.

The results showed that the main features of the flow were predicted for stationary and rotating wheels. A slight increase in static pressure to Cp = 1.1 was predicted at the contact patch. There were little differences between the coarse and refined grids (therefore the solutions were mesh independent). The pressure distributions were largely affected by the differencing scheme employed with the QUICK scheme predicting more accurately the early flow separation at the top of the rotating wheel. The most accurate pressure distribution was obtained using the QUICK differencing scheme and the RNG k-$\epsilon$ turbulence model. The law-of-the-wall wall function predicted better the pressure distribution compared to the two-layer method, although this depends on what measure of accuracy was used (e.g. predicted lift and drag forces, predicted separation, etc.). Moreover, the two-layer approach required further discretisation of the near wall region which increased the computational demands. It was found that the choice of turbulence model, differencing scheme and wall treatment all influenced the mesh independent solutions.

Kellar et al [28] conducted an experimental and computational study into F1 car

wheel aerodynamics. The study was aimed at evaluating the interaction between the wheels and body. A 40% front right-hand quarter of a generic F1 car was used. Different vehicle configurations were analysed, namely front wing endplates. The CFD code used was the Cambridge University 3D Navier-Stokes solver. This code was derived from turbomachinery applications and the development of incompressible versions is still ongoing. The wheel and front wing CFD model consisted of 340524 cells. Kellar et al found that wheel drag could be reduced by the interactions of the front wing. Wheel drag was significantly affected by the wheel wake symmetry whereby a symmetrical wake appeared to reduce drag. This symmetry was found to be dependent on the vortical flow shed from the front wing. Drag measurement/calculation was the only consideration in this study with no reference made to wheel lift forces, even though predicting the lift force is extremely important in the aerodynamic development of a racing car.

Hinson [22] conducted an investigation into rotating wheel aerodynamics using a new surface pressure measurement system. A stationary wheel was initially used to aid experimental set-up for the rotating programme. The Cranfield University College of Aeronautics 8' x 4' wind tunnel was used for the stationary wheel investigation and the 8' x 6' tunnel with MGP was used for the rotating wheel work. The stationary wheel work was carried out at a freestream velocity of 16 $ms^{-1}$ giving a Reynolds number of $3.4 \times 10^5$ based on wheel diameter. The stationary wheel tested was a hollow aluminium 50% scale model of a F1 rear tyre with hub. The wheel diameter was 0.325m with a width of 0.195m (AR = 0.6) and contained 36 static pressure tappings at one angular position located across the wheel. The static pressure was measured at each tapping sequentially using a scanivalve and Setra 239 pressure transducer in 10 degree intervals.

The rotating wheel runs were conducted at speeds between 17 and 46 $ms^{-1}$ giving test Reynolds numbers, again based on wheel diameter, of $Re = 3.5 \times 10^5$ to $9.6 \times 10^5$. The wheel tested for the rotating aspects of the work was a 50% scale model manufactured from carbon fibre with the tread region coated in rubber around 3mm thick.

The wheel diameter was 0.324m and the width was 0.19m. This time the pressure measurement system comprised of 9 separate SDX 01D4 pressure transducers, one for each tapping located across the tread region of the tyre; no tappings were located on the sidewall of the wheel or in the hub region. The inside of the tyre assembly was used as the reference pressure for the transducers although the cavity was not sealed and therefore the reference pressure will have varied during experimentation. Hinson discusses the effects of this in more detail.

The pressure measurement system was mounted inside the tyre and was battery powered. The transducer outputs were sampled at a frequency of 2kHz and a modulator converted the output to a frequency modulated radio signal, which was transmitted from the wheel via a small wire antenna. This signal was received by a standard radio unit and an analogue voltage of $\pm 10$V was measured. A wheel position sensor was used to monitor wheel position. The pressure data and trigger signal were recorded using a PC and integral lift and drag forces were computed using the surface pressure data.

Static pressures were reported below the freestream stagnation pressure for the front region of the wheel on the centreline. This was put down to temperature effects on the transducers affecting the transducer offset and the data were subsequently corrected based on the data of Fackrell [19]. This method appears perfectly reasonable, however different pressure coefficient offsets were used depending on whether the particular tapping to be corrected was in a similar position to that of Fackrell's wheel. A more appropriate method would have been to use an offset based on the centreline of Fackrell's wheel (where the flow does stagnate) and to apply this offset correction to all pressure tappings. It is thought that what Hinson actually observed were centrifugal effects (mechanical effects) acting on the transducers which caused a reduction in static pressure in the measured distributions. The proposed correction method suggested here would have improved the results accuracy for the pressure distributions and hence the lift and drag force data. Additionally, the reference pressure would cause measurement errors and Hinson proposes a method to resolve

this.

The results of Hinson [22] show a large positive pressure peak (Cp = 7) at the front of the contact patch. This value does appear large compared to the results of Fackrell [19] and indeed to the results presented in Chapter 8 for this work. This was put down to the volume reduction and resultant pressure increase as the rubber layer of the tyre was compressed at the contact patch. Hinson repeated the experiments with the wind off to establish what "non-aerodynamic" effects were present at the contact patch. A large pressure peak (of reduced magnitude (Cp = 2.5)) was observed and this was put down to non-aerodynamic effects, however even with the wind off there will still exist a small annulus of fluid rotating with the wheel due to the no-slip condition at the wall where the relative velocity there is zero. Similarly, fluid will move with the MGP, due to the translational velocity of the belt system, so the viscous actions will still be present at the contact region albeit probably with reduced effect compared to when the wind is on. Hinson corrected her pressure distributions to show the jetting phenomenon of Fackrell [19]. She also suggested using rigid tubing for the pressure measuring holes to prevent the flexible tubing from being compressed and therefore increasing the measured pressures at the wheel surface.

A negative pressure peak was observed after the line of contact and Hinson expected to observe this based on the theoretical prediction of Fackrell [19]. Due to the excessive jetting at the front of the contact patch Hinson was not sure whether the negative pressure peak was a genuine aerodynamic phenomenon or caused by non-aerodynamic effects such as tubing. Oscillations were observed after the line of contact and these were thought to be caused by the belt lifting and contacting the wheel.

Skea et al [62] also carried out an experimental/computational aerodynamic study using two wheel models. The wheels both had a diameter of 400mm with widths of 50mm and 200mm, which equates to aspect ratios of 0.125 and 0.5, respectively. The wheel of aspect ratio 0.125 appears to be very narrow, especially in the context

of automobile wheels, although it may have been used to develop the instrumentation. The Reynolds number of the wheels, based on wheel diameter, was $5.51 \times 10^5$. In order to measure the static pressure on the surface of the wheel, battery-powered pressure transducers were mounted in the wheel. They were connected to pressure tappings on the surface of the wheel along the centreline and had a pressure range of $\pm$ 10mbar. The transducer analogue output voltage was connected to a data logger via slip rings located at the wheel hub and the voltage signal was read at 1400Hz. Pressure coefficients greater than 2 were observed at the contact patch followed immediately by values less than -2. Fackrell [19] observed the jetting phenomenon before the line of contact and expected to also see jetting at the rear of the contact patch. As a test to ascertain the cause of this, the tappings were taped over and the experiment repeated. A pressure coefficient value of zero was measured until the contact patch was reached and the value rose to Cp = 2 and then rapidly decreased to -2. Skea et al put this down to vibrations in the rolling road causing errors to be read by the transducer, although it seems unlikely that vibrations alone acting on the transducer would cause such a change in amplitude of the pressure signature. If the tappings had been blocked with a less flexible material than tape the pressure coefficient would probably have remained at zero during the complete wheel revolution. The pressure at the contact patch would be sufficiently high to cause the tape to deflect and therefore reduce the small volume of air in the tubing and transducer body thereby increasing the pressure. On the other side of the contact patch the negative pressure would have a similar effect except this time increasing the small volume of air and hence reducing the pressure. This would have proved that what Skea et al [62] had actually measured and observed was the "jetting" phenomenon. The remainder of the work presented by Skea et al [62] was concerned with wheelhouse cavity flows and CFD predictions.

As a matter of interest the publications from this point onwards were all published during the course of the present work. In addition to these publications the published work derived from this research are shown in Appendix A.

Knowles et al [31] carried out experimental and computational (CFD) investigations into the flow around an isolated racing car front wheel rotating in ground contact. The Shrivenham open-jet closed-return wind tunnel with a 1.52m by 1.14m working section was used for the investigations, which has a moving groundplane. A 40% scale non-deformable Champ car front wheel was tested which had a diameter of 263mm. The tyre was manufactured from carbon fibre with a machined aluminium hub that comprised spokes that replicated BBS multi-spoke alloy wheels currently used in Champ car racing. The wheel was supported by a sting and these effects are discussed in the paper.

An LDA system was used to analyse the velocity field in the wake of the wheel, positioned in the flow using a three axis traverse system. The laser probes were positioned outside of the jet to minimise flow disturbances. A JEM Hydrosonic fog generator was placed inside the wind tunnel to provide seeding. The experiments were carried out at a freestream velocity of $20ms^{-1}$ giving a Reynolds number, based on the wheel diameter, of $3.69 \times 10^5$. Measurements were made in four vertical planes perpendicular to the axial flow. These planes being 10, 25, 50 and 100mm downstream of the rearmost part of the wheel, and each plane contained 441 equally spaced data points. A load cell was used to directly measure the drag force acting on the wheel.

The CFD aspects of the work by Knowles et al [31] used the wheel CAD data to aid model development. A viscous-hybrid meshing strategy was adopted whereby regions of hexahedral cells were used to resolve regions where viscous effects dominate. The remainder of the domain was filled with tetrahedral cells. The wheel and sting were placed in a rectangular domain with the inlet 5 wheel diameters upstream, the outlet 16 wheel diameters downstream, a width of 10 and a height of 5 wheel diameters. The sting was meshed to allow it to be removed from the solution domain to analyse the effects of stings on the flow-field. The contact patch was modelled by slightly truncating the wheel by raising the groundplane by 0.8mm and Knowles et al report that this greatly improved cell skewness. The final mesh

contained 930,000 cells.

The boundary conditions were set to represent the experiment. A uniform velocity inlet of $20ms^{-1}$ was chosen for the inlet to the domain with a pressure outlet chosen for the outlet of the domain. A translational velocity and a rotational velocity of $20ms^{-1}$ were chosen for the groundplane and wheel, respectively. A number of turbulence models were tested during the initial stages of the study. These included the RNG k-$\epsilon$, Realisable k-$\epsilon$, Spalart-Allmaras, Shear Stress Transport (SST) k-$\omega$ and the Reynolds Stress Transport Model. It was concluded that the standard k-$\omega$ model offered the best results over the other models, although the front jetting phenomenon was predicted, in terms of the static pressure coefficient, to be Cp = 1.1, which is much lower than the pressures observed and reported in this region experimentally. However, the choice of mesh type and contact patch modelling may be factors here since similar results were predicted by Skea et al [61] (this is discussed further in the discussion (Chapter 10)). It was reported by Knowles et al [31] that solution convergence was achieved within three thousand iterations, which required around 30 CPU hours on a Compaq Alpha DEC-based Beowulf cluster.

The vector fields presented showed an over-prediction in terms of velocity magnitude. As mentioned previously the pressure distribution for the centreline of the wheel shows little sign of any significant jetting when compared to the results of Axon [7] (Cp = 1.9). Also there is a low pressure peak over the top of the wheel as though the flow is accelerating over the top of the wheel and the separation position is predicted to be around 25 degrees after the top of the wheel. The base pressure was reasonably constant. The predicted drag coefficient was $C_{Dw} = 0.638$ which is comparable to the coefficients of other investigators and the sting effects were found to suppress the formation of the upper trailing vortex on the opposite side of the wheel to the sting. The upper region of the wake structure could not be measured due to the presence of an overhead force balance gantry.

Knowles et al [30] also carried out an experimental investigation into the near-wake

of a rotating, 40% scale champ car wheel. LDA measurements were made at four transverse planes in the near wake within half a wheel diameter downstream of the "trailing edge" of the wheel. Two wheels were tested, one standard and the other cambered, both with a diameter of 263mm giving a Reynolds number of $3.69 \times 10^5$ at a freestream velocity of $20ms^{-1}$.

Again, as was the case with the previous investigation by Knowles et al [31], the Shrivenham open-jet closed-return wind tunnel with a 1.52m by 1.14m working section was used for the investigations. As mentioned above the facility is fitted with a MGP whose speed was manually synchronised to the tunnel freestream velocity using an optical tachometer. The boundary layer was removed upstream and the thickness of the layer was quoted as 5.7mm at the wheel position which corresponded to 99% of the freestream dynamic pressure.

A Dantec 3D LDA system was used for the LDA measurements and a JEM Hydrosonic fog generator was used to seed the wind tunnel flow. The LDA system was set-up by the side of the wind tunnel "jet" in order to maximise the non-intrusive nature of LDA, although it is worthy of note that the non-intrusive nature of the technique is dependent on particle size since large particles can change the particle trajectory and hence the flow-field. The seeding generator was placed inside the tunnel, upstream of the working section, to increase the seeding density. This method would also improve the homogeneity of the seeding, especially for closed-return wind tunnels where the seeding is effectively recycled.

It was reported that the gantry for the tunnel's overhead balance restricted access to the working section. Therefore, the results presented do not show the complete top of the wheel and although this would not be a problem for the stationary wheel with fixed ground, it is a problem for the rotating wheel where the flow separates before the top of the wheel and results in a wake structure that is taller than the wheel.

The measurement planes were restricted to a 250mm square due to the gantry

problem. Four transverse planes located 10, 25, 50 and 100mm downstream of the "trailing edge" of the wheel were measured. Each plane consisted of 441 equally spaced data points and each point was sampled for 15 seconds for a total of 2500 samples. The velocity field and streamwise vorticity were computed at each plane.

A load cell was used to measure the drag force acting on the wheel. Tare readings were initially taken to correct for the frictional contact forces.

Wake asymmetry for both the parallel and cambered set-ups was reported and put down to the wheel support sting effects and the through hub flow as a result of having spokes. It was reported that the cambered wheel exhibited more flow asymmetry towards the left side of the wheel and reversed flow which needed further investigation. The wake structure for the cambered wheel, however, should be asymmetric due to the geometry of the cambered wheel. The conical geometry of the tread region of the wheel is effectively subjected to yawed flow which will alter the flowfield. The static pressure distribution on the surface of the wheel will be altered as a result of yawed flow as will be seen in Chapter 8. The ideal resolution to the conical cambered wheel problem would be to use a pneumatic tyre whereby the correct contact patch can be achieved whilst adjusting the camber of the wheel. This technique would probably require additional sting loads to deform the tyre and this could lead to premature belt failure on the MGP caused by overheating. The results of Knowles et al [30] do show the trailing vortices which are prominent towards the top region of the wheel and are consistent with those produced by lifting bodies. Drag forces were reported and it was found that the cambered wheel produced more drag compared to the parallel wheel ($C_{Dw} = 0.76$ cambered, $C_{Dw} = 0.68$ parallel) and this is in line with wheels at small angles of yaw showing increased drag, as reported by Cogotti [14].

Wäschle et al [67] conducted an investigation into the flow around an isolated 33% full scale formula one wheel, and this is the most recent publication ignoring publications by the author of this thesis. In the paper comparisons were made between

experimental data and data obtained through two different CFD codes. The flow field was investigated experimentally using LDA and a total pressure probe in the University of Stuttgart model wind tunnel. The numerical results were obtained using the commercial CFD packages STAR-CD and EXA PowerFLOW.

The wheel was 215.8mm in diameter with a tread width of 80mm, giving a test Reynolds number, based on wheel diameter, of $5.37 \times 10^5$ at a freestream velocity of $45 ms^{-1}$. The wheel was manufactured from aluminium with a glass fibre tyre. The wheel model was relatively complex as it incorporated features such as spokes and a brake disc.

A Dantec 3D-LDA system was used for the flow-field measurements yielding all three components of the velocity field. Di-Ethyl-Hexyl-Sebacat (DEHS) was used as seeding, injected into the diffuser of the wind tunnel and it was noted that this was to prevent any disturbance in the test section, although it is not only the potential disturbance problem that is important but the homogeneous distribution and quantity of seeding that is critical with such techniques. Introducing the seeding into the diffuser of the wind tunnel will ensure as much as possible a uniform distribution.

The simulation set-up for the STAR-CD and PowerFLOW work modelled the wheel and sting as per experiment with the relevant identical boundary conditions. The 3D mesh consisted of $6.7 \times 10^6$ volume cells for the STAR-CD case and $7 \times 10^6$ voxels for the PowerFLOW model. The RNG k-$\epsilon$ turbulence model was used for the PowerFLOW simulations, this being fixed in the code, and the standard k-$\epsilon$ turbulence model with law-of-the-wall near wall treatment was chosen for the STAR-CD simulations. Additionally, the near wall treatment was changed to a two-layer approach for the STAR-CD model, again using the standard k-$\epsilon$ model. The latter wall treatment requires the boundary layer to be discretised and results in additional grid points; the grid in this case grew to $13.5 \times 10^6$ cells. No CPU time was quoted but the two-layer approach would be more computationally expensive due to the increased mesh density.

Good agreement was had between the LDA data and all CFD simulations. There were little differences between the PowerFlow k-$\epsilon$ RNG and the STAR-CD standard k-$\epsilon$ models using wall functions and the two-layer wall treatment. The main flow structures were predicted for the streamwise and spanwise planes investigated, although small local discrepancies existed between different models and wall conditions. No surface static pressure data were presented for the simulations. Due to the good agreement of the flow-field, the lift and drag coefficients showed good correlation with the experimental measurements.

Wäschle et al used an 8-probe rake of total pressure probes to investigate the flow-field in the wheel wake. This set-up could only measure accurately if the flow incidence relative to the probe was within a 15 degree cone. The results presented for the data acquired using the probe rake are extremely limited as the angle of incidence exceeded the limits of the probes at most stations in the wake. The outline of the wake was presented but is of limited use in furthering the understanding of the mechanics of the wheel wake.

## 2.3 Summary

The literature review has highlighted some important aspects regarding the experimental set-up and pressure measurement methods. The use of intrusive methods to measure the static pressure on the surface of the wheel, such as static pressure probes, should be avoided. Wheel-to-ground contact is vital if the flow-field is to be correct. From a CFD point of view the general consensus of opinion is that the k-$\epsilon$ RNG turbulence model offers the best accuracy. Axon [7] found the two-layer wall treatment to be more accurate, whereas Skea et al [61] found that the law-of-the-wall wall functions were more accurate. However, it depends on what measure of accuracy is used i.e. predicted lift and drag forces, separation position, jetting prediction. Surely the true test of accuracy is the ability of the CFD code to predict all of these with a good degree of accuracy, rather than just one of them.

The current level of understanding of the aerodynamics of isolated/exposed wheels has been shown through the work of previous investigators. In summary, the time-averaged lift and drag forces acting on the wheel decrease due to wheel rotation. Several studies have been conducted to acquire the surface static pressure data from a rotating wheel, and this has proved extremely difficult technically. Relatively little is known about the wheel wake structures since (prior to this work and the work of Knowles et al [31], [30]) only a Kiel tube showing the outline of the wake has been used by Fackrell [19], and a multi-hole pressure probe has been used by Bearman et al [9], albeit only at one axial measurement station. Suffice to say there is considerable research needed to further understand the flow physics associated with exposed/isolated wheels.

# Chapter 3

# Wheel Design and Experimental Configuration

This chapter addresses all issues with respect to the design of the wheel assembly and describes in detail the important aspects of the wheel design. The experimental configuration, used for all experiments, is presented and discussed. The knowledge derived from the literature reviewed significantly aided the experimental design techniques. References are frequently made to the instrumentation (radio telemetry system) which is described in the next chapter (Chapter 4).

## 3.1 Introduction

A 40% full-scale pneumatic tyre/wheel was used throughout this research. The diameter of the wheel was 246mm with a width of 130mm (AR = 0.53) giving a test Reynolds number, based on the wheel diameter, of $Re = 2.5 \times 10^5$ at a freestream velocity of 14.7ms$^{-1}$.

A pneumatic tyre was primarily chosen for this work because the contact patch could be varied and therefore the influence such deformation had on the airflow and aerodynamic forces could be studied. However, due to time constraints developing the instrumentation the tyre was effectively run as a solid tyre with constant inflation pressure and sting load. The specific tyre chosen was a go-kart front tyre and the

aspect ratio (AR) closely matches that of a Formula One front tyre. This particular tyre had no tread pattern. Figure 3.1 shows the aspect ratio for various car wheels (racing and passenger) and the go-kart wheel.

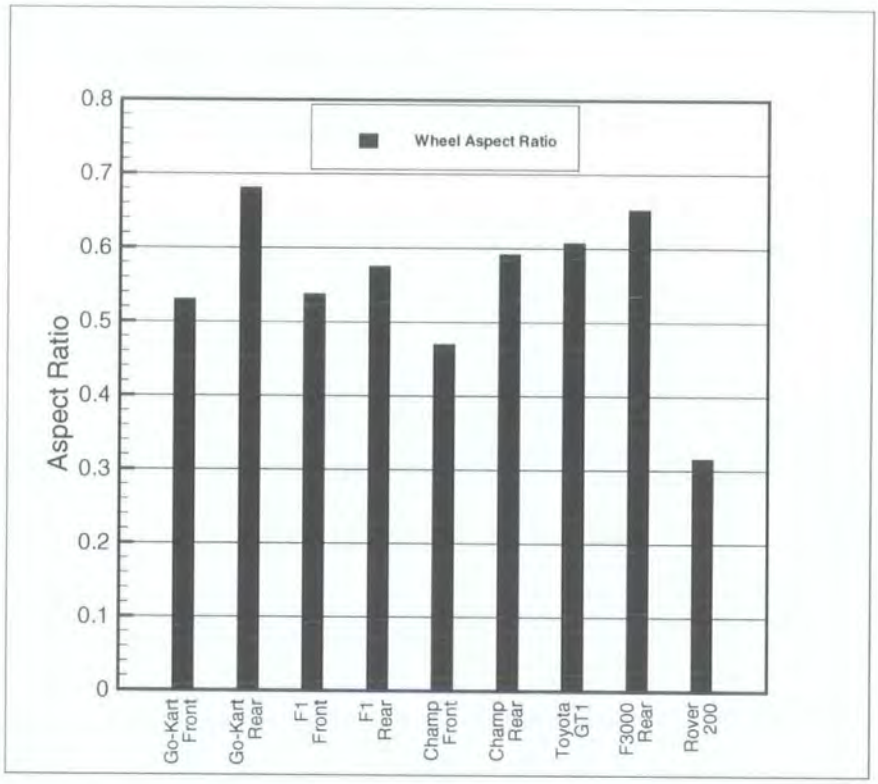


Figure 3.1: Aspect Ratios for Various Car Wheels and the Go-Kart Wheel.

The basic experimental configuration comprised of the wheel either rotating in contact with the MGP or being fixed on a fixed groundplane, which are described in Section 3.7.1. The stationary (fixed) wheel with fixed groundplane was used for comparative purposes with the rotating wheel since the stationary wheel does not represent any practical scenario. This was necessary to further understand the fundamentals of the flow physics of rotating wheels.

## 3.2 Experimental Requirements

The experimental requirements can be split into two parts; firstly, aerodynamic analysis requirements and secondly, but by no means less significant, the mechani-

cal requirements of the wheel assembly.

The aerodynamic requirements are mainly the need to reproduce as much as possible the on-road, or on-track, conditions. The word "simulation" has deliberately not been used in this context, since it can be confused with numerical simulation (CFD). Correct wheel-to-ground contact conditions are essential to analyse the aerodynamics of wheels, and this was stated in the relevant literature. To reproduce the "real world" conditions the circumferential velocity of the wheel was matched to the freestream and MGP velocities. No attempts were made throughout this work to vary the circumferential velocity relative to that of the freestream. The velocity ratio of the freestream to circumferential to MGP was constant at unity ($V_{ref} = V_C = V_B = 1$).

The mechanical requirements are the need to be able to install the necessary instrumentation inside the tyre. This is both to ease instrumentation set-up and minimise any damage as the wheel rotates. The wheel rim/tyre assembly and instrumentation must be able to withstand the centrifugal forces caused by rotation. Several simple stress analysis calculations were made to determine the structural characteristics of the assembly, whilst a concerted effort was made to minimise the mass of the rotating system, as reduced mass reduces the centrifugal forces.

## 3.3 The Multi-Element Wheel Rim

A multi-element wheel rim was specially designed to meet the experimental criteria. A schematic exploded view of the multi-element wheel rim assembly is shown in Figure 3.2. The wheel rim is of the split rim type and was specifically designed to enable it to be assembled inside the tyre. The wheel rim components were all fabricated using aluminium to minimise mass. The centre section has a number of radial tapped holes to allow the instrumentation to be attached. A Schraeder type tyre valve is also screwed into the rim centre section allowing the tyre to be inflated. The rim ends were designed in such a way to seal the tyre onto the rim. This was

achieved, after several plastic prototypes, using a method employing tapered rim ends whereby on inflation the tyre rides up the tapers and seals on the wheel rim ends seating regions. The "O" ring seals provide sealing between the rim centre section and the rim ends. The endplates are fitted prior to full inflation pressure to ensure the tyre does not slide off the seating regions. Figure 3.3 shows a photograph of the assembled wheel rim (less tyre) from the sting side of the wheel. The cavity can be clearly seen in this photograph which allows the wheel assembly to be fixed onto the sting. A flat plate was used on the other side (hub side) of the wheel to prevent any through-hub flow, thus avoiding additional flow complexities, in an attempt keep the flow-field as relatively "simple" as possible. Figure 3.4 shows 3D solid models of the wheel/tyre assembly from the "spoke" and sting sides of the wheel.

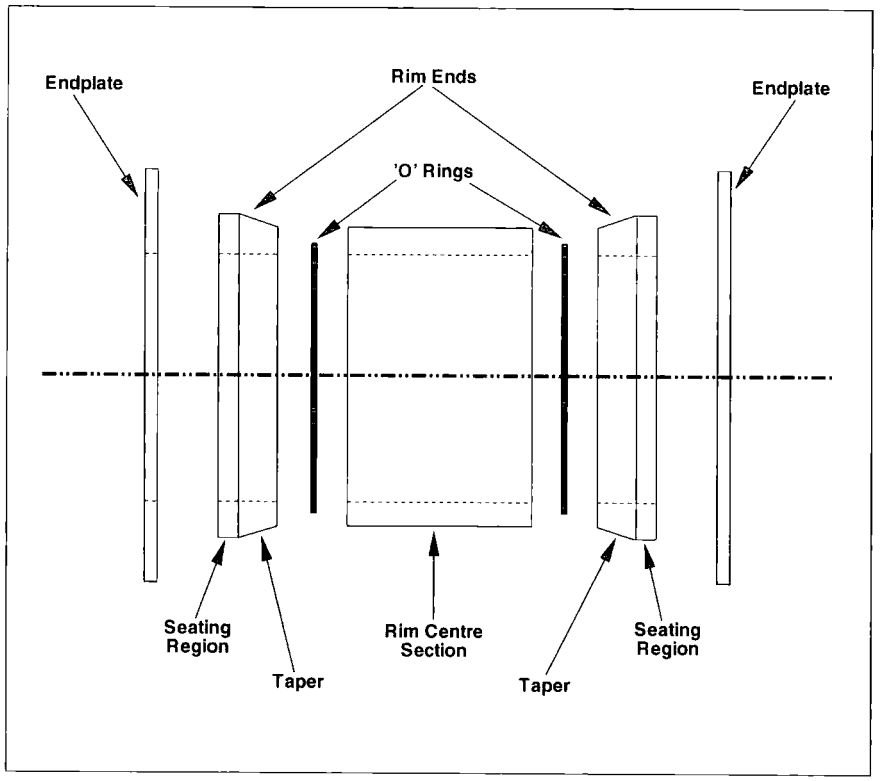


Figure 3.2: Schematic Exploded View of the Multi-Element Wheel Rim Assembly.

Figure 3.3: The Assembled Multi-Element Wheel Rim Assembly.

## 3.4 Tyre Edge Profile

Hereinafter the tyre used throughout this study will be referred to as the "P1" tyre / wheel assembly. The edge profile of the pneumatic tyre was measured using a basic coordinate measuring machine (CMM) that consisted of a touch probe connected to a computer-controlled traverse system (the traverse system is described in Chapter 5). The measurements were taken with the tyre inflated to a pressure of 7psi, which was found to be the pressure that gave the most flat tread region of the tyre. Figure 3.5 shows the results of the CMM exercise. Higher inflation pressures caused the tread region to balloon outwards creating a convex surface, and conversely under inflation caused the tyre tread region to adopt a concave geometry. Both scenarios (under and over inflation pressure) caused poor contact patch characteristics, whereby the sting would need additional loading, such to force the tyre against the MGP. Obtaining the correct geometry of the edge profile was necessary for the CFD investigation (discussed in Chapter 6).

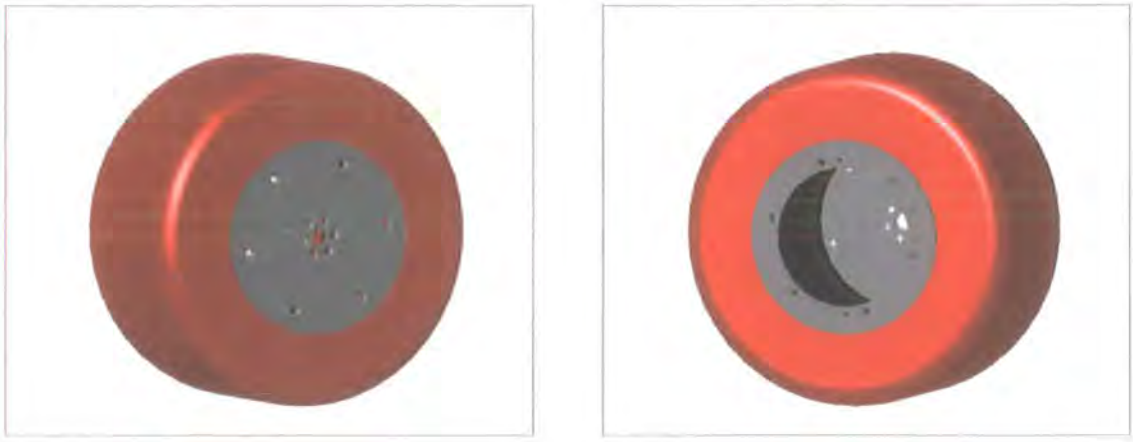

(a) Spoke Side.

(b) Sting Side.

Figure 3.4: 3D Solid Model of the P1 Wheel/Tyre Assembly.

## 3.5 Surface Pressure Tapping Location

In order to obtain the surface static pressure distribution around the wheel, flush fitting surface pressure tappings were installed in the tyre. The pressure tappings used were stainless steel hypodermic tubes with an outer diameter (OD) of 1.24mm and an internal diameter (ID) of 1.00mm. The length of the hypodermic tubing was dictated mainly by the distance between the inside of the tyre and the wheel rim assembly/instrumentation maximum radial position; a length of 10mm satisfied this constraint and enabled easy tubing connections between the pressure scanner (the pressure scanner is described in Chapter 4) and the pressure tappings. Nalgene 2.00mm OD with a 1.00mm ID tubing was used throughout this work. The length of the tubing was 120mm for all pressure tappings, as this was found to be a good compromise between tubing attenuation effects (caused by having long lengths of tubing, see Section 4.8.3) and the need for easy tubing connectivity.

Figures 3.6 and 3.7 show the location of the tread and sidewall region pressure tappings, respectively. As shown the pressure tappings occupied only one side of the tyre; the tyre being initially fitted on one side of the wheel and then swapped onto the other side during an experimental run, in order to obtain a complete time-averaged surface pressure distribution. This was also beneficial since the same pressure tap-

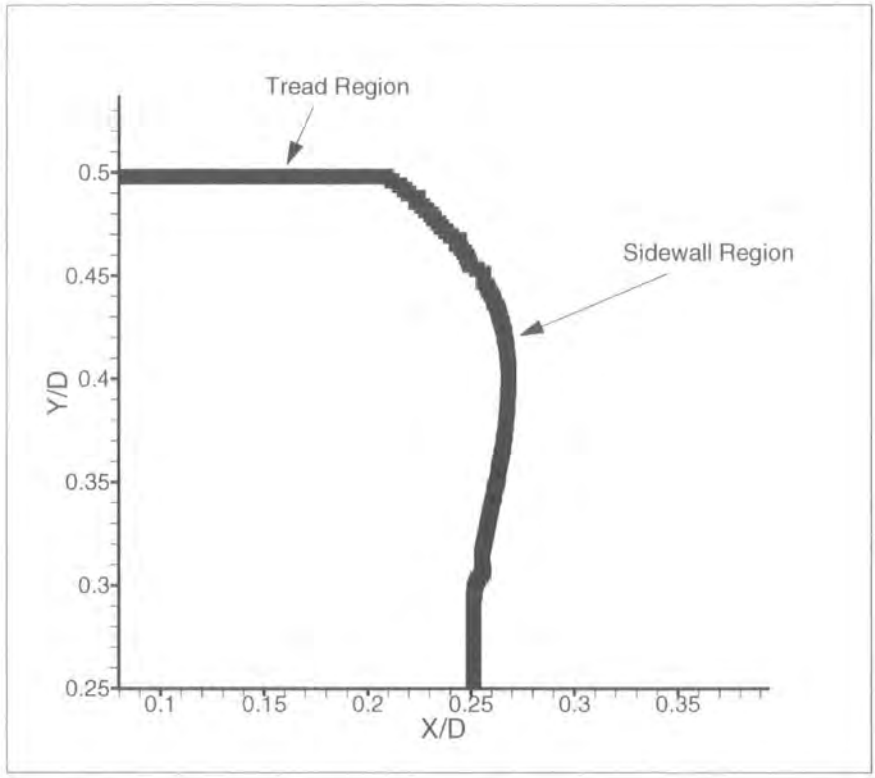


Figure 3.5: Pneumatic P1 Tyre Sidewall Geometry Profile, Measured using CMM.

ping was used on both sides of the wheel, hence reducing any errors associated with the tapping geometry or installation. The pressure tappings were fitted into the tyre tread and sidewall regions of the tyre using a miniature drill with 0.8mm drill bit, positioned normal to the tyre surface. The tappings were sealed on the inside of the tyre using an epoxy resin solution. Inflation of the tyre was realised when all tappings were either connected to the pressure scanner or were blanked off. The distance between the pressure tappings was fixed at 9mm in order to suit Simpson's rule of approximate integration (discussed in Section 4.7.5 of Chapter 4) when integrating the static pressure across the wheel width. Table 3.1 presents the geometric positions of the surface pressure tappings, in terms of $\theta$, $\phi$, width ($W$) and tapping radius ($r_S$), of all pressure tappings. The wheel notation is shown in Figure 3.9. The width ($W$) refers to the distance from the centreline of the wheel and the tapping radius ($r_S$) is the radial position of the pressure tapping relative to the wheel axle.

The angular position offset of the pressure tappings (Figure 3.7) was used to aid

tubing connections since having every sidewall tapping on the zero degree radial position caused some tappings to touch one another, making tubing connections impossible. These offsets were written into a geometry input file and dealt with in the post-processing software. The sidewall tappings either led or lagged the tread tappings depending on whether data were being acquired on the hub or sting side of the wheel, and again these were corrected to be in-phase with the tread tappings during data post-processing.

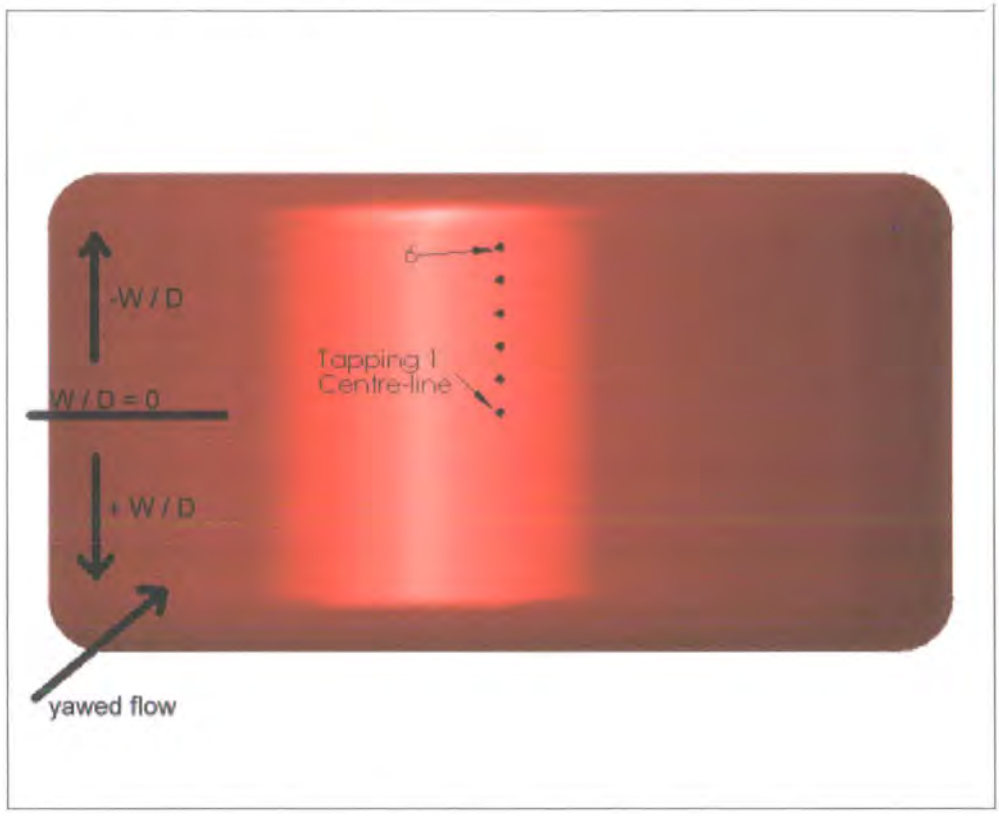


Figure 3.6: Location of Tread Region Pressure Tappings.

## 3.6 Wheel Support Method

The wheel was supported by a sting. The sting geometry was a symmetrical aerofoil section to minimise the effects the sting had on the flow-field about the wheel. The wheel bearing housing was mechanically attached to the sting via a short stub axle and the sting was secured by the side of the MGP.

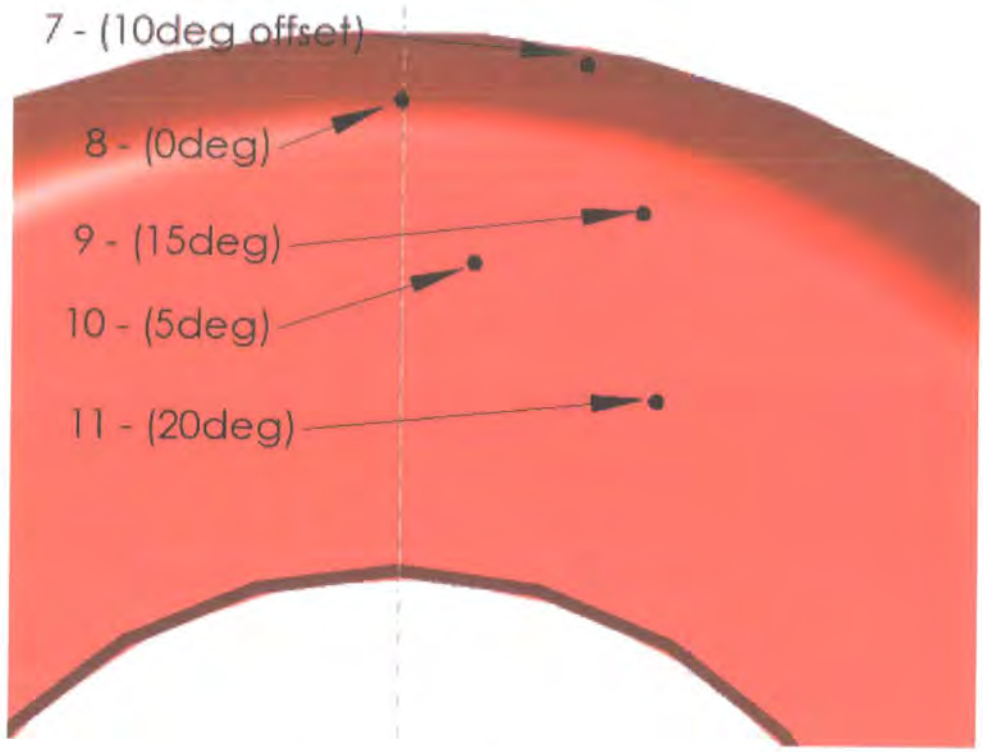


Figure 3.7: Location of Sidewall Pressure Tappings.

## 3.7 Experimental Configuration

The basic experimental configuration consisted of the pneumatic tyre/wheel assembly rotating in contact with the MGP. Figure 3.8 shows the experimental wheel configuration. The pressure probe shown was not the type used here; it was used to set-up the traverse system (discussed in Chapter 5). The wheel notation used for the surface static pressure data is shown in Figure 3.9.

### 3.7.1 Wind Tunnel and Moving Groundplane

The Durham University open-jet open-return wind tunnel with moving groundplane (MGP) was used throughout this research. The dimensions of the "jet" are 0.855m wide and 0.55m high yielding a working section cross-sectional area of 0.470m$^2$. The facility permits the wheel to rotate in contact with the MGP and wheel rotation is realised by the MGP driving the wheel. The MGP yaw angle can be adjusted relative to the freestream airflow up to an angle of approximately 25 degrees. The wind

| Tapping | $\theta$ (deg) | $\phi$ (deg) | $W$ (mm) | $r_S$ (mm) |
|---|---|---|---|---|
| 1 (Centreline) | 0 | 0 | 0 | 123 |
| 2 | 0 | 0 | 9 | 123 |
| 3 | 0 | 0 | 18 | 123 |
| 4 | 0 | 0 | 27 | 123 |
| 5 | 0 | 0 | 36 | 123 |
| 6 | 0 | 0 | 45 | 123 |
| 7 | 10 | 33 | 54 | 121 |
| 8 | 0 | 53 | 60 | 115 |
| 9 | 15 | 75 | 66 | 106 |
| 10 | 5 | 88 | 69 | 97 |
| 11 | 20 | 105 | 67 | 88 |

Table 3.1: Geometrical Positions of the Surface Pressure Tappings.

tunnel freestream velocity was fixed at 14.7ms$^{-1}$ (33mph) and turbulence intensity (streamwise component) levels were approximately 5%. Notably the freestream turbulence being relatively high compared to most low turbulence wind tunnel flows (a typical low turbulence intensity wind tunnel being around 0.2% (streamwise component)). A pitot-static pressure probe was used to measure the freestream total and dynamic pressures, and hence the freestream velocity was computed using Bernoulli's equation. The translational velocity of the MGP belt was variable using a variable speed AC drive, although for this work the MGP velocity was matched with the freestream velocity. This was achieved by initially logging a wheel reference trigger and then computing the circumferential velocity of the wheel. The circumferential, MGP and freestream velocities were all matched at 14.7ms$^{-1}$. The tunnel boundary layer was bled off upstream of the moving groundplane.

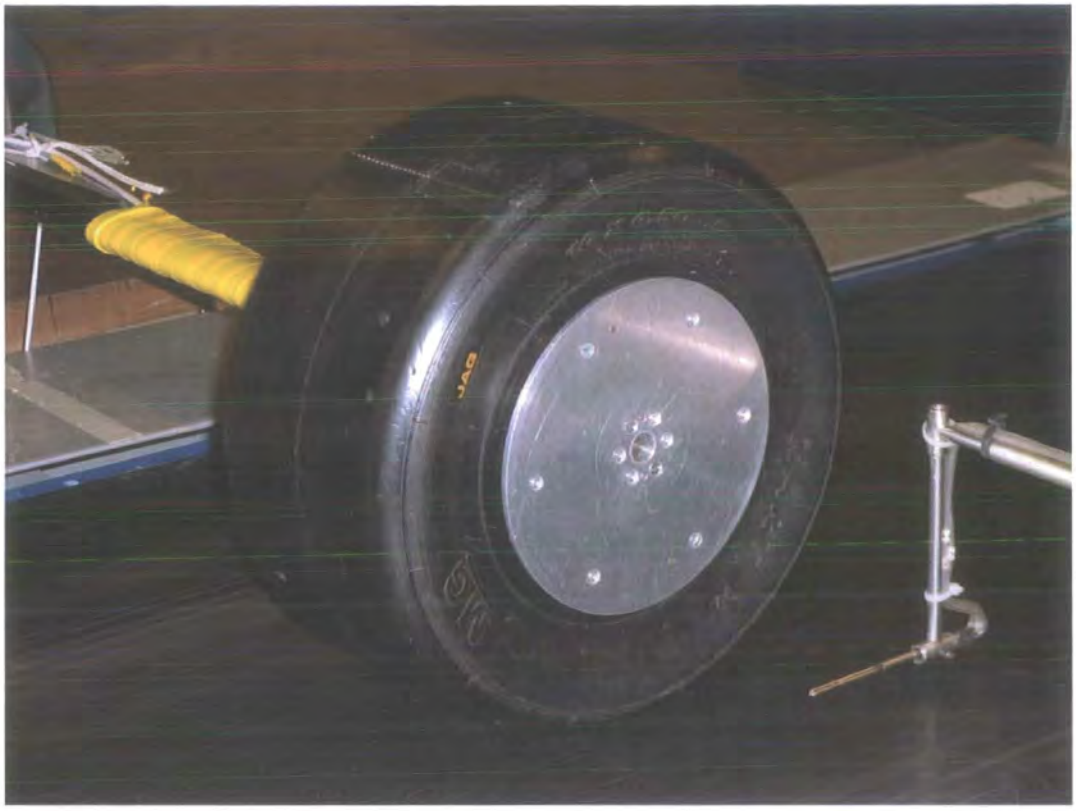

Figure 3.8: Experimental Wheel Configuration.

## 3.8 Summary

This chapter has described the pneumatic tyre/wheel assembly that was used experimentally throughout this work. The pressure tapping locations have been shown and the wind tunnel/MGP major features discussed. A description of the multi-element wheel rim has been given along with the motivating factors behind its design. The method adopted to enable tyre inflation has been described.

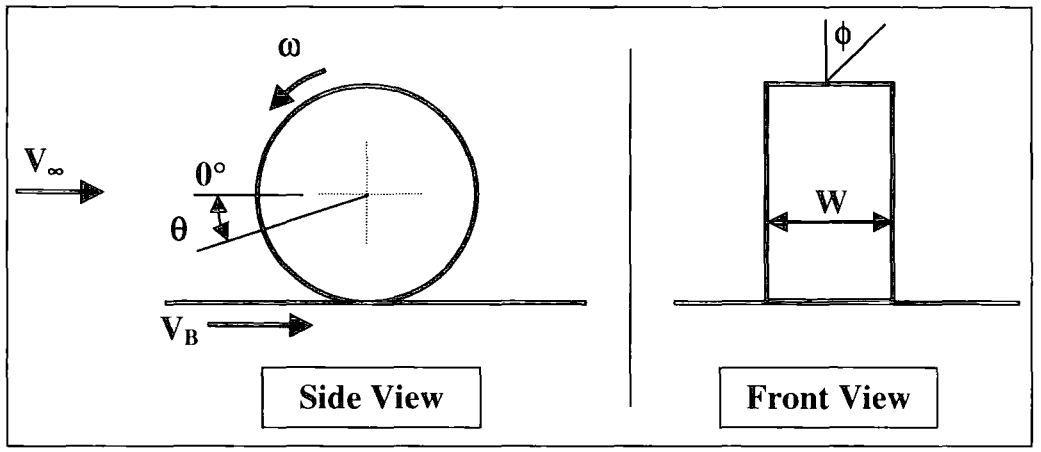


Figure 3.9: Wheel Notation.

# Chapter 4

# The Surface Static Pressure Measurement Instrumentation

This chapter focuses on the design, development and commissioning of the radio telemetry system used to transmit surface static pressure data from a rotating or stationary (non-rotating) wheel to a local host PC where data acquisition and analysis takes place. System requirements and specifications, along with the motivating factors behind the development of the system are discussed.

## 4.1 Introduction

The difficulty of separating the aerodynamic lift force from the varying wheel-ground reaction force precludes direct force measurement using a conventional force balance and hence an alternative method must be used. The method adopted here was to measure the static pressure on the surface of the wheel and obtain the lift and drag forces by integration. Additional information, with respect to the flow-field, are also obtained using this technique, such as how much each part of the wheel contributes towards the overall forces acting on the wheel. However, acquiring data from any rotating system is not straightforward as demonstrated by Fackrell [19], Fackrell and Harvey [20] and [21], Uawithya [65], Child [13], Mowatt [44], Skea et al [62] and Hinson [22], especially if an aerodynamically non-intrusive method is required.

A radio telemetry system has been designed and developed, specifically for this work, that enables surface static pressure data to be transmitted from a rotating wheel to a local data acquisition PC where data acquisition and analysis is carried out. The telemetry system is a uni-directional data communication device capable of transmitting data at rates of up to 19.2kbps, which equates to approximately 400 pressure samples/second.

## 4.2 Conceptual Overview

The system developed by Fackrell [19] during the 1970's operated using slip rings to get the surface static pressure data off the wheel. One problem with transmitting data via slip rings is that electrical noise can manifest itself in the data. Also, they are relatively large in size and are therefore inflexible in terms of using them with different hub geometries. For this reason an alternative method of transmission was sought. Initially it was thought that a digital signal could be transmitted using slip rings. Essentially the system could have been heavily based on the telemetry system described in this work, but instead of using a radio transmitter and receiver to transmit the pressure data out of the microcontroller slip rings could have been employed. The effects of any electrical noise would be minimised because of the discretely sampled digital signal not being affected as much as the continuous analogue signal. However, this system would still be subject to the necessary external apparatus that could potentially disrupt the air flow around the wheel and was therefore not pursued.

Another method of getting the surface pressure data off the rotating wheel is infrared telemetry such as the system used by Uawithya [65]. The system was a prototype designed and developed by Child [13] and Mowatt [44] and was excessively large and intrusive to the flow-field. Uawithya [65] did suggest that the size of the unit could be reduced and located on-board the wheel, although it is doubtful that the dimensions of the system would be reduced sufficiently. The centreline pressure distribution obtained by Uawithya [65] did not compare favourably with Fackrell [19]

and the system needed major development.

The transmission of pressure data via a Rf connection was thought to be the most suitable solution to this, although it was not without technical difficulties associated with radio transmission. Initially, the pneumatic tyre was X-rayed to establish the location of any reinforcing steel belts to ensure the Rf antenna would not be in close proximity, as this can significantly affect transmission. It was found that these belts were located at the lower part of the sidewall, where the tyre contacts the wheel rim, therefore they were not likely to impair transmission. The remainder of this chapter gives details of the radio telemetry system and shows some preliminary development stage results. Correction methods have also been developed in order to ensure as much as possible the accuracy of the aerodynamic data.

## 4.3 System Requirements

In addition to the mechanical requirements of the wheel rim/telemetry system, such as the need for straightforward instrumentation installation and adequate structural characteristics (discussed in Chapter 3) there were electronic and data related system requirements. The electronic system must be robust in the sense that it must operate correctly and not behave erratically. It was therefore decided to ensure the electronic system was as simple as possible and reliable. Keeping the system as simple as possible reduced the diagnostic time and complexity if a fault occurred. The on-wheel circuitry was to be battery-powered so there was a concerted drive towards minimising the power consumption to allow the system to be used for at least one full working day, before requiring recharging. The system must operate correctly from within the pneumatic tyre, such to meet the objectives for the radio telemetry system of it being a non-intrusive instrumentation technique.

The aerodynamic data obtained using the surface static pressure measurement instrumentation must be of sufficient quality and repeatability. This was to be achieved by implementing a number of error detection and prevention methods in addition

to the aforementioned correction methods.

## 4.4 System Description

The radio telemetry system comprises of two parts; the on-wheel telemetry circuitry located inside the wheel/tyre assembly and the off-wheel circuitry located by the side of the MGP. The off-wheel system is powered by a small mains-powered DC power supply and interfaces with the data acquisition laboratory PC (the data acquisition system is described in Section 4.6). The on-wheel system is a remote battery-powered system and was designed with size and mass reduction in mind. The batteries used are of the Ni-Cd (Nickel Cadmium) type and are fully rechargeable with a nominal voltage output of 1.2V per cell. Lightweight lithium "coin" cells were initially going to be used but it was calculated that they would not power the system for more than 20 minutes. The cells chosen are connected in series and are capable of powering the system for approximately 10 hours (1200mAh @ system current draw of 120mA). A total of 10 battery cells were used for each 12V battery power pack, and two packs were used for the system, which were diametrically opposed to balance the system.

Figure 4.1 shows a schematic representation of the telemetry system and data acquisition system. The main components are highlighted in the figure and are described in the following sections. In essence the system works by sampling the pressure scanner output voltage, which is connected to a particular pressure tapping, and converts this analogue signal into a digital signal using an A/D converter (on-wheel telemetry). This digital signal is then read into the microcontroller before being transmitted via the radio transmitter to its off-wheel receiving counterpart. The data is then read by the off-wheel microcontroller and the data interrogated to establish what was transmitted. The digitised pressure data is then clocked into a D/A converter where the analogue output voltage is connected to the logging card in the local laboratory PC. A wheel positional reference trigger is provided for the rotating wheel case (see Section 4.4.7) and a potentiometer is used to monitor wheel

position for the stationary wheel case (see also Section 4.4.7). The data valid pin is discussed in Section 4.7.2 and the digital address lines are discussed in Section 4.5.3.

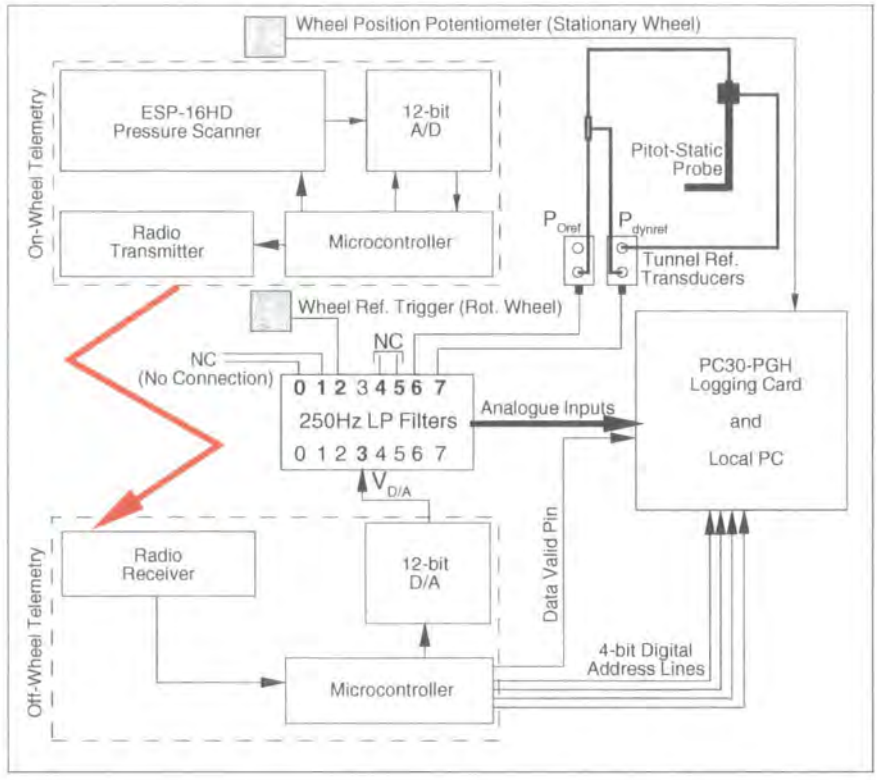


Figure 4.1: Schematic Representation of the Uni-directional Radio Telemetry System Instrumentation and Data Acquisition System.

Figure 4.2 shows photographs of the instrumentation assembly fitted to the wheel rim assembly.

### 4.4.1 Miniature Pressure Scanner

The ESP-16HD miniature pressure scanner was selected for all wheel surface static pressure measurements as it is particularly suited to applications where space is limited. It is a differential pressure measurement device consisting of 16 silicon piezo-resistive pressure transducers whose analogue outputs are amplified onboard the scanner. Transducer selection is made via a multiplexer within the scanner by means of digital addresses at 12VDC logic levels. The scanner can be multiplexed between

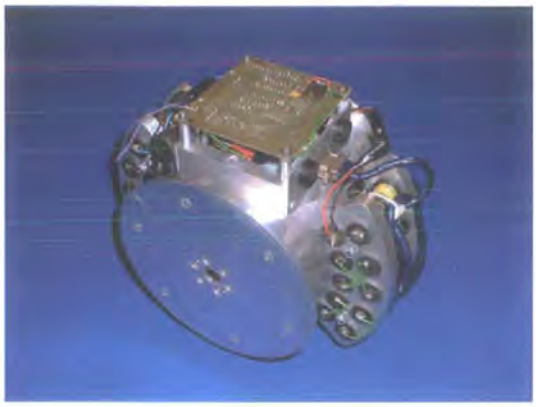

(a) Hub Side.

(b) Sting Side.

Figure 4.2: The Instrumentation Assembly Fitted onto the Wheel Rim.

transducers at a frequency of 20kHz and has a nominal full-scale voltage output of ±4VDC. The salient features of the ESP-16HD pressure scanner are presented in Table 4.1. For further information regarding the pressure scanner consult reference [27].

| | |
|---|---|
| Manufacturer | Pressure Systems, Inc. |
| Type | ESP-16HD |
| Number of Transducers | 16 |
| Pressure Range | ±2500 Pa |
| Rise time | 50$\mu$s |
| Power Supply | +12VDC,-12VDC,+5VDC |
| Output range | ±4VDC |
| Zero pressure offset | 0VDC |
| Dimensions | L(6.60cm)W(2.75cm)D(1.27cm) |
| Weight | 157 grams (5.6oz) |

Table 4.1: Salient Features of the ESP-16HD Pressure Scanner.

### 4.4.2 Analogue-to-Digital (A/D) Converter

The Burr-Brown ADS7808P [15] is a 12-bit serial data out A/D converter with sample and hold capability. It can be operated in either internal or external clock mode

and the data out is synchronised with a falling edge on the clock pulse. For this application a non-continuous external clock pulse was generated using the microcontroller. Several input voltage ranges can be used with this particular converter and the most suitable, in terms of pressure scanner output voltage compatibility, was ±5VDC. A sampling rate of up to 100kHz is specified and the output can be either in the form of straight binary or binary two's complement; the output chosen was straight binary with serial data out being MSB (most significant bit) first. The A/D chip also benefits from very low power consumption at typically less than 100mW making it a favourable choice for battery powered applications.

### 4.4.3 The Microcontroller

Both the on-wheel and off-wheel telemetry circuits use the Atmel 89C2051-24PC microcontroller which is based on the architecture of the very popular 8051 family. The microcontroller controls the system and enables data communication between the on-wheel telemetry and its off-wheel counterpart. A serial data interface allows the microcontroller to transmit or receive 8-bits of data at any one time and can be operated in three different modes depending on application. For the radio telemetry system there was a requirement to transmit data at as high a frequency as possible, therefore the serial interface was used in mode 1 (see references [49], [64] and [4]). This mode allows the baud rate to be doubled, and when coupled with an oscillator crystal frequency of 22.1184MHz, a baud rate of 19.2kbps (19200 bits/second) is realised. In mode 1, ten bits are transmitted/received for each 8-bit word, these being: start bit (0); 8 data bits (LSB first); stop bit (1). Since only 8-bits of data can be transmitted/received at any one time and the A/D converter has 12-bit resolution the software was adapted to send two 8-bit words containing the necessary digitised pressure data.

The on-wheel microcontroller digital input/output pins control the A/D converter and digital address lines for transducer selection. The off-wheel microcontroller digital input/output pins control the digital-to-analogue (D/A) converter and communicate with the digital port of the logging card for transducer selection information.

The telemetry system software was custom written in the programming language C. Once written the software was compiled into hexadecimal language using a hex compiler and then programmed into each microcontroller. The microcontroller has an erasable FLASH memory and can be re-programmed up to 2000 times.

### 4.4.4 Radio Transmitter and Receiver

A Radiometrix transmitter (Tx2) and receiver (Rx2) provided the wireless data communication link between the on-wheel and off-wheel microcontrollers, respectively. The maximum data transmission rate of the transmitter/receiver pair was up to 160kbps [51], however the slower baud rate of the microcontrollers (19.2kbps) dictated the transmitter/receiver rate accordingly (also 19.2kbps).

### 4.4.5 Digital-to-Analogue (D/A) Converter

To allow simple interfacing with the data acquisition system it was desirable to convert the digitised pressure data back into an analogue signal. This was achieved by employing a Linear Technology LTC1451 12-bit serial D/A converter. An external clock pulse was generated by the off-wheel microcontroller to which data was synchronised. The analogue voltage output from the D/A is 0 to 4VDC, which is input into the logging card by means of a BNC cable. The digital data into the D/A converter was in the format of straight binary.

### 4.4.6 Transistor Circuit for 12VDC Digital Address Logic

A transistor based circuit was designed to "step up" the microcontroller 5VDC TTL logic output lines to 12VDC logic levels. This is necessary for the pressure scanner digital addresses. The transistor circuit is an inverter circuit and the software was written accordingly.

### 4.4.7 Wheel Reference Position

A once-per-revolution reference trigger (Schmitt trigger) was used to monitor wheel position for the rotating case. The output voltage of the trigger was connected to one of the analogue input channels of the logging card and was logged simultaneously with the surface static pressure data. A rising edge on the trigger signal indicated a wheel position of zero degrees, which was used for ensemble averaging (discussed in section 4.7.3). The optical trigger was mechanically fastened to the wheel sting and positioned at the recommended distance from a small strip of reflective tape located on the sting side of the bearing housing. When the reflective tape traverses the optical trigger (as the wheel rotates) it causes a change in output state from low (0VDC) to high ($\approx$ +5VDC).

For the stationary wheel case a fully electronic continuous track 360 degree potentiometer was used to obtain the wheel angular position. The potentiometer has a nominal full-scale voltage output range of 0 to 5V and was modified to fit into a hexagonal slot located on the side of the wheel; the potentiometer was removed after each angular position adjustment. The voltage output was linearly proportional to the wheel angular position and was acquired using one of the analogue channels on the logging card. At the start of every experimental investigation the potentiometer output voltage datum reading was acquired with the wheel positioned at zero degrees. The software was coded to prompt the user to physically rotate the wheel to the next angular position and the output voltage logged again and the new angular position computed based on the slope of the calibration data and the datum reading. Several attempts were usually needed to get the correct angular position. Figure 4.3 shows a typical example of the potentiometer calibration data. Additionally, a protractor was used to mark the tyre in 10 degree increments to enable the user to position the wheel in approximately the correct position prior to inserting the potentiometer into the hexagonal slot and logging the position.

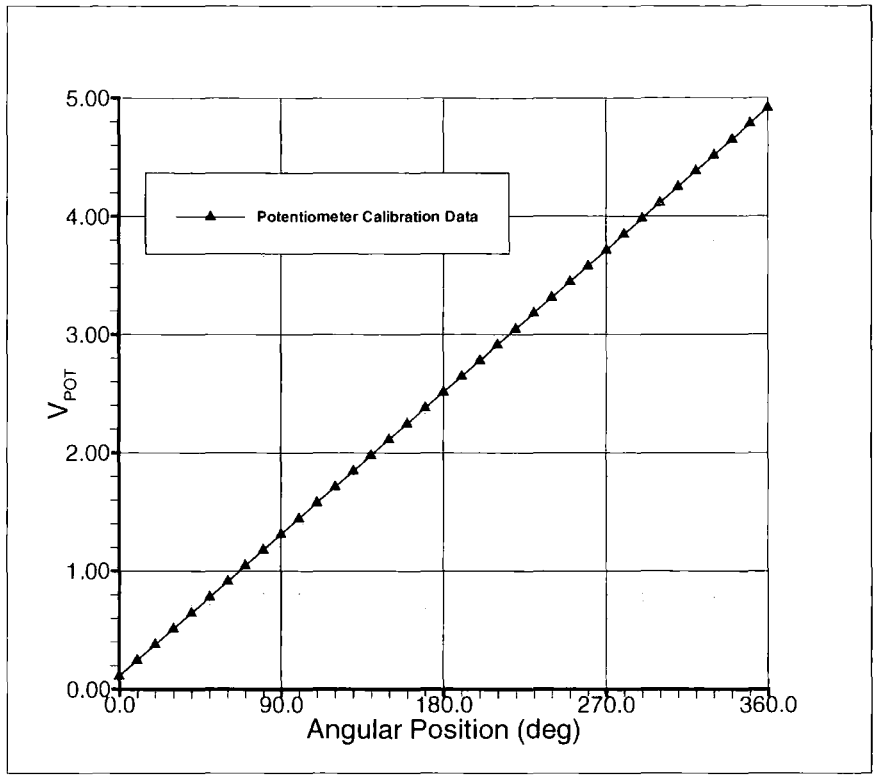


Figure 4.3: Typical Calibration Data from the Wheel Position Potentiometer.

### 4.4.8 System Specification

The radio telemetry system major specifications are presented in Table 4.2 and are based on the key components that make up the system. The sensitivity of the system, or rate of change of the output voltage to applied pressure is shown, however this is largely governed by the quantization error associated with the A/D converter. There were slight sensitivity deviations between transducers, therefore it is the nominal sensitivity that is shown in Table 4.2. The quantization error, that occurs when the analogue output from the pressure scanner is discretely sampled, means that the pressure must change by approximately 1.9Pa before the digital output from the A/D will register a change. The warm-up time is the amount of time required before the telemetry voltage output became stable; this was determined using the pressure scanner reference chamber (see Section 4.8.5).

| Instrumentation | Radio Telemetry System |
|---|---|
| Number of Transducers | 16 |
| Pressure Range | ±2500 Pa |
| Rise time | 50$\mu$s |
| Sampling Frequency (On-wheel) | 20kHz (max.) |
| Power Supply (On-wheel) | +12VDC,-12VDC,+5VDC |
| Power Supply (Off-wheel) | +12VDC |
| Output range | 0-4VDC |
| Zero pressure offset | 2VDC |
| Sensitivity | 1.56Pa/mV |
| Quantization Error | ±0.95Pa/LSB |
| Transmission Frequency | 370Hz |
| Warm-up Time | 1 hour |

Table 4.2: Major Specifications of the Radio Telemetry System.

## 4.5 System Operation and Algorithms

This section gives details on system operation and highlights the algorithms that make the telemetry system function. A brief overview of how the system works was given in Section 4.4 and more details are given here.

### 4.5.1 BITWISE Operators - WORD Generation

The generation of an 8-bit digital word utilises the bitwise operator "<<", which means "left-shift". Table 4.3 shows an example of WORD generation using bitwise operators. The external clock is toggled on/off to which data out of the A/D is synchronised. The data out pin of the A/D is then read by the microcontroller to establish whether a particular bit is high or low. In the example in Table 4.3 the first 6 bits of the 12-bit word output from the A/D converter are "100110" (see bottom row of table and read bits left (MSB) to right). The two remaining bits (LSB and BIT1) are reserved for word identification, which is the least significant

bit (LSB), and BIT1 which is used to flag when the transducer number is about to be changed. How the words are built up is relatively straightforward and starts at the LSB and works across to the MSB position in the memory variable register of the microcontroller. When the MSB is output from the A/D converter the value (high or low) is established and the data is left-shifted and a 1 is added to the word (see $2^{nd}$ row from top). The next bit in the example has the value 0 and this results in a left-shift only (see $3^{rd}$ row from top). The remainder of the word generation continues using the same method until the MSB from the A/D converter occupies the MSB of the memory variable register. In the example shown BIT1 is in fact high (1) indicating that the next word to be received by the off-wheel telemetry contains transducer selection information (described in Section 4.5.3). Two 8-bit words are generated containing the 12-bit digitised pressure data and the relevant word number and transducer selection flag. Both words are sent sequentially through the serial port of the microcontroller to the off-wheel telemetry system for word interrogation.

| MSB(7) | BIT6 | BIT5 | BIT4 | BIT3 | BIT2 | BIT1 | LSB(0) | OPERATOR |
|---|---|---|---|---|---|---|---|---|
| - | - | - | - | - | - | - | 0 | - |
| - | - | - | - | - | - | 0 | 1 | << +1 |
| - | - | - | - | - | 0 | 1 | 0 | << |
| - | - | - | - | 0 | 1 | 0 | 0 | << |
| - | - | - | 0 | 1 | 0 | 0 | 1 | << +1 |
| - | - | 0 | 1 | 0 | 0 | 1 | 1 | << +1 |
| - | 0 | 1 | 0 | 0 | 1 | 1 | 0 | << |
| 0 | 1 | 0 | 0 | 1 | 1 | 0 | 1 | << +1 |
| 1 | 0 | 0 | 1 | 1 | 0 | 1 | 0 | << |

Table 4.3: WORD Generation Example using Bitwise Operators.

### 4.5.2 BITWISE Operators - WORD Interrogation

Once the two 8-bit digital words are received they are stored in two variables. In order to find out whether each bit is high or low the bitwise operator "&" (AND) is utilised. To evaluate the MSB the AND operator is used in conjunction with the hexadecimal code 0x80 (binary 10000000). This can be written as,

Var & 0x80

If the MSB of the variable (Var) were high (1) the result would be 1. If the MSB were low (0) the result would be 0, since we know that all other values down to the LSB are 0. To evaluate the next bit down from the MSB, the bitwise operator AND would be used in conjunction with the hexadecimal code 0x40 (binary 01000000). The value 1, in the binary code, corresponds to the bit that is being evaluated since all other values equal 0. To evaluate the remaining six bits the hexadecimal codes 0x20, 0x10, 0x08, etc. would be used.

### 4.5.3 Transducer Selection Method

The transducer selection process starts when the on-wheel telemetry system selects the next transducer after a predefined number of samples. Due to the system being one-way communication all of the information including pressure data, transducer number and word number has to be included in two 8-bit words, as was described in Sections 4.5.1 and 4.5.2. Transducer selection would be made easier if the on-wheel and off-wheel systems could talk to one another, therefore the PC/logging card could be programmed to ask for the next transducer, indeed any transducer and not necessarily choose a transducer sequentially. Two-way communication was in fact devised but interference between the transmitter / receiver pairs proved troublesome and a decision was made to focus on the one-way communication system.

The method chosen to inform the off-wheel system of a change in transducer is to send a transducer selection initialisation word, or initialisation flag. The bit used to carry out this task is BIT1 and has been mentioned briefly in Section 4.5.1. Every word received by the off-wheel telemetry system is initially tested using the

bitwise operator & and the hexadecimal code 0x02 (binary 00000010). If the result of this operation is non-negative (i.e. 1) then the off-wheel telemetry goes into transducer information word standby, as the next word to be transmitted contains the vital transducer number information. Table 4.4 shows the transducer selection 4-bit words and corresponding transducer numbers. When the transducer information word is received it is interrogated using the aforementioned method, starting with the MSB down to BIT4. The remainder of the word is ignored and the digital port of the logging card is set accordingly depending on transducer word information. The off-wheel telemetry then resumes normal operation and waits to receive the first word of the pressure data.

| MSB(7) | BIT6 | BIT5 | BIT4 | TRANSDUCER |
|---|---|---|---|---|
| 0 | 0 | 0 | 0 | 1 |
| 0 | 0 | 0 | 1 | 5 |
| 0 | 0 | 1 | 0 | 3 |
| 0 | 0 | 1 | 1 | 7 |
| 0 | 1 | 0 | 0 | 2 |
| 0 | 1 | 0 | 1 | 6 |
| 0 | 1 | 1 | 0 | 4 |
| 0 | 1 | 1 | 1 | 8 |
| 1 | 0 | 0 | 0 | 9 |
| 1 | 0 | 0 | 1 | 13 |
| 1 | 0 | 1 | 0 | 11 |
| 1 | 0 | 1 | 1 | 15 |
| 1 | 1 | 0 | 0 | 10 |
| 1 | 1 | 0 | 1 | 14 |
| 1 | 1 | 1 | 0 | 12 |
| 1 | 1 | 1 | 1 | 16 |

Table 4.4: Transducer Selection 4-Bit Words and Corresponding Transducer Numbers.

### 4.5.4 System Initialisation and Error Detection

The main source of error for the radio telemetry system was the initialisation of the radio link. An inherent problem with the radio transmitter/receiver pair is that the output state always defaults back to the low (0) state (typically after 20ms) for the receiver irrespective of whether the transmitter is held in the high (1) state. This may not be of concern when dealing with other applications, however for the microcontroller it relies on the receive pin of the serial data port being held in the high state when waiting for the start bit (0). When the off-wheel telemetry was switched on the receiver would pull the receive pin low and the microcontroller would accept this as a start bit (0). It was therefore necessary to modify the software to force the receive pin to wait until it was in the high state for more than 2ms due to random noise on the receiver pin at it waited for transmitter initialisation. Random fluctuating effects were generally of the order of microseconds and therefore the receive pin would effectively ignore this until it received data in the high state for more than 2ms. This condition was not met until the transmitter sent an initialisation pulse, which sent the receiver into the high state and initialised the radio transmission. Once initialised there was no problem with this as the receive pin was never in the high state for more than 20ms, therefore the receiver could not default back to its preferred default low state.

Another problem with the system was such that if the two words containing the pressure data got mixed up, for example the off-wheel telemetry system read in WORD2 as if it were WORD1 the D/A output voltage would fluctuate. The fluctuations are due to the bits at the LSB end of the A/D scale changing more frequently, even at small pressure changes, and move towards the MSB position in the microcontroller variable register. To counter this problem the LSB of WORD1 and WORD2 were given the values 0 and 1, respectively, and therefore the microcontroller could check these values against what was expected, and if necessary they would be swapped with one another and into the correct order.

Additionally, if data synchronisation was not achieved at system initialisation, a

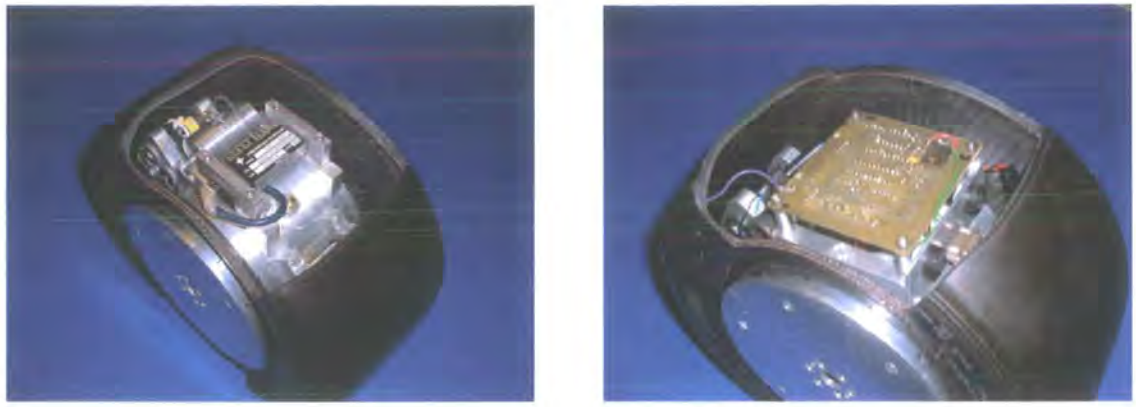

(a) Pressure Scanner Side. (b) Telemetry Circuit Side.

Figure 4.4: The Instrumentation Assembly Fitted Inside the Pneumatic Tyre.

start bit (0) may be interpreted but in fact the "0" could belong to the pressure data. The rest of the pressure data would then be read incorrectly and the system may then treat a "1", also from the pressure data, as the required stop bit. This causes the system to behave very erratically. A visual method of detecting this, and the word mix up problem, was to implement a light-emitting diode (LED), which was programmed to light up if either the words received were the wrong way around or the system behaved erratically. A digital voltage meter (DVM) was also used to visually monitor the D/A output voltage during an experimental run. All experimental investigations were repeated if the LED illuminated and/or the DVM voltage exhibited random fluctuations.

Figure 4.4 shows the instrumentation assembly when fitted inside the pneumatic tyre.

## 4.6 Development of Data Acquisition System

Data acquisition was carried out using an Amplicon PC30-PGH, 12-bit ADC card run on a MS-DOS based PC. This type of logging card has a maximum of 16 analogue input channels and an additional three 8-bit digital I/O ports. The card was operated in differential mode, therefore limiting the number of analogue inputs to 8. The input voltage range was set to 0-10V, with each channel having an individual

software controlled gain setting of either 1, 2, 4 or 8.

A matched set of second-order 250Hz analogue low-pass filters were used to provide anti-aliasing.

The data logging and post-processing software, used throughout this work, were custom written in FORTRAN.

This basic data acquisition system (logging card and PC) was used for all experimental investigations throughout this work except the PIV investigations.

## 4.7 Post-Processing Techniques

The majority of the post-processing techniques were developed in-house and clear references are made to the contribution of others.

### 4.7.1 Data Analysis Requirements

The data that were required for this work, using the pressure measurement instrumentation, were the time-averaged surface static pressure distributions across the surface of the rotating and stationary wheel. These data were presented in terms of the static pressure coefficient, $Cp$, as a function of the angular position of the wheel, $\theta$.

The time-averaged integral lift and drag forces and coefficients were required for the stationary and rotating wheel cases.

### 4.7.2 Data Validation Method

A data validation method was devised to resolve a particular problem due to the logging frequency being greater than the transmission frequency; these being 1600Hz and 370Hz for the logging and telemetry transmission frequencies, respectively. Figure 4.5 shows this schematically. The reason for the higher logging frequency was

to meet the desired angular position measurement resolution of a reading less than every 4 degrees for the rotating wheel case. As discussed in Section 4.4.8 the acquisition frequency of the on-wheel telemetry was sufficiently high at 20kHz, and the lower frequency of 370Hz for the transmission of data did not have any effect on the pressure data; essentially all this meant was that the data was sampled at a higher frequency (on-wheel) and then relatively slowly transferred to the local host PC (the data transmission being a bottleneck). However, the problem is that the D/A converter analogue output voltage was held at a particular voltage level whilst waiting for the next two words of pressure data to update the output voltage. The logging frequency being higher than this "refresh" rate of change of the D/A converter causes data to be logged at a particular angular position that corresponds to another previous position. This is still the case even when phase angle offset correction has been applied (discussed in Section 4.8.1). This problem does not have any significant effect for the base region of the wheel, due to the pressure being relatively constant and therefore incorporating some data from a previous angular position does not affect the average since the pressure values are almost the same, although this does not mean that including data from a previous angular position is acceptable. Where this effect is accentuated is at the contact patch, where the pressure gradients are profoundly increased and any data that is incorporated into the average from a previous angular position reduces the magnitude of the pressure peak.

Figure 4.6 shows how the data validation method is implemented using the D/A chip select (CS) pulse. It is worth noting that the units on the $x$ and $y$ axes are arbitrary for clarity, and do not represent the logic levels (0-5VDC) normally expected for a D/A converter chip select pulse. When the chip select pulse is set to the low state the D/A is enabled and a conversion started. On a rising edge of the chip select pulse the output voltage from the D/A converter has been updated. It is the rising edge on the chip select pulse that prompts a change in state on the data validation pin as can be seen in the figure. Therefore, the software looks for a change in state on the data valid pin to signify valid, or updated, pressure data.

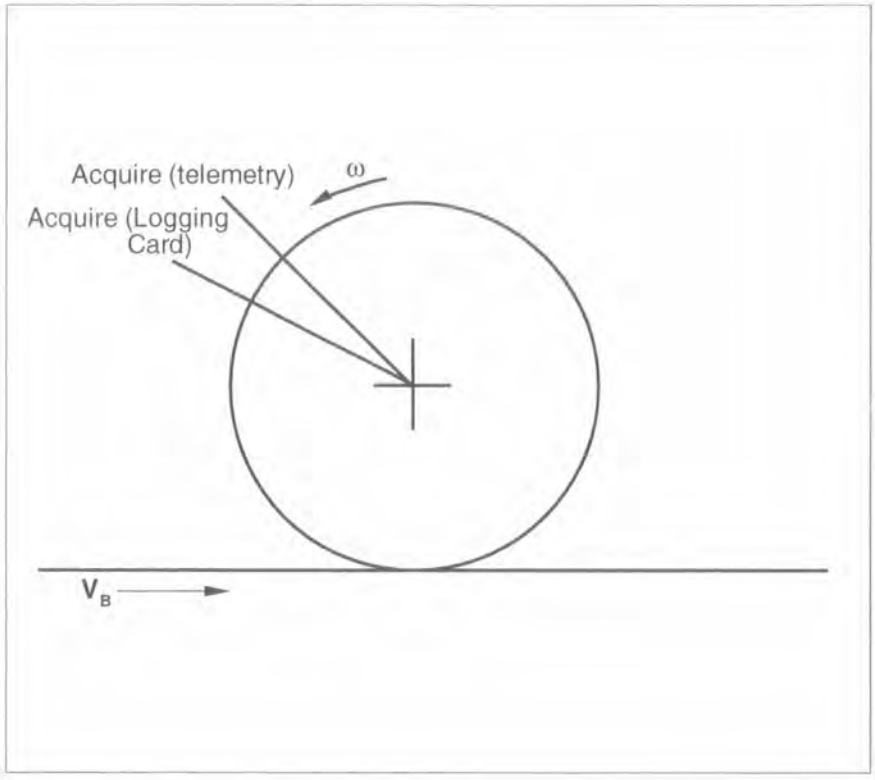


Figure 4.5: Telemetry/Logging Card Acquisition Schematic.

The reason why the data valid pin was used, and not simply the chip select pulse, is due to the short time period (high frequency) when the chip select pulse is in the low state. At the specified PC sampling frequency (1600Hz (logging card acquisition frequency)) it was difficult to ascertain when the chip select pulse changed states, hence the implementation of the lower frequency data valid pin. The data valid pin was logged simultaneously with the surface pressure data and the trigger signal.

The surface pressure data were sorted based on the data valid pin output. Any data point following a rising or falling edge on the data valid pin were accepted to be carried forward to ensemble averaging. All other data points remained unused resulting in a large amount of void data, although ensuring good quality data and adequate angular position measurement resolution.

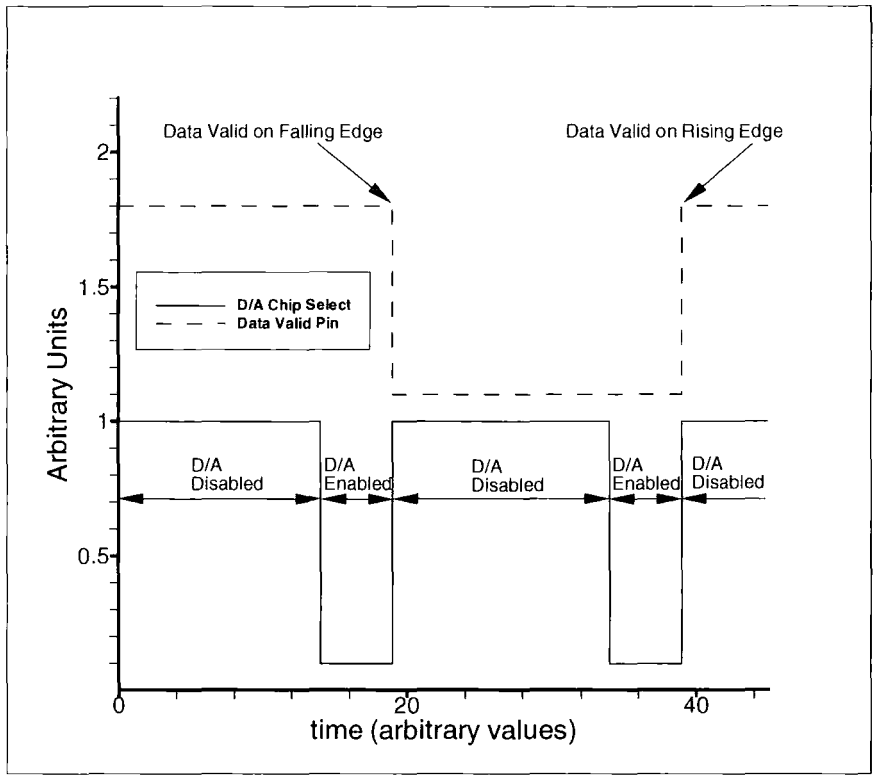


Figure 4.6: Data Validation Method using D/A Chip Select Pulse Train.

### 4.7.3 Ensemble Averaging Method

Ensemble time-averaging of the data was a necessary part of the analysis for the rotating wheel case. The stationary wheel pressure data averaging was simply a case of computing the average of the voltage time history, since it wasn't time dependant in the sense that the rotational frequency was zero and therefore the averaging was for a fixed position pressure tapping. For the rotating case the pressure tapping angular position varies as a function of time. Figure 4.7 shows a sample D/A output voltage time history for the centreline pressure tapping of the rotating wheel including the once-per-revolution reference trigger signal. $\Delta$t is the time period for one complete wheel revolution and therefore the rotational frequency, $f_{rot}$, is expressed in Eq. 4.1.

$$f_{rot} = \frac{1}{\Delta t} \tag{4.1}$$

It is worth noting that the figure is based on data that originated during the development of the system and thus at t=0 (i.e. the start of a wheel revolution) the angular

position of the wheel does not necessarily correspond to zero degrees. Within the post-processing software whenever a rising edge is observed on the trigger signal the time history, which was previously stored in a two-dimensional array, is modified and the time is set to zero (t=0). Therefore, the time history that originally started at t=0 and finished at t=end, now has a series of micro time histories all starting at t=0, each history representing one complete wheel revolution. In the ensemble averaging all values at t=0 are averaged, as are all values at any specific time during the wheel rotational cycle, corresponding to a specific angular position.

The effects of ensemble averaging can be seen in Figure 4.8 where the effects of increasing the number of data sets is presented. Data were acquired in sets of 2048 measurements. The number of sets logged were increased from 2 sets, which yielded an oscillatory surface pressure distribution, through to 64 sets. The incremental set number increase was fixed at double the previous set number (i.e. 16 sets doubled to 32 sets). The time-averaged data got progressively more stable as the number of sets were increased until the differences between 32 sets and 64 sets were insignificant since the pressure traces were almost identical. From this experimental test it was decided that 32 sets would provide a sufficient quantity of data points in the ensemble averaging to ensure good quality, repeatable aerodynamic data. One factor that potentially led to the large number of sets being logged was the effects of radio frequency interference (RFI), which is discussed in Section 4.7.4. Also, due to the data validation method that effectively "dumps" large amounts of unused data, the number of data sampled increased in order to achieve a reasonably high number of valid data points.

The static pressure distributions hereinafter are all presented in terms of the static pressure coefficient ($Cp$), which is shown in Eq. 4.2.

$$Cp = \frac{P_S - P_{S\_ref}}{P_{O\_ref} - P_{S\_ref}} \tag{4.2}$$

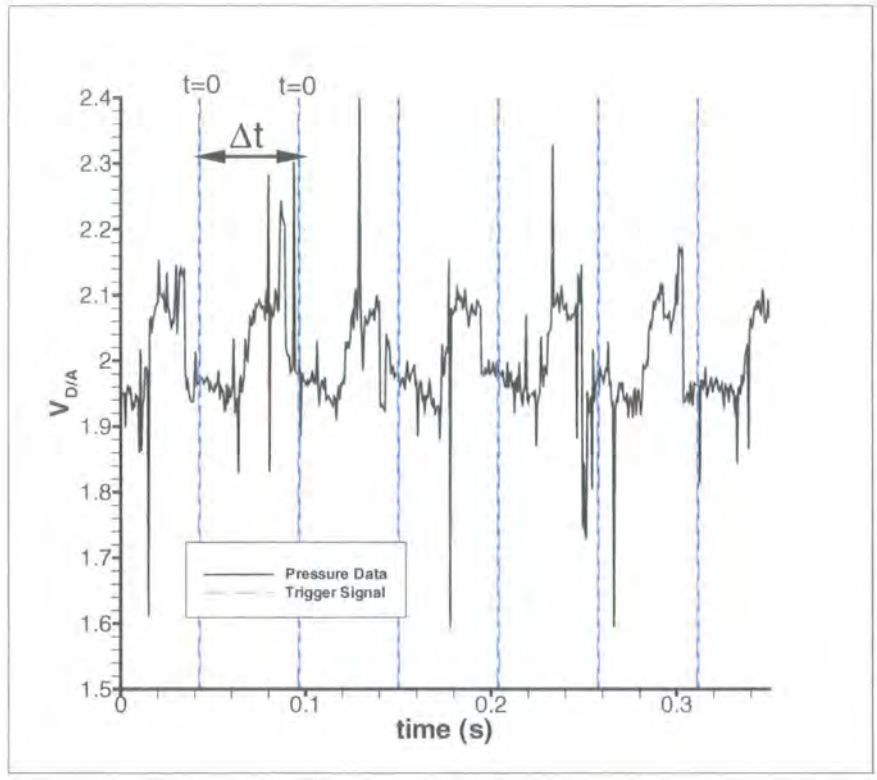


Figure 4.7: Sample Voltage Time History of the D/A Converter Output including Trigger Signal used for Ensemble Averaging for the Rotating Wheel Centreline.

### 4.7.4 Elimination of Outliers

As a direct consequence of using an inverter on the MGP, problems with electrical noise (Radio Frequency Interference (RFI)) became evident for the rotating case only. It was initially thought that the low-pass analogue filter would eliminate the high frequency components of the signal and the problem would be resolved. However, as described by Alley [1] RFI largely affects electronic systems with microchip-based integrated circuits (IC's) and the laboratory data acquisition system is home to a large number of resident microchips. Other equipment, such as the cathode ray oscilloscope were little affected by RFI. Special RFI filtering techniques can be used but the laboratory power supply wasn't suitable for these methods. The effects it had on the surface pressure data were to superimpose random peaks, or spikes, in the data with a relatively large magnitude. These spikes, or outliers, can be seen in Figure 4.7 and some were actually outside the voltage output range of the D/A; such spikes were removed manually. However, due to the data valida-

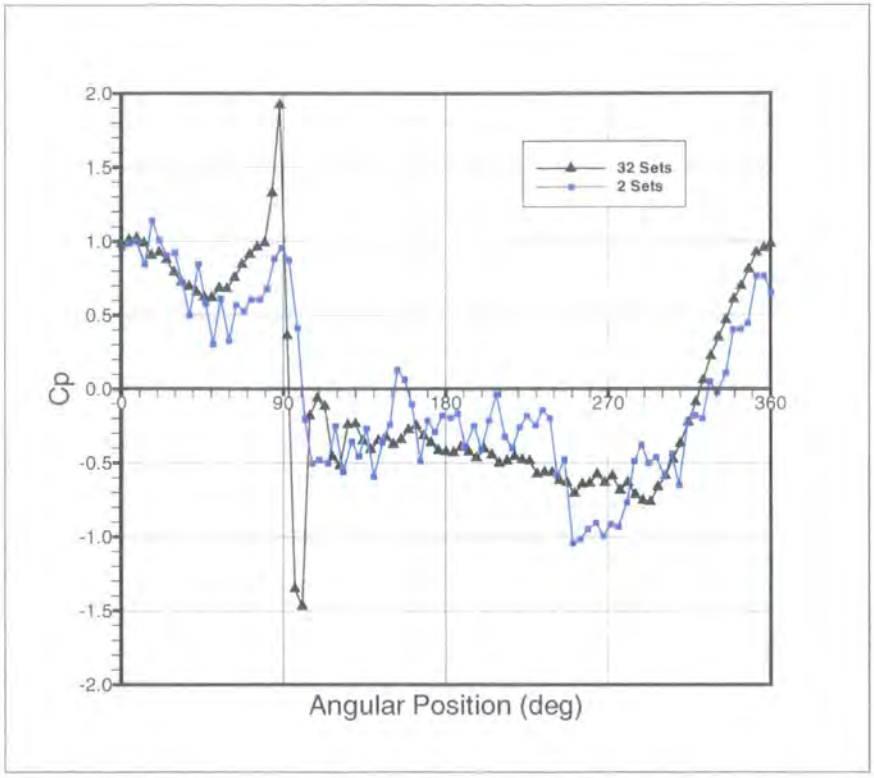


Figure 4.8: The Effects of the Number of Data Sets.

tion method, where large amounts of data are unused, it was this method coupled with the ensemble averaging that minimised the RFI effects. The low pass filters, used to provide anti-aliasing, were removed due to the RFI effects since these effects were prevalent with or without them fitted. The removal of excessive peaks in the data further reduced the problem. The technique employed to remove these random peaks in the data was to initially perform the data validation method and reduce the number of "outliers". The ensemble average was then computed along with the standard deviation of the data set. The pressure data were then scanned to establish whether a particular data point was less than or greater than the average $\pm 2.5$ standard deviations. Obviously the average was computed based on these outliers, however it must be reiterated that the excessive peaks were removed manually and therefore did not have an erroneous effect on the average. Any data point that was found to be an outlier was removed and the average recalculated. Several experiments were conducted to check the repeatability of the surface pressure data and it was found to be within 1.5% between successive tests; thus the combination of

the techniques employed had significantly reduced the random RFI effects for the time-averaged surface static pressure data. For time resolved measurements careful analysis procedures would be needed to reduce the RFI effects, unless the unsteady surface pressure field could be discretely sampled simultaneously with a reference hotwire probe in the wheel wake using the unsteady reconstruction method developed by Sims-Williams [56], although this method does rely on the flow exhibiting some periodicity. Using this method any outliers could be removed in the same way as discussed above for this work.

An alternative method to reduce the RFI effects could have been to remove the inverter on the MGP and replace it with a fixed gear system between the motor and the MGP pulley system. Bearing in mind the MGP translational velocity was fixed for this work at 14.7ms$^{-1}$ this appeared to be a reasonable solution. However, it was not a practical solution as the wind tunnel facility was not solely used for this work. Also, the above data analysis procedures and the repeatability of the results gave confidence in the quality of all subsequently logged surface static pressure data, for both the stationary and rotating wheel cases.

### 4.7.5 Integral Lift and Drag Forces

The time-averaged lift and drag forces acting on the wheel were calculated by integrating the surface static pressure data across the surface of the wheel. The derivation of the integral lift and drag forces is shown below.

Figures 3.9 and 4.9 show the wheel and element notation used for the derivation, respectively. Consider the force acting on the element in the direction of the airflow (drag force). The area of the element, $A_e$, is defined in Eq. 4.3. The pressure, P, acts normal to the surface of the wheel and thus needs to be resolved into horizontal (drag) and vertical (lift) components. The drag force acting on the element, $F_{De}$, is shown in Eq. 4.4. The $\cos\phi$ term in Eq. 4.4 resolves the pressure into the direction normal to the line of contact (or normal to the tread region of the tyre). The value of $\phi$ for the tread region tappings (tappings 1 to 6 of Figure 3.6 in Chapter 3) is

zero and therefore the $\cos\phi$ term of Eq. 4.4 applies only to the sidewall pressure tappings, where $\phi$ is non-zero (see Figure 3.7 in Chapter 3).

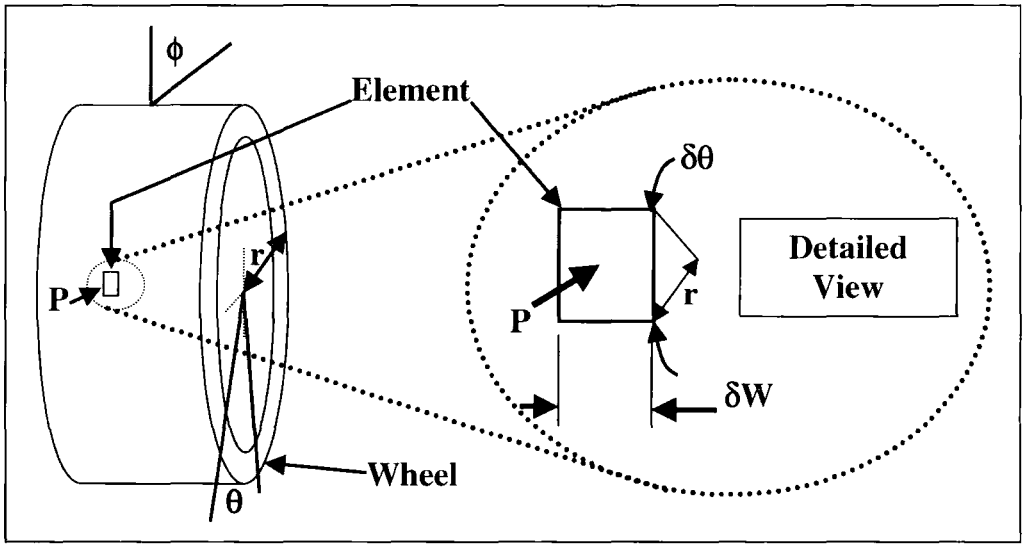


Figure 4.9: Element Notation for Lift and Drag Force Derivation.

$$A_e = r\,\delta\theta\,\delta W \tag{4.3}$$

where $r$ is the radius of wheel, $\delta W$ is the elemental width, and $\delta\theta$ is the swept angle for the element.

$$F_{De} = P\cos\theta\, r\,\delta\theta\cos\phi\,\delta W \tag{4.4}$$

Therefore by integrating across the complete surface of the wheel, the integral lift and drag forces are derived. Eqs. 4.5 and 4.6 show the integral pressure lift and drag forces, respectively (i.e. no contribution from skin friction).

$$F_{Lw} = \int_0^W \int_0^{2\pi} P\sin\theta\cos\phi\, r\, d\theta\, dW \tag{4.5}$$

$$F_{Dw} = \int_0^W \int_0^{2\pi} P\cos\theta\cos\phi\, r\, d\theta\, dW \tag{4.6}$$

The lift and drag coefficient equations are shown in Eqs. 4.7 and 4.8, respectively.

$$C_{Lw} = \frac{F_{Lw}}{\frac{1}{2}\rho V^2 A_w} \tag{4.7}$$

$$C_{Dw} = \frac{F_{Dw}}{\frac{1}{2}\rho V^2 A_w} \tag{4.8}$$

where $A_w$ is the projected frontal area of the wheel.

The numerical integration of the surface pressure data can be computed by calculating the area under the curve by using Eq. 4.9.

$$Area = \int_a^b y\,dx \tag{4.9}$$

Simpson's rule of approximate integration was used to compute the lift and drag forces acting on the wheel. Eq. 4.10 shows Simpson's one-third rule equation for approximating the area under a curve.

$$Area = \int_a^b y\,dx \approx \frac{\Delta x}{3}[y_{(a)} + 4y_{(1)} + 2y_{(2)} + \ldots + 2y_{(b-2)} + 4y_{(b-1)} + y_{(b)}] \tag{4.10}$$

The Simpson's one-third rule requires the data set to have an odd number of equally spaced data points that can be split into an even number of equally spaced strips, or panels. This was achieved by sampling the pressure data at 1600Hz, resulting somewhat coincidentally in an odd number of data points for the static pressure distributions, and therefore resulting in equally spaced data points approximately every 4 degrees for the rotating case. For the stationary wheel the pressure data were again sampled at 1600Hz, although unlike the rotating case this had no bearing on angular position measurement resolution. The data were sampled every 10 degrees corresponding to an odd number of data points. The numerical integration was then carried out for each individual pressure tapping before being applied across the wheel width; the forces were then output and all coefficients calculated. Integrating across the wheel width also satisfied Simpson's rule as there were an odd number of equally spaced pressure tappings; hence, an even number of strips. A subroutine was custom written for integrating the pressure data using Simpson's one-third rule. The errors associated with approximate integration are discussed in Section 4.9.1.

## 4.8 Correction Methods Applied to Pressure Data

A number of corrections were applied to the surface static pressure data for both the stationary and rotating cases. Although, most of the corrections were only applicable to the rotating case, such as phase angle correction (see Section 4.8.1) and centrifugal effects caused by wheel rotation (see Section 4.8.2).

### 4.8.1 Phase Angle Correction

Phase correction was required to correct for the telemetry system time lag, or throughput time. This means that when the telemetry system acquires the pressure data at a particular angular position it takes a small quantifiable time to be transmitted to the data acquisition PC. Figure 4.10 shows the telemetry throughput lag with the use of a signal generator connected to the input of the A/D converter. A saw wave of constant frequency was chosen for this test, set at 250Hz. The units on the y-axis are arbitrary for clarity since the input voltage range was different (±5VDC) to the voltage output of the D/A converter (0-4VDC). The time period, t, in the figure was 4ms ($f = 1/0.004 = 250$Hz) and the output is constantly lagging the input by a constant amount of time, $\tau$, of 2.7ms. The transfer lag in no way affects the signal amplitude.

Figure 4.5 again shows schematically the problem associated with the telemetry time lag when applied to the wheel. The rotational frequency of the wheel is constant at 18.5Hz, which significantly aids correction implementation. If no correction were made then the pressure data acquired by the logging card would be from a previous angular position, acquired by the on-wheel telemetry system. The exact angular position offset, or phase angle offset, in terms of $\theta$ can be expressed in Eq. 4.11 as,

$$\theta_{PHASE(OFFSET)} = \tau \times f_{rot} \times 360 \tag{4.11}$$

As Eq. 4.11 shows, due to the telemetry time lag, $\tau$, being constant the phase angle offset is a function of rotational frequency, $f_{rot}$, only. Indeed, the rotational frequency is also constant, hence the phase angle offset is constant, thus significantly

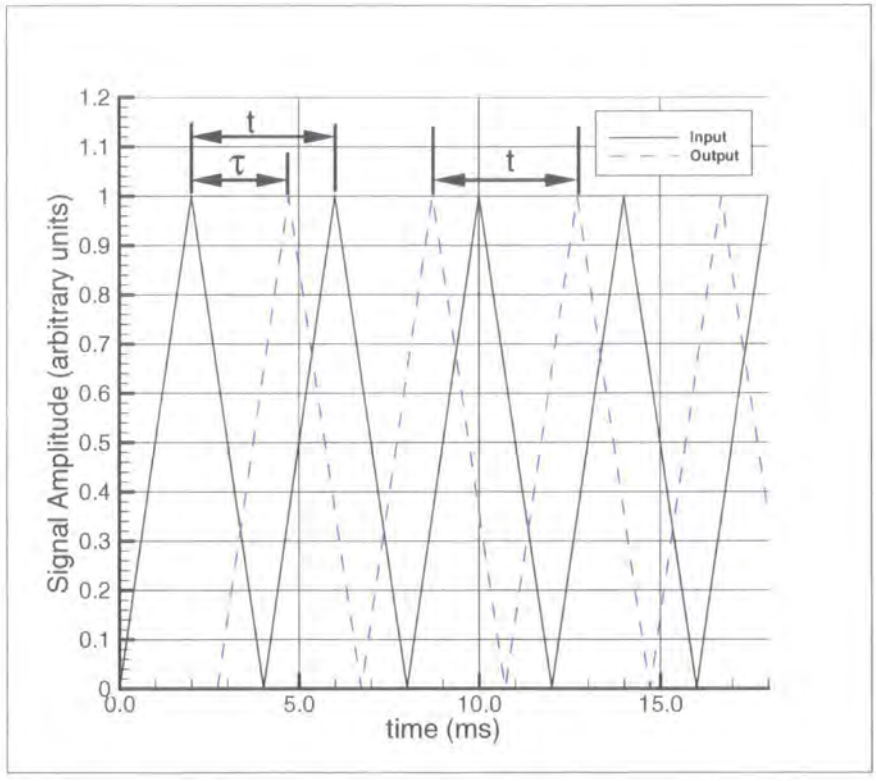


Figure 4.10: Example showing the Telemetry Transfer Lag, Saw Wave Constant Frequency @250Hz .

simplifying the software algorithm.

Figure 4.11 shows the phase angle offset as a function of rotational frequency and highlights that at a rotational frequency, $f_{rot}$, of 18.5Hz the phase angle offset is 18 degrees (see point (A)). All phase angle offset corrections were applied to the pressure data after ensemble averaging.

### 4.8.2 Centrifugal Corrections

The centrifugal effects acting on the pressure measurement system can be split into two areas regarding the system mechanics, and are obviously related to the rotating case only. The first area refers to the mechanical effects with respect to the behaviour of the pressure scanner as a result of being subjected to the centrifugal forces. The second area is concerned with the centrifugal pressure gradient due to the radial position of the pressure scanner in relation to the pressure tapping radial

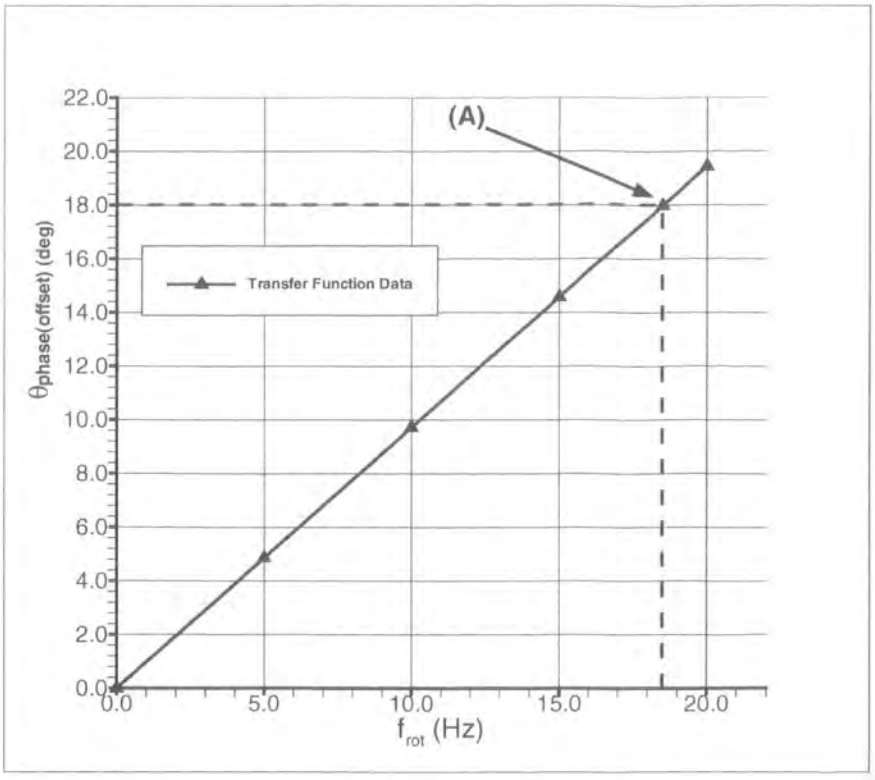


Figure 4.11: Phase Angle Offset as a Function of Rotational Frequency.

position.

The design of the wheel assembly and telemetry system radial location within the assembly was carefully considered. It was decided in order to minimise centrifugal effects the pressure scanner would be located as close as possible to the axis of rotation, hence reducing the centrifugal effects acting on the pressure scanner. The pressure scanner mounting was in fact designed in such a way that the scanner was located in a sideways orientation on the wheel rim assembly, thus preventing the diaphragm from being subjected axially to the centrifugal force. Once designed and manufactured this was tested by fitting the pressure scanner onto the wheel rim and connecting one particular transducer to the reference port of the scanner. Therefore, the differential pressure between the transducer and the reference port was zero, resulting in the same voltage output from the scanner. The wheel was then rotated at a number of rotational frequencies such to analyse the voltage output change as a function of the rotational frequency. The results of this test are presented in Figure

4.12 and show the change in pressure as a function of $\omega^2 r_M$, non-dimensionalised by $g$. This shows a strong inverse linearly proportional relationship between pressure change and the square of the rotational speed, which was to be expected as the centrifugal force acting on any rotating system is a function of the square of the angular velocity. Only three data points are presented but the strong negative correlation between the data is evident. Although a line of best fit is shown in Figure 4.12, the equation of this line was not used due to the angular velocity of the wheel being constant, therefore only the value of the correction specific to the experimental rotational frequency of the wheel for the investigations was used. Eq. 4.12 shows the relationship between the change in pressure as a function of the product of the wheel rotational speed squared ($\omega^2$) and the pressure scanner radial position ($r_M$), non-dimensionalised by $g$.

$$-\Delta P \propto \frac{\omega^2 r_M}{g} \tag{4.12}$$

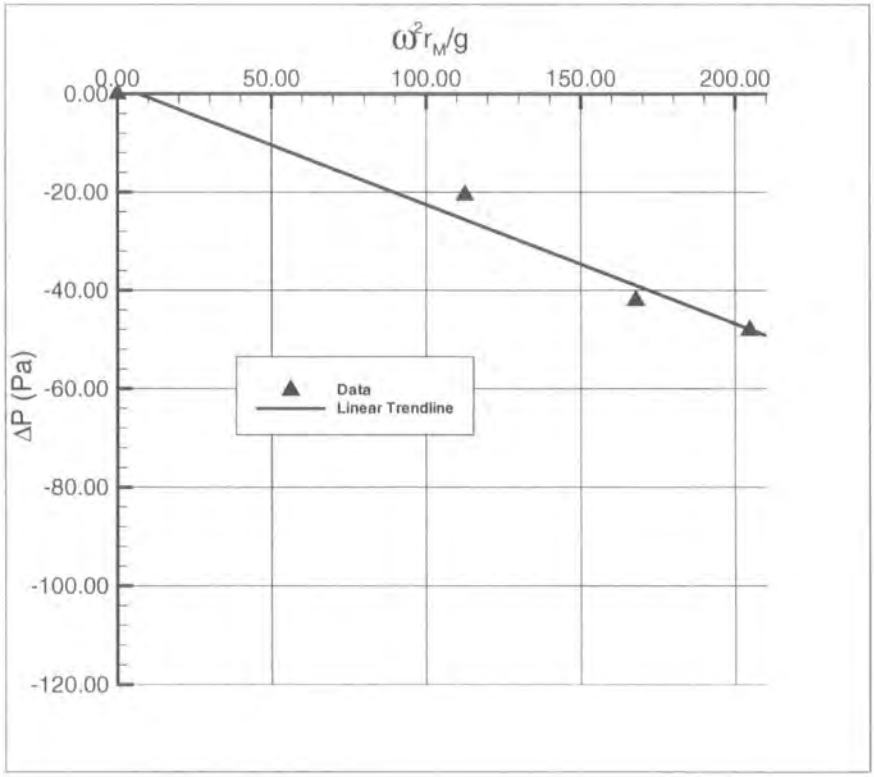


Figure 4.12: Centrifugal Effects - Change in Pressure as a function of $\omega^2 r_M$, non-dimensionalised by $g$.

The pressure data had to be corrected for the effects of the centrifugal pressure gradient caused by measuring the pressure at a small radius from the pressure tapping. Eq. 4.13 shows the equation used for the correction (see Nomenclature for details of the notation). The centrifugal pressure gradient correction could be eliminated by mounting the pressure transducer at the pressure tapping radial position, which is a method used by Chell [12]. The drawbacks to this method are that the centrifugal effects acting on the transducer are increased and the geometrical limitations of installing transducers at the wheel surface (i.e. only a small number of transducers can be used in a given space). It is therefore concluded that the methods described for this work offer increased flexibility, over alternatives, at the expense of a very minor and quantifiable drawback in correcting for the centrifugal pressure gradient.

$$P_S = P_M + \frac{\rho V_\infty^2}{2}\left(\frac{r_S^2 - r_M^2}{r_W^2}\right) \tag{4.13}$$

### 4.8.3 Tubing Transfer Function Correction

Tubing transfer function correction (TTFC) is used routinely for unsteady aerodynamic measurements. However, the inclusion of such a correction for time-averaged aerodynamic data was due to some oscillatory behaviour observed in the time-averaged surface static pressure distributions for the rotating wheel. It was unknown whether the short length of tubing (120mm) between the pressure scanner and tapping were causing this effect, possibly due to the pressure signal frequency being near to the natural frequency of the tubing, or one of its harmonics.

The Pressure Systems Inc. ESP-16HD transducers have a nominal response time of 50$\mu$s (1/20000Hz) and it is common for pressure transducers to have high frequency responses far in excess of the frequencies associated with the aerodynamics of both road and racing car wheels. However, the tubing between the surface of the wheel and the pressure scanner can exhibit a response that is highly frequency dependant and this usually limits the frequency response of the pressure measurement system. A system is required that neither attenuates, amplifies or phase shifts the pressure signal between the point of measurement and the pressure scanner [53]. The tubing

frequency response is a function of viscous, momentum and elastic, or compressibility, effects. Due to the transducer chamber having a finite volume (indeed any associated connector) and the compressibility of air, a certain quantity of air must flow down the tube in order to pressurise this volume. Viscosity effects act against this movement of air and cause the response of the system to be dampened. The tubing will also exhibit a natural frequency due to the combined presence of fluid mass and elasticity (compressibility) and this results in signal amplification near the natural frequency or its harmonics. The tubing transfer function correction technique used in this work corrects for both amplitude and phase, and is described by Sims-Williams and Dominy [57], [58]. In addition, the technique employed here and its development are comprehensively described by Sims-Williams [56].

Figure 4.13 shows the apparatus used to measure the transfer function of the tubing and pressure tapping. The loud speaker pressurises a closed volume which is connected via a short length of rubber hose (to isolate mechanical vibrations) to a small chamber. The instantaneous pressure inside the chamber is recorded by a reference pressure transducer and the pressure tapping and tubing are connected to the other side of the chamber. The tubing is then connected to the test transducer used in the wind tunnel measurements. The loudspeaker was excited with a swept sine wave (typically from 6Hz to 600Hz with a sweep period of 0.75s) and the pressures measured at both transducers are logged in sets of 2048 samples (2048 being an integer power of 2 for the FFT). The results of the tubing transfer function correction are shown in Appendix B.1 (see Figures B.1 and B.2).

Fast Fourier Transforms (FFT's) of the pressure signals were calculated using a routine due to Press et al [50], and the complex transfer function of each tube is defined in Eq. (4.14).

$$T(f) = \frac{B(f)}{A(f)} = \frac{B(f)A*(f)}{|A(f)|^2} \tag{4.14}$$

where $A$ is the Fourier transform of the pressure recorded by the reference signal, and $B$ is the Fourier transform of the transducer connected to the tubing under test.

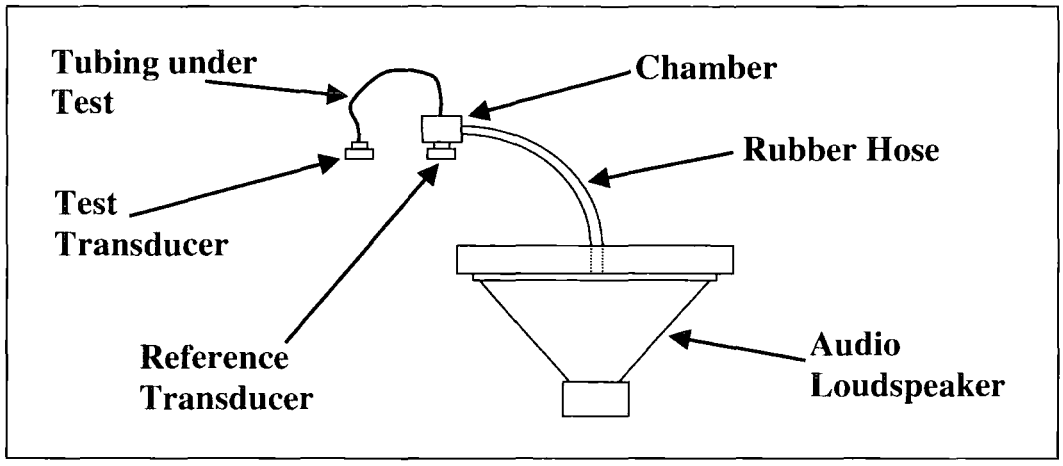


Figure 4.13: Apparatus Used to Measure the Transfer-Function of the Static Pressure Tapping and Tubing.

In order to ensure high quality results the data were logged in sets of between 50 and 500 sets of 2048; the average transfer function was then computed. To reduce the effect of the finite data set length a Hanning window function was applied, thus significantly improving the quality of the results.

Figure 4.14 shows the effects of tubing transfer function correction on the time-averaged centreline surface static pressure distribution for the rotating case. The figure shows graphically that the tubing transfer function correction does not have any effect on the time-averaged data; both data sets are identical. As a result of this all subsequent time-averaged data were not corrected using tubing transfer function correction. However, the resonance peak (see Figure B.1)) and signal attenuation will have an effect on the instantaneous pressure data and it is surprising that the corrected time-averaged data do not differ from the uncorrected data. In particular the oscillations behind the contact patch remain (after the negative pressure peak (rear jetting)) and could be caused by resonance effects in the tubing at a particular unsteady pressure frequency, although the tubing transfer function correction suggests otherwise. The negative pressure peak is a characteristic associated with the rear jetting phenomenon and is discussed fully in Chapter 10. For time resolved measurements the application of tubing transfer function correction would be necessary. For time-averaged measurements the effects of the tubing requires further

investigation and analysis to establish fully whether the oscillations are a function of the tubing or an intrinsic aerodynamic flow feature. This is discussed in the recommendations for future work (Chapter 11). Details of the oscillations exhibited in the surface pressure distributions are given in Chapter 10.

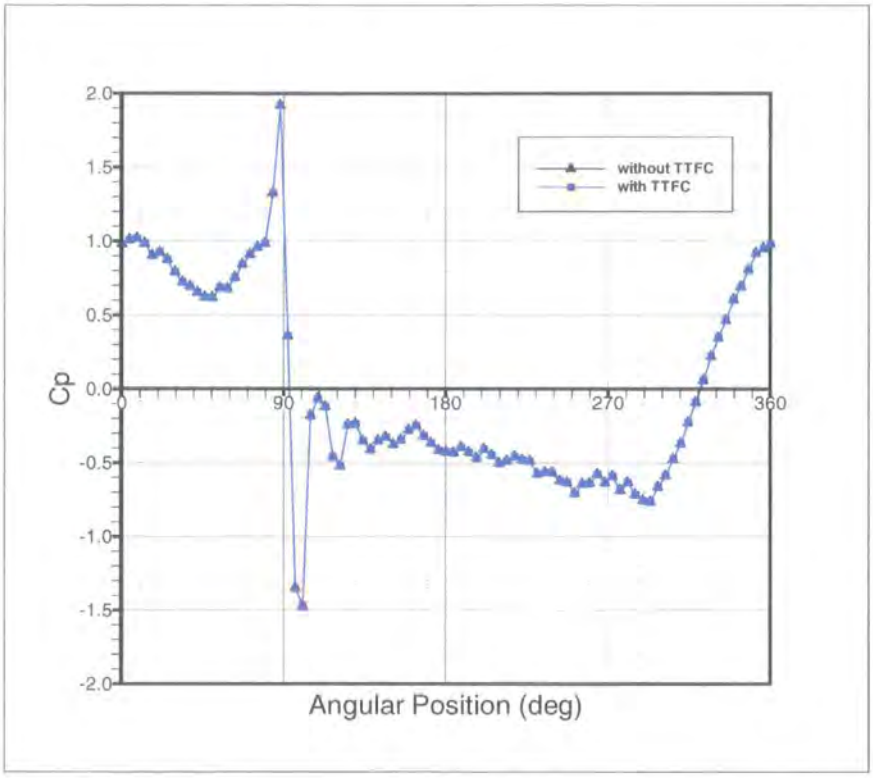


Figure 4.14: The Effects of TTFC on the Centreline Time-Averaged Surface Static Pressure Distribution for Rotating Wheel.

### 4.8.4 Blockage Correction

As a direct consequence of the aims of this work, where the emphasis is put on flow structure and not precise quantification of the absolute forces acting on the wheel, no blockage correction was applied. Incremental changes in the body forces were considered to be sufficient in further understanding the current knowledge, especially when coupled with detailed flow-field measurements. Also, the model blockage was fixed at less than 7% and was deemed sufficiently low for an open-jet wind tunnel to justify the omission of blockage correction.

### 4.8.5 The Effects of Temperature Variation on Transducer Reference Pressure

Since the tyre required inflation a further complexity was added in that the pressure scanner is located within the tyre and cannot be exposed to the inflation pressure (typical inflation pressure being 7psi ($\approx$ 0.5bar)). To resolve this problem a sealed reference chamber was designed to connect onto the reference port of the pressure scanner, although this was at the expense of slight voltage output drift due to temperature changes within the tyre during an experimental run. The sealed reference chamber was 25.4mm in diameter with a bore of 14mm. Figure 4.4a shows the cylindrical reference chamber located in between the pressure scanner and one of the batteries. The temperature variation typically caused the reference pressure to increase slightly and therefore reduce the measured static pressure at the surface of the wheel. Quantification of this effect was realised through additional data that were gathered and the effects were found to be small. The tests carried out were to initially log the datum voltage from the off-wheel telemetry system and then rotate the wheel over a given time and then acquire the datum voltage once again. Figure 4.15 shows the effects on the datum voltage against time for the rotating wheel. It is worth noting here that the D/A analogue voltage output range was 0-4VDC and therefore the drift was relatively small in comparison. Over the tests conducted the voltage offset appears to drift linearly with time. The integration time for the data acquisition of the surface pressure data was 40.96s (32 sets of 2048 measurements sampled at 1600Hz), which translates to a change in voltage offset of approximately 7mV corresponding to a change in pressure of 6.5Pa. In terms of the maximum dynamic pressure change this equates to 5%, at the end of an experimental run, which is reasonably low. However, the voltage time history data were corrected to account for this voltage offset drift as a function of time and the results obtained showed no significant differences between the uncorrected pressure data. Hence, this correction was not implemented into the post-processing routines.

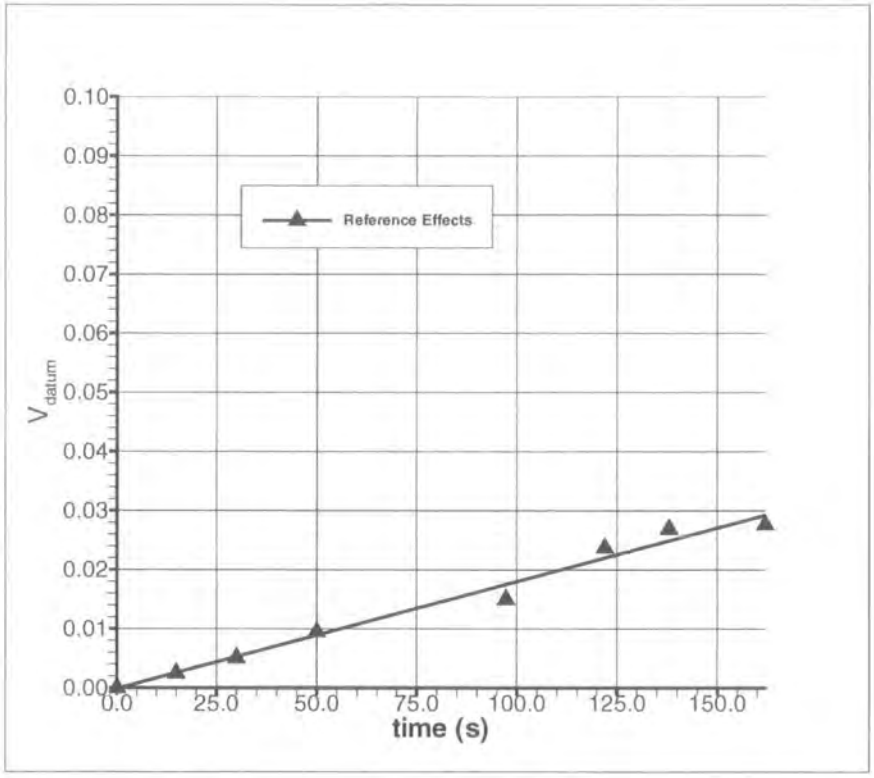


Figure 4.15: Telemetry Datum Voltage Drift as a Function of Time Due to Wheel Rotation.

## 4.9 Experimental Accuracy

Errors in aerodynamic measurements can be classed as being either systematic or random. Systematic errors can be compensated for in theory, whereas random errors cannot be compensated for. For example, when considering the pressure measurement instrumentation systematic errors will occur in the measurements due to thermal drift (i.e. the reference pressure effects discussed in Section 4.8.5) of both zero datum values and sensitivity of the pressure scanner.

### 4.9.1 Approximate Integration Errors

Simpson's one-third rule has been shown to produce reduced errors compared to the three-eighth Simpson's rule, or indeed the trapezium rule (Dyer [18]). If the data set happens to contain an even number of measurements the three-eighth rule can be used. The number of data points for this work is dependant on the sampling and rotational frequencies only, since the geometrical positions of the pressure tappings

are fixed. The combined effect of these two frequencies yielded an odd number of measurements in each data set, therefore the one-third rule was used throughout, however, the post-processing software could deal with even sets of data by using the three-eighth rule for the first three data points and the one-third rule for the remainder of the data set.

### 4.9.2 Telemetry System Error

The overall telemetry system error is a combined effect of various different constituent components. There are static errors associated with the pressure scanner and the A/D and D/A converters, although these are proportionally small relative to the full scale deflection of such devices. The quantization random error present in the A/D converter is also small and therefore it is thought that the errors associated with the complete telemetry system are less than 1% of the full scale deflection of the pressure scanner. Obviously this value does not include numerical integration errors and in fact this error would increase as a smaller pressure range of the scanner was used.

### 4.9.3 Logging Card Error

Probably the smallest contribution to error, but one that is common to all data acquisition cards, is the quantization error of the logging card. The maximum quantization error is 1/2 LSB (least significant bit) [2], and this corresponds to $1.22\times 10^{-3}$V for the card, which equates to $\pm$ 0.95Pa/LSB for the pressure measurement instrumentation, which translates in terms of dynamic pressure, $P_{dyn\_ref}$, of less than 1.5%. This error is directly proportional to the resolution of the A/D converter, in this case all A/D and D/A converters have 12-bit resolution, and this error is random as it cannot be compensated for. However, Morris [43] states that time-averaging of the voltage signal from a relatively large number of samples almost eliminates any error.

### 4.9.4 Anti-Aliasing

Aliasing is the phenomenon where a continuous signal is sampled and converted into a discrete signal, and in that sampling process a high-frequency signal can be transmuted into a lower-frequency one [43]. To avoid aliasing, the sampling frequency, $f_S$, was set to 1600Hz for reasons that are two-fold: firstly, this frequency is approximately twice the critical (Nyquist) frequency, and is therefore four times greater than the expected highest frequency signal. The expected highest frequency was approximately 400Hz and was based on the rate of change of the pressure signal at the contact patch at the rotational frequency, $f_{rot}$=18.5Hz, which means that the discrete sampled signal should be a very close approximation to the original analogue pressure scanner voltage signal in both amplitude and frequency; secondly, having a sampling frequency, $f_S$, of 1600Hz means that the angular measurement resolution is increased as there are more discrete points in one revolution of the wheel. The minor drawback to this is that more data is wasted due to the data validation process (previously discussed in Section 4.7.2), although it must be said that this is of no significant concern.

## 4.10 Summary

The pressure measurement instrumentation has been comprehensively described in this chapter. System specifications have been presented and the operation of the system has been discussed in detail. The correction methods employed have been discussed and how they are implemented have been described. Finally, the errors associated with the instrumentation have been highlighted. The details of the investigations that were conducted using the pressure measurement instrumentation are presented in Chapter 7.

# Chapter 5

# The External Flow-Field Instrumentation

This chapter focuses on the techniques and methods that were employed to investigate and analyse the external flow-field about the wheel. Two different methods were chosen for the analysis and their respective advantages and disadvantages are discussed. Pressure probe methods were developed to take discrete point measurements in the wheel wake and particle image velocimetry (PIV) was used to acquire and analyse both time-averaged and instantaneous velocity fields. Both methods were employed to analyse the wake structure of the wheel such to further the understanding of the wake mechanics.

## 5.1 Introduction

Detailed measurements in the wheel wake had not been carried out until the work of Mears et al [40], [39], [38] and Knowles et al [31], [30]. As discussed in the literature review (Chapter 2) the work of Fackrell and Harvey [20], [21] provided only a loose indication into the outline of the wake, and more recently Bearman et al [9] expanded on this but not exhaustively.

The experimental flow-field investigation was conducted using two different instrumentation methods in order to analyse the wake structures. A pneumatic five hole

pressure probe with remote transducers (non-embedded) was designed and fabricated in-house. The probe was traversed at a number of different stations in the wheel wake, and these stations are shown in Chapter 7. The Durham University engineering staff have a wealth of expertise in designing and using pressure probes, which aided the investigation significantly.

Particle image velocimetry (PIV) was also used to investigate the flow-field. The PIV system is a commercially available product supplied with its own analysis software. Again, a number of different stations were interrogated using PIV and these stations are shown in Chapter 7.

## 5.2 The Five Hole Pressure Probe

### 5.2.1 Experimental Configuration

Figure 5.1 shows a schematic representation of the pressure probe experimental configuration. The basic wheel/MGP set-up and the co-ordinate system can be seen.

### 5.2.2 The Probe

The five-hole probe used for this work was of the forward facing pyramid type with a cone angle of 60 degrees (as categorised by Dominy and Hodson [17]). A photograph of the probe is shown in Figure C.3 (Appendix C). The probe head and support sting can be seen in the photograph. An angle of 60 degrees provided increased sensitivity in both pitch and yaw at the expense of a reduced pitch/yaw angle range envelope [11]. The probe geometry allows up to 360-degree rotation of the probe about the longitudinal, or pitch axis, without altering the measurement location. This particular design feature is particularly useful for swirling flows as discussed by Hooper and Musgrove [23], and was expressly designed to enable measurements to be taken close behind the wheel and near to the ground at any pitch angle, therefore permitting reversed flow to be measured, with relative ease, in the highly

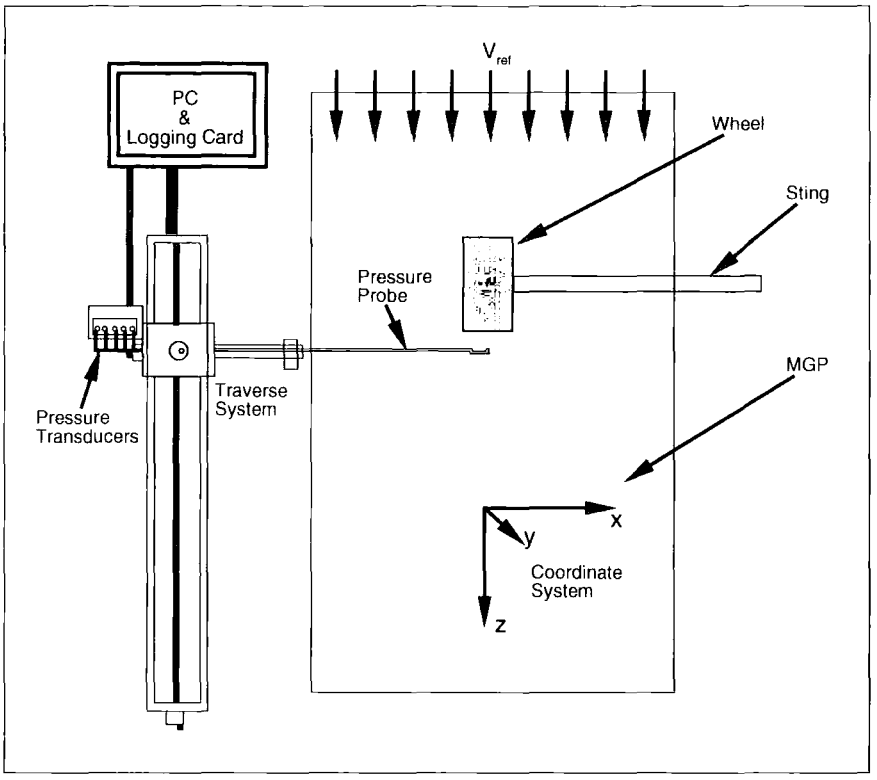


Figure 5.1: Schematic Representation of the Pressure Probe Experimental Configuration.

separated near-wake. The probe was constructed from five stainless steel hypodermic tubes each with a 0.71mm outer diameter (OD) and 0.51mm bore (gauge 22). These tubes then interfaced with stainless tubing of 1.24mm OD and 1.00mm bore to enable Nalgene 2.0mm OD, 1.0mm bore PVC tubing to connect the probe to the pressure transducers.

The probe was calibrated to $\pm 30$ degrees in 2.5 degree increments in both pitch and yaw using a purpose built calibration facility. The calibration was conducted at the same freestream velocity that the open-jet wind tunnel was operated at, this being 14.7 $ms^{-1}$ ($P_{dyn} \approx 130$ Pa). The probe Reynolds number, based on probe diameter, was $Re_{5H} = 2940$. A Reynolds number sensitivity investigation was not undertaken, but pyramid type probes have previously been shown to be relatively insensitive to Reynolds number [17]. Typical probe calibration maps and the coefficient equation definitions can be seen in Appendix C. Figure C.1 shows

the pitch/yaw calibration map. In order that errors were minimised the probe was calibrated using the same pressure transducers and data acquisition system used for the experimental investigations. Positioning the probe in the working section was achieved using a 4-axis traverse system (3 linear and 1 angular (pitch)) controlled by the MS-DOS based data acquisition PC.

### 5.2.3 The Pressure Transducers

Five SensorTechnics 103LP10D-PCB fast response pressure transducers with on-board power supply stabilisation, signal amplification and precision temperature compensation were used for the measurement of the individual five hole probe pressures. Table 5.1 shows the salient features of the type of transducer used and more details are given in [55]. A common 12VDC power supply was used to power the transducers and they were operated in differential mode. The transducers were frequently calibrated simultaneously against a silicon oil micromanometer and the calibration slopes were stored in a lookup table. The transducer offsets were logged prior to each experimental investigation. The wind tunnel reference conditions were measured using a further two identical pressure transducers for all experiments.

| Manufacturer | Sensor Technics |
|---|---|
| Type | 103LP10D-PCB |
| Pressure Range | $\pm$1000 Pa |
| Rise time (10-90 % F.S.) | 200$\mu$s |
| Natural frequency | $\sim$ 20kHz |
| D.C. supply | 12V |
| Output range | 1-6V |
| Zero pressure offset | 3.5V |

Table 5.1: The Salient Features of the Pressure Transducers.

### 5.2.4 Traverse System and Notation

The traverse system shown in Figure 5.1 is a 4-axis (3 linear, 1 angular (pitch)) system used to position the probe in the working section of the wind tunnel. The traverse is under computer control via the Amplicon PC30-PGH logging card digital port.

### 5.2.5 Instrumentation Description

Figure 5.2 shows schematically the instrumentation used for the five-hole pressure probe investigations. The aforementioned Sensor Technics pressure transducers are shown connected to the five-hole probe via Nalgene 2.00mm OD/1.00mm ID tubing; each pressure hole number corresponding to transducer number. The pitot-static pressure probe, common to all experimental work, is shown. The digital port of the PC30-PGH logging card was connected via a 9-pin "D" type connector to the stepper motors through their associated driver board, providing computer control over $x$, $y$, $z$ and *pitch* axes. The matched set of second-order 250Hz low-pass analogue filters shows connectivity between the transducers and the analogue channels of the logging card.

### 5.2.6 Data Acquisition/Analysis

The data were acquired in sets of 2048 samples at a sampling frequency, $f_S$, of 800Hz for all wake measurements using the pneumatic pressure probe. Further details of the acquisition settings are given in Chapter 7 where the experimental and computational investigations conducted using the instrumentation techniques are described.

Once the probe data were acquired the following were computed using the calibration data: total pressure coefficient; dynamic pressure coefficient; standard deviation of the dynamic pressure coefficient; velocity components ($u$, $v$ and $w$); streamwise vorticity. The streamwise vorticity was computed using Eqn. 5.1.

$$\xi = \frac{\partial v}{\partial x} - \frac{\partial u}{\partial y} \tag{5.1}$$

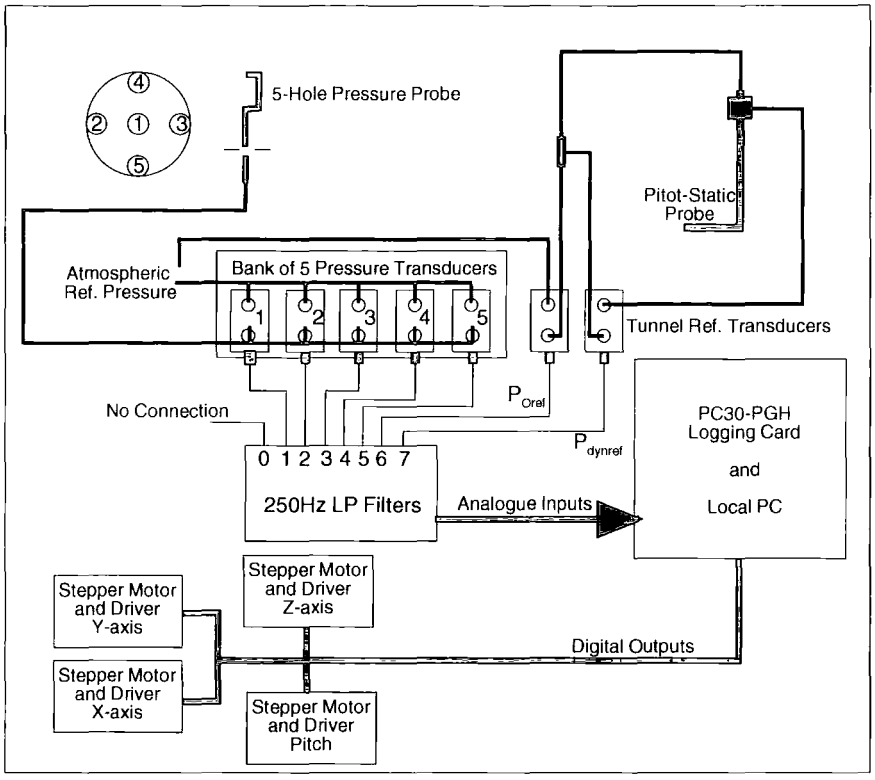


Figure 5.2: Schematic Representation of the Five-Hole Pressure Probe Instrumentation.

### 5.2.7 Wake Integral Method

The wake integral method used here was developed by Ryan [53]. The technique uses the one-dimensional momentum equation and this is extrapolated to full three-dimensional flow. The wheel drag was computed by integrating the microdrag for a particular measurement station. The microdrag refers to the local contribution, or contribution from a single measurement point, to the overall wheel drag since the wake integral is derived from experimental data measured at discrete points in the flow. For further details including the derivation of the wake integral method consult Ryan [53].

## 5.3 Particle Image Velocimetry (PIV)

### 5.3.1 Introduction

PIV has distinct advantages over other flow-field measurement techniques, such as Laser Doppler Velocimetry (LDV) and Hot-Wire Anemometry (HWA), in that it uses the whole-field method of acquisition whereby the instantaneous flow-field can be analysed, as opposed to taking single-point discrete measurements where traversing is a requirement. The whole field measurement technique is particularly useful in the characterisation of turbulent flow fields. According to Lourenço [36] the large spectrum in turbulent flow scales demands that simultaneous flow measurements are made over regions large enough to capture larger flow scales and with sufficient spatial resolution to analyse the smaller flow structures. LDV and HWA use the discrete single-point measurement technique and the resulting measurements are combined to form the time-average of the flow-field. Typically no more than a few points at a time can be measured [66]. Alternatively, for quasi-periodic flows the LDV system can be configured to acquire phase-locked LDV measurements. Such a system is described by Leder and Geropp [34] for bluff body flows. Leder and Geropp positioned a hot-wire probe six diameters downstream of a flat plate positioned normal to the axial flow. The hot-wire output was input into a signal conditioner and this system formed the phase detector circuit. Phase averaged velocity and vorticity field data were presented.

Additionally, PIV is relatively non-intrusive, dependant on particle size, compared to positioning hot-wires and their associated support methods in the flow. There are also arguments that PIV is less time consuming compared to traversing and acquiring single-point measurements, however, PIV requires careful, accurate set-up of the camera and laser system and this can be relatively labour intensive and time consuming. Admittedly, once set-up the acquisition of PIV measurements is usually extremely fast, but one must consider the complete set-up and acquisition time in order to directly compare whole-field and single-point methods. The major advantage of PIV being the acquisition of the instantaneous velocity field.

The PIV system used for this part of the investigations was a commercially available system built by Oxford Lasers [32]. The system came complete with all hardware and VidPIV4.0 acquisition/analysis software. One CCD camera was used for the investigations although the system has full stereoscopic capability, therefore only two components of velocity were measured (this is discussed in Chapter 10).

### 5.3.2 Experimental Configuration

The experimental configuration for the PIV aspects of the work is presented in Figure 5.3. The figure shows schematically a plan view of the set-up for the centreline streamwise YZ analysis plane; details of the other analysis planes are given in Chapter 7. The laser arm was positioned 3.5 wheel diameters downstream of the wheel axle and the laser sheet was vertically directed onto the rear region of the wheel for the YZ plane analysis regions. The CCD camera was located by the side of the MGP perpendicular to the laser sheet for the YZ planes and above the MGP, again normal to the laser sheet, for the overhead XZ planes. Seeding was distributed into the flow at the nozzle outlet (this is discussed in Section 5.3.5).

### 5.3.3 Synchroniser and Laser

The PIV system utilises a dual head Nd:Yag laser (a solid-state Yttrium Aluminium Garnet crystal doped with Neodymium (Nd)) to illuminate the seeding. An ILA TC412 PIV synchroniser was also employed and this controls the laser in terms of laser power and time delay between the acquisition of the image pair. In addition the synchroniser controls image acquisition. Table 5.2 shows the major synchroniser and laser settings that were used. The data were acquired at a sampling frequency of 5Hz with the camera aperture set to number 2. This aperture setting was found (after several experiments) to provide the best image pair quality since opening the aperture further caused the images to be too light and closing the aperture resulted in darker images. The pulse interval between the two laser pulses was set to be $\Delta t_{1-2} = 30\mu s$ and this was based on the displacement of the particles for an image

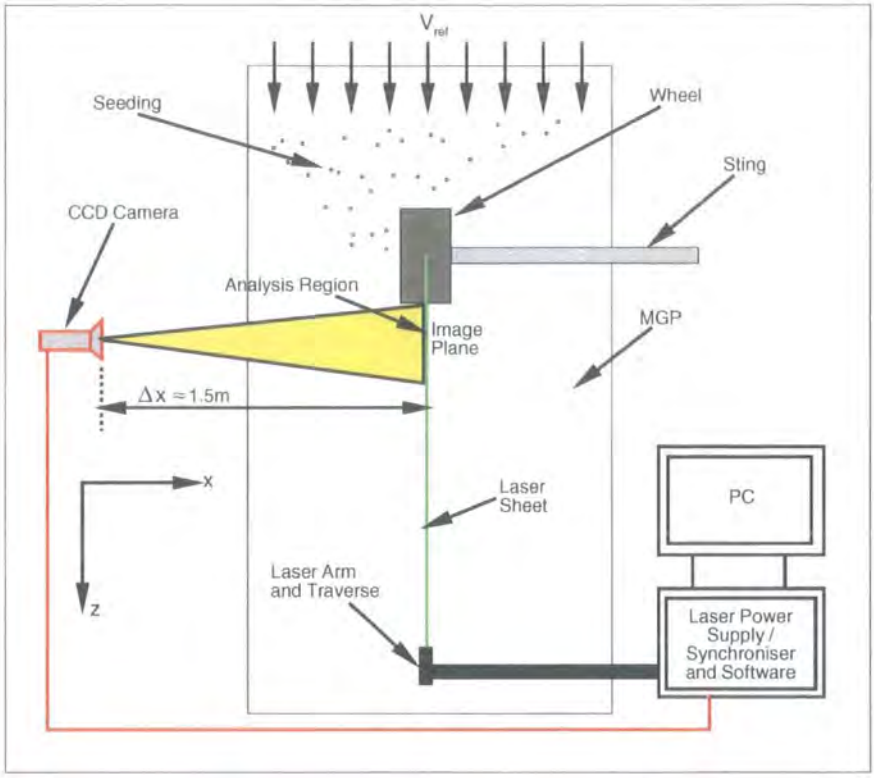


Figure 5.3: Schematic Plan View of the PIV Experimental Configuration.

pair, and is therefore dependant on the freestream velocity. This was determined to a large degree by trial and error. A pulse energy delay of 120$\mu$s for laser 1 and 2 was used. This translates into the Q-switch delay for laser 1 and 2 and at this setting this equates to a medium-high power setting. The maximum delay possible is 186$\mu$s but this was found to cause excessive reflections on the back of the wheel that affected the cross-correlation of the image pair.

| $V_{ref}$ ($ms^{-1}$) | Sampling Frequency (Hz) | Camera Aperture No. | Pulse Distance $\Delta t_{1-2}$ ($\mu$s) | Pulse Energy 1+2 ($\mu$s) |
|---|---|---|---|---|
| 14.7 | 5 | 2 | 30 | 120 |

Table 5.2: The Major Synchroniser and Laser Settings used for the Investigations.

### 5.3.4 CCD Camera

A PCO Sensicam was used, which is a 12-bit CCD camera featuring thermo-electrical cooling of the image sensor (down to -12 Deg. C) and very low noise. This type of camera provides 1280 by 1024 pixel resolution in the horizontal and vertical directions, respectively. The camera is capable of image capturing at 8fps (frames-per-second), e.g. 8 image pairs per second.

The camera was located approximately 1.5m from the laser sheet (for both YZ and XZ planes) as this was found to be the optimal distance in terms of the best compromise between maximising the interrogation region size and maintaining good spatial resolution. The field of view was adjusted to a rectangular region of 250mm (wide) x 200mm (high). The camera was adjusted precisely until it was perpendicular to the laser sheet since a slight deviation from perpendicular caused extreme focusing problems and had to be resolved.

### 5.3.5 Seeding Methods

Seeding tracer particles, using DEHS (Di-Ethyl-Hexyl-Sebacat), were distributed into the flow using an Oxford Lasers atomiser producing a mean particle size of 1$\mu$m. Tubing with an internal diameter of 12mm, with multiple radially drilled fine holes, was fitted to the upper and lower regions of the wind tunnel nozzle exit (in the jet) upstream of the wheel to ensure a homogeneous distribution of the particulate in the flow. The atomiser was set-up with a maximum pressure difference between inlet and outlet of 1 bar and this provided a sufficient quantity of particulate with adequate distribution.

### 5.3.6 Spatial Calibration

A spatial calibration was taken for each analysis region to allow velocity vectors to be computed. Figure 5.4 shows a typical spatial calibration image. The analysis software calculates the displacement of the particles, in terms of pixels, in a given time (t). Section 5.3.7 gives a more detailed explanation of the analysis software.

This displacement against time is the velocity in pixels/second, therefore the spatial calibration gives information relating pixels to distance, in metres. The resultant is a velocity vector with a magnitude in the SI units of $ms^{-1}$.

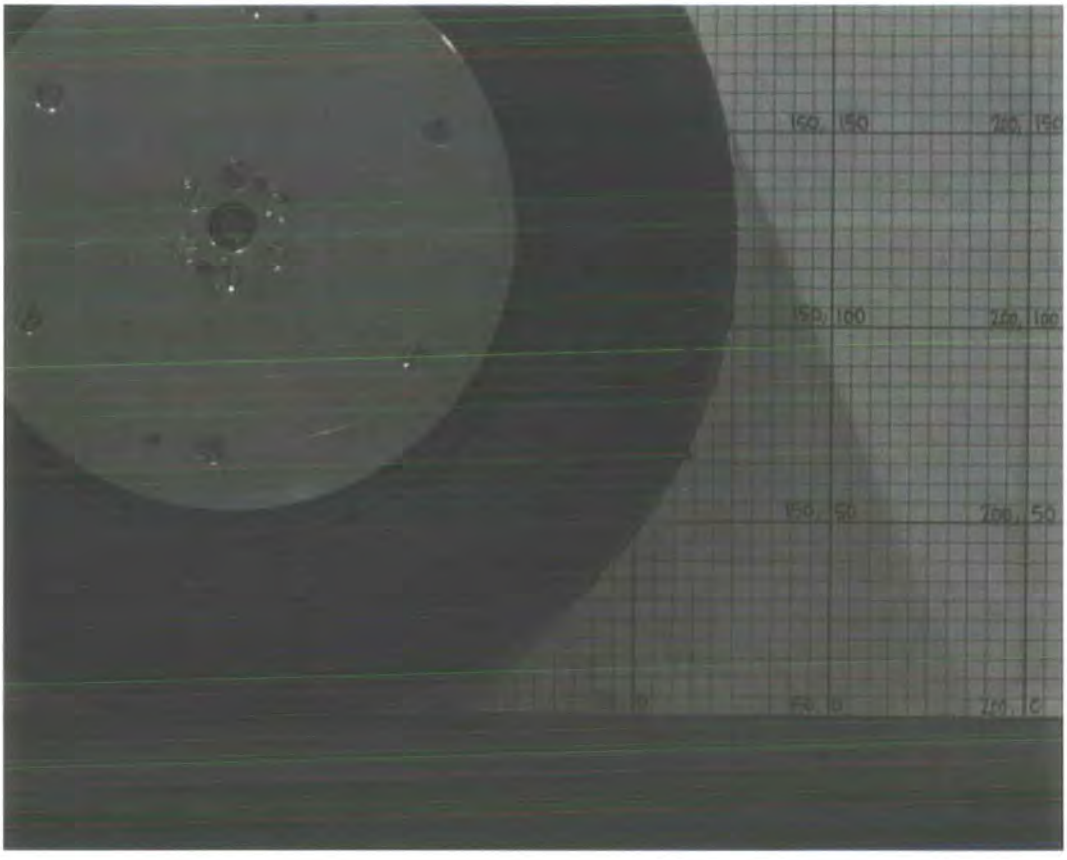

Figure 5.4: A Typical PIV Spatial Calibration Image.

### 5.3.7 Cross-Correlation and Analysis

As mentioned above the image pairs were acquired at a frequency of 5Hz. Increasing the temporal resolution would have been beneficial and this is discussed in Chapter 10. The images were cross-correlated to extract the instantaneous velocity field. The grid used for the cross-correlation was set to separations of 32 pixels in both $x$ and $y$ directions and the interrogation window size was set to 64. This corresponded to a vector spatial resolution of 10mm x 10mm over an imaging area of 250mm x 200mm. The in-plane character of the flow was acquired and the two components of velocity were computed for the in-plane image region since only one CCD camera

was used. Any particles flowing through the in-plane region usually resulted in erroneous vectors since the cross-correlation would typically not exhibit a definite peak in the cross-correlation function. Rather a random array of peaks of similar amplitude.

The velocity data were then filtered using velocity filters to highlight any spurious velocity values (outliers) prior to interpolating any outliers by using adjacent valid data points. All PIV data presented in this thesis have a minimum of 80% and a maximum of 97% valid velocity vectors.

To obtain the time-averaged flow structure 100 instantaneous velocity fields were obtained for each station in the flow. These instantaneous velocity fields were ensemble averaged to obtain the time-averaged velocity field. In the context of PIV measurements the "ensemble" time-average relates to the time-average of the images at each spatial grid point (this being dependant on the velocity vector spatial resolution) and does not therefore mean time-averaging of a signal that is periodic in time. Lawson et al [33] used a similar number of images (70 images) to obtain an ensemble averaged PIV velocity field about a GA(W)-1 aerofoil section in ground effect.

Having performed the analysis of the velocity field data the instantaneous and time-averaged spanwise vorticity fields were computed using Eq. 5.2.

$$\zeta = \frac{\partial v}{\partial z} - \frac{\partial w}{\partial y} \tag{5.2}$$

## 5.4 Experimental Accuracy

An assessment of the experimental accuracy was conducted for both flow-field measurement techniques.

### 5.4.1 Pressure Probe Accuracy

The degree of variability, and therefore repeatability, of the time-averaged data for the five hole probe was quantified during probe development. Time-averaged data were acquired a number of times at the same flow-field station on different days to test for repeatability. The pitch angle of the probe was also varied slightly (whilst ensuring the probe remained in-range) in order to completely test for measurement variance at the same flow-field position. Here the term variance refers to the time-averaged variance between successive data and is not meant to be indicative of the unsteadiness in the wake since the integration time and number of samples are sufficiently large relative the frequency of unsteadiness. Statistical analyses were then performed, in terms of computing the standard deviation of the data and the correlation between data sets at the same measurement stations. High correlation of the pressure field ($\rho_{x,y} = 0.98$) was found between data sets with low variance. The frequency distribution of the data sets yielded a normal distribution about the mean value for the probe data. Statistically therefore, 99.7% ($3\sigma$) of the probe data has the degree of repeatability, in terms of pressure coefficient (whether total, static, etc.), of Cp $\pm 0.023$.

The relatively small probe diameter (3.0mm) will reduce measurement errors in regions of high shear compared to a larger diameter probe. This is caused when the different tubes of the probe head are subjected to different flow conditions. For highly sheared flows it is likely that incorrect values for pitch and yaw will be measured. The smaller probe geometry therefore has increased resolution.

### 5.4.2 PIV Accuracy

There are a number of factors influencing the accuracy of PIV systems such as spatial resolution. Insufficient seeding quantity and distribution can cause poor cross-correlation as can a lack of in-plane flow, and these examples are easily observed during preliminary analysis and can usually be resolved. Image quantization can cause errors but the CCD cameras used here have 12-bit resolution, which

Lourenço [36] recommends for use in PIV. Despite all this if the system is set-up correctly then, according to Vlachos and Hajj [66], the estimated error associated with PIV velocity measurements should be in the order of 1% of the freestream velocity. Vlachos and Hajj [66] quote this error estimate for time-resolved PIV measurements of the unsteady flow over a surface-mounted prism.

## 5.5 Additional Instrumentation

### 5.5.1 Direct Measurement of Drag Force

The wheel drag force was measured directly using a conventional load cell that was connected between the wheel stub axle and sting. The load cell was calibrated and showed excellent linearity with almost zero hysteresis. The drag force data were compared directly with the surface static pressure and wake integral derived wheel drag forces. Figure 5.5 shows a schematic of the load cell instrumentation system. Again the logging card, pitot-static probe and low-pass filters, common to all experiments except PIV, are present. The load cell was connected to the low-pass filters via an instrumentation amplifier to amplify the signal from the strain gauges. Drag force data were acquired at a sampling frequency of 1600Hz and the trigger signal was logged simultaneously for the rotating case. Details of the investigations that were conducted using the drag force load cell are given in Chapter 7. Tare readings were taken for the rotating case with the MGP on and the wind off. Datum readings were logged prior to an experimental run and the forces computed based on the calibration slope. A total of 8192 measurements (4 sets of 2048) were acquired for the rotating and stationary wheels. The time-averaged drag force and drag coefficient were computed simply as an average of the load cell voltage time history for the rotating and stationary cases.

## 5.6 Summary

The instrumentation used for the flow-field investigations has been described in detail. The design and fabrication of a pneumatic five-hole pressure probe has been



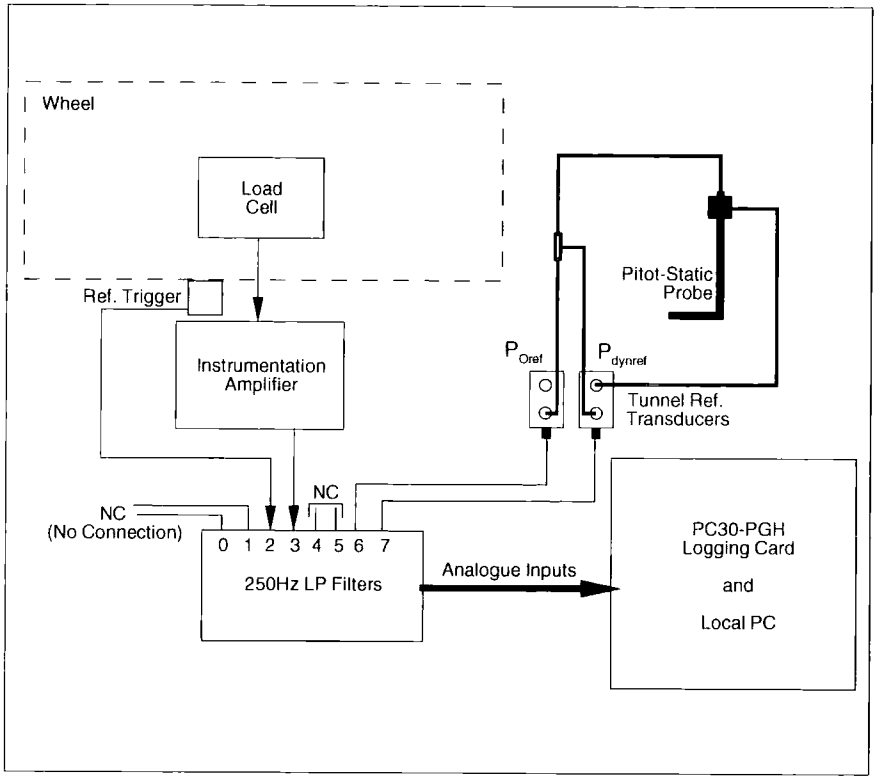


Figure 5.5: Schematic Representation of the Load Cell Instrumentation System.

shown and the errors associated with it have been identified. The commercially available PIV apparatus have been discussed and the major components and settings presented. Finally the load cell used for direct wheel drag force measurement has been described. Chapter 7 gives details of the investigations carried out using these techniques.

# Chapter 6

# Computational Modelling of the Wheel Flows

This chapter gives details of the three-dimensional computational modelling that was conducted for this work. The majority of the work in this thesis is experimental and the computational aspects were necessary for comparative purposes and to analyse the "interesting" regions of the flow-field that were observed using the experimental techniques; namely the jetting phenomenon. The relevant CFD literature, with respect to wheels, was consulted to try and minimise the model development time and to choose the appropriate turbulence model and differencing scheme. The CFD modelling relates to the rotating wheel only due to the above motivation for the analyses.

## 6.1 Introduction

The CFD investigation was carried out using the commercially available Fluent 6.0 CFD package and its associated pre-processing software GAMBIT, both of which are distributed by Fluent Incorporated. These software packages were accessed remotely on the Durham University networked computationally intensive hardware facility. The principal motivation for the computational element to the work was to supplement the experimental data and to establish whether the front and rear jetting phenomena could be resolved at the contact region using numerical simulation

methods.

It was identified and discussed in the literature review that a number of research papers have been published on the prediction of the aerodynamic characteristics of wheels using CFD. As a result of this it was decided to utilise previous research such that the computational modelling development time could be reduced whilst maximising model accuracy. Axon [7] conducted a comprehensive study into wheel flow simulations using Fluent but the data presented did not show the same regions of the flow-field as this work.

Verification and validation is paramount in CFD (Oberkampf and Trucano [46]), indeed any computational simulation technique, although for this work verification was not considered since this is concerned with the accuracy of the solution of the computational model compared with known solutions. CFD validation, which is concerned with the numerical model in comparison with the physics of the flow, was conducted using the experimental data acquired during this work.

## 6.2 Hardware Specification

A Sun Microsystems Sun Enterprise 420R system with four UltraSPARC-II 450MHz processors is one of the systems on the Durham University network, and was used for all aspects of the CFD investigations. The system has a clock frequency of 113MHz and a memory size of 4096MB. A typical three-dimensional, high-order, steady state solution consisting of $3 \times 10^6$ cells usually converged in less than 36 hours, although this was to a large degree dependant on other system users.

## 6.3 Wheel Geometry

The geometry of the pneumatic tyre was modelled using reverse engineering where the tyre sidewall profile (see Figure 3.5 in Chapter 3) was measured using CMM and the resultant data exported to SolidWorks CAD. The CMM data were repre-

sented by several arcs in the CAD model. The CAD wheel geometry data were then imported into the GAMBIT pre-processor and a volume geometry created. The wheel sting and the cavity of the wheel were not modelled in order to ease mesh generation and simplify the analysis. It was thought that the sting and wheel cavity effects would not have a significant influence when resolving the viscous actions at the contact region.

The contact region was modelled by initially fitting a large flow domain around the wheel, which extended ten wheel diameters upstream of the wheel axle, twenty wheel diameters downstream of the wheel axle, ten wheel diameters vertically above the groundplane, and five wheel diameters on either side of the centreline of the wheel. These spatial parameters were derived by varying them and analysing their effects on the static pressure distribution around the wheel. It was found that having the outlet of the domain less than twenty wheel diameters downstream of the wheel caused an upstream effect on the pressure field due to the atmospheric pressure boundary constraint not being appropriate at any streamwise station closer to the wheel; hence, twenty wheel diameters downstream was chosen as this had no upstream effect on the pressure field. Figure 6.1 shows the wheel geometry within the large flow domain. The coordinate system employed was identical to the experimental investigations.

Measurements were taken to ascertain the size of the contact patch for the experimental work and this was taken into account for the CFD modelling. It was found that, in terms of $\theta$, the contact patch spanned the angular positions from 80 to 100 degrees. Therefore the computational model reflected this by raising the groundplane by 1.5mm and creating a groundplane that truncated the bottom of wheel using a similar approach as Knowles et al [31]. The CFD contact patch was checked and it spanned the angular position of between approximately 80 to 100 degrees.

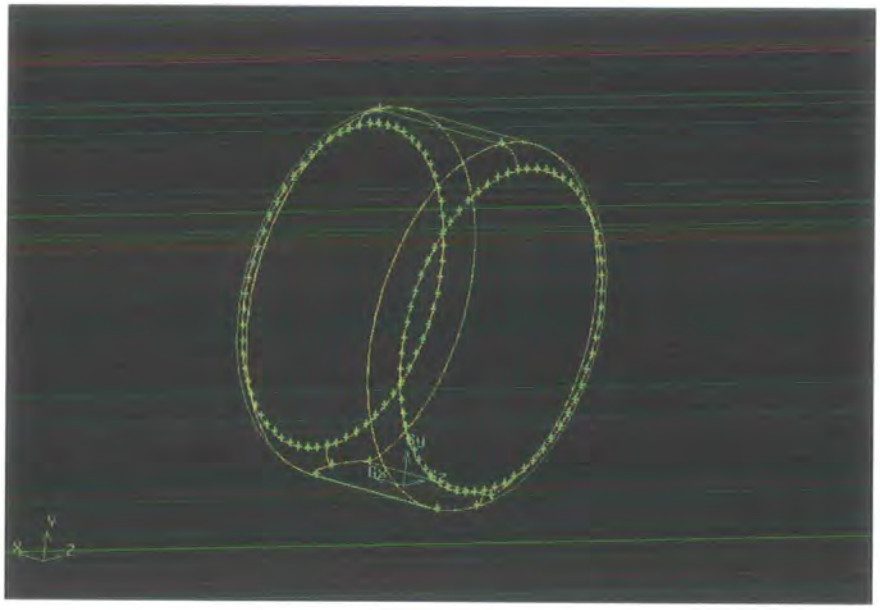

Figure 6.1: The Wheel Geometry within the Flow Domain.

## 6.4 Mesh Generation

Figure 6.2 shows the generated tetrahedral volume mesh on the centreline of the wheel (YZ plane). The mesh contained $4.3 \times 10^6$ tetrahedral cells. The volume mesh generated was an unstructured tetrahedral mesh with an associated fixed size function applied in such a way to allow the cells to be concentrated in the near-field of the wheel. Table 6.1 shows the size function parameters and associated attachment faces. The cell sizes near to the wheel were set to 1mm with a growth factor of 10% for successive cells further away from the wheel. The fixed size function was attached to the tread region of the wheel and also to a section of the groundplane that extended one wheel diameter upstream from the wheel axle and two and a half wheel diameters downstream from the wheel axle, which corresponded to the maximum permissible experimental wake traverse station. Adequate spatial resolution was realised by attaching the size function to the groundplane and allowing the volume mesh to grow in a controlled manner.

Tetrahedral cells were chosen due to reduced skewness when compared to hexahedral cells at the contact patch. Indeed, a simple study was carried out whereby hexahedral cells were chosen to mesh the regions of the contact patch. Comparisons

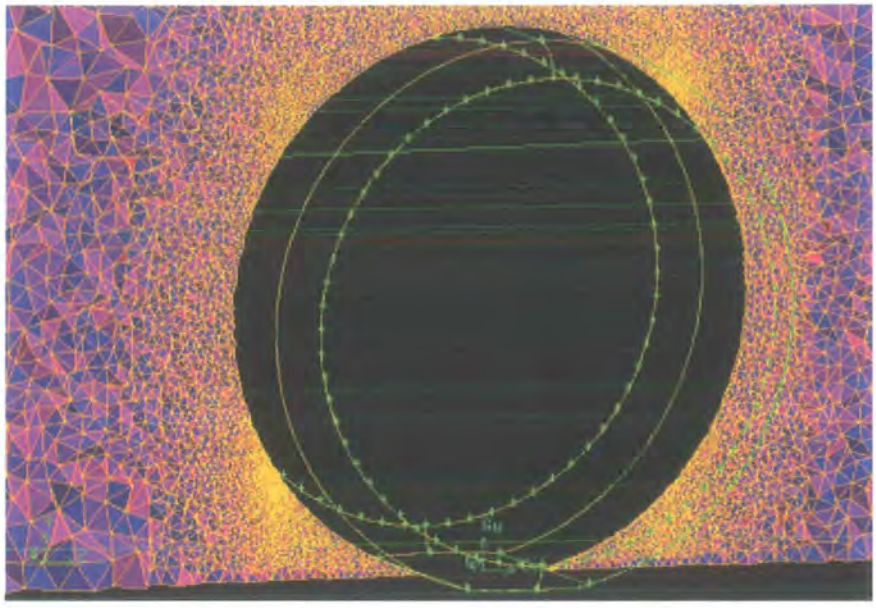

Figure 6.2: Computational Wheel and Tetrahedral Volume Mesh (Centreline YZ Plane).

| S.F. Type | Start Size (m) | Growth Rate | Max. Cell Size | Attachments |
|---|---|---|---|---|
| Fixed | 0.001 | 1.1 | 0.2 | Tread/Road |

Table 6.1: The Size Function Parameters and Associated Attachment Faces.

were made with tetrahedral cells in the same region and the tetrahedral cells showed reduced skewness compared to the hexahedral cells. Moreover, Fluent [26] state that tetrahedral cells are a better choice for the discretisation of complex regions of the domain, such as the contact region of the wheel, and can be more highly skewed than hexahedral cells.

### 6.4.1 Wall Treatment

Skea et al [61] stated that the standard law-of-the-wall wall function predicted accurately the aerodynamics of rotating wheels. Conversely, Axon [7] claimed that a two-layer approach offered the best accuracy for the predicted wheel flows. For this work the enhanced wall treatment within Fluent was utilised. This has the benefits of not requiring the near-wall mesh to be sufficiently fine and therefore reduces the computational requirements [26]. If the y+ values are approximately unity the

laminar sublayer will be resolved using the traditional two-layer zonal model. If the mesh is not fine enough to use the two-layer model enhanced wall functions are used. Fluent [26] show the effects of using enhanced wall treatment with different y+ values and the results are almost indiscernible. The effects of pressure gradients were also used with the enhanced wall treatment.

### 6.4.2 Grid Adaptation

In addition to the size function, grid adaptations were also carried out to ensure the y+ values (defined in Eq. 6.1) were within the recommended values for the prescribed wall treatment. For enhanced wall treatment with pressure gradient effects the y+ values can be in the range of $30 < y+ < 60$. This range is corroborated by Middendorf [41] for flow about a rotating circular cylinder using the same wall treatment. The y+ values were computed for the wheel surface and groundplane after convergence and any out-of-range regions were marked for adaption. Grid adaptations were necessary in regions where large gradients in the flow-field properties existed in order to properly capture the physics of the flow. A physical boundary layer can be incorrectly computed if the nodal distribution normal to a surface is low. According to Anderson [3] a velocity profile will still be computed due to the no-slip (u = 0) boundary condition at the wall but the boundary layer thickness will typically be excessive. The motivation for the grid adaptations was to initially start with a relatively fine grid topology at the wheel surface and progressively refine it to meet the y+ requirements. Originally the size function parameters were set such that the first cell size at the wheel surface would be $1 \times 10^{-4}$m although this required excessive computational effort during mesh generation and would have resulted in a mesh too large to run using the hardware available, and was therefore abandoned. The rule of thumb for current CFD models is that the hardware must have around 50MB of RAM for every 100,000 structured volume mesh cells and around 100MB of RAM for every 100,000 unstructured volume mesh cells.

Having a first cell y+ value of around unity would have been beneficial in solving the boundary layer right down to the wall, although as discussed by Fluent [26]

this is not always possible and can result in an unnecessary computational effort in discretising the boundary layer. Fluent suggest to alleviate the extra computational effort the y+ values for the first cell centroid should be set to between 30 and 60. Data provided by Fluent give details regarding varying y+ values for the first cell and there is little difference between a y+ value of 1 and that of 30.

$$y+ = \frac{y}{\nu}\sqrt{\frac{\tau_w}{\rho}} \tag{6.1}$$

where $y$ is the normal distance from the wall to the centroid of the first cell, $\tau_w$ is the wall shear stress, $\nu$ is the kinematic viscosity and $\rho$ is the density.

Volume grid adaptation was also conducted to ensure the entire volume grid did not grow by more than 50% for successive cells, although the only cells marked during adaption were those in the far-field.

To summarise, the modelling strategy adopted here was to start with a reasonable grid and refine it in regions where large gradients existed in order to obtain grid independent solutions.

## 6.5 Boundary Conditions

The boundary conditions chosen reflected that of the experimental configuration. The wheel and groundplane were modelled as no-slip walls (relative velocity zero). The wheel was set to a moving wall rotating about the axis of rotation. The angular velocity, $\omega$, was set to -116 rad/s, which corresponds to a wheel circumferential velocity of 14.7 $ms^{-1}$. The groundplane translational velocity was set to 14.7 $ms^{-1}$ ($+z$ direction).

A velocity inlet condition was used for the inlet face of the domain set to a velocity of 14.7 $ms^{-1}$ ($+z$ direction) normal to the boundary. A pressure outlet condition was prescribed for the outlet face of the domain, which was set to atmospheric pressure (gauge pressure = 0Pa). The internal regions of the domain were set to a continuum

condition with air as the working fluid.

## 6.6 Turbulence Modelling

Fluent has a number of turbulence models available and various wall treatment techniques and variable solution parameters, which lead to a large number of possible permutations for turbulence modelling. To use all of them was far beyond the aims of the computational aspects of this work. Moreover, several such studies have already been conducted whose findings were used for this work.

The k-$\epsilon$ RNG turbulence model was initially chosen for the investigations and this was largely based on the work of Axon et al [6] and Skea et al [61] in which the front jetting and early boundary layer separation were predicted, respectively, for a rotating wheel. However, during preliminary computational runs it was found that the k-$\epsilon$ RNG turbulence model exhibited instabilities and poor convergence, which was also noted by Axon [7]. An alternative was used in the form of the standard k-$\epsilon$ turbulence model and this choice was based on the results of Wäschle et al [67] who showed excellent predictions of the velocity field and force coefficients. The standard k-$\epsilon$ model is also generally more robust than the RNG variant. Second-order discretisation was adopted for all of the convective terms due to an unstructured volume mesh being employed.

## 6.7 Solution Convergence Criteria

A steady-state three-dimensional solution approach was chosen. Solution convergence was monitored and governed by the standard residuals such as continuity, turbulence dissipation rate, etc., all of which were kept at their default values. Under-relaxation factors were also kept at their default settings.

## 6.8 Summary

The CFD aspects of the research have been described in this chapter. A tetrahedral volume mesh was used for the complete flow domain and this was largely due to reduced skewness of the cells at the contact region compared to hexahedral cells. The choice of turbulence modelling has been addressed and the standard k-$\epsilon$ showed increased robustness over the RNG variant. Boundary conditions were chosen to reflect the experimental rotating wheel conditions.

# Chapter 7

# Experimental and Computational Investigations

## 7.1 General Overview

The purpose of this chapter is to give details of the experimental and computational investigations that were conducted using the techniques already described. The basic wheel experimental configuration was used for all of the work and the specific instrumentation set-up around it. The CFD investigations reflected that of the experimentation and related to the rotating wheel only.

## 7.2 Tunnel Reference Velocity

The freestream wind tunnel reference velocity was calculated using the reference dynamic pressure, $P_{dyn\_ref}$, from the pitot-static pressure probe transducers, for all experimental work, using Eq. 7.1.

$$V_{ref} = \sqrt{\frac{2 \times P_{dyn\_ref}}{\rho}} \tag{7.1}$$

## 7.3 Surface Static Pressure Distributions

The surface static pressure distributions were acquired for the rotating and stationary cases at a yaw angle, $\beta$, of zero degrees. The effects of yawed flow on the pressure

distributions were analysed for the rotating case whereby the yaw angle was fixed at zero and five degrees. Five degrees was chosen to represent a tyre slip condition, although it must be clarified that the MGP was also yawed relative to the freestream flow. The relative yaw angle between the MGP and the wheel remained at zero. Preliminary experiments were conducted with only the wheel yawed relative to the freestream flow and MGP, but the pneumatic tyre caused the MGP continuous belt system to rapidly run off track resulting in the MGP power supply being cut-off. It was thought that a solid plastic tyre may permit such an experimental set-up, but this was not considered in the research programme timetable. The surface pressure data were only logged on the hub side of the wheel for the zero degrees yaw case.

Table 7.1 shows the major data acquisition settings used for the surface static pressure investigations.

| Experimental Configuration | $V_{ref}$ ($ms^{-1}$) | $f_{rot}$ (Hz) | Sampling Frequency (Hz) | N_Sets | N_Samples (per set) | Integration Time (s) |
|---|---|---|---|---|---|---|
| Rotating | 14.7 | 18.5 | 1600 | 32 | 2048 | 40.96 |
| Stationary | 14.7 | - | 1600 | 2 | 2048 | 2.56 |

Table 7.1: Major Data Acquisition Settings for the Surface Static Pressure Investigations.

## 7.4 Load Cell Data

The load cell data were acquired for the stationary and rotating wheels at a yaw angle, $\beta$, of zero degrees. To reiterate, tare readings were taken, for the rotating case only, with the MGP on and the wind off. Table 7.2 shows the major data acquisition settings used when acquiring the load cell data.

| Experimental Configuration | $V_{ref}$ ($ms^{-1}$) | $f_{rot}$ (Hz) | Sampling Frequency (Hz) | N_Sets | N_Samples (per set) | Integration Time (s) |
|---|---|---|---|---|---|---|
| Rotating | 14.7 | 18.5 | 1600 | 4 | 2048 | 5.12 |
| Stationary | 14.7 | - | 1600 | 4 | 2048 | 5.12 |

Table 7.2: Major Data Acquisition Settings for the Load Cell Investigations.

## 7.5 PIV Investigations

The PIV investigations were conducted for the stationary and rotating cases with the wheel at a yaw angle, $\beta$, of zero degrees. The major data acquisition settings used for the PIV investigations are shown in Table 7.3. 100 image pairs were acquired, at a sampling frequency of 5Hz, and used to calculate the time-averaged flow-field.

| Experimental Configuration | $V_{ref}$ ($ms^{-1}$) | $f_{rot}$ (Hz) | Sampling Frequency (Hz) | N_Image Pairs |
|---|---|---|---|---|
| Rotating | 14.7 | 18.5 | 5 | 100 |
| Stationary | 14.7 | - | 5 | 100 |

Table 7.3: Major Data Acquisition Settings for the PIV Investigations.

A number of planes were analysed using PIV and Figure 7.1 shows the streamwise centreline analysis regions as seen by the CCD camera, and the inset shows a 50% scale plan view indicating the position of the analysis regions across the wheel (in this case midpoint (centreline)). The regions (A-D) were acquired separately, rather than only acquiring one large region, in order to maintain sufficient spatial resolution of the images. An adequate amount of overlap between the images was permitted when setting up the CCD camera to prevent any data being missed during acquisition.

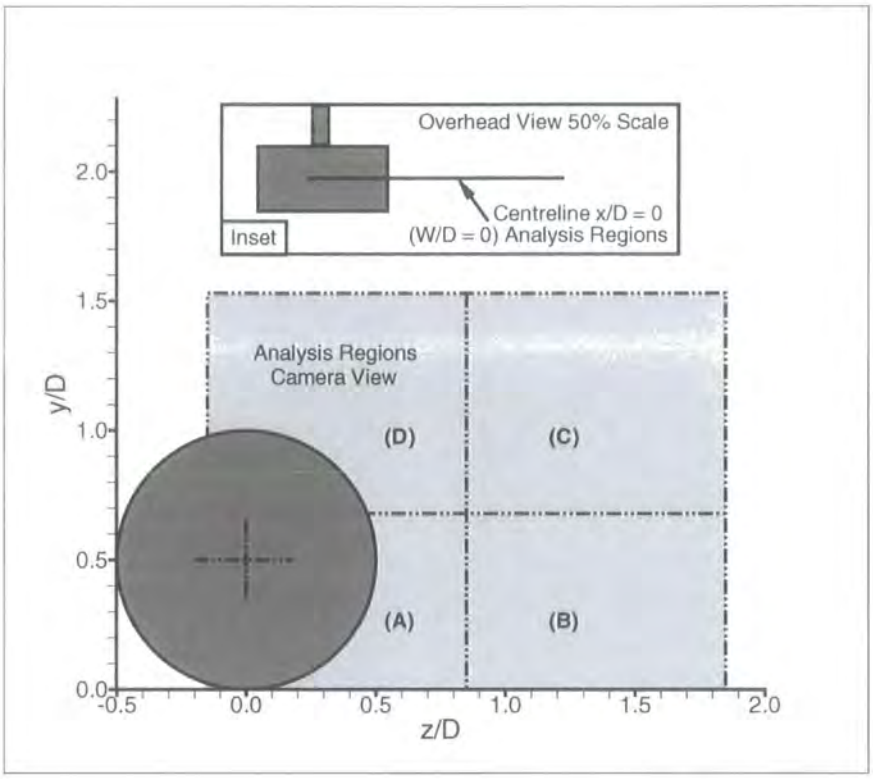


Figure 7.1: Centreline Streamwise PIV Analysis Regions.

Figure 7.2 shows the analysis region acquired at the edge of the wheel (W/D = +0.18). As shown this analysis region was the same as the centreline region A but located at the edge of the tread region of the wheel. This particular location was chosen due to the increased "jetting" observed in the surface static pressure data, which will be discussed in the discussion chapter (Chapter 10).

Figure 7.3 shows the overhead analysis regions. The CCD camera was located above the wind tunnel, therefore the camera view is a plan view of the wheel and MGP. The inset shows a side view and highlights the vertical position of the analysis region, this being 65mm ($y/D = +0.26$). This particular region was chosen to see if the "jetting" at the front of the contact patch passed down by the side of the wheel, and if so, to establish its effect on the flow-field.

To allow quantitative comparisons of the vector fields the velocity coefficient, shown

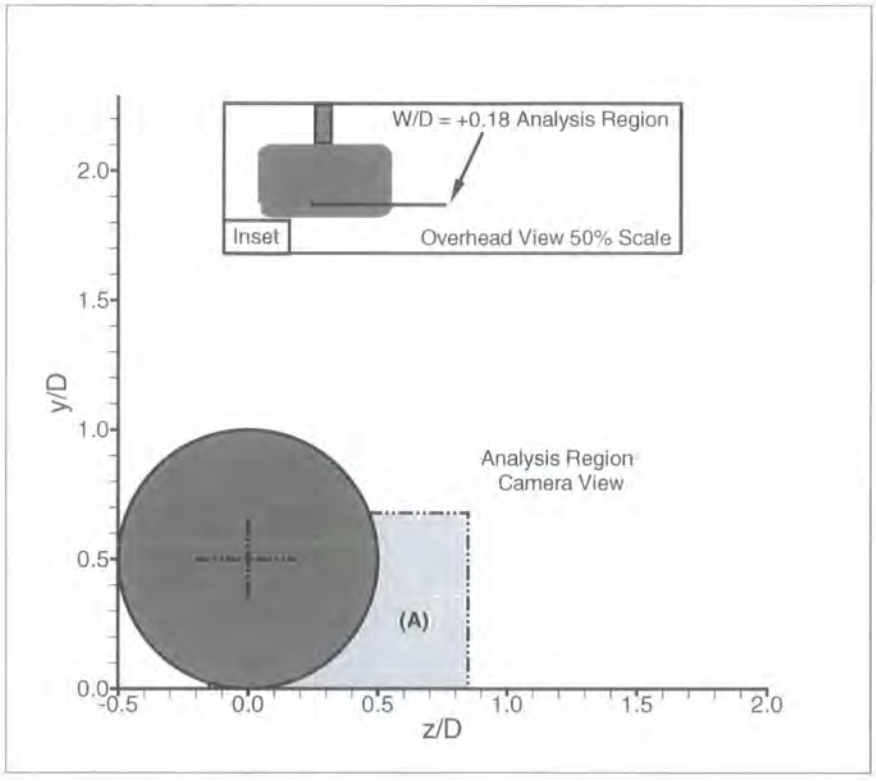


Figure 7.2: Wheel Edge Streamwise PIV Analysis Region.

in Eq. 7.2, was computed to yield the fraction of the local velocity to the freestream reference velocity.

$$Cv_i = \frac{v_i}{V_{ref}} \tag{7.2}$$

where $v_i$ represents the velocity in one of the three orthogonal directions x, y or z and $V_{ref}$ is the reference freestream axial velocity, as defined in Eq. (7.1).

## 7.6 Five-Hole Pressure Probe Wake Surveys

The time-averaged wake surveys were conducted for the rotating and stationary cases at a yaw angle, $\beta$, of zero degrees only. The effects of yaw were not analysed as it was thought to be more important to further understand the zero degrees case, using the pressure probe and other techniques. A number of spanwise $xy$ planes were traversed at different streamwise stations and these are shown in Figure 7.4. The

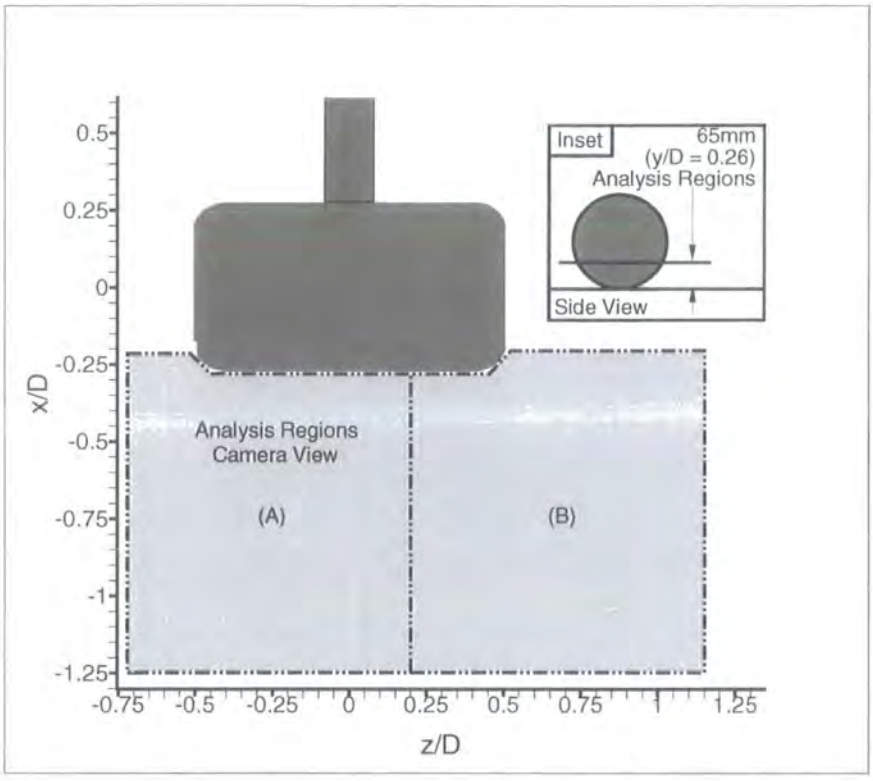


Figure 7.3: Overhead XZ Streamwise PIV Analysis Regions.

details of these planes (A-G) are given in Table 7.4 in terms of streamwise (axial) location ($z/D$) and the $x/D$ and $y/D$ measurement range.

The major data acquisition settings for the pressure probe investigations are shown in Table 7.5. The wheel drag force was computed using the five-hole probe data based on the wake integral method previously described in Chapter 5.

## 7.7 Smoke Flow Visualisation

An Aerotech smoke generator was used in the flow visualisation investigation. The probe was positioned at a number of different stations in the flow-field about the rotating and stationary wheels. The majority of the stations were on the wheel centreline and the results of the investigation are presented in the experimental results chapter (Chapter 8).

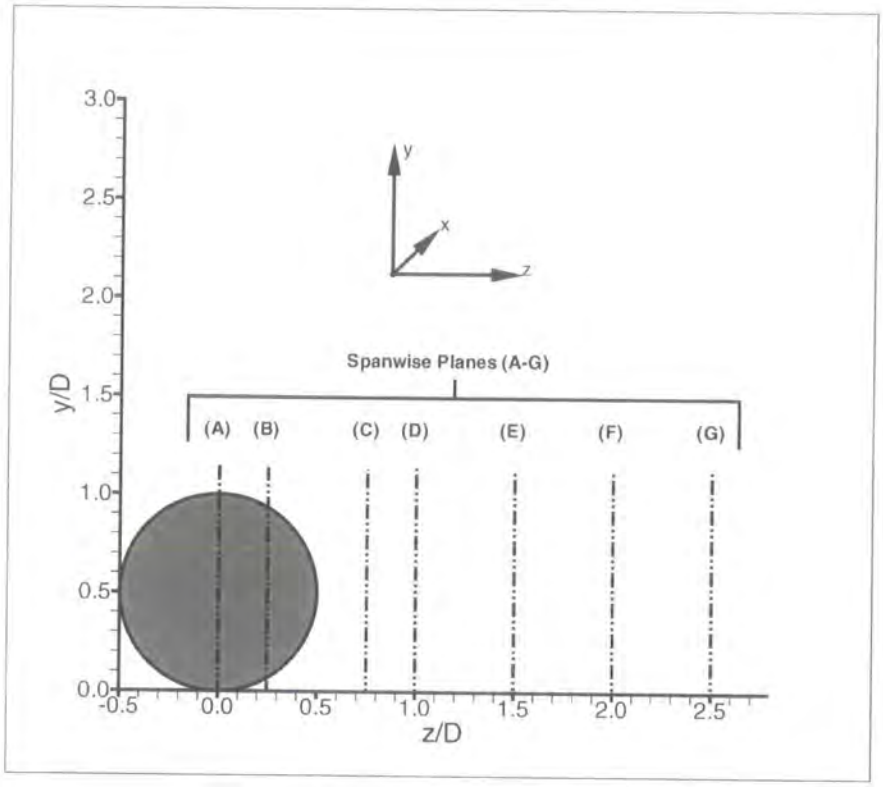


Figure 7.4: The Spanwise Traverse Planes at Different Streamwise Stations.

## 7.8 CFD Investigations

The CFD techniques have been described in Chapter 6 and relate to the rotating wheel. The data that were exported from the CFD package Fluent were: the steady-state predicted lift and drag coefficients; the static surface pressure distribution; the XY planes identical to the pressure probe wake survey planes shown in Figure 7.4, which included exporting the streamwise vorticity field, velocity field and the total pressure field at each streamwise station; the YZ planes identical to the PIV planes shown in Figure 7.1, which included exporting the velocity field.

| Plane | z/D | x/D Range | y/D Range |
|---|---|---|---|
| A | 0.00 | -0.28 to -0.7 | 0.04 to 0.4 |
| B | 0.25 | -0.28 to -0.7 | 0.04 to 0.4 |
| C | 0.75 | -0.9 to 0.9 | 0.04 to 1.25 |
| D | 1.00 | -0.9 to 0.9 | 0.04 to 1.25 |
| E | 1.50 | -0.9 to 0.9 | 0.04 to 1.25 |
| F | 2.00 | -0.9 to 0.9 | 0.04 to 1.25 |
| G | 2.50 | -0.9 to 0.9 | 0.04 to 1.25 |

Table 7.4: XY Streamwise Planes for Wake Traverse

| Experimental Configuration | $V_{ref}$ ($ms^{-1}$) | $f_{rot}$ (Hz) | Sampling Frequency (Hz) | N_Sets | N_Samples (per set) | Integration Time (s) |
|---|---|---|---|---|---|---|
| Rotating | 14.7 | 18.5 | 800 | 1 | 2048 | 2.56 |
| Stationary | 14.7 | - | 800 | 1 | 2048 | 2.56 |

Table 7.5: Major Data Acquisition Settings for the Pressure Probe Investigations.

# Chapter 8

# Experimental Results

## 8.1 Introduction

This chapter presents the wind tunnel results for the rotating and stationary wheel, acquired using the aforementioned instrumentation techniques. The results from each instrumentation technique are presented in separate sections. Detailed examination of the results and their importance in advancing the current knowledge of wheel flows will be discussed in Chapter 10 Discussion. In addition to the figures showing short sequences of images, the images are presented in their entirety as animations in .avi format on the CD-ROM which accompanies this thesis.

## 8.2 Time-Averaged Lift and Drag Coefficients

Table 8.1 presents the time-averaged lift and drag coefficients for the stationary and rotating cases, acquired from the static pressure distributions, load cell, wake integral method and CFD. The CFD results have been included here rather than have them in a separate section. The data of Fackrell [19] is included for comparative purposes, although it should be noted that the Fackrell geometry is not identical to that used for this study. Additionally, the surface static pressure data derived lift and drag coefficients for the rotating wheel at yaw (yaw = 5 degrees) are presented.

| Wheel/Tyre Type | Rotating/ Stationary | Acquisition Method | $C_{Dw}$ | $C_{Lw}$ |
|---|---|---|---|---|
| P1 | Stationary | Static Pressure Distribution | 0.73 | 0.60 |
| B2 (from [19]) | Stationary | Static Pressure Distribution | 0.77 | 0.76 |
| P1 | Stationary | Load Cell | 0.70 | N/a |
| P1 | Stationary | Wake Integral | 0.77 | N/a |
| P1 | Rotating | Static Pressure Distribution | 0.56 | 0.42 |
| B2 (from [19]) | Rotating | Static Pressure Distribution | 0.58 | 0.44 |
| P1 | Rotating | Load Cell | 0.63 | N/a |
| P1 | Rotating | Wake Integral | 0.63 | N/a |
| P1 | Rotating | CFD | 0.61 | 0.29 |
| P1 (Yaw=5deg) | Rotating | Static Pressure Distribution | 0.59 | 0.35 |

Table 8.1: Experimental and CFD Derived Time-Averaged Lift and Drag Coefficients.

## 8.3 Surface Static Pressure Distributions

The time-averaged surface static pressure distributions, acquired using the radio telemetry system, are presented in this section. Figure 8.1 shows the stationary and rotating surface static pressure distributions for the centreline of the wheel. One minor difference in the data for this figure (at the contact patch), which arose during experimentation, was the need to use a length of tubing connected between the reference port of the pressure scanner and atmosphere for the stationary wheel, and resulted in different contact patch characteristics. This was a direct consequence of deviations in the reference chamber temperature and hence pressure, caused during lengthy data logging procedures as the wheel was systematically rotated between angular positions, compared to the rotating case where the angular position changed rapidly as the wheel rotated. Consequently the tyre was inflated to the required pressure, to ensure correct seating of the tyre on the wheel rim, before the tyre valve was removed and the reference pressure tubing connected via the pressure valve hole. Due to the nature of the tyre profile when deflated it was decided that the sting

load would be increased in order to seal the gap that now existed at the contact patch due to zero inflation pressure. It was thought that this additional loading would not affect the validity of the results significantly, compared to what would be the case if a gap existed under the wheel where air could accelerate under the wheel into the base region of the wheel. Therefore the stationary and rotating wheel results are comparable. This can be seen in Figure 8.1 where the flow stagnates, for the stationary case, at around 80 degrees due to the slight tyre deformation. Cp = 1 confirms that the tread lay flat on the ground. This pressure distribution is discussed alongside all the other distributions in Chapter 10.

Figure 8.2 presents the time-averaged pressure distribution for the rotating case of the present work compared to that of Fackrell [19]. Figure 8.3 shows the time-averaged pressure distribution for the stationary case compared to that of Fackrell [19].

The time-averaged rotating and stationary pressure distributions for tapping 2 (W/D = +0.037) on the hub side of the wheel are shown in Figure 8.4. Figure 8.5 shows the time-averaged static pressure distribution for tapping 3 (W/D = +0.073) for the stationary and rotating cases. Figure 8.6 presents the time-averaged surface static pressure distribution for the rotating and stationary cases at tapping 4 (W/D = +0.110). Figure 8.7 shows the time-averaged pressure distribution for the rotating and stationary cases at tapping 5 (W/D = +0.146). The time-averaged rotating and stationary pressure distributions for tapping 6 (W/D = +0.183) are shown in Figure 8.8. Figure 8.9 presents the time-averaged pressure distribution for tapping 7 (W/D = +0.220). The time-averaged rotating and stationary pressure distributions for tapping 8 (W/D = +0.244) are presented in Figure 8.10. Figure 8.11 shows the time-averaged rotating and stationary surface static pressure distribution for tapping 9 (W/D = +0.268). The time-averaged pressure distribution for tapping 10 (W/D = +0.280) is shown in Figure 8.12. Figure 8.13 shows the time-averaged surface pressure distribution for tapping 11 (W/D = +0.272).

The centreline (W/D = 0) rotating time-averaged surface static pressure distributions at yaw angles ($\beta$) of zero and five degrees are shown in Figure 8.14. Figures 8.15 and 8.16 show the rotating time-averaged surface static pressure distributions for tappings -2 (W/D = -0.037) and +2 (W/D = +0.037), respectively at yaw angles ($\beta$) of zero and five degrees. Two figures were generated here for reasons of clarity and show identical yaw = 0 degree traces on each graph.

The rotating time-averaged surface static pressure distributions, with the wheel positioned at yaw angles ($\beta$) of zero and five degrees, for tappings -3 (W/D = -0.073) and +3 (W/D = +0.073) are presented in Figures 8.17 and 8.18, respectively. Figures 8.19 and 8.20 show the rotating time-averaged surface static pressure distributions for tappings -4 (W/D = -0.110) and +4 (W/D = +0.110), respectively at yaw angles ($\beta$) of zero and five degrees. The rotating time-averaged surface static pressure distributions, with the wheel positioned at yaw angles ($\beta$) of zero and five degrees, for tappings -5 (W/D = -0.146) and +5 (W/D = +0.146) are presented in Figures 8.21 and 8.22, respectively. Figures 8.23 and 8.24 show the rotating time-averaged surface static pressure distributions for tappings -6 (W/D = -0.183) and +6 (W/D = +0.183), respectively at yaw angles ($\beta$) of zero and five degrees. The rotating time-averaged surface static pressure distributions, with the wheel positioned at yaw angles ($\beta$) of zero and five degrees, for tappings -7 (W/D = -0.220) and +7 (W/D = +0.220) are presented in Figures 8.25 and 8.26, respectively. Figures 8.27 and 8.28 show the rotating time-averaged surface static pressure distributions for tappings -8 (W/D = -0.244) and +8 (W/D = +0.244), respectively at yaw angles ($\beta$) of zero and five degrees. The rotating time-averaged surface static pressure distributions, with the wheel positioned at yaw angles ($\beta$) of zero and five degrees, for tappings -9 (W/D = -0.268) and +9 (W/D = +0.268) are presented in Figures 8.29 and 8.30, respectively. Figures 8.31 and 8.32 show the rotating time-averaged surface static pressure distributions for tappings -10 (W/D = -0.280) and +10 (W/D = +0.280), respectively at yaw angles ($\beta$) of zero and five degrees. The rotating time-averaged surface static pressure distributions, with the wheel positioned at yaw angles ($\beta$) of zero and five degrees, for tappings -11 (W/D = -0.272) and +11 (W/D = +0.272)

are presented in Figures 8.33 and 8.34, respectively.

## 8.4 Smoke Flow Visualisation

Figures 8.35 and 8.36 show the smoke flow visualisation for the stationary and rotating wheel, respectively, with the smoke generator probe head positioned on the wheel centreline at approximately 200 degrees.

Figures 8.37 and 8.38 show the smoke flow visualisation for the stationary and rotating wheel, respectively, with the smoke generator probe head positioned on the wheel centreline at approximately 225 degrees.

Figures 8.39 and 8.40 show the smoke flow visualisation for the stationary and rotating wheel, respectively, with the smoke generator probe head positioned on the wheel centreline at approximately 250 degrees.

Figures 8.41 and 8.42 show the smoke flow visualisation for the stationary and rotating wheel, respectively, with the smoke generator probe head positioned on the wheel centreline at approximately 340 degrees.

Figures 8.43 and 8.44 show the smoke flow visualisation for the stationary and rotating wheel, respectively, with the smoke generator probe head positioned by the side of the contact patch at approximately 90 degrees.

## 8.5 Wake Surveys

The flow-field results, acquired using the five-hole pressure probe, are presented in this section. Each spanwise XY traverse plane is shown in a separate section.

### 8.5.1 XY Spanwise Plane at Streamwise Station Z/D = 0

This section presents the flow-field data with respect to the XY spanwise plane at the streamwise station Z/D = 0. Figure 8.45 shows time-averaged contours of constant total pressure coefficient at the side of the wheel, for the rotating wheel. The total pressure coefficient results at the same station for the stationary wheel are presented in Figure 8.46. Contours of constant standard deviation of the dynamic pressure coefficient are presented for the rotating and stationary cases in Figures 8.47 and 8.48, respectively. Contours of constant streamwise vorticity ($\xi$) for the rotating and stationary cases are presented in Figures 8.49 and 8.50, respectively. The time-averaged secondary flow velocity vectors are presented in Figures 8.51 and 8.52 for the rotating and stationary cases, respectively.

### 8.5.2 XY Spanwise Plane at Streamwise Station Z/D = 0.25

The results from the spanwise (XY) plane located at the streamwise station Z/D = 0.25 are presented in this section. Figures 8.53 and 8.54 show time-averaged contours of constant total pressure coefficient for the rotating and stationary cases, respectively. Figures 8.55 and 8.56 show contours of constant standard deviation of the dynamic pressure coefficient for the rotating and stationary cases, respectively. Figures 8.57 and 8.58 show contours of constant streamwise vorticity ($\xi$) for the rotating and stationary cases, respectively. The time-averaged secondary flow velocity vectors for the rotating and stationary cases are shown in Figures 8.59 and 8.60, respectively.

### 8.5.3 XY Spanwise Plane at Streamwise Station Z/D = 0.75

This section presents the results for the spanwise XY traverse plane located at the streamwise station Z/D = 0.75. Figures 8.61 and 8.62 show time-averaged contours of constant total pressure coefficient for the rotating and stationary cases, respectively. Figures 8.63 and 8.64 show contours of constant standard deviation of the dynamic pressure coefficient for the rotating and stationary cases, respectively. Figures 8.65 and 8.66 show contours of constant streamwise vorticity ($\xi$) for the ro-

tating and stationary cases, respectively. The time-averaged secondary flow velocity vectors for the rotating and stationary cases are shown in Figures 8.67 and 8.68, respectively.

### 8.5.4 XY Spanwise Plane at Streamwise Station Z/D = 1.0

The results for the spanwise XY traverse plane located at the streamwise station Z/D = 1.0 are shown in this section. Figures 8.69 and 8.70 show time-averaged contours of constant total pressure coefficient for the rotating and stationary cases, respectively. Figures 8.71 and 8.72 show contours of constant standard deviation of the dynamic pressure coefficient for the rotating and stationary cases, respectively. Figures 8.73 and 8.74 show contours of constant streamwise vorticity ($\xi$) for the rotating and stationary cases, respectively. The time-averaged secondary flow velocity vectors for the rotating and stationary cases are shown in Figures 8.75 and 8.76, respectively.

### 8.5.5 XY Spanwise Plane at Streamwise Station Z/D = 1.5

This section presents the results for the spanwise XY traverse plane located at the streamwise station Z/D = 1.5. Figures 8.77 and 8.78 show time-averaged contours of constant total pressure coefficient for the rotating and stationary cases, respectively. Figures 8.79 and 8.80 show contours of constant standard deviation of the dynamic pressure coefficient for the rotating and stationary cases, respectively. Figures 8.81 and 8.82 show contours of constant streamwise vorticity ($\xi$) for the rotating and stationary cases, respectively. The time-averaged secondary flow velocity vectors for the rotating and stationary cases are shown in Figures 8.83 and 8.84, respectively.

### 8.5.6 XY Spanwise Plane at Streamwise Station Z/D = 2.0

The results for the spanwise XY traverse plane located at the streamwise station Z/D = 2.0 are shown in this section. Figures 8.85 and 8.86 show time-averaged contours of constant total pressure coefficient for the rotating and stationary cases, respectively. Figures 8.87 and 8.88 show contours of constant standard deviation of the dynamic pressure coefficient for the rotating and stationary cases, respectively. Figures 8.89

and 8.90 show contours of constant streamwise vorticity ($\xi$) for the rotating and stationary cases, respectively. The time-averaged secondary flow velocity vectors for the rotating and stationary cases are shown in Figures 8.91 and 8.92, respectively.

### 8.5.7 XY Spanwise Plane at Streamwise Station Z/D = 2.5

This section presents the results for the spanwise XY traverse plane located at the streamwise station Z/D = 2.5. Figures 8.93 and 8.94 show time-averaged contours of constant total pressure coefficient for the rotating and stationary cases, respectively. Figures 8.95 and 8.96 show contours of constant standard deviation of the dynamic pressure coefficient for the rotating and stationary cases, respectively. Figures 8.97 and 8.98 show contours of constant streamwise vorticity ($\xi$) for the rotating and stationary cases, respectively. The time-averaged secondary flow velocity vectors for the rotating and stationary cases are shown in Figures 8.99 and 8.100, respectively.

## 8.6 Particle Image Velocimetry

### 8.6.1 Centreline (W/D = 0) Streamwise Regions (PosA-D)

Figures 8.101 and 8.102 show the ensemble time-averaged velocity vectors for the complete analysis regions (PosA-D) for the rotating and stationary cases, respectively.

Figures 8.103 and 8.104 show the ensemble time-averaged velocity vectors for PosA for the rotating and stationary cases, respectively. Figure 8.105 shows a time sequence of instantaneous velocity vectors for the rotating and stationary cases at PosA. Figures 8.106 and 8.107 show contours of constant standard deviation of the velocity field for PosA for the rotating and stationary cases, respectively.

Ensemble time-averaged contours of constant spanwise vorticity for PosA are presented in Figures 8.108 and 8.109 for the rotating and stationary cases, respectively.

Figure 8.110 shows a sequence of instantaneous spanwise vorticity ($\zeta$) contours for the stationary and rotating cases at PosA.

Figures 8.111 and 8.112 show the ensemble time-averaged velocity vectors for PosB for the rotating and stationary cases, respectively. Figure 8.113 shows a sequence showing velocity vectors for the stationary and rotating cases at PosB.

Figures 8.114 and 8.115 show ensemble time-averaged contours of constant spanwise vorticity for the rotating and stationary cases, respectively. Figure 8.116 shows a sequence of instantaneous spanwise vorticity ($\zeta$) contours for the stationary and rotating cases at PosB.

Figures 8.117 and 8.118 show the ensemble time-averaged velocity vectors for PosC for the rotating and stationary cases, respectively. Figure 8.119 shows a sequence showing velocity vectors for the stationary and rotating cases at PosC.

Figures 8.120 and 8.121 show the ensemble time-averaged velocity vectors for PosD for the rotating and stationary cases, respectively. Figure 8.122 shows a sequence showing velocity vectors for the stationary and rotating cases at PosD.

Figures 8.123 and 8.124 show contours of constant standard deviation of the velocity field for PosD for the rotating and stationary cases, respectively.

Ensemble time-averaged contours of constant spanwise vorticity for PosD are presented in Figures 8.125 and 8.126 for the rotating and stationary cases, respectively. Figure 8.127 shows a sequence showing contours of constant spanwise vorticity ($\zeta$) for the stationary and rotating cases at PosD.

### 8.6.2 Wheel Edge (W/D = 0.18) Streamwise Region (PosA)

Figures 8.128 and 8.129 show the ensemble time-averaged velocity vectors for the analysis region (PosA) for the rotating and stationary cases, respectively. Figure

8.130 shows a sequence showing velocity vectors for the stationary and rotating cases at PosA.

Figures 8.131 and 8.132 show contours of constant standard deviation of the velocity field for PosA for the rotating and stationary cases, respectively.

### 8.6.3 Overhead (y/D = 0.26) Streamwise Regions (PosA-B)

Figures 8.133 and 8.134 show the ensemble time-averaged velocity vectors for the analysis region PosA (overhead) for the rotating and stationary cases, respectively. Figures 8.135 and 8.136 show contours of constant standard deviation of the velocity field for PosA (overhead) for the rotating and stationary cases, respectively. Figure 8.137 shows a sequence of velocity vectors for the stationary and rotating cases at PosA (overhead).

Figures 8.138 and 8.139 show the ensemble time-averaged velocity vectors for the analysis region PosB (overhead) for the rotating and stationary cases, respectively. Figures 8.140 and 8.141 show contours of constant standard deviation of the velocity field for PosB (overhead) for the rotating and stationary cases, respectively. Figure 8.142 shows a sequence of velocity vectors for the stationary and rotating cases at PosB (overhead).

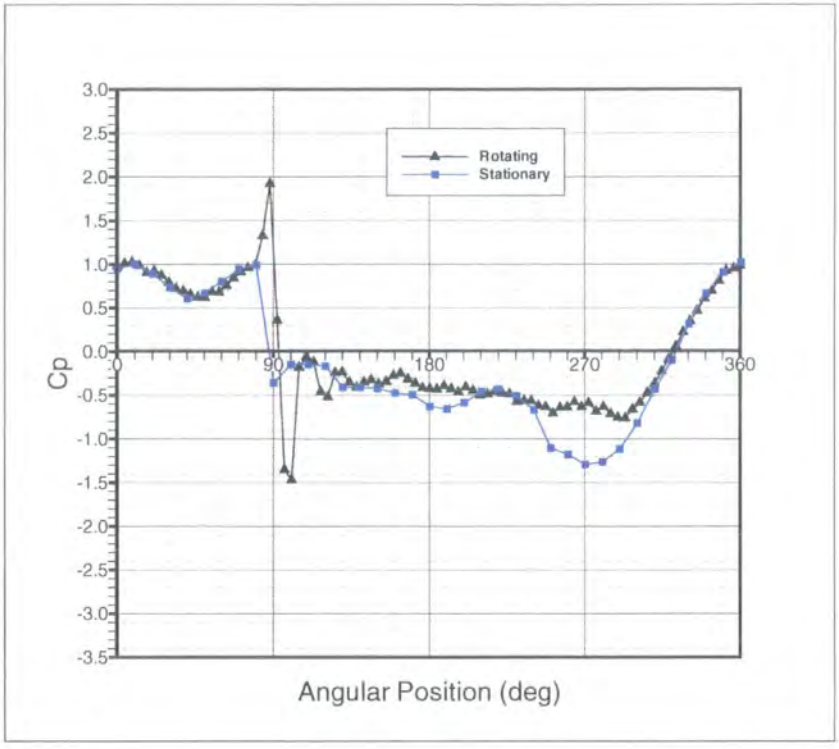


Figure 8.1: Rotating and Stationary Time-Averaged Surface Static Pressure Distributions for the Wheel Centreline.

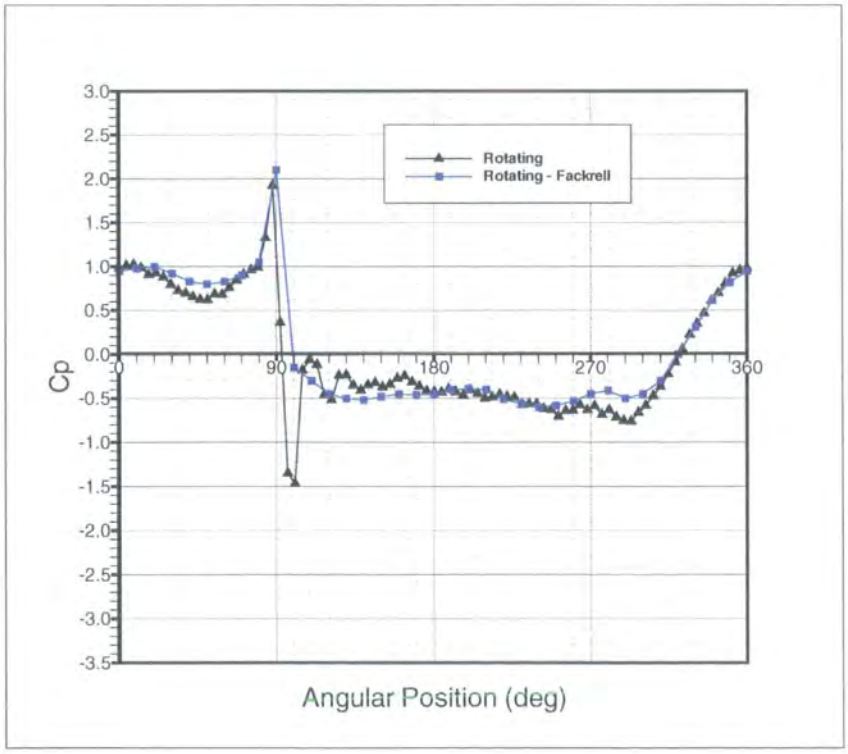


Figure 8.2: Rotating Surface Static Pressure Distribution for the Centreline, compared with Fackrell [19].

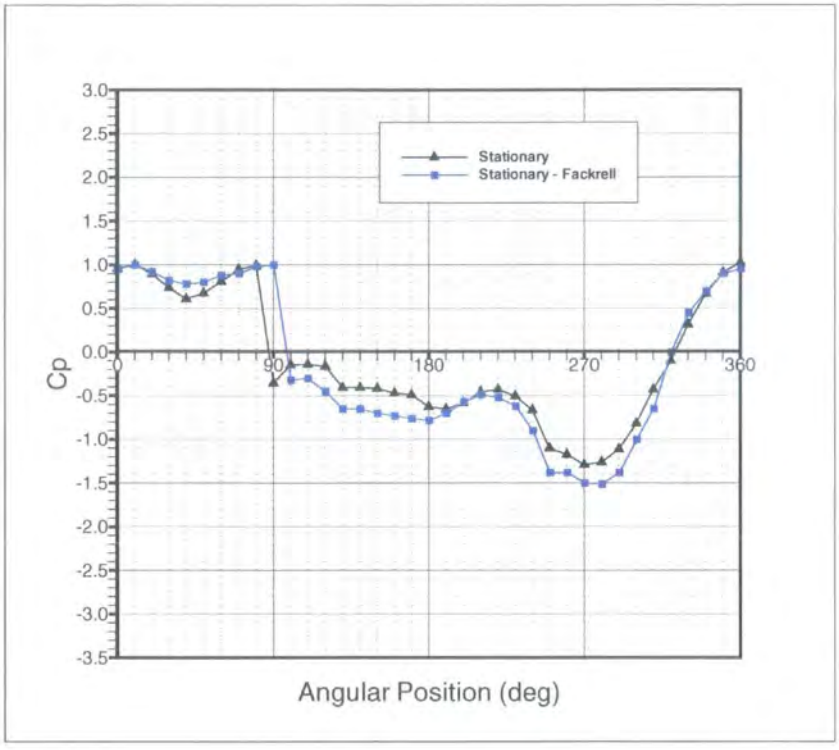


Figure 8.3: Stationary Surface Static Pressure Distribution for the Centreline, compared with Fackrell [19].

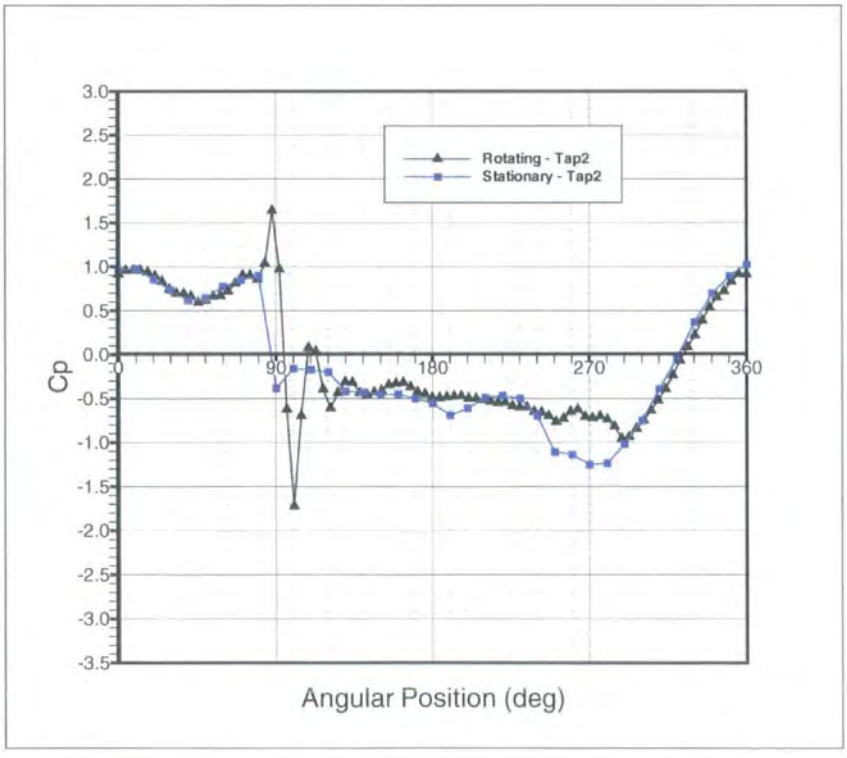


Figure 8.4: Rotating and Stationary Surface Static Pressure Distribution for Tapping 2 (W/D=+0.037).

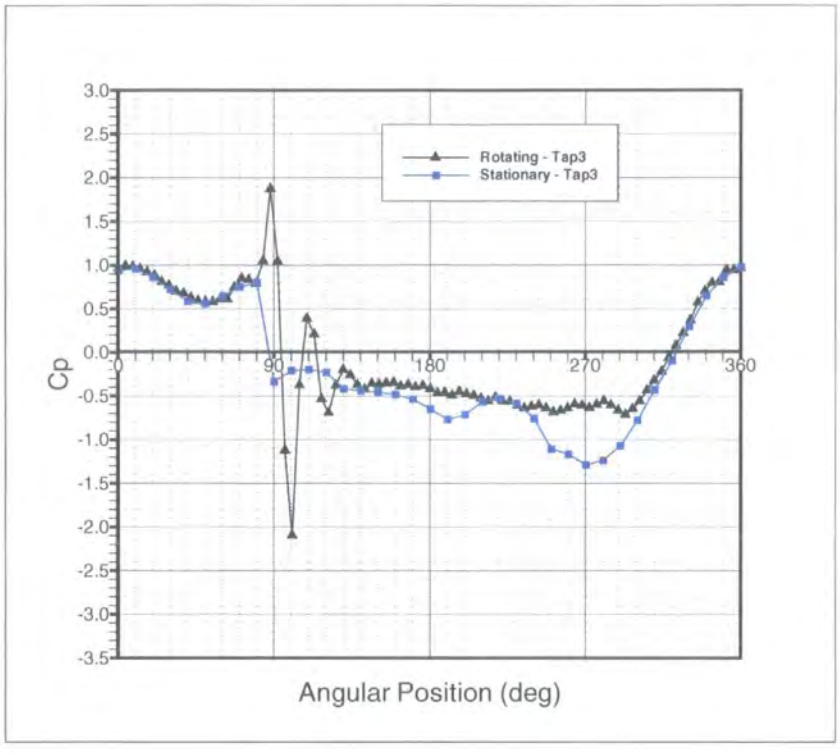


Figure 8.5: Rotating and Stationary Surface Static Pressure Distribution for Tapping 3 (W/D=+0.073).

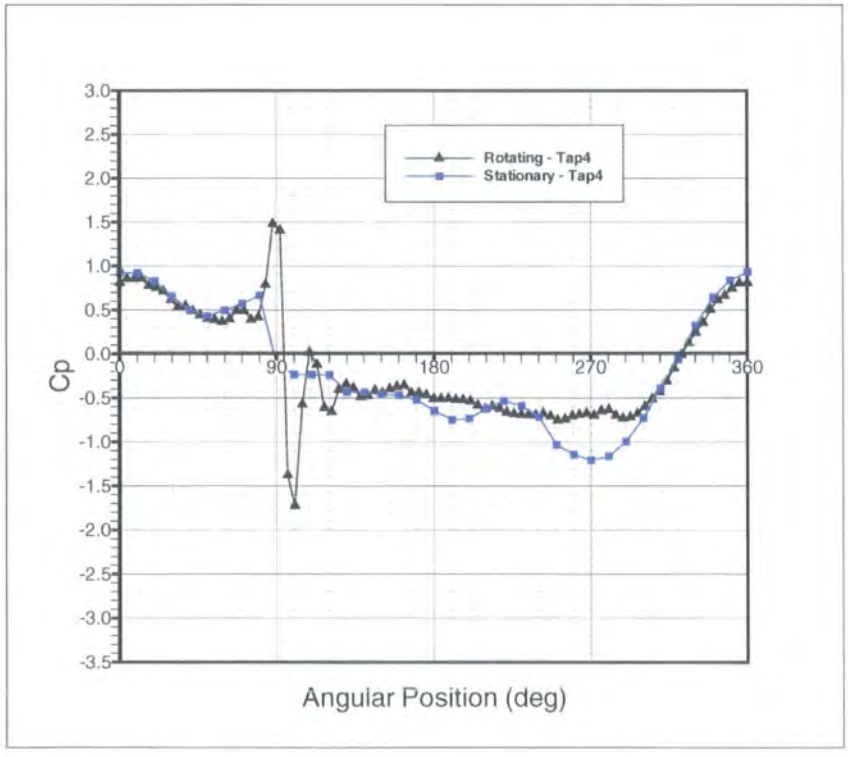


Figure 8.6: Rotating and Stationary Surface Static Pressure Distribution for Tapping 4 (W/D=+0.110).

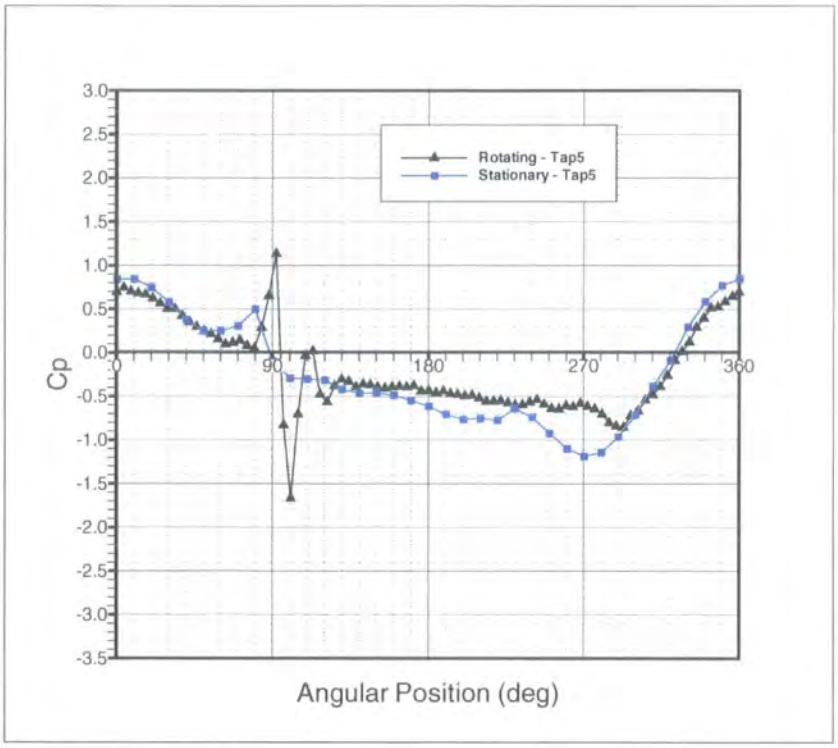


Figure 8.7: Rotating and Stationary Surface Static Pressure Distribution for Tapping 5 (W/D=+0.146).

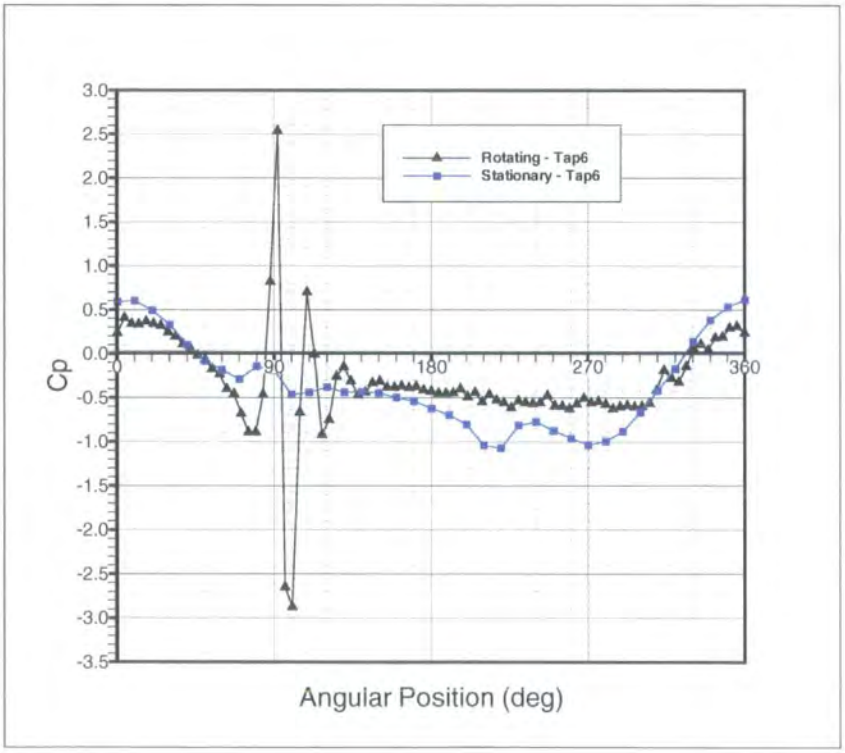


Figure 8.8: Rotating and Stationary Surface Static Pressure Distribution for Tapping 6 (W/D=+0.183).

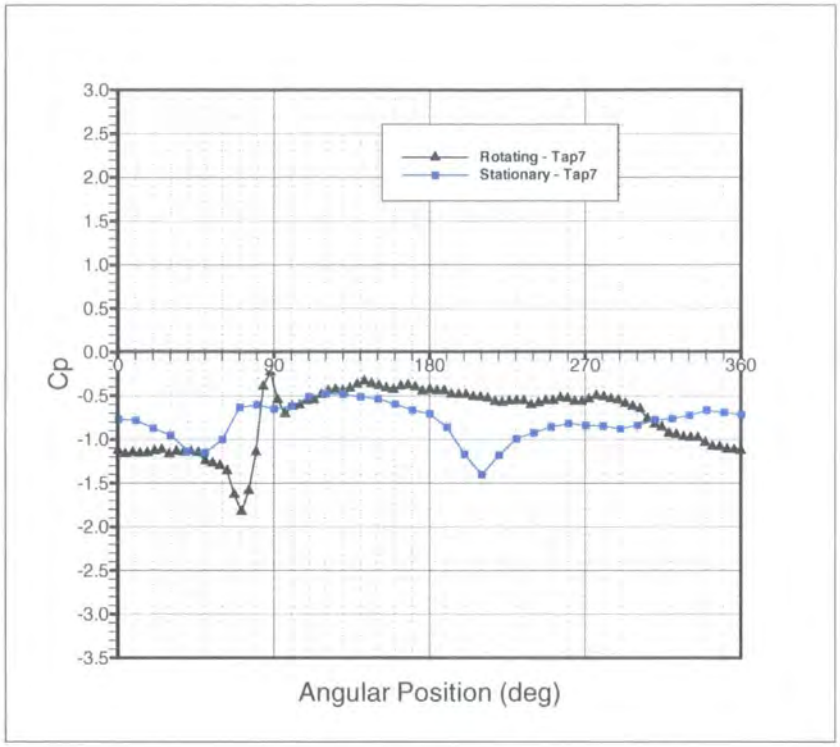


Figure 8.9: Rotating and Stationary Surface Static Pressure Distribution for Tapping 7 (W/D=+0.220).

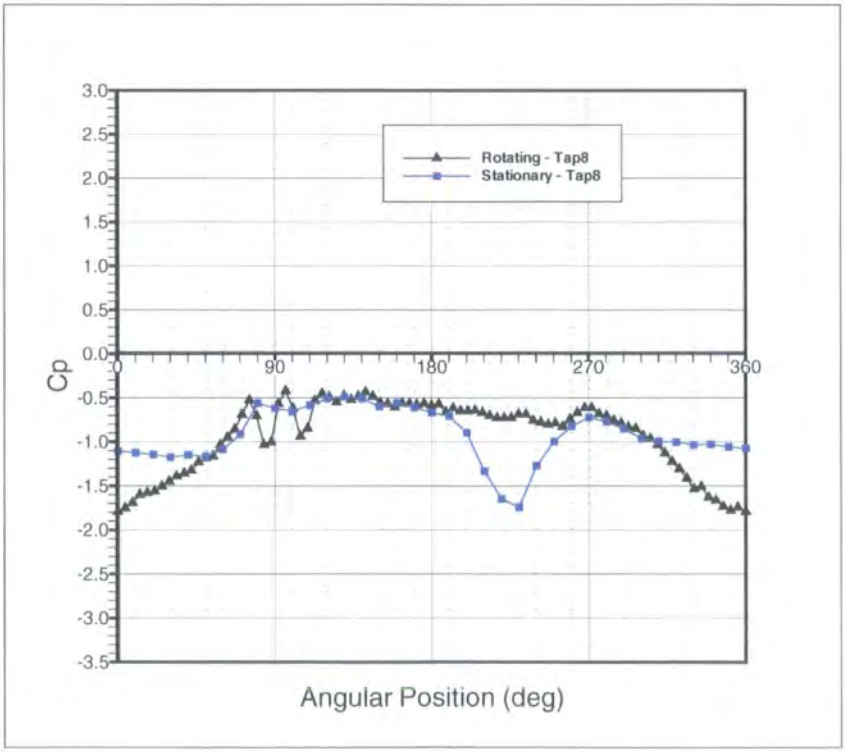


Figure 8.10: Rotating and Stationary Surface Static Pressure Distribution for Tapping 8 (W/D=+0.244).

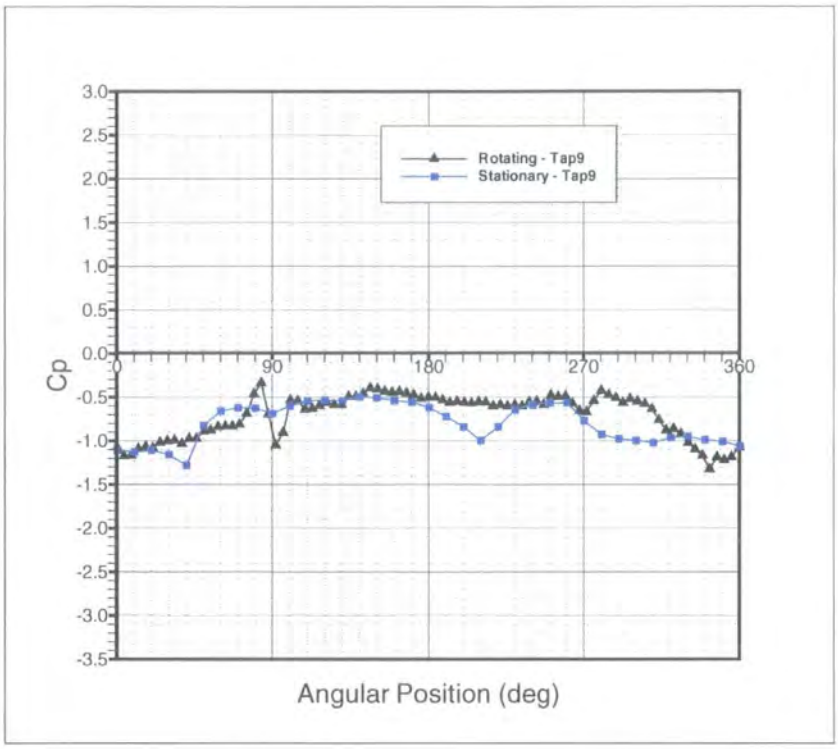


Figure 8.11: Rotating and Stationary Surface Static Pressure Distribution for Tapping 9 (W/D=+0.268).

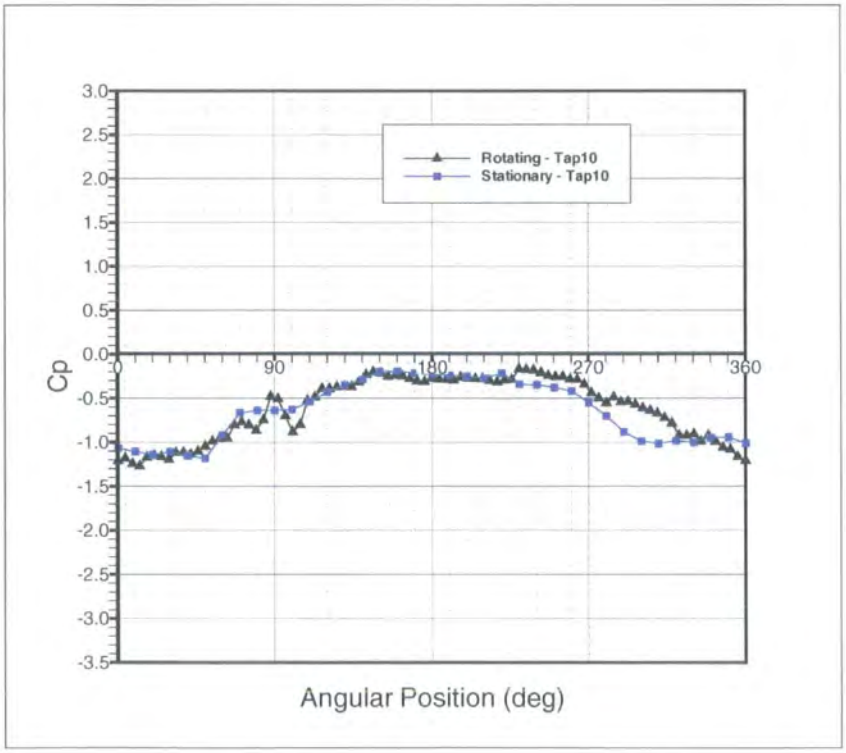


Figure 8.12: Rotating and Stationary Surface Static Pressure Distribution for Tapping 10 (W/D=+0.280).

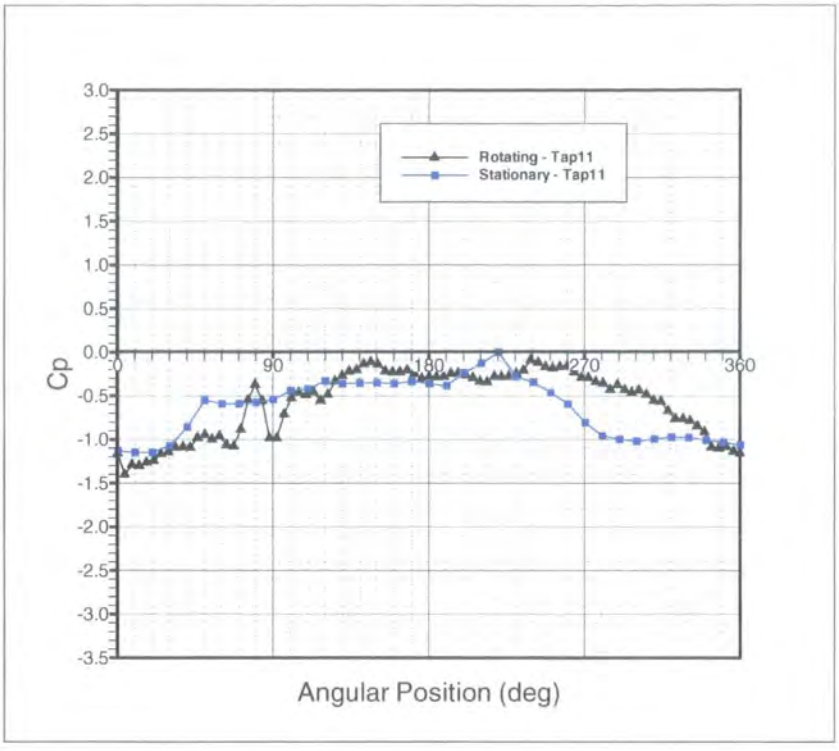


Figure 8.13: Rotating and Stationary Surface Static Pressure Distribution for Tapping 11 (W/D=+0.272).

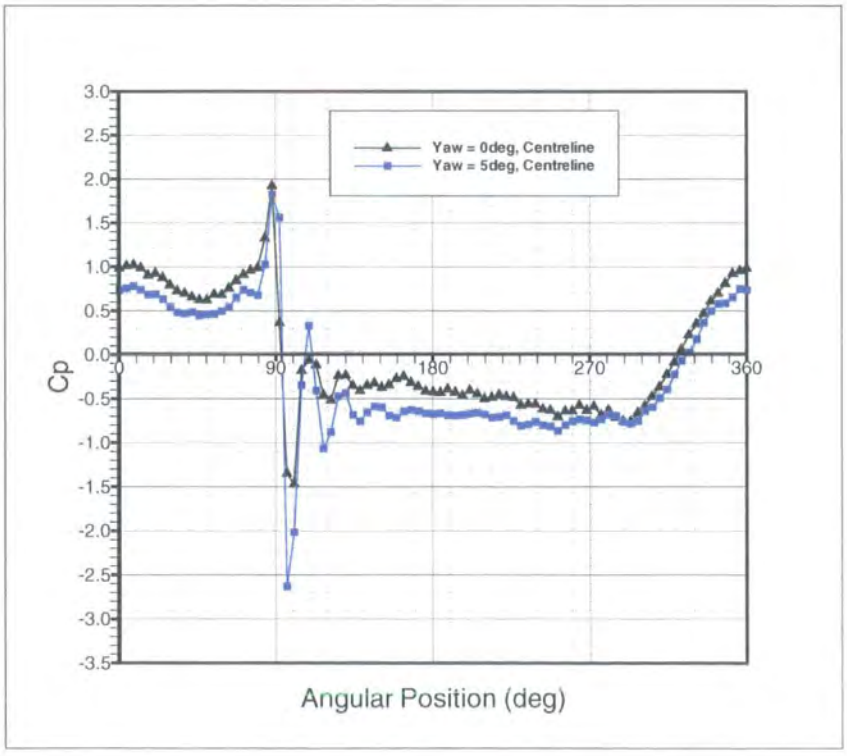


Figure 8.14: Rotating Surface Static Pressure Distribution for the Centreline at Yaw Angles ($\beta$) of 0 and 5 degrees.

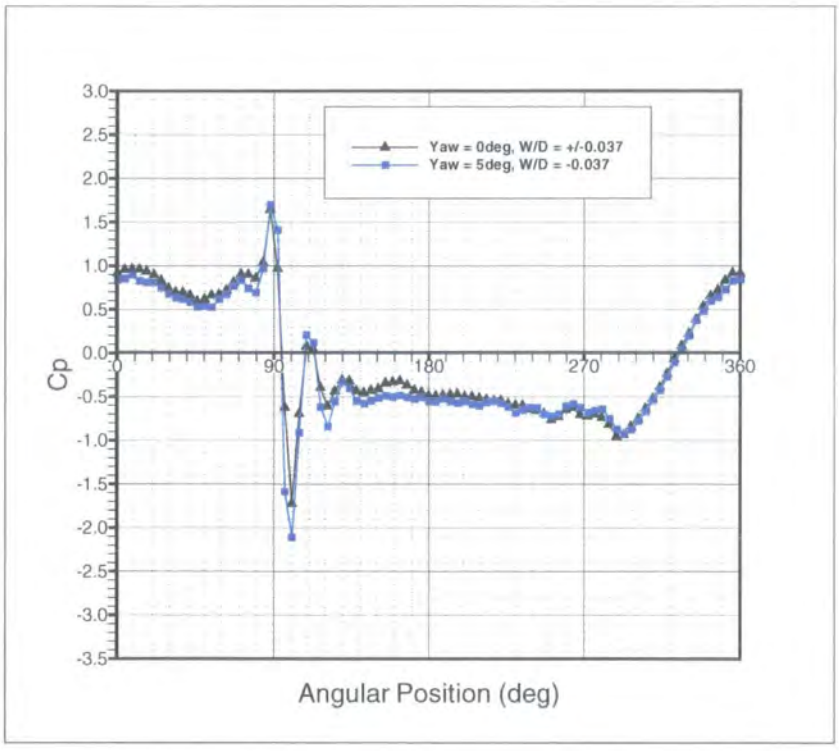


Figure 8.15: Rotating Surface Static Pressure Distribution for Tapping -2 at Yaw Angles ($\beta$) of 0 and 5 degrees.

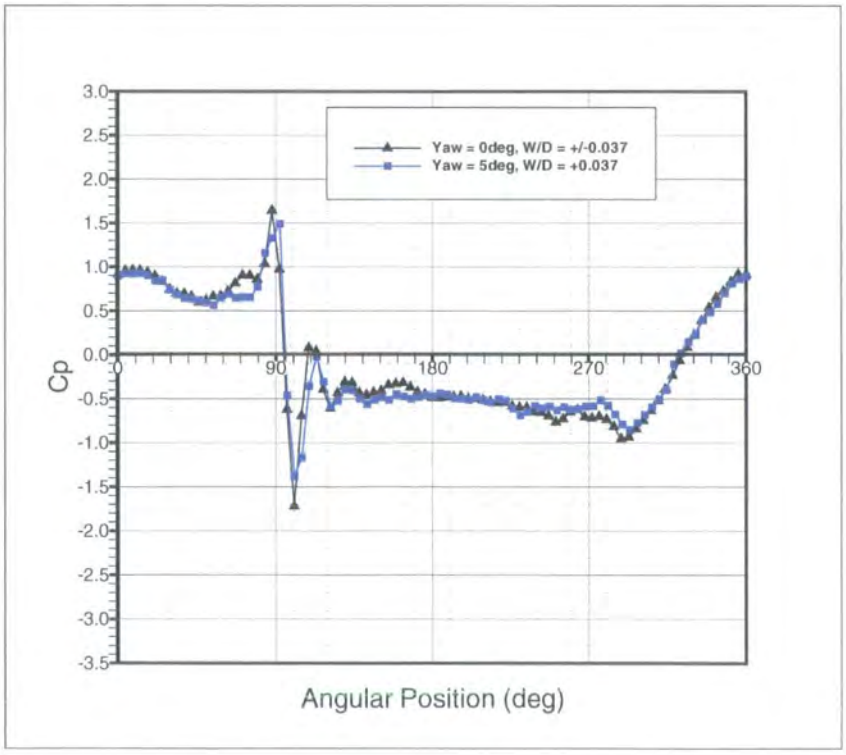


Figure 8.16: Rotating Surface Static Pressure Distribution for Tapping +2 at Yaw Angles ($\beta$) of 0 and 5 degrees.

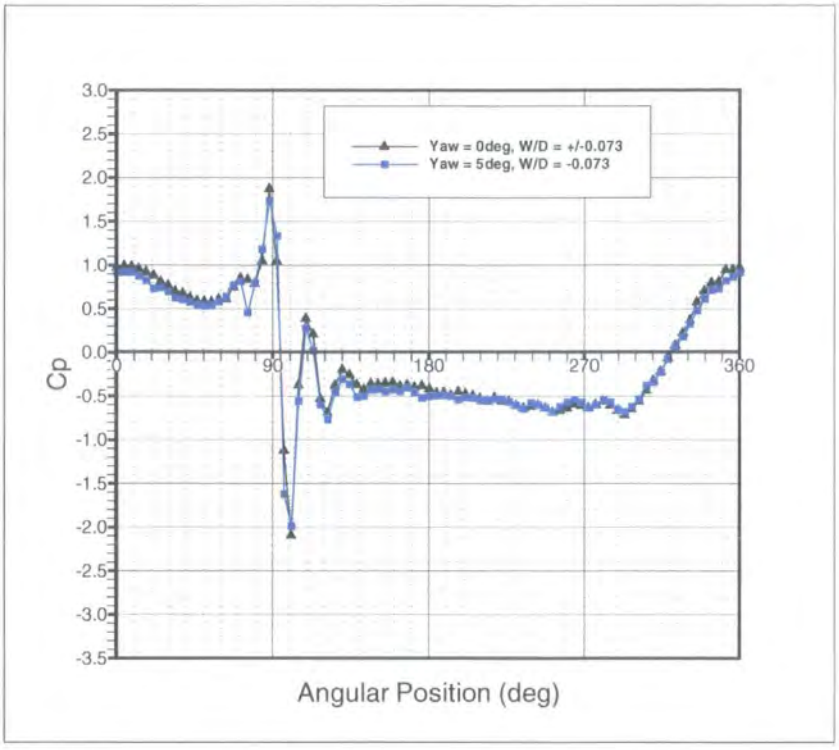


Figure 8.17: Rotating Surface Static Pressure Distribution for Tapping -3 at Yaw Angles ($\beta$) of 0 and 5 degrees.

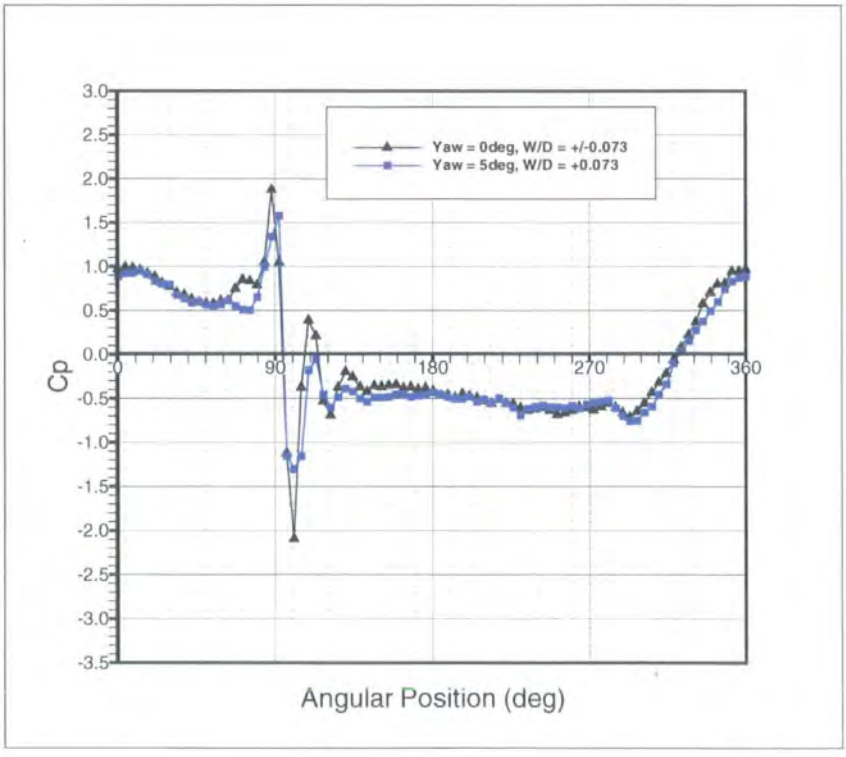


Figure 8.18: Rotating Surface Static Pressure Distribution for Tapping +3 at Yaw Angles ($\beta$) of 0 and 5 degrees.

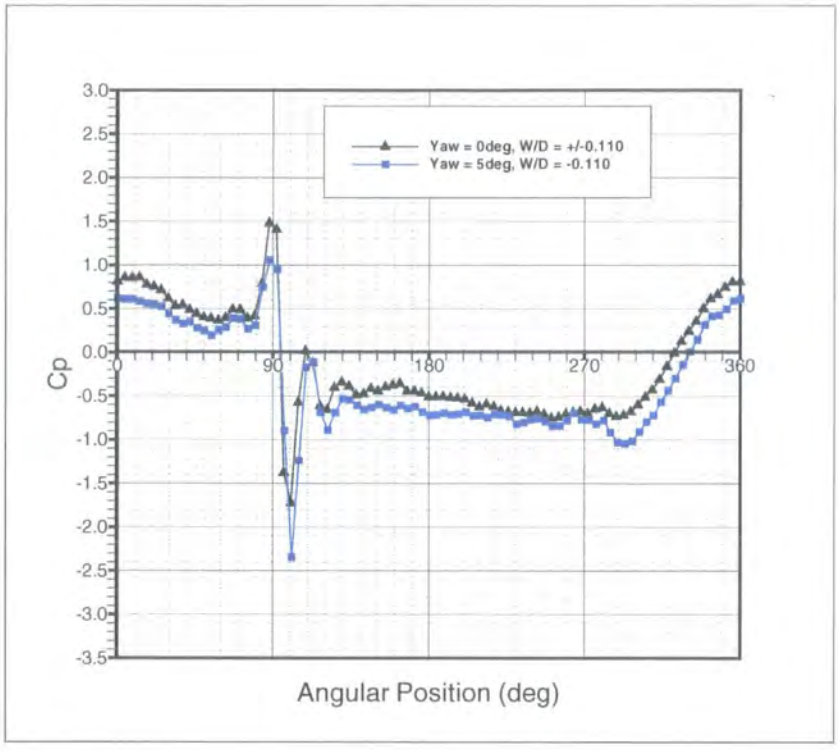


Figure 8.19: Rotating Surface Static Pressure Distribution for Tapping -4 at Yaw Angles ($\beta$) of 0 and 5 degrees.

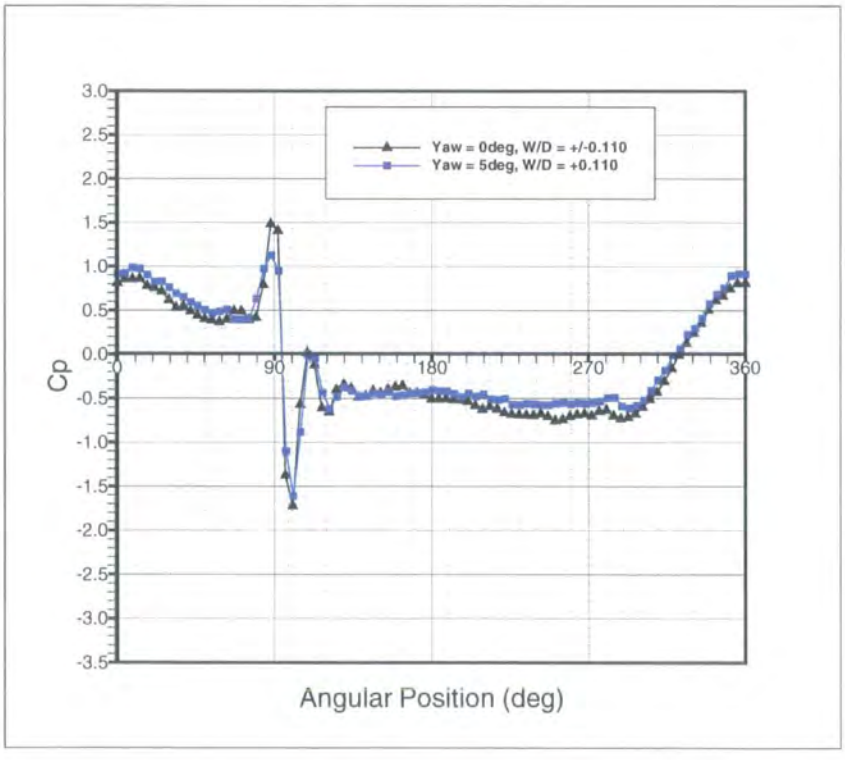


Figure 8.20: Rotating Surface Static Pressure Distribution for Tapping +4 at Yaw Angles ($\beta$) of 0 and 5 degrees.

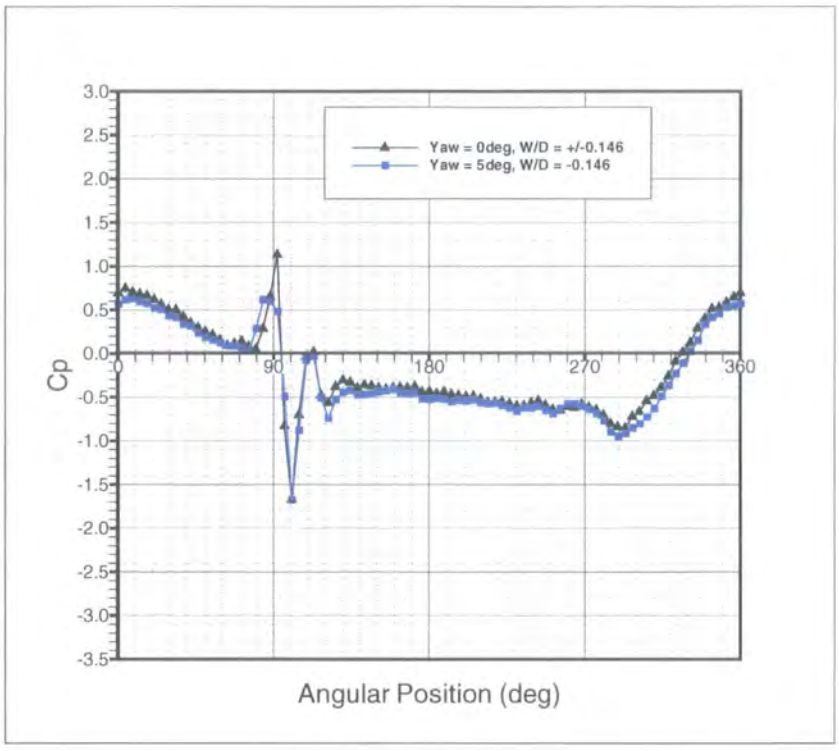


Figure 8.21: Rotating Surface Static Pressure Distribution for Tapping -5 at Yaw Angles ($\beta$) of 0 and 5 degrees.

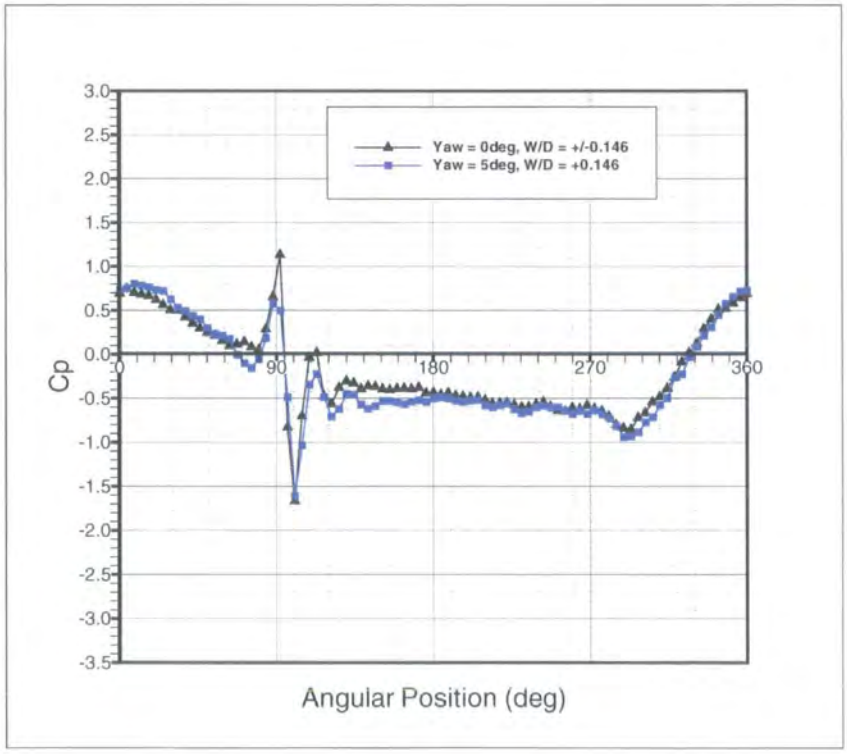


Figure 8.22: Rotating Surface Static Pressure Distribution for Tapping +5 at Yaw Angles ($\beta$) of 0 and 5 degrees.

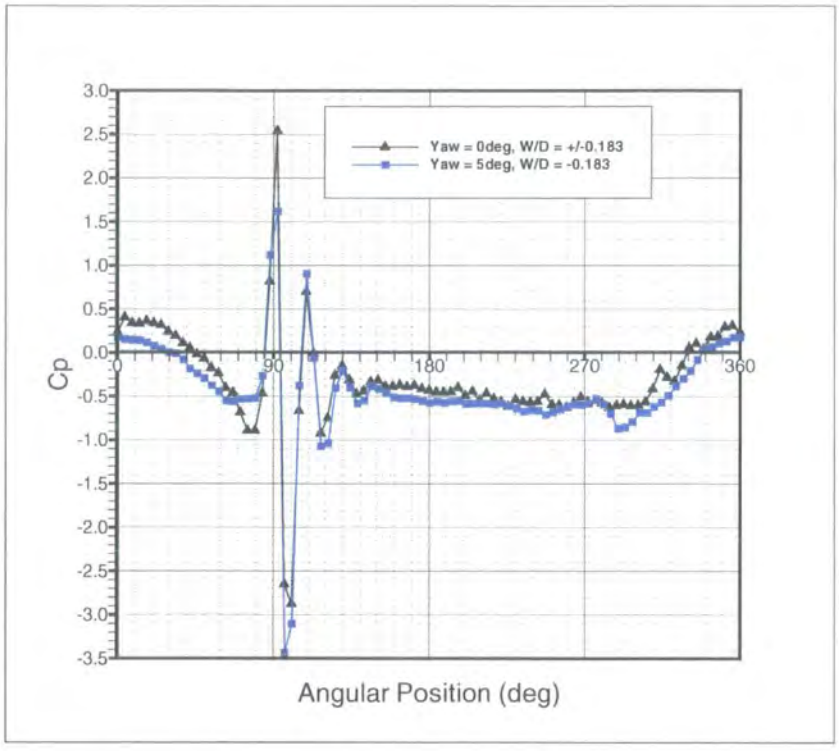


Figure 8.23: Rotating Surface Static Pressure Distribution for Tapping -6 at Yaw Angles ($\beta$) of 0 and 5 degrees.

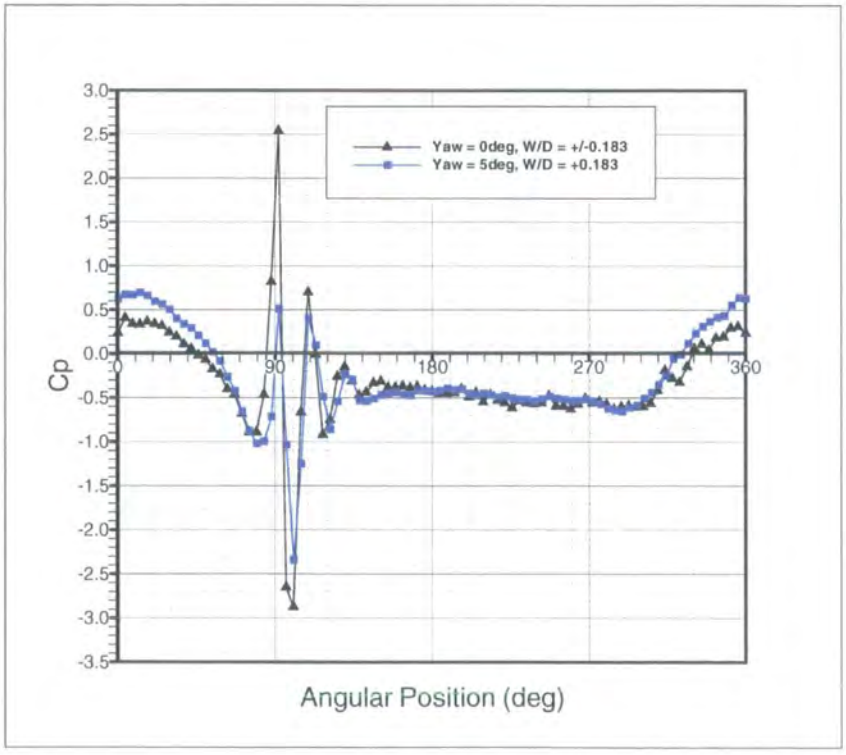


Figure 8.24: Rotating Surface Static Pressure Distribution for Tapping +6 at Yaw Angles ($\beta$) of 0 and 5 degrees.

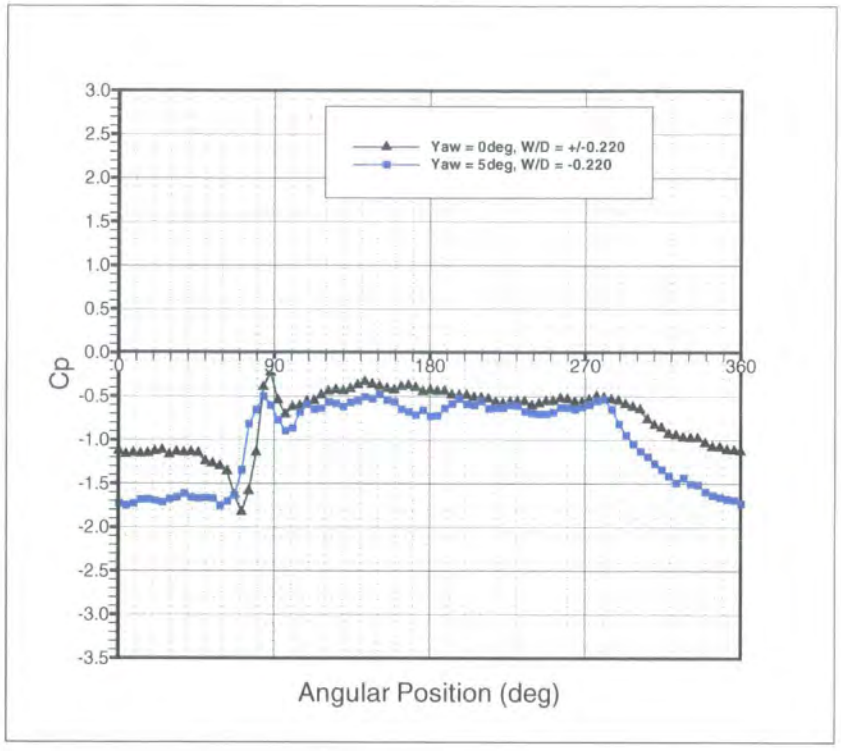


Figure 8.25: Rotating Surface Static Pressure Distribution for Tapping -7 at Yaw Angles ($\beta$) of 0 and 5 degrees.

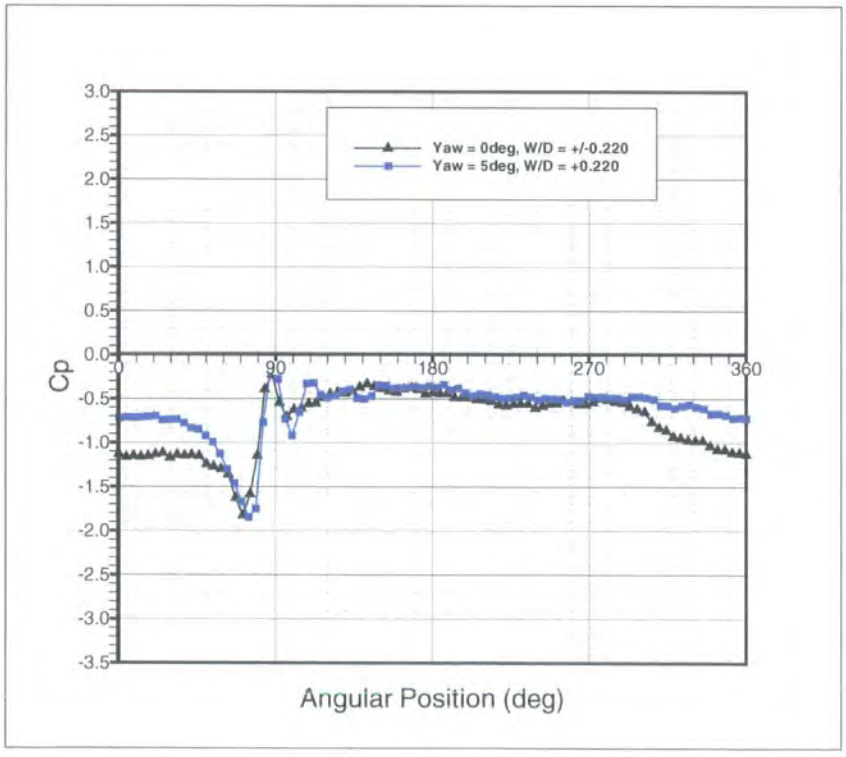


Figure 8.26: Rotating Surface Static Pressure Distribution for Tapping +7 at Yaw Angles ($\beta$) of 0 and 5 degrees.

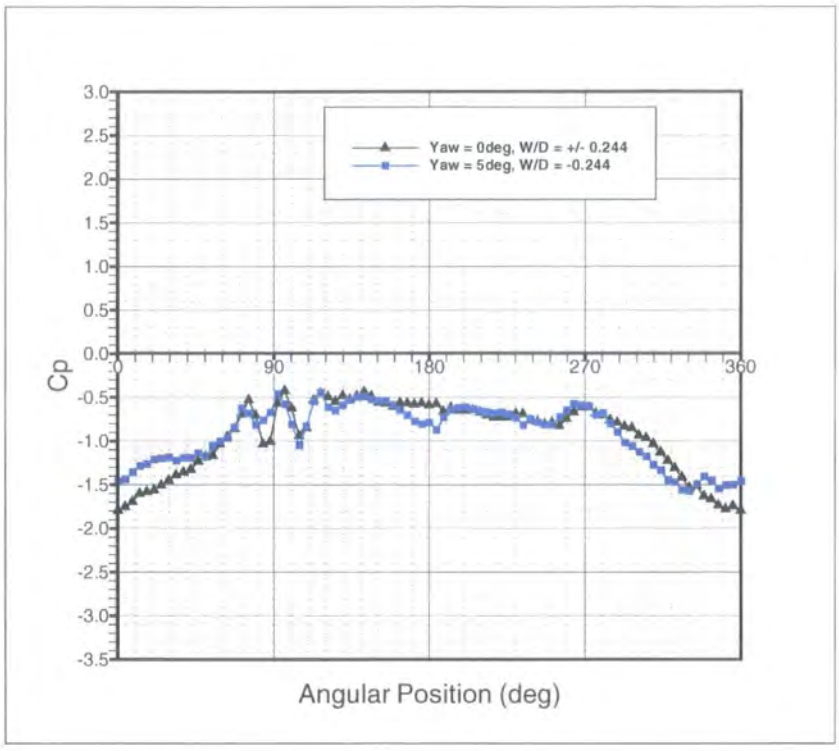


Figure 8.27: Rotating Surface Static Pressure Distribution for Tapping -8 at Yaw Angles ($\beta$) of 0 and 5 degrees.

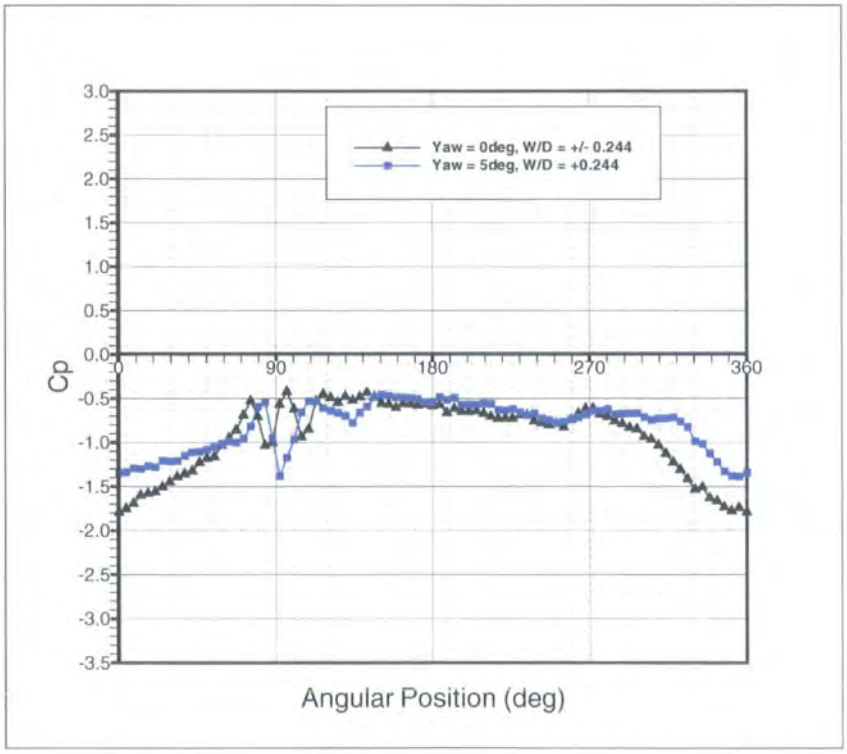


Figure 8.28: Rotating Surface Static Pressure Distribution for Tapping +8 at Yaw Angles ($\beta$) of 0 and 5 degrees.

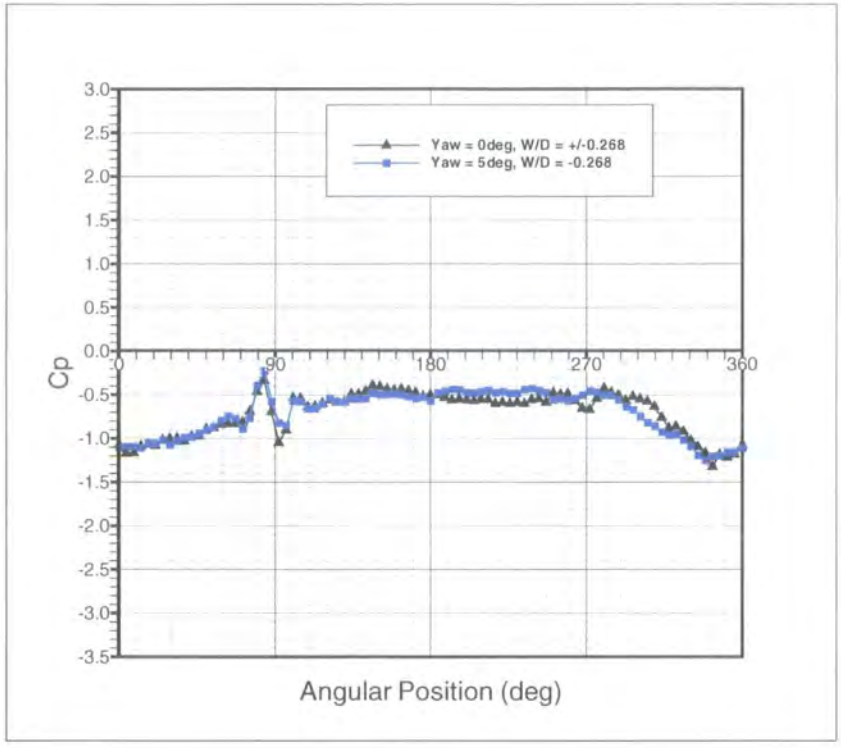


Figure 8.29: Rotating Surface Static Pressure Distribution for Tapping -9 at Yaw Angles ($\beta$) of 0 and 5 degrees.

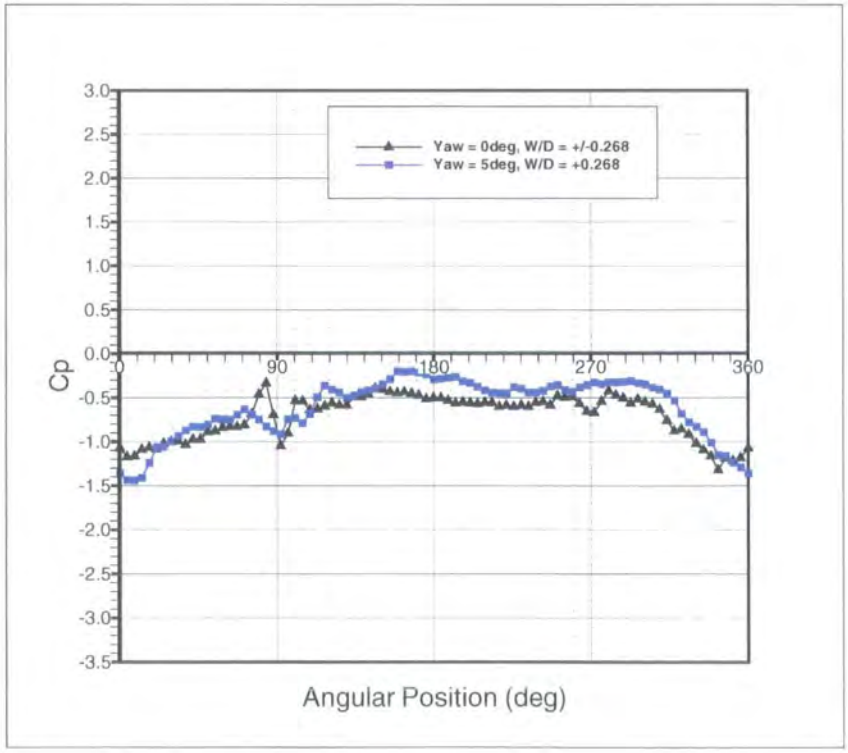


Figure 8.30: Rotating Surface Static Pressure Distribution for Tapping +9 at Yaw Angles ($\beta$) of 0 and 5 degrees.

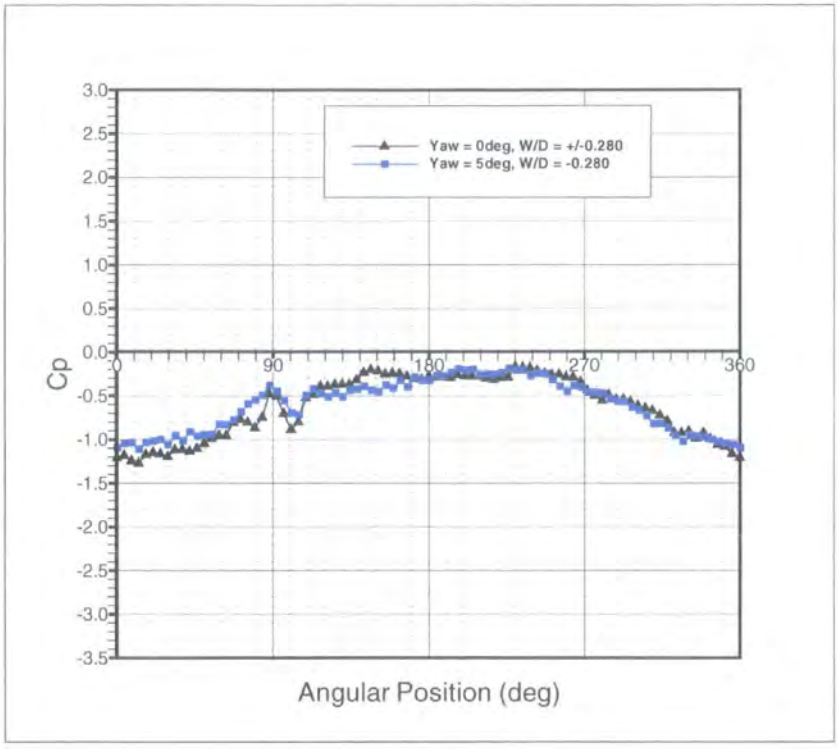


Figure 8.31: Rotating Surface Static Pressure Distribution for Tapping -10 at Yaw Angles ($\beta$) of 0 and 5 degrees.

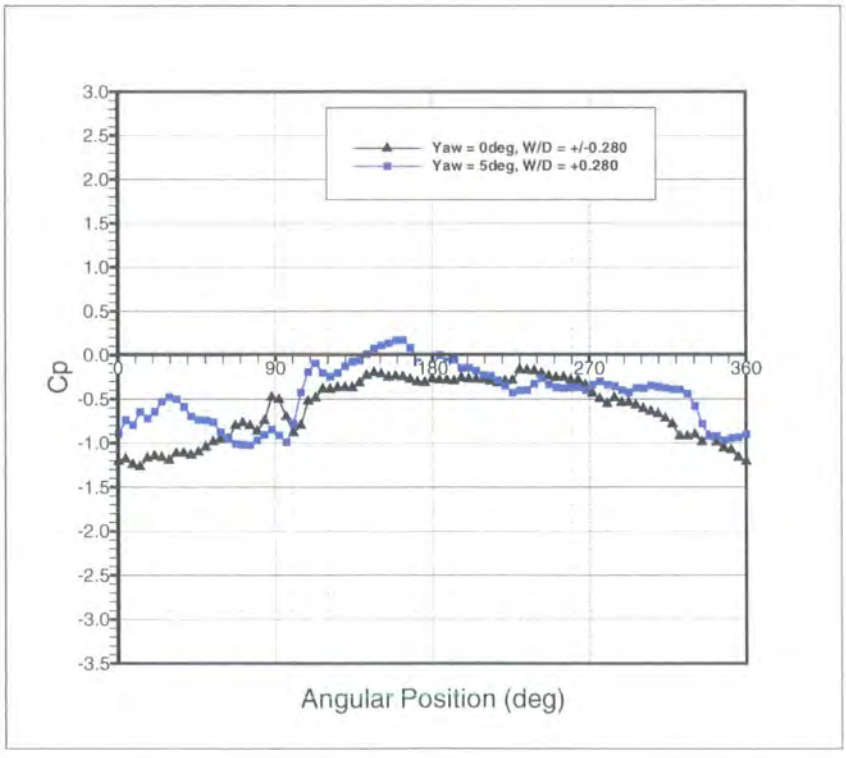


Figure 8.32: Rotating Surface Static Pressure Distribution for Tapping +10 at Yaw Angles ($\beta$) of 0 and 5 degrees.

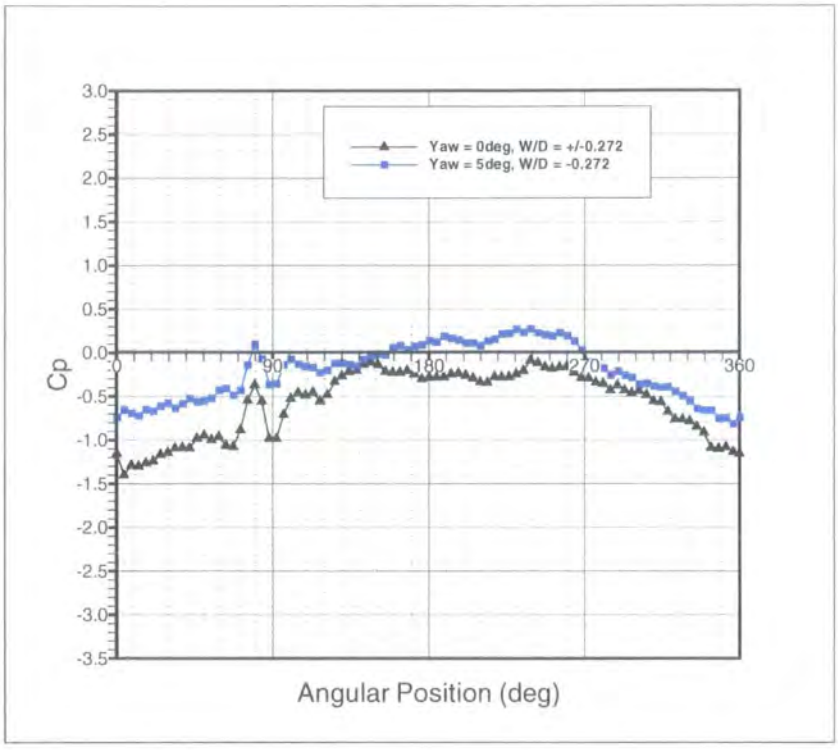


Figure 8.33: Rotating Surface Static Pressure Distribution for Tapping -11 at Yaw Angles ($\beta$) of 0 and 5 degrees.

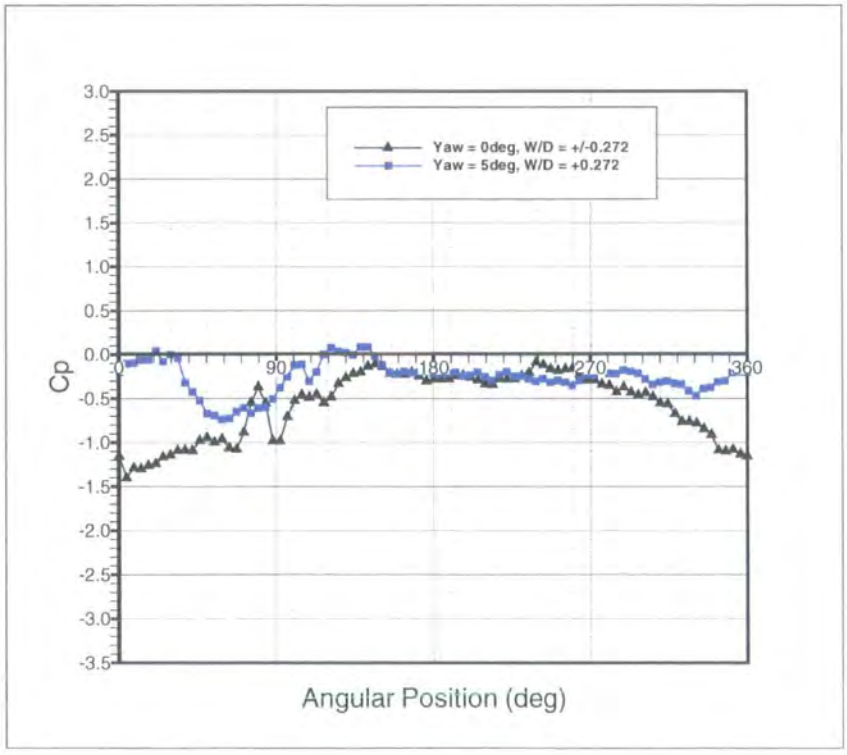


Figure 8.34: Rotating Surface Static Pressure Distribution for Tapping +11 at Yaw Angles ($\beta$) of 0 and 5 degrees.

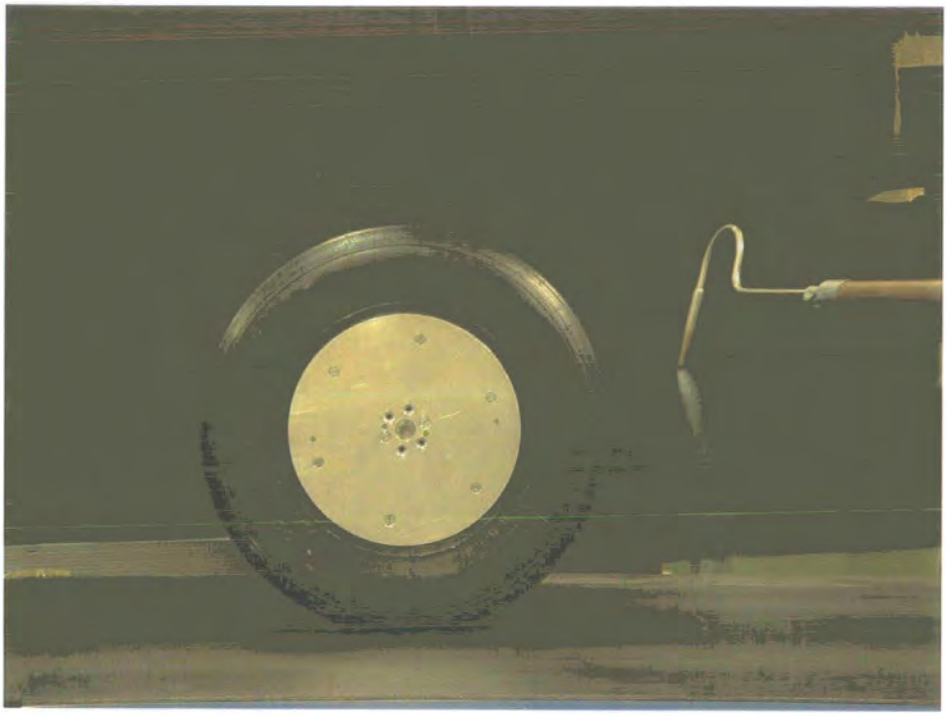

Figure 8.35: Smoke Flow Visualisation for the Stationary Wheel with the Smoke Probe Positioned on the Centreline at 200 degrees.

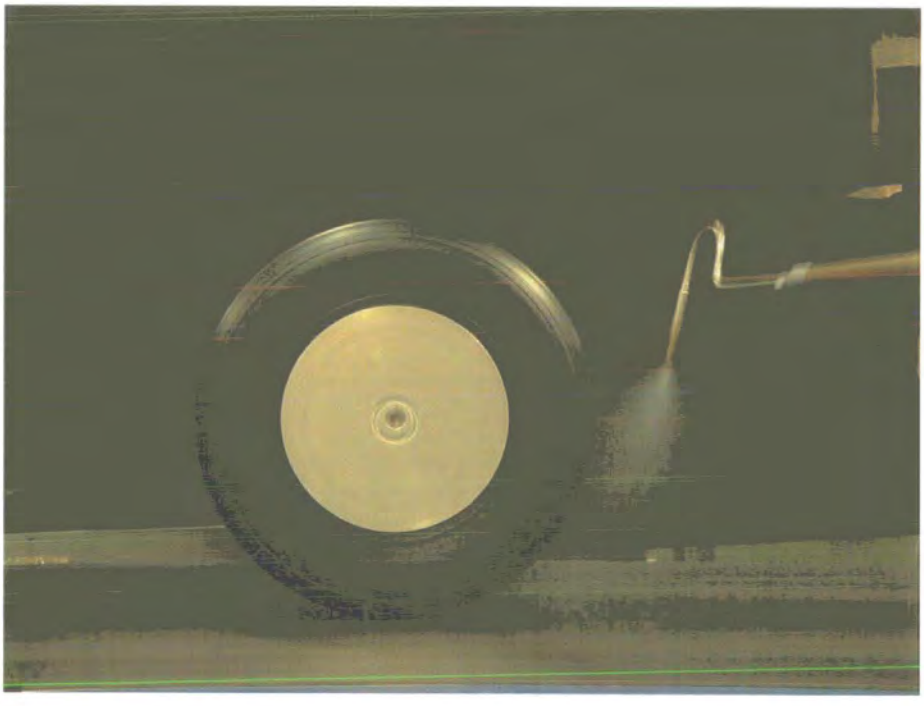

Figure 8.36: Smoke Flow Visualisation for the Rotating Wheel with the Smoke Probe Positioned on the Centreline at 200 degrees.

Figure 8.37: Smoke Flow Visualisation for the Stationary Wheel with the Smoke Probe Positioned on the Centreline at 225 degrees.

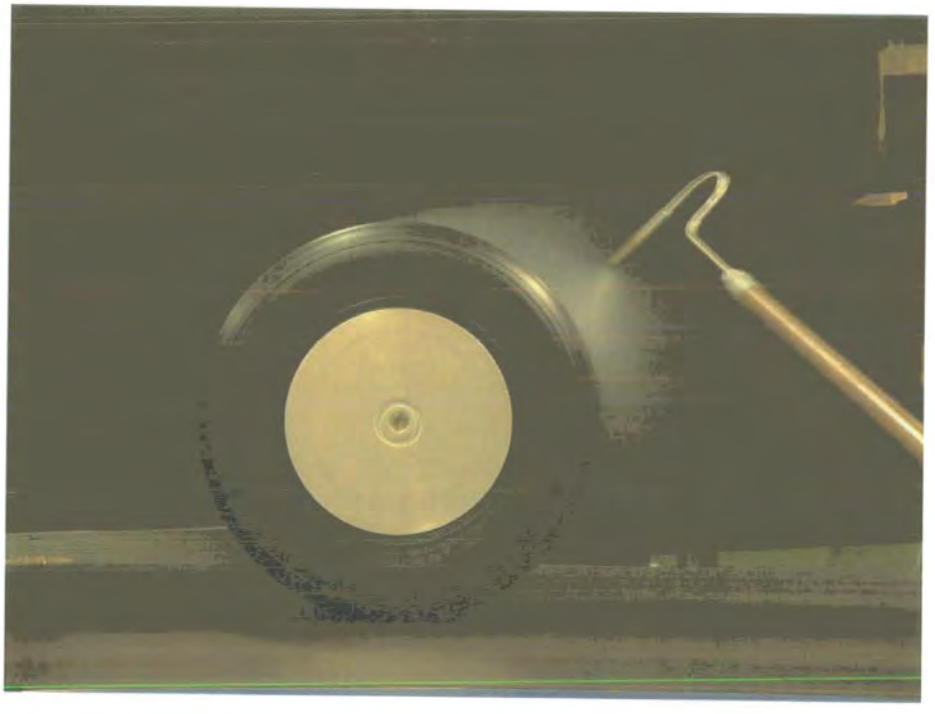

Figure 8.38: Smoke Flow Visualisation for the Rotating Wheel with the Smoke Probe Positioned on the Centreline at 225 degrees.

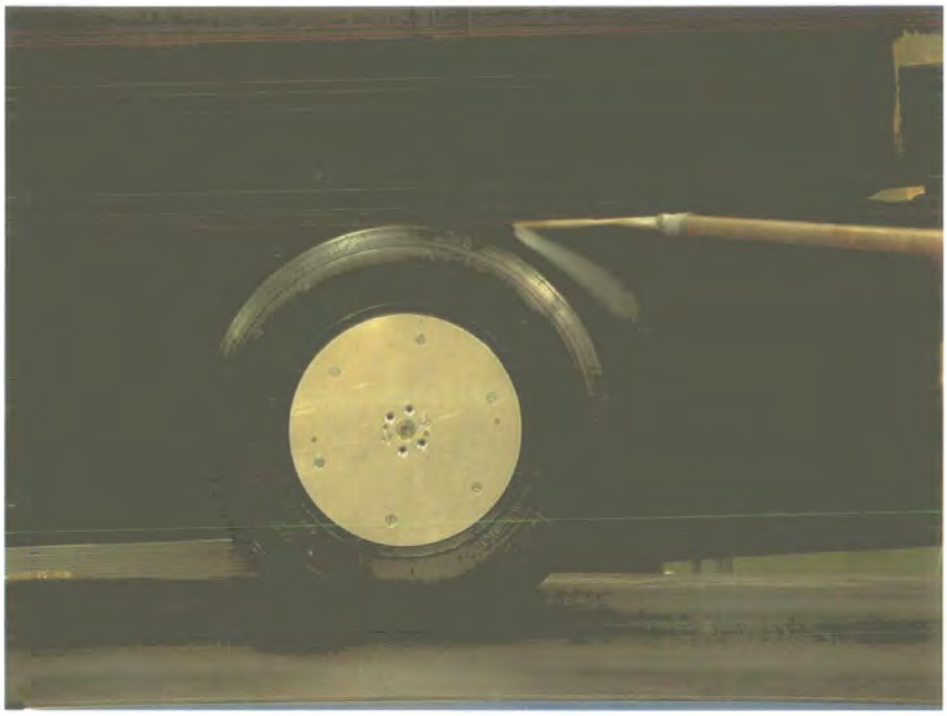

Figure 8.39: Smoke Flow Visualisation for the Stationary Wheel with the Smoke Probe Positioned on the Centreline at 250 degrees.

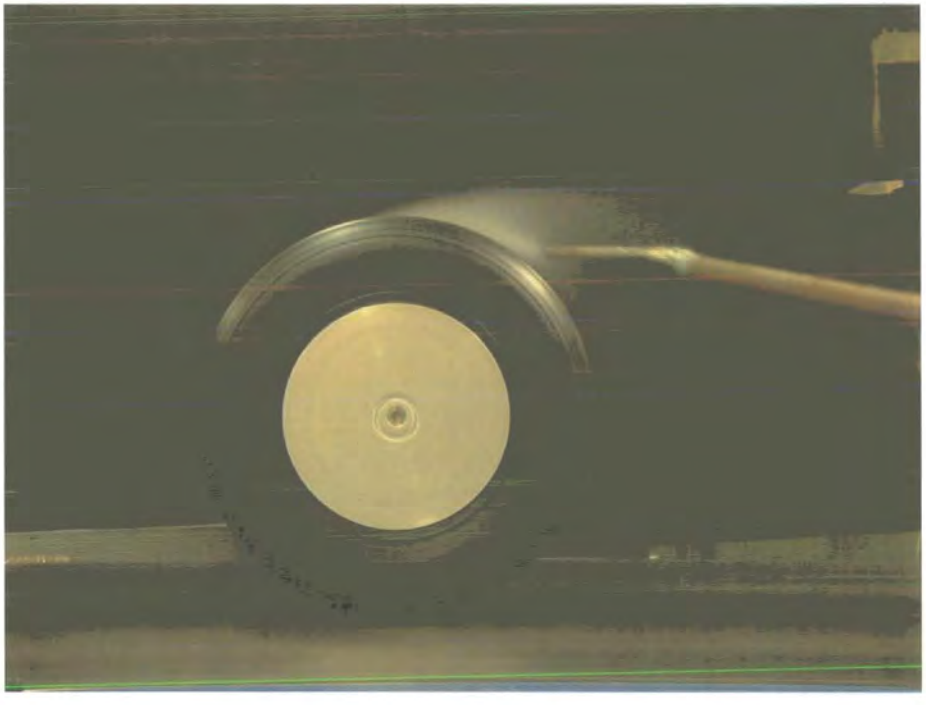

Figure 8.40: Smoke Flow Visualisation for the Rotating Wheel with the Smoke Probe Positioned on the Centreline at 250 degrees.

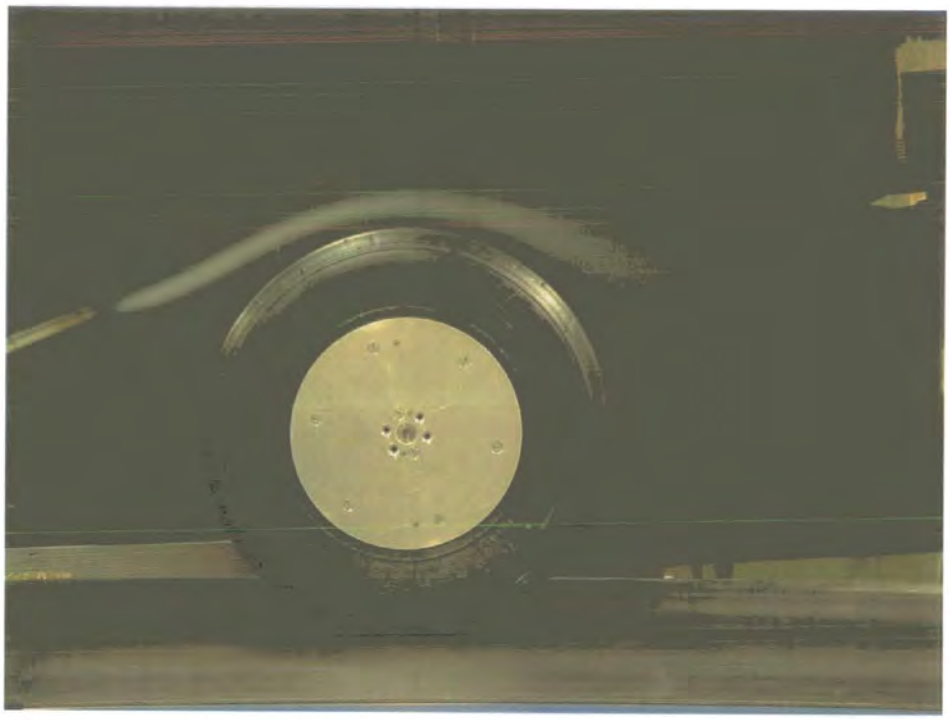

Figure 8.41: Smoke Flow Visualisation for the Stationary Wheel with the Smoke Probe Positioned on the Centreline at 340 degrees.

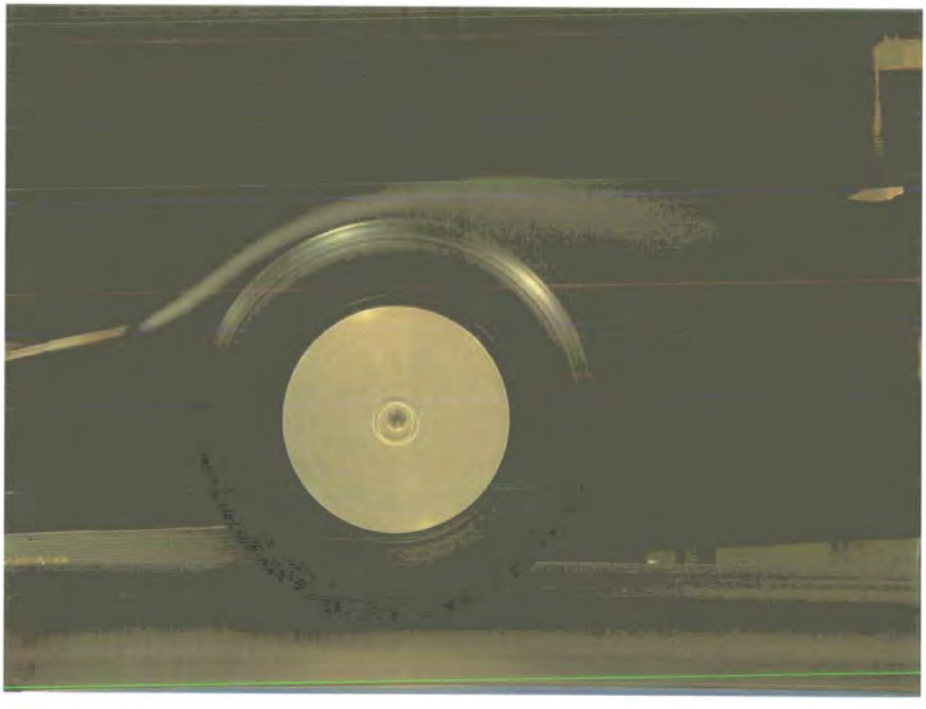

Figure 8.42: Smoke Flow Visualisation for the Rotating Wheel with the Smoke Probe Positioned on the Centreline at 340 degrees.

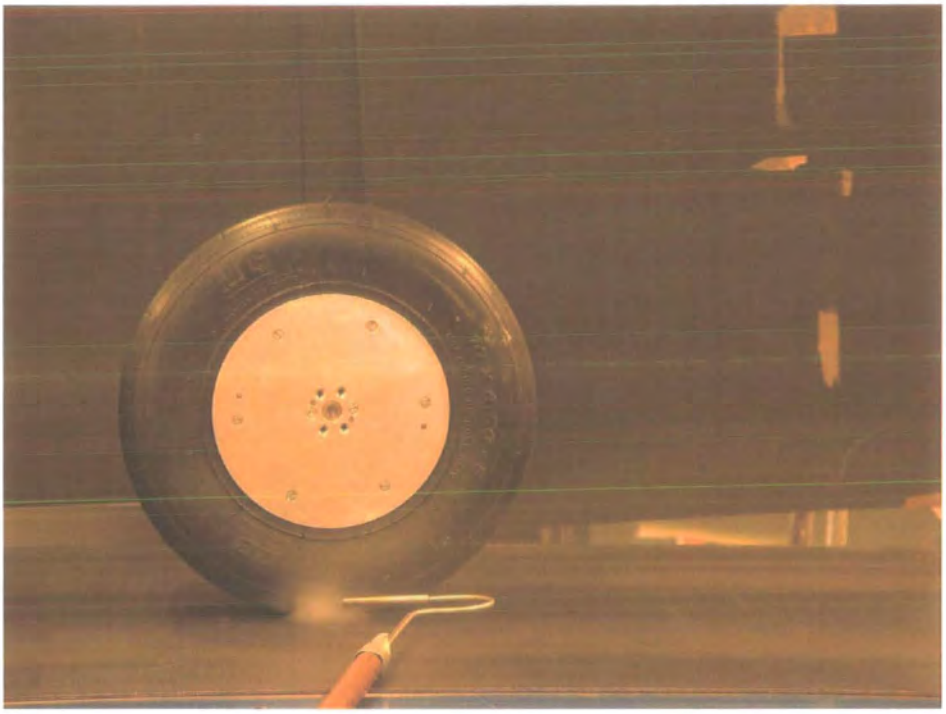

Figure 8.43: Smoke Flow Visualisation near the Contact Patch, Stationary

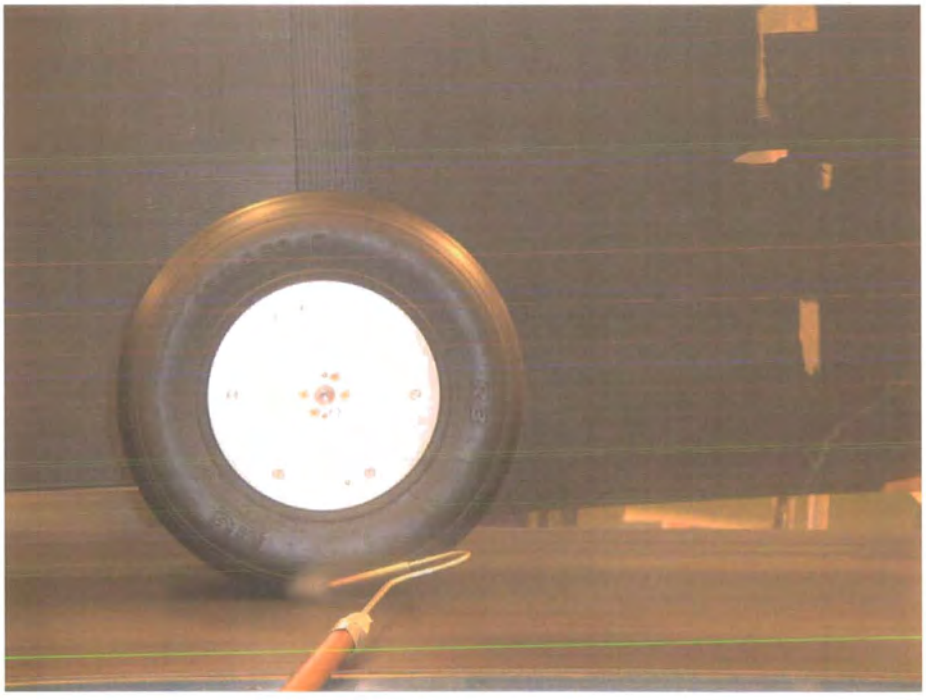

Figure 8.44: Smoke Flow Visualisation near the Contact Patch, Rotating

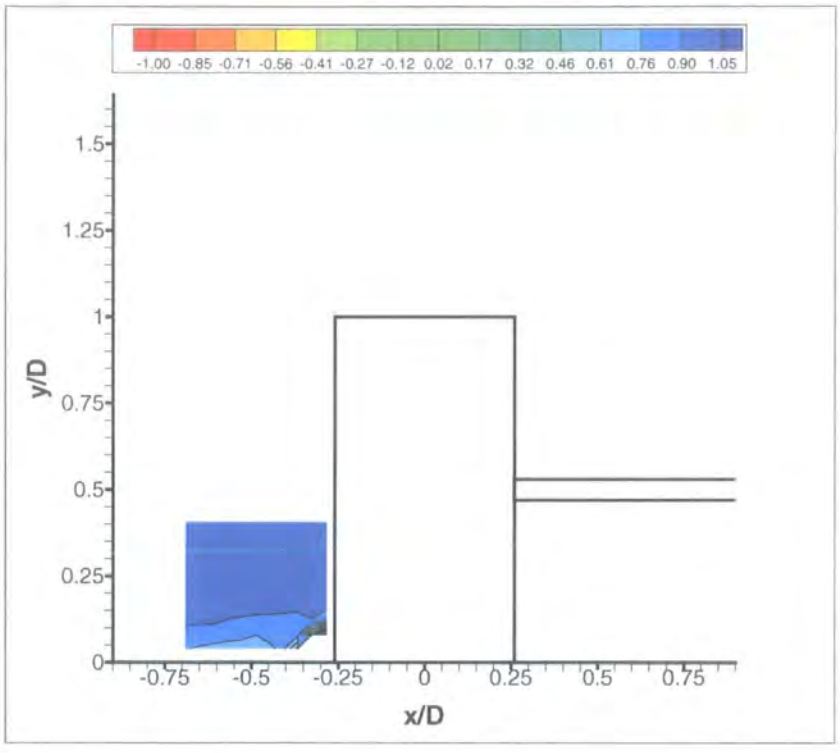


Figure 8.45: Time-Averaged Contours of Constant Total Pressure Coefficient, Rotating, XY Plane @ Z = 0D.

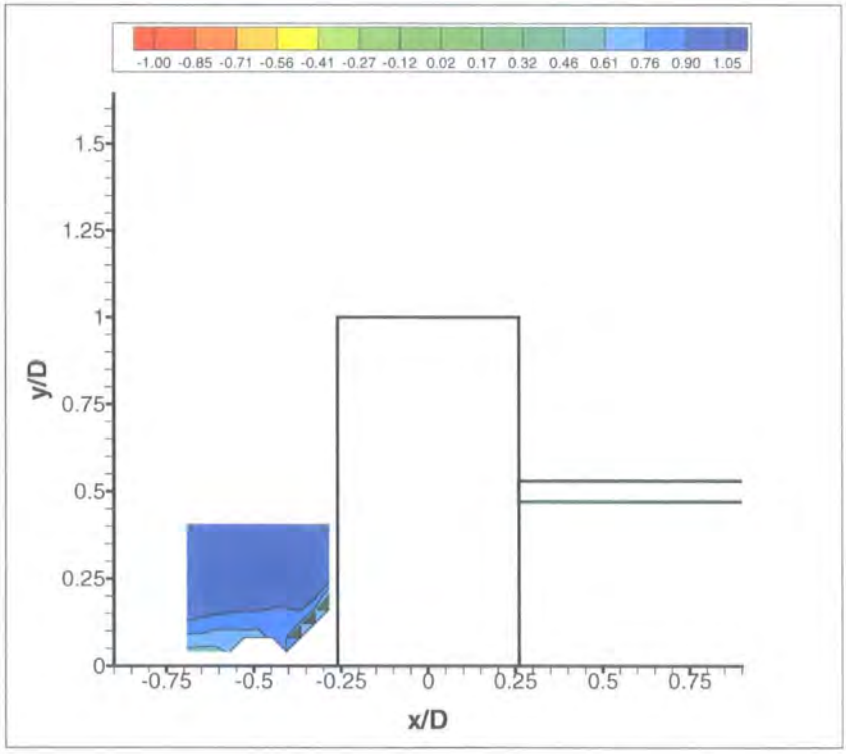


Figure 8.46: Time-Averaged Contours of Constant Total Pressure Coefficient, Stationary, XY Plane @ Z = 0D.

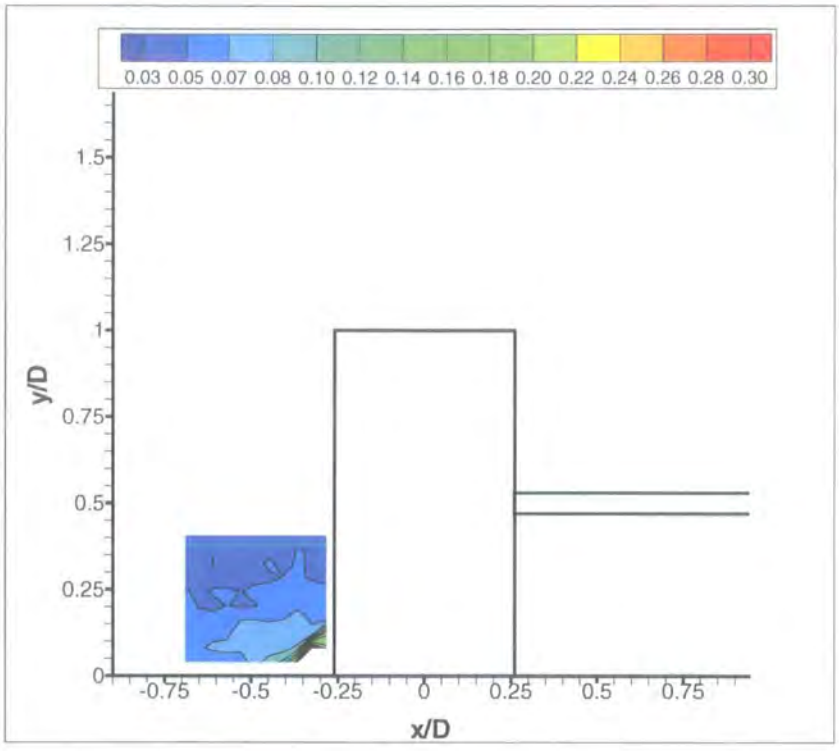


Figure 8.47: Time-Averaged Contours of Constant Standard Deviation for Dynamic Pressure Coefficient, Rotating, XY Plane @ Z = 0D.

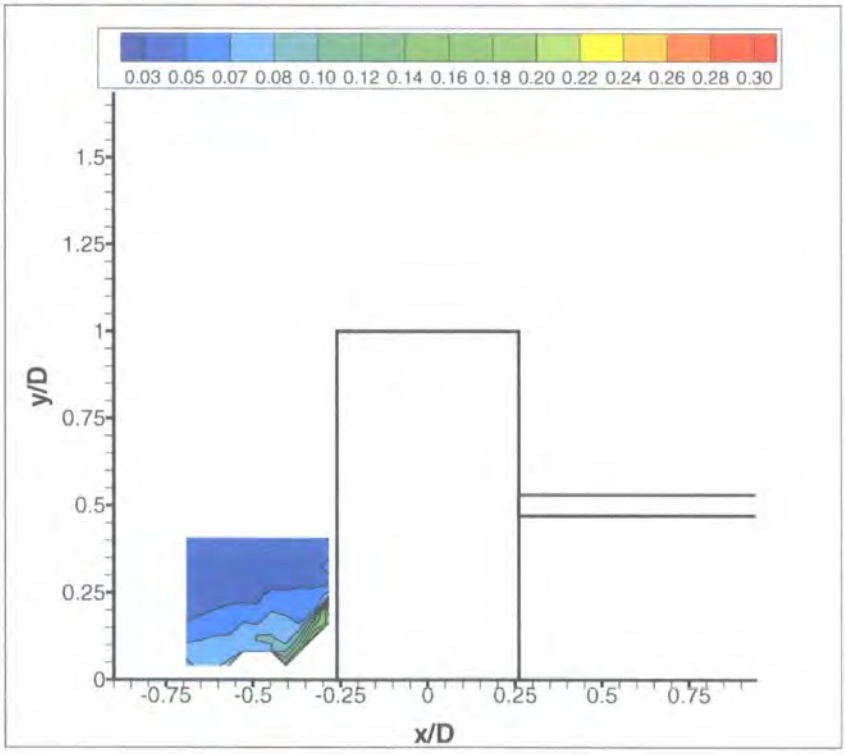


Figure 8.48: Time-Averaged Contours of Constant Standard Deviation for Dynamic Pressure Coefficient, Stationary, XY Plane @ Z = 0D.

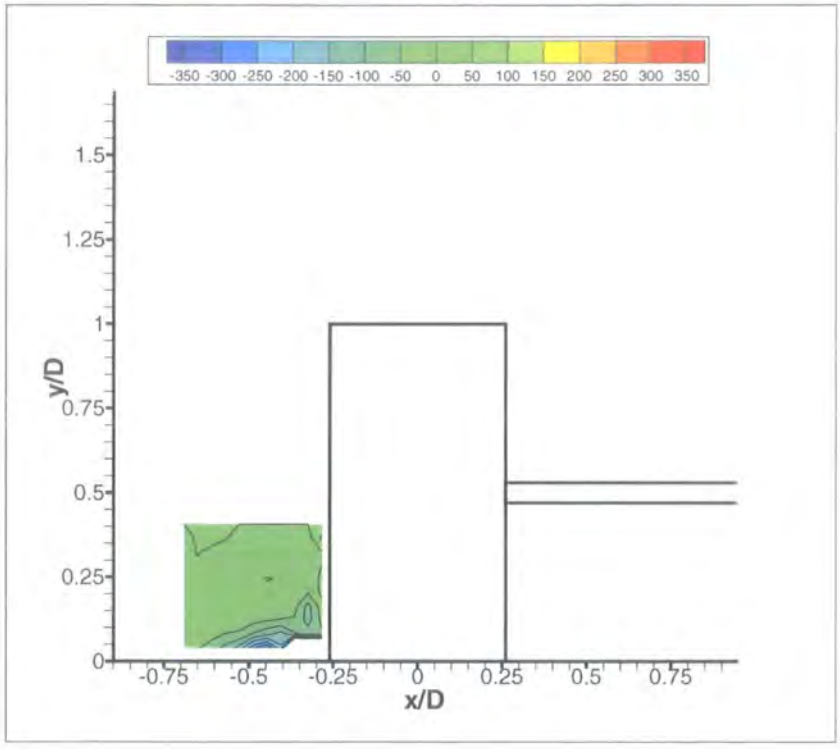


Figure 8.49: Time-Averaged Contours of Constant Streamwise Vorticity ($\xi$), Rotating, XY Plane @ Z = 0D.

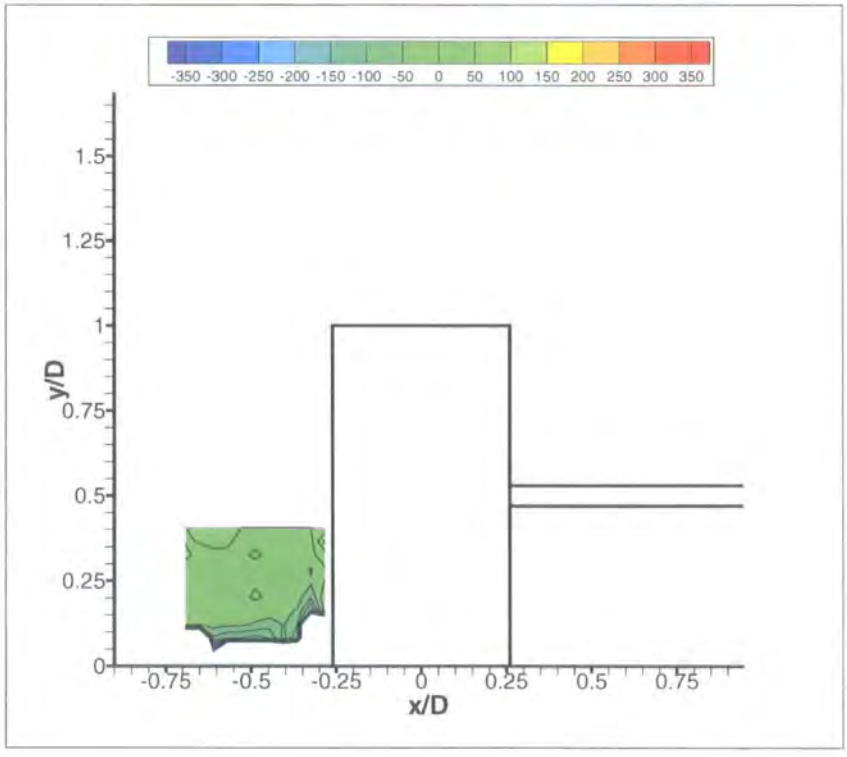


Figure 8.50: Time-Averaged Contours of Constant Streamwise Vorticity ($\xi$), Stationary, XY Plane @ Z = 0D.

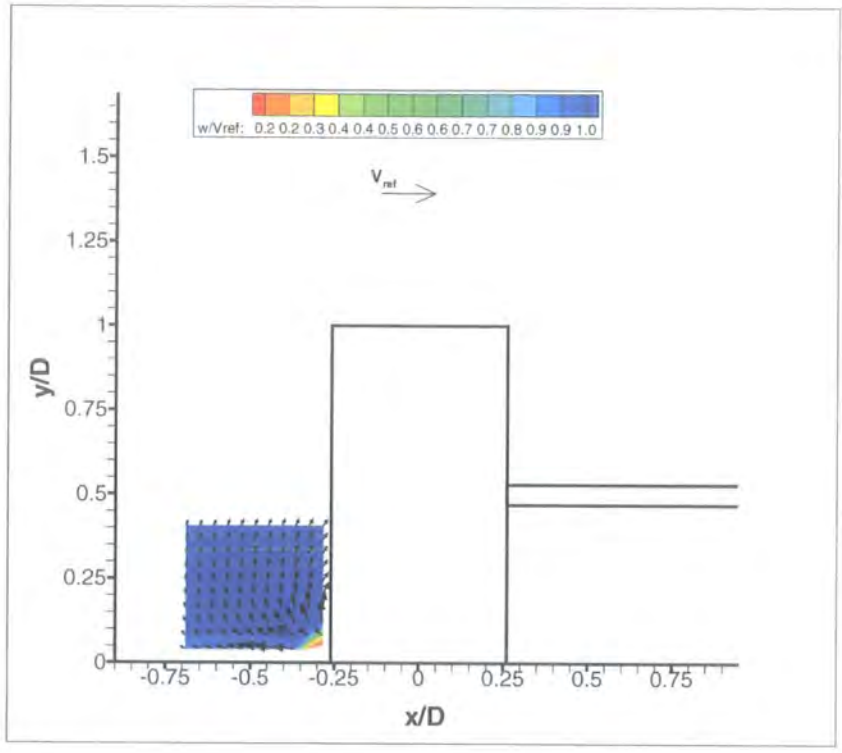


Figure 8.51: Time-Averaged Secondary Flow Velocity Vectors Coloured by Contours of $w/V_{ref}$ Velocity, Rotating, XY Plane @ Z = 0D.

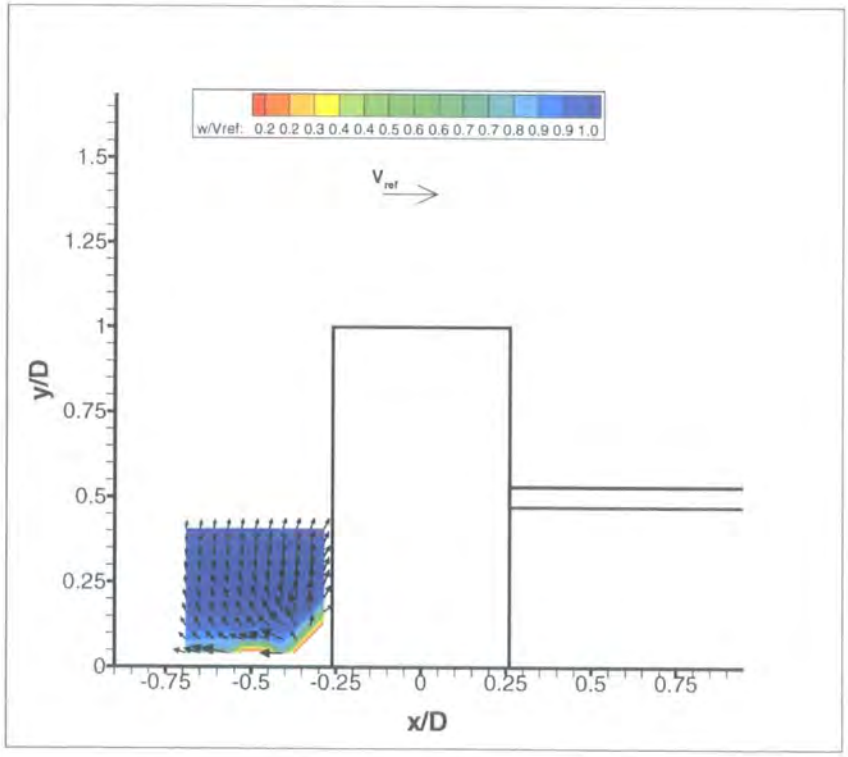


Figure 8.52: Time-Averaged Secondary Flow Velocity Vectors Coloured by Contours of $w/V_{ref}$ Velocity, Stationary, XY Plane @ Z = 0D.

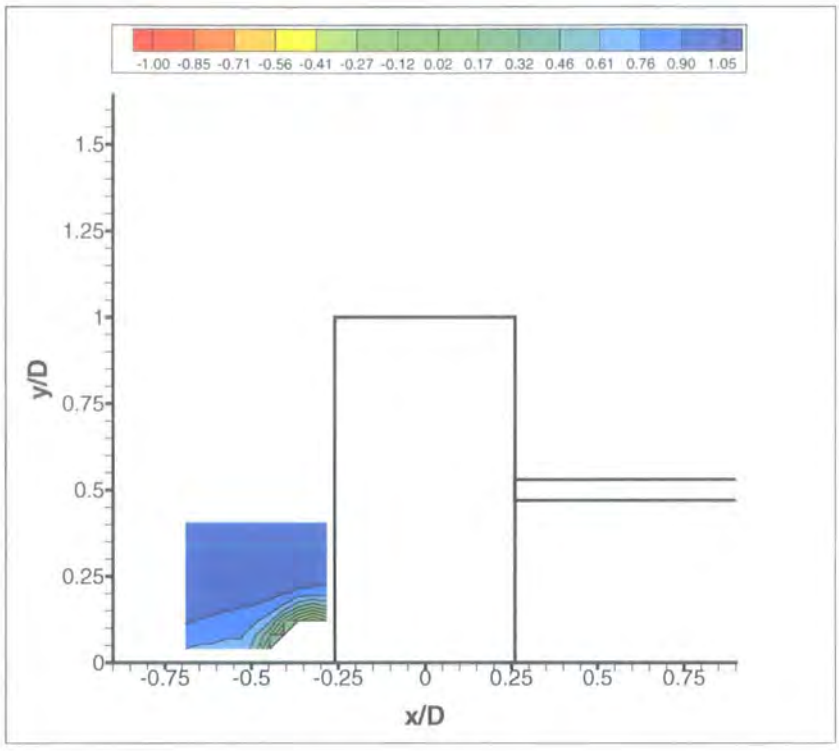


Figure 8.53: Time-Averaged Contours of Constant Total Pressure Coefficient, Rotating, XY Plane @ Z = 0.25D.

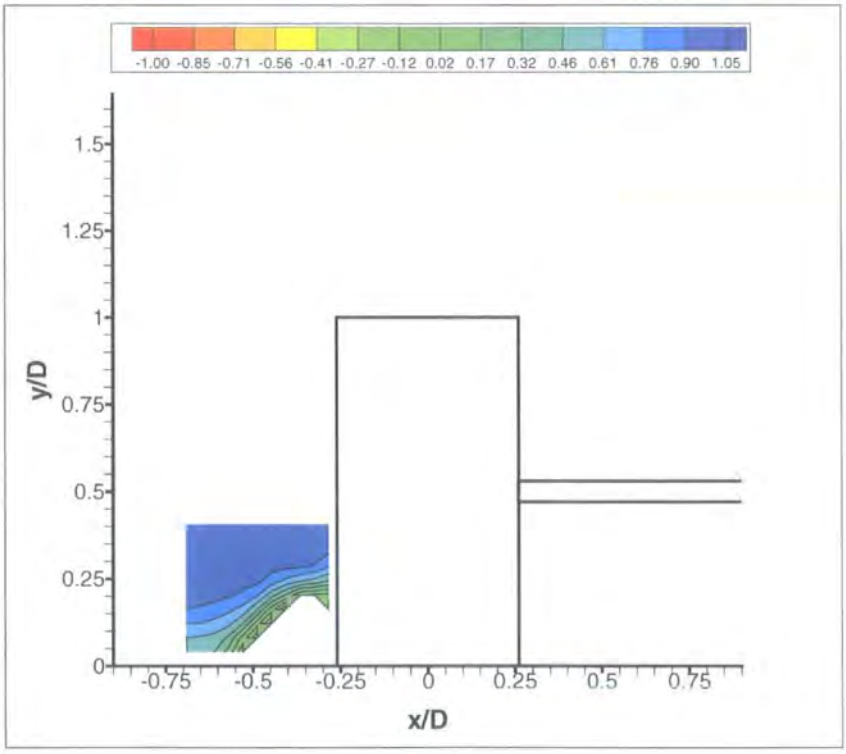


Figure 8.54: Time-Averaged Contours of Constant Total Pressure Coefficient, Stationary, XY Plane @ Z = 0.25D.

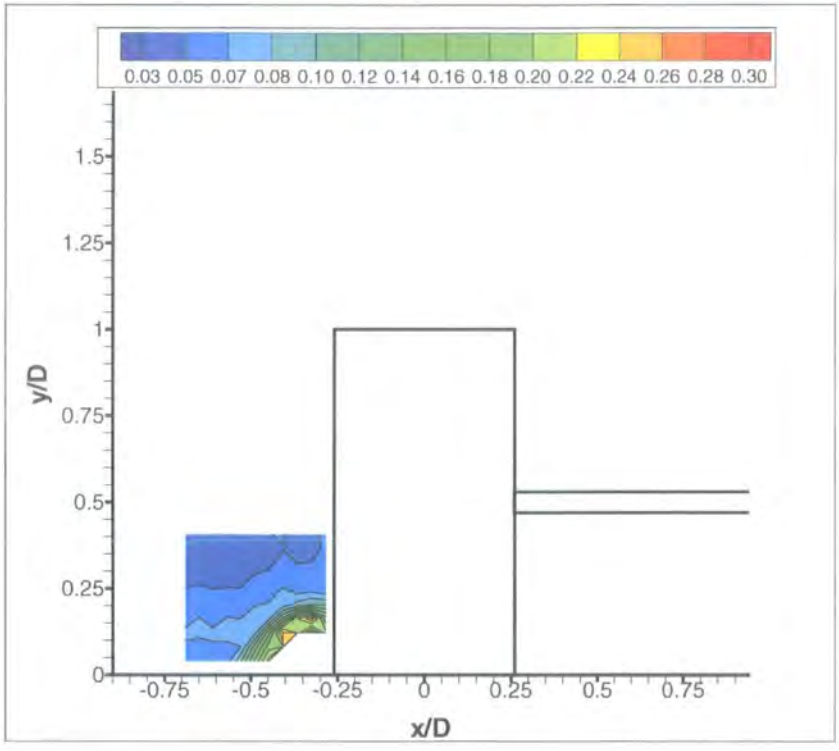


Figure 8.55: Time-Averaged Contours of Constant Standard Deviation for Dynamic Pressure Coefficient, Rotating, XY Plane @ Z = 0.25D.

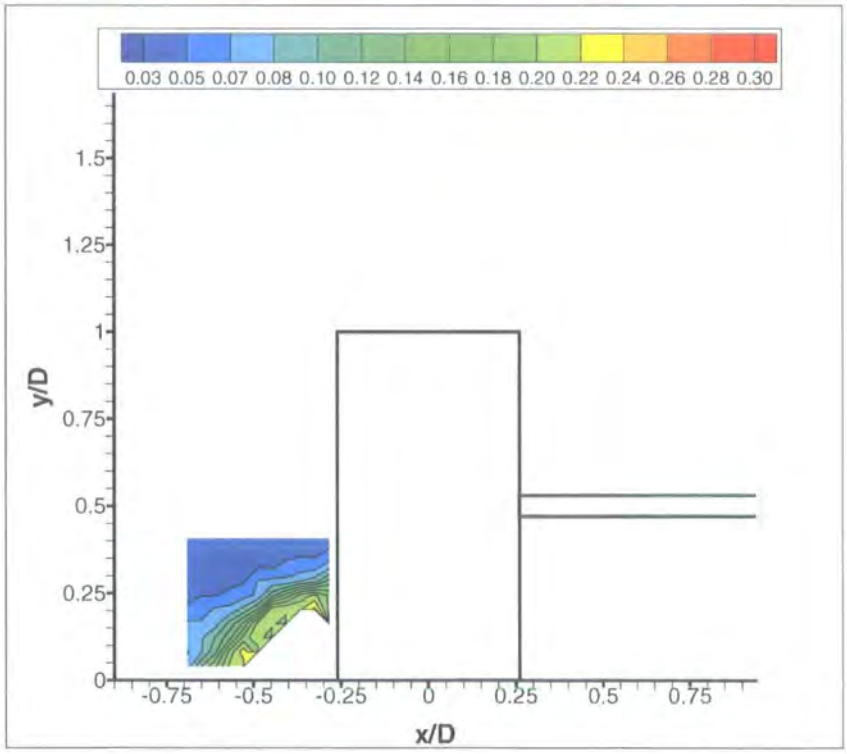


Figure 8.56: Time-Averaged Contours of Constant Standard Deviation for Dynamic Pressure Coefficient, Stationary, XY Plane @ Z = 0.25D.

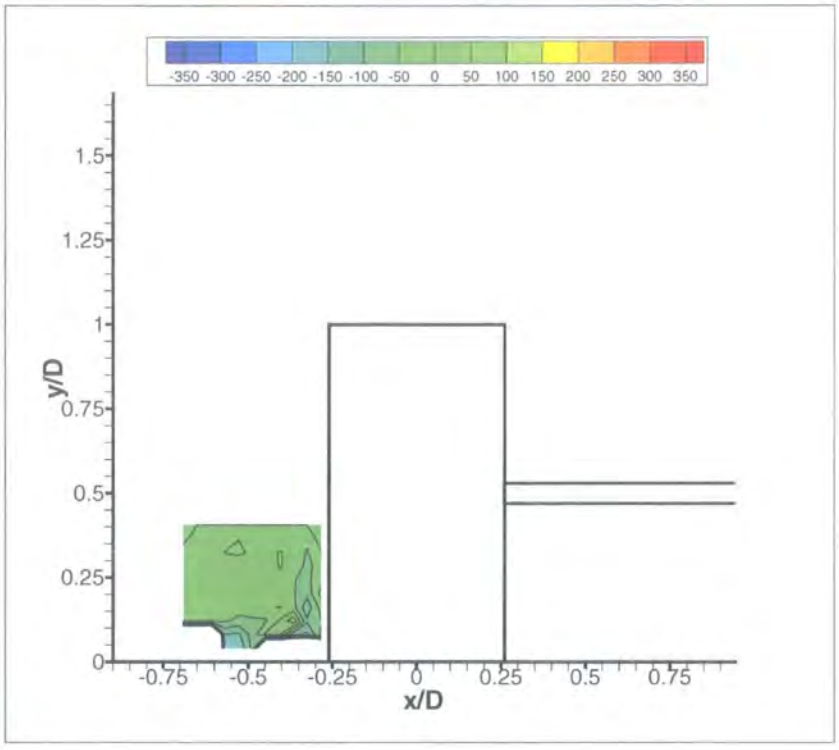


Figure 8.57: Time-Averaged Contours of Constant Streamwise Vorticity ($\xi$), Rotating, XY Plane @ Z = 0.25D.

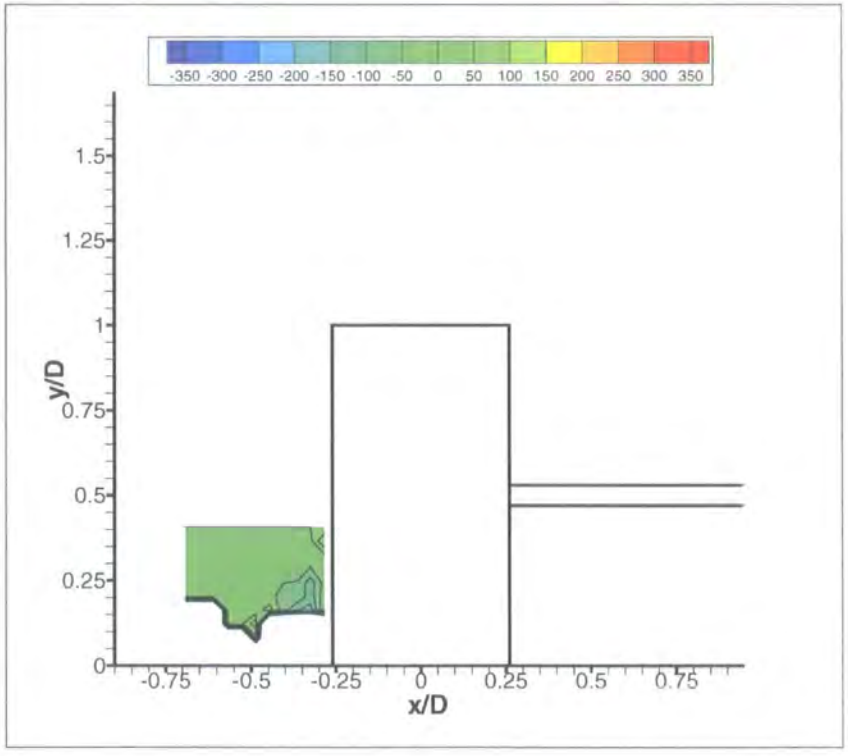


Figure 8.58: Time-Averaged Contours of Constant Streamwise Vorticity ($\xi$), Stationary, XY Plane @ Z = 0.25D.

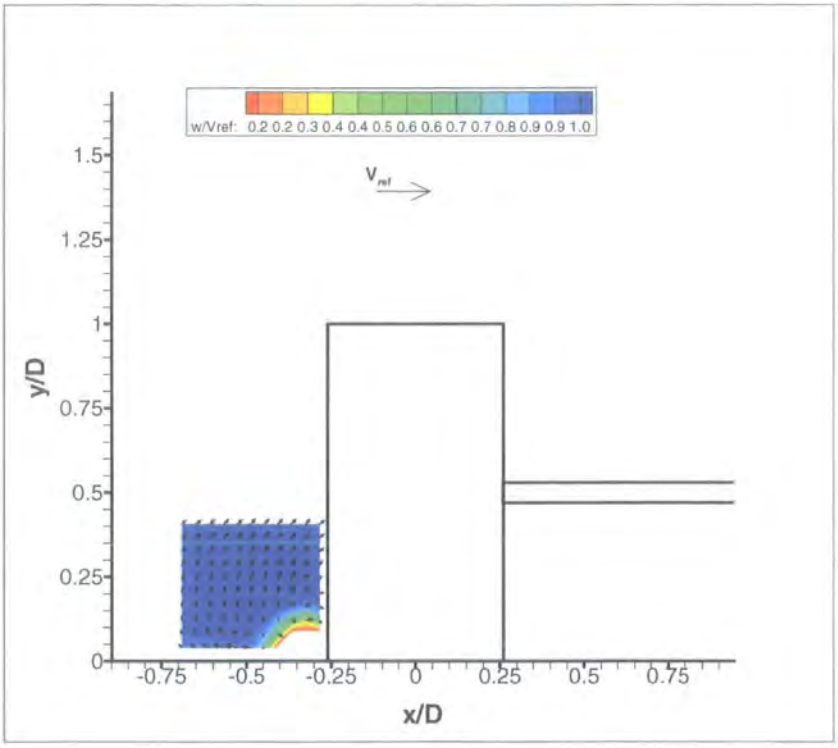


Figure 8.59: Time-Averaged Secondary Flow Velocity Vectors Coloured by Contours of $w/V_{ref}$ Velocity, Rotating, XY Plane @ Z = 0.25D.

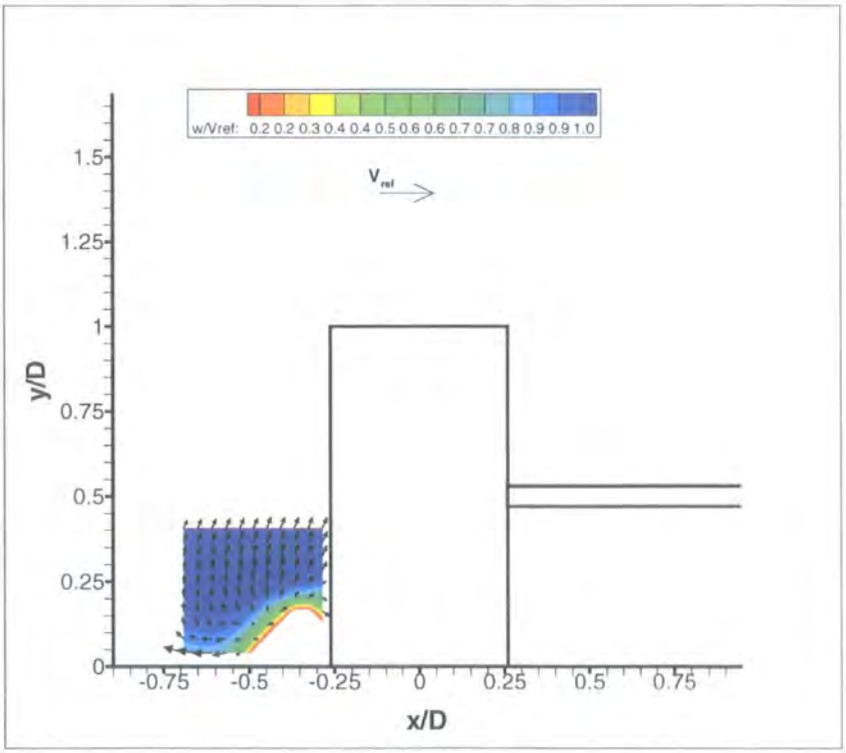


Figure 8.60: Time-Averaged Secondary Flow Velocity Vectors Coloured by Contours of $w/V_{ref}$ Velocity, Stationary, XY Plane @ Z = 0.25D.

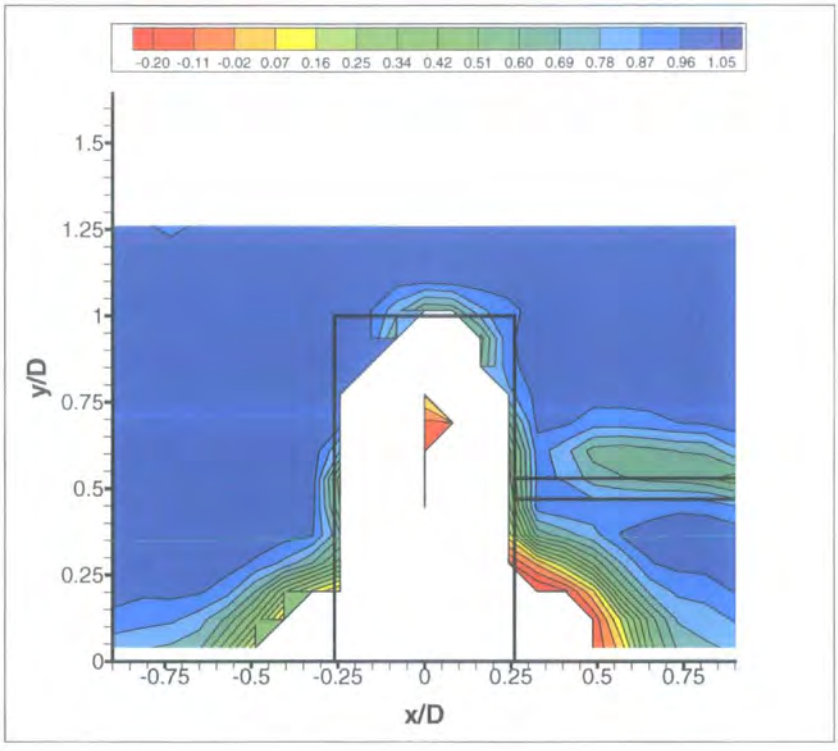


Figure 8.61: Time-Averaged Contours of Constant Total Pressure Coefficient, Rotating, XY Plane @ Z = 0.75D.

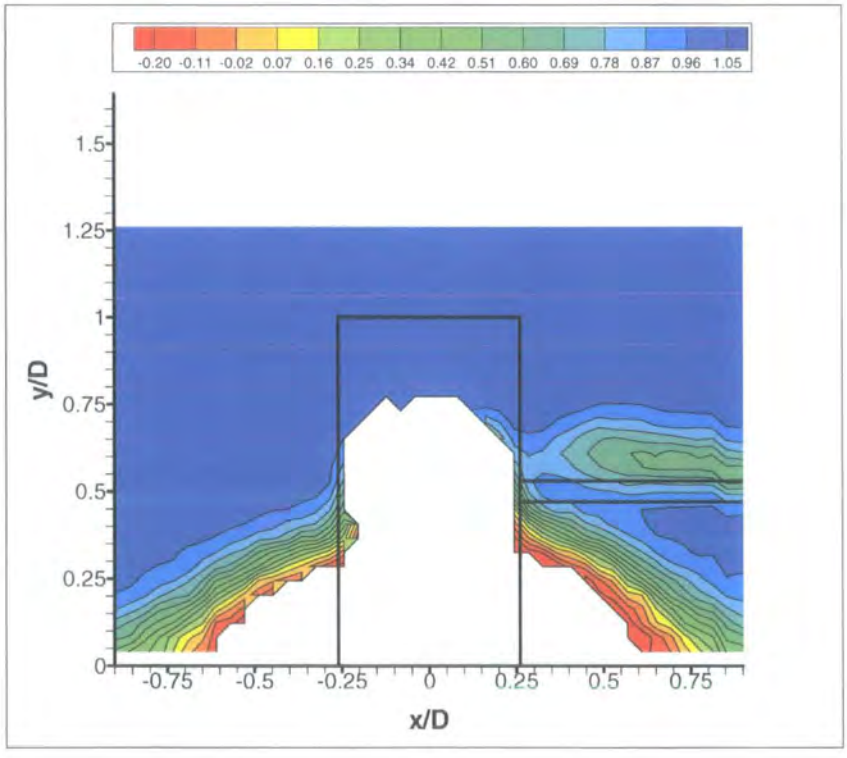


Figure 8.62: Time-Averaged Contours of Constant Total Pressure Coefficient, Stationary, XY Plane @ Z = 0.75D.

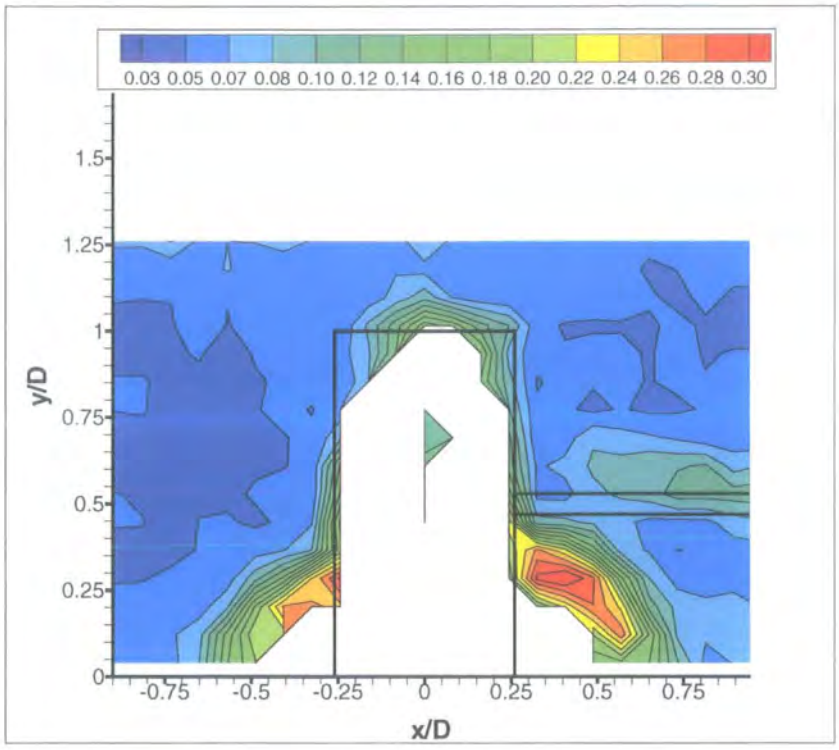


Figure 8.63: Contours of Constant Standard Deviation for Dynamic Pressure Coefficient, Rotating, XY Plane @ Z = 0.75D.

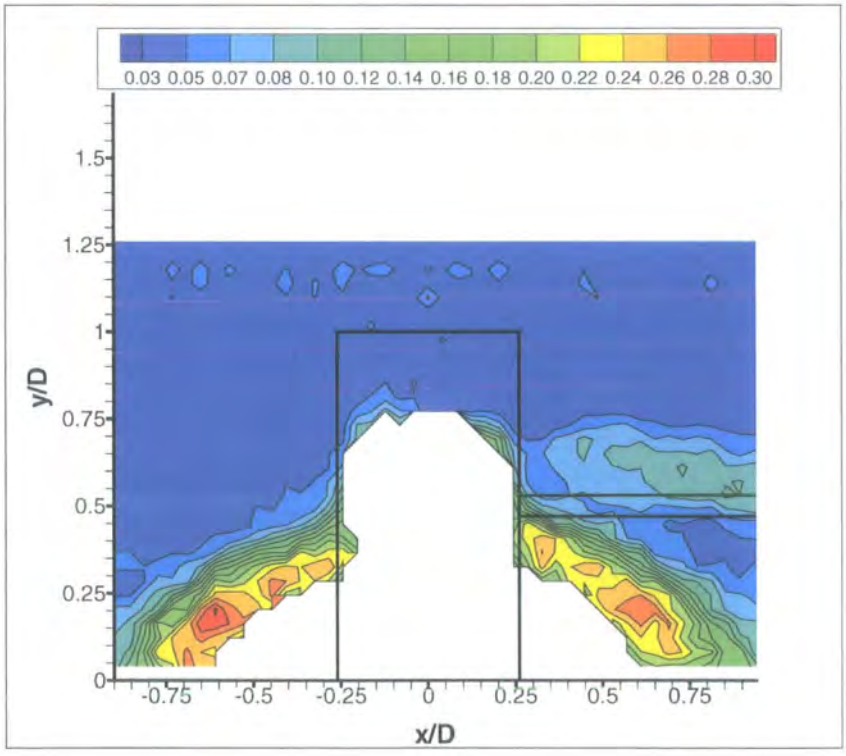


Figure 8.64: Contours of Constant Standard Deviation for Dynamic Pressure Coefficient, Stationary, XY Plane @ Z = 0.75D.

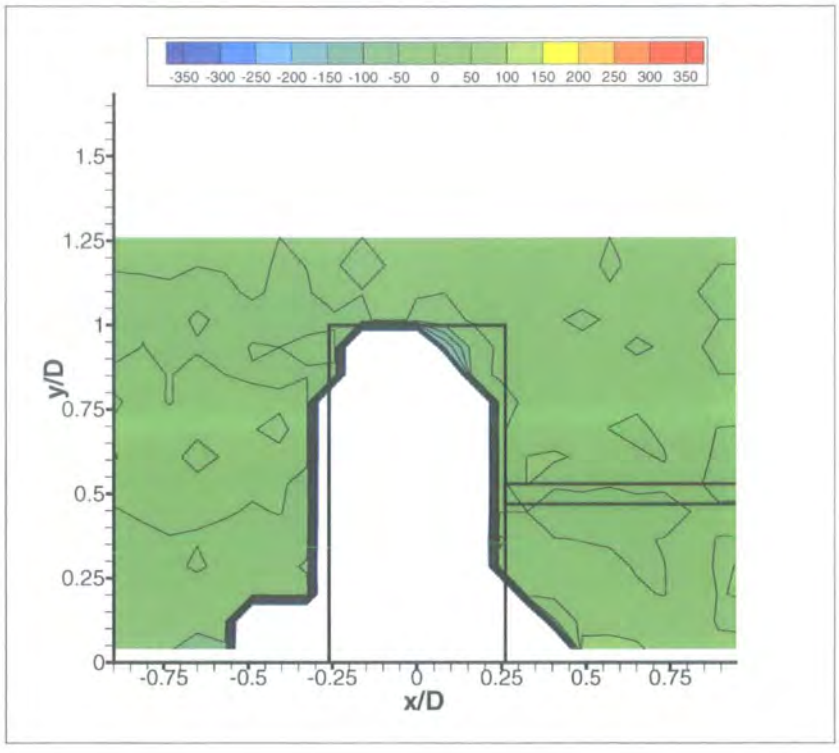


Figure 8.65: Time-Averaged Contours of Constant Streamwise Vorticity ($\xi$), Rotating, XY Plane @ Z = 0.75D.

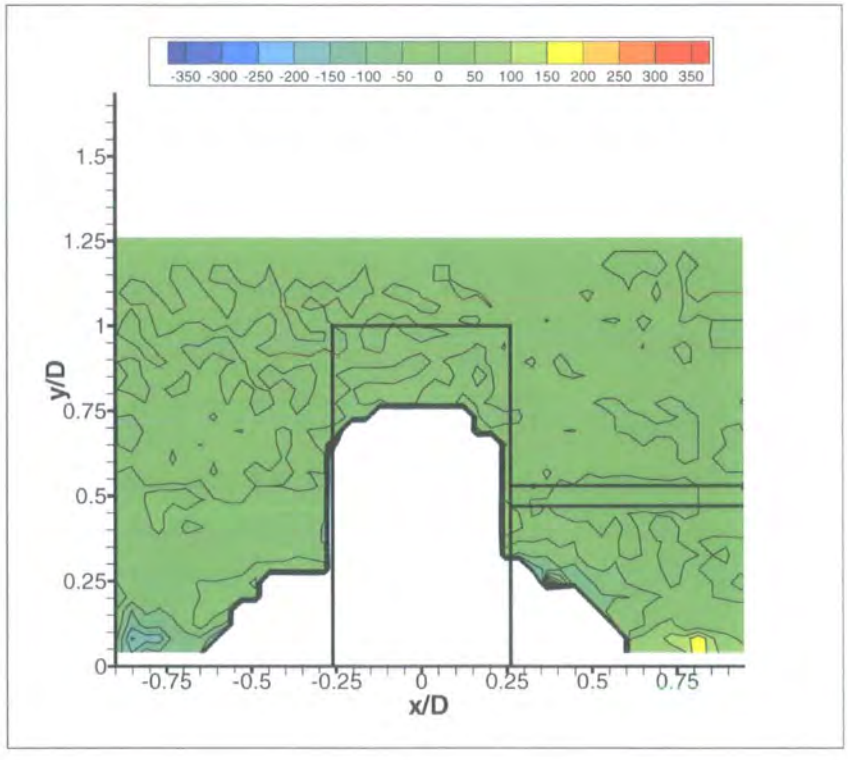


Figure 8.66: Time-Averaged Contours of Constant Streamwise Vorticity ($\xi$), Stationary, XY Plane @ Z = 0.75D.

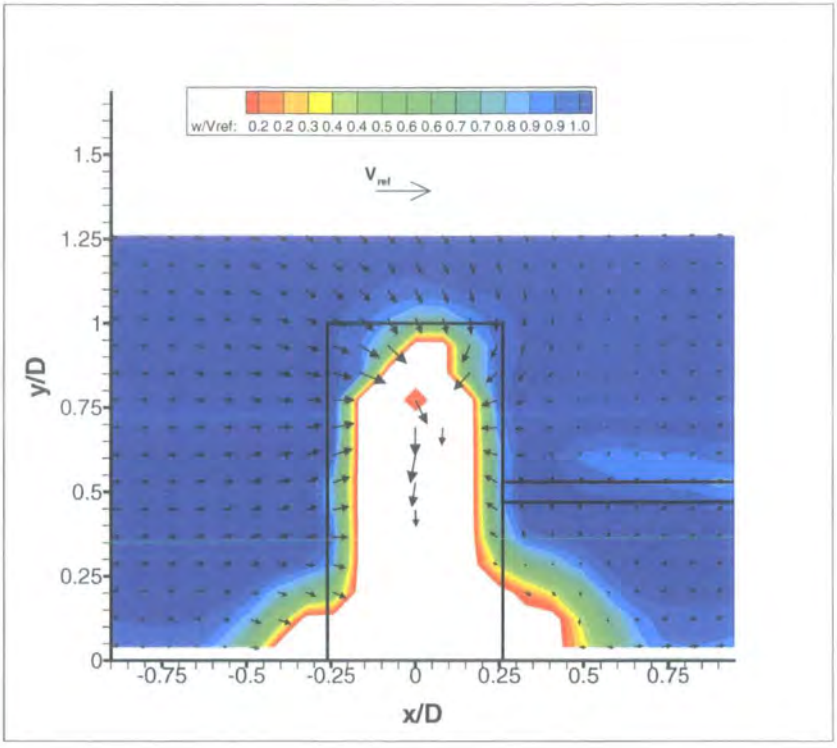


Figure 8.67: Time-Averaged Secondary Flow Velocity Vectors Coloured by Contours of $w/V_{ref}$ Velocity, Rotating, XY Plane @ Z = 0.75D.

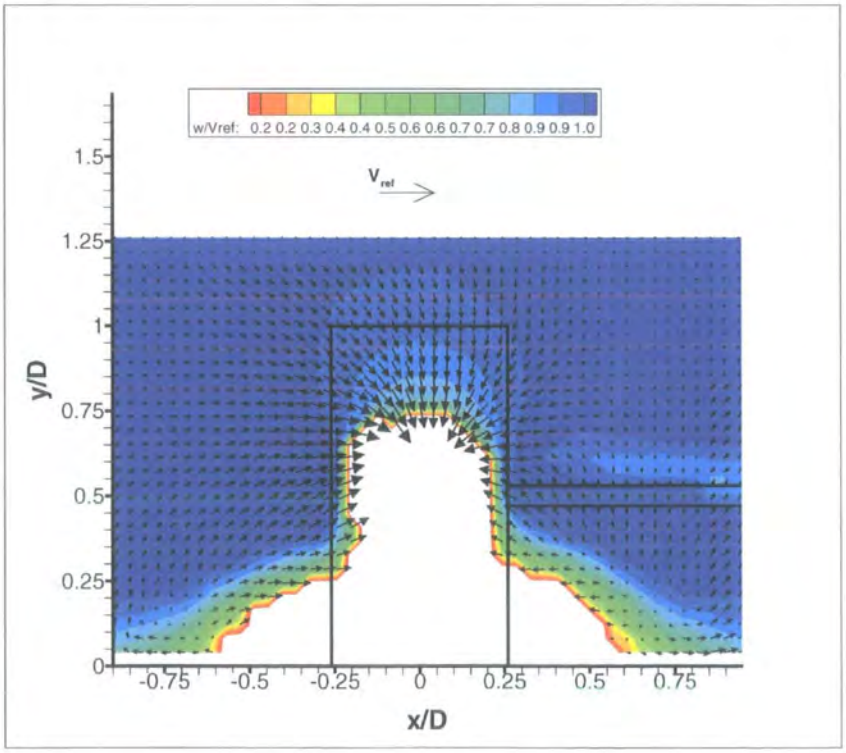


Figure 8.68: Time-Averaged Secondary Flow Velocity Vectors Coloured by Contours of $w/V_{ref}$ Velocity, Stationary, XY Plane @ Z = 0.75D.

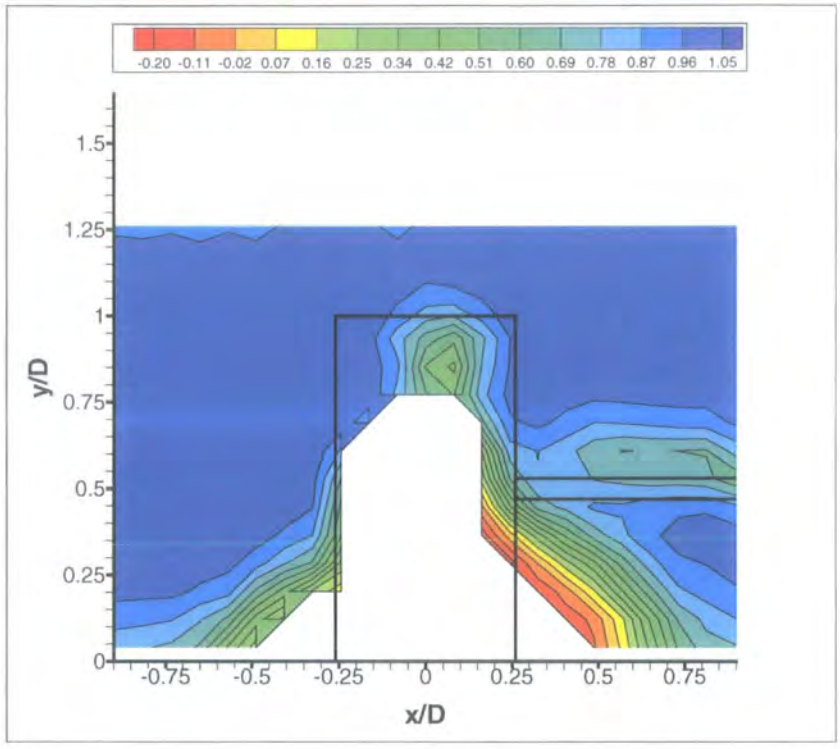


Figure 8.69: Time-Averaged Contours of Constant Total Pressure Coefficient, Rotating, XY Plane @ Z = 1.0D.

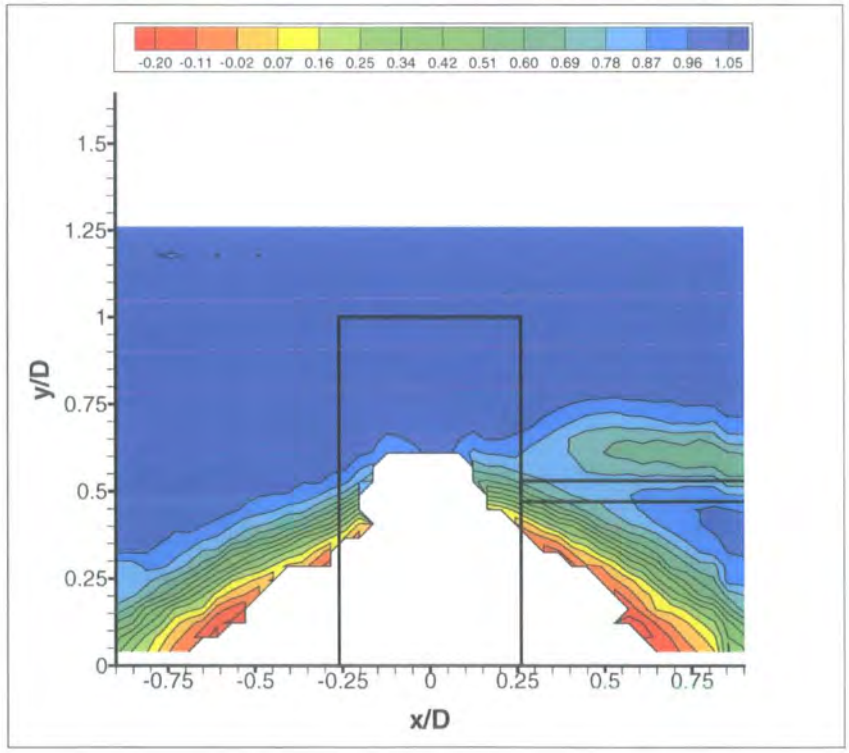


Figure 8.70: Time-Averaged Contours of Constant Total Pressure Coefficient, Stationary, XY Plane @ Z = 1.0D.

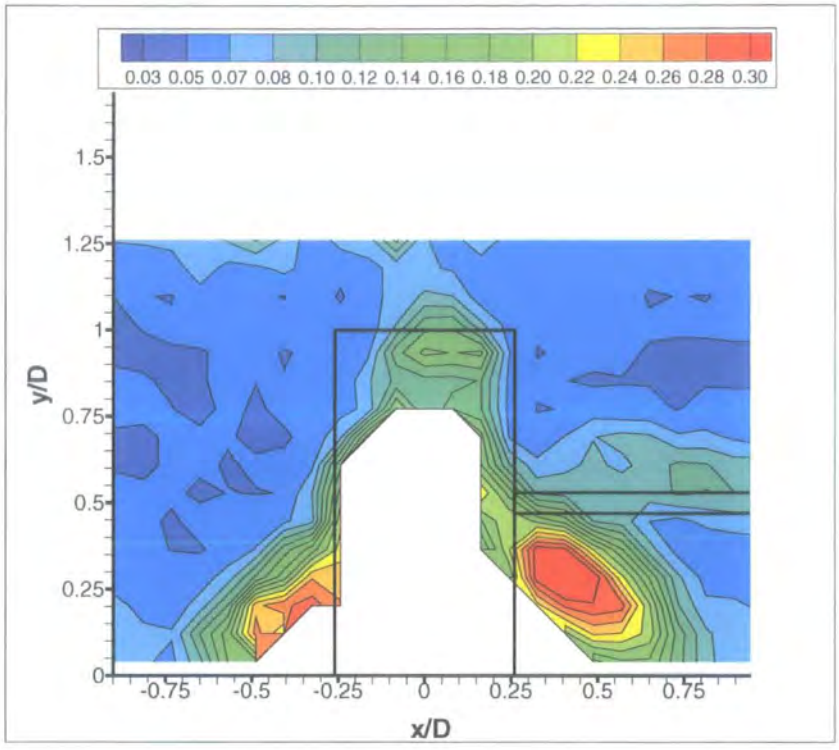


Figure 8.71: Time-Averaged Contours of Constant Standard Deviation for Dynamic Pressure Coefficient, Rotating, XY Plane @ Z = 1.0D.

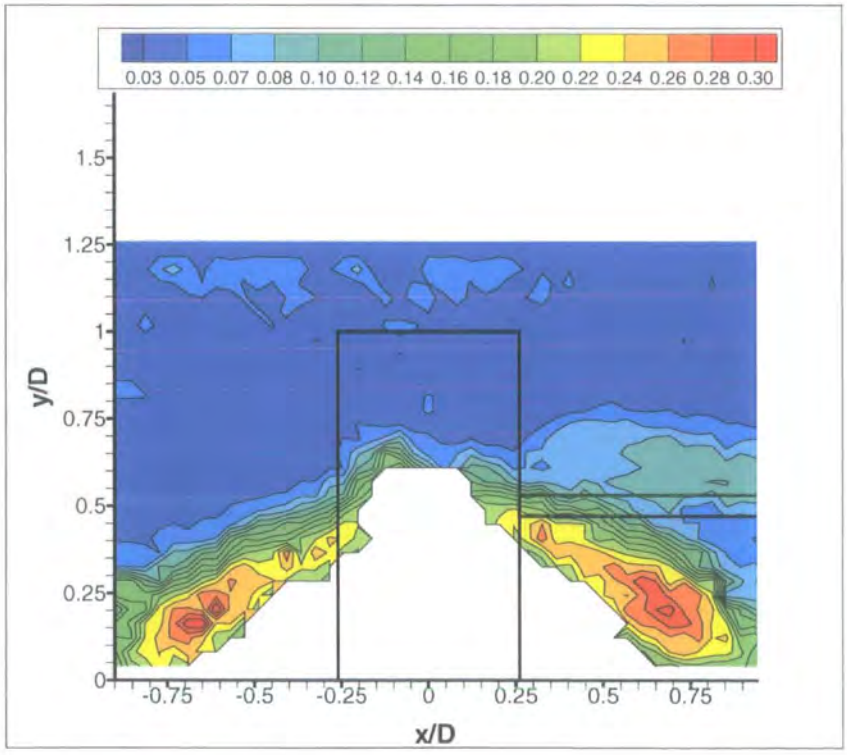


Figure 8.72: Time-Averaged Contours of Constant Standard Deviation for Dynamic Pressure Coefficient, Stationary, XY Plane @ Z = 1.0D.

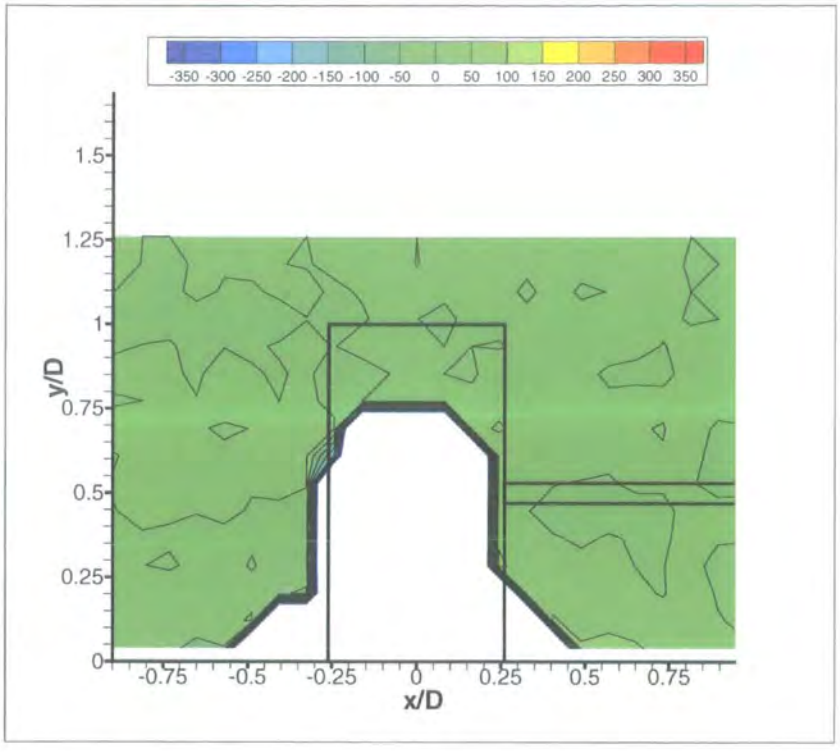


Figure 8.73: Time-Averaged Contours of Constant Streamwise Vorticity ($\xi$), Rotating, XY Plane @ Z = 1.0D.

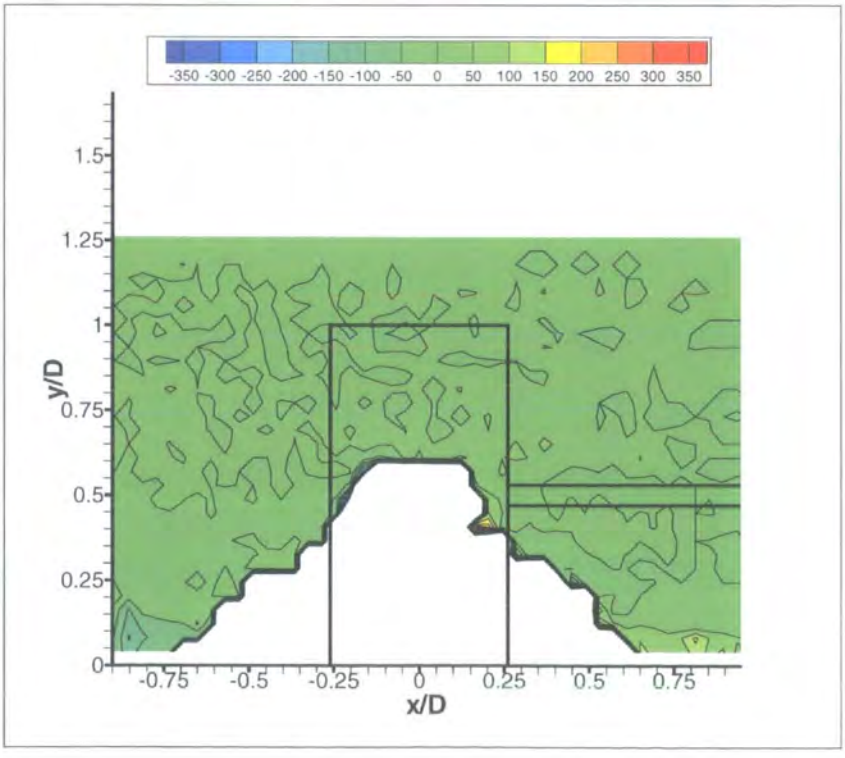


Figure 8.74: Time-Averaged Contours of Constant Streamwise Vorticity ($\xi$), Stationary, XY Plane @ Z = 1.0D.

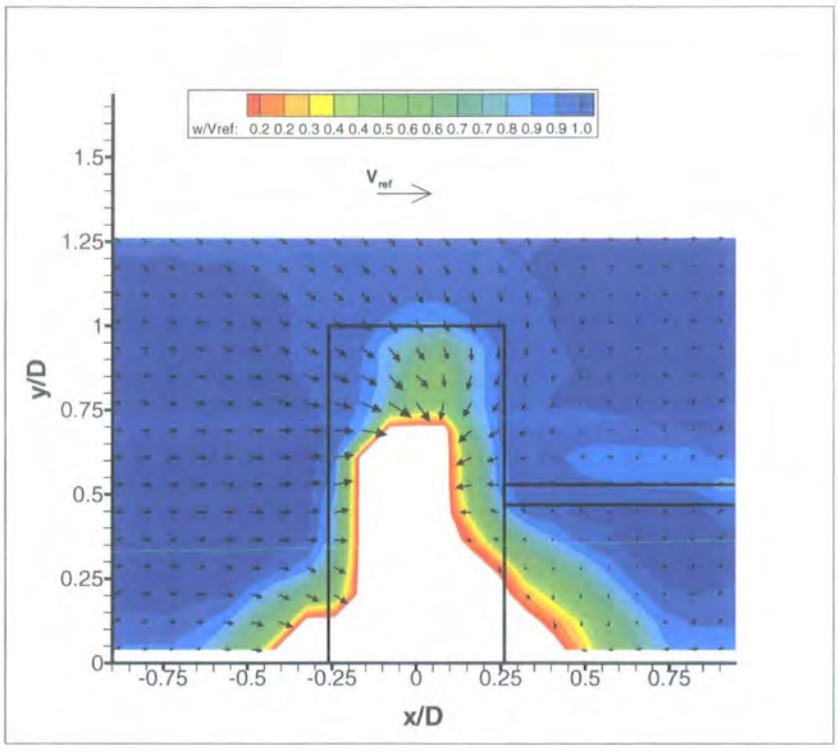


Figure 8.75: Time-Averaged Secondary Flow Velocity Vectors Coloured by Contours of $w/V_{ref}$ Velocity, Rotating, XY Plane @ Z = 1.0D.

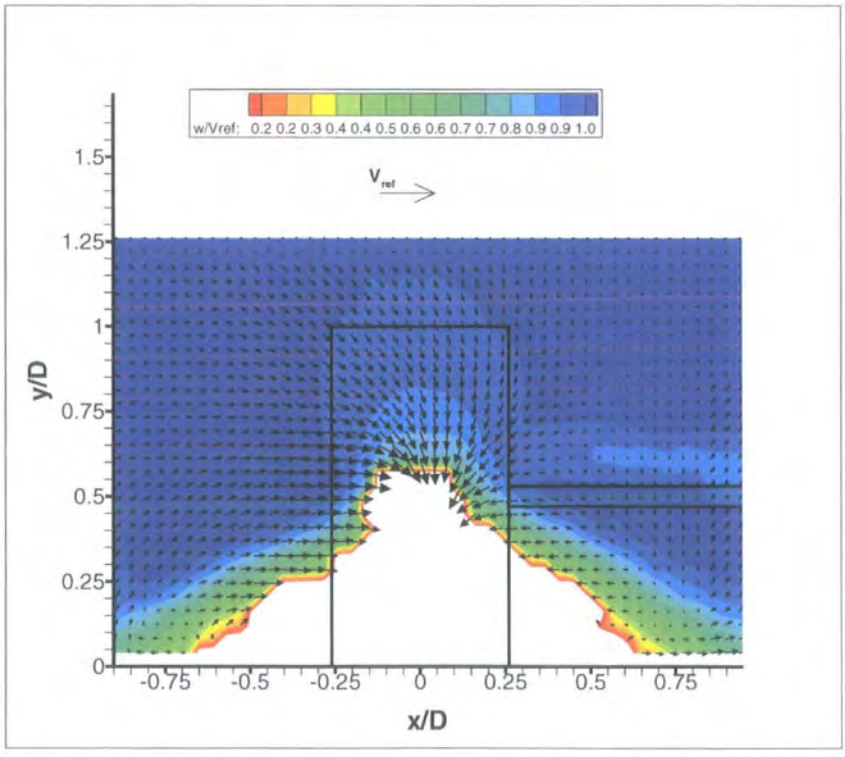


Figure 8.76: Time-Averaged Secondary Flow Velocity Vectors Coloured by Contours of $w/V_{ref}$ Velocity, Stationary, XY Plane @ Z = 1.0D.

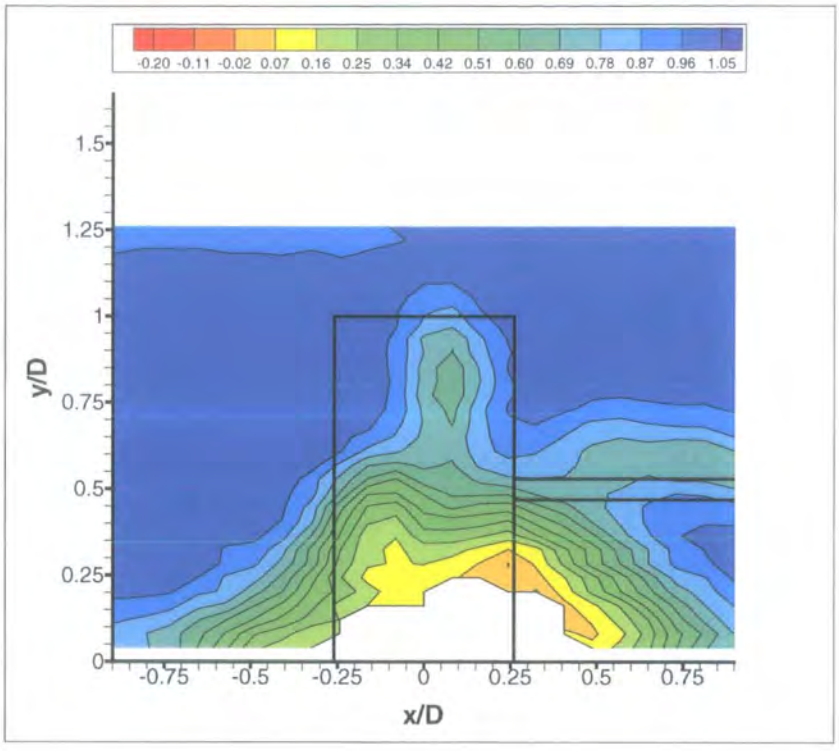


Figure 8.77: Time-Averaged Contours of Constant Total Pressure Coefficient, Rotating, XY Plane @ Z = 1.5D.

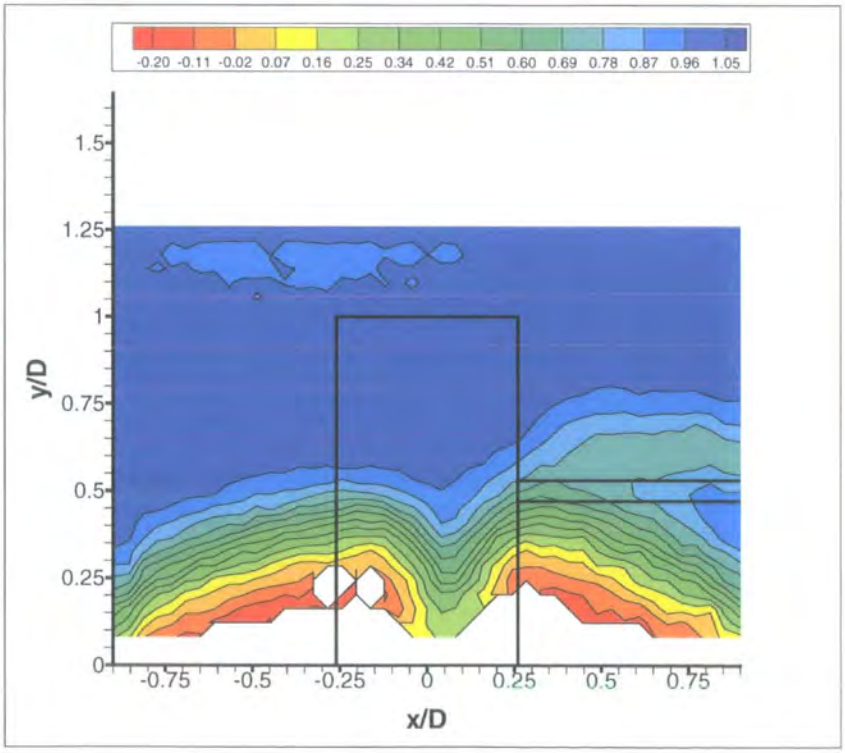


Figure 8.78: Time-Averaged Contours of Constant Total Pressure Coefficient, Stationary, XY Plane @ Z = 1.5D.

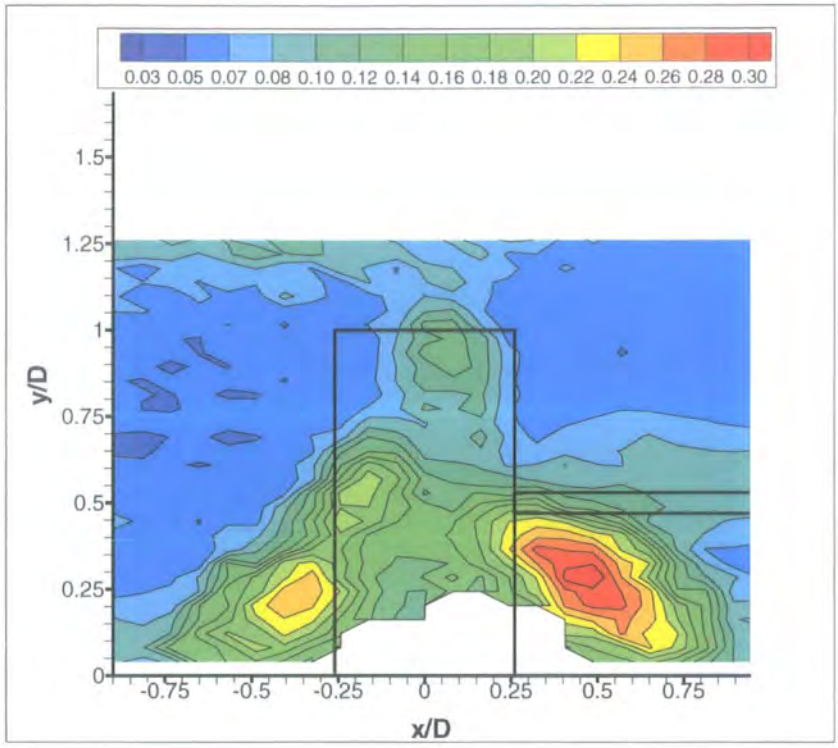


Figure 8.79: Time-Averaged Contours of Constant Standard Deviation for Dynamic Pressure Coefficient, Rotating, XY Plane @ Z = 1.5D.

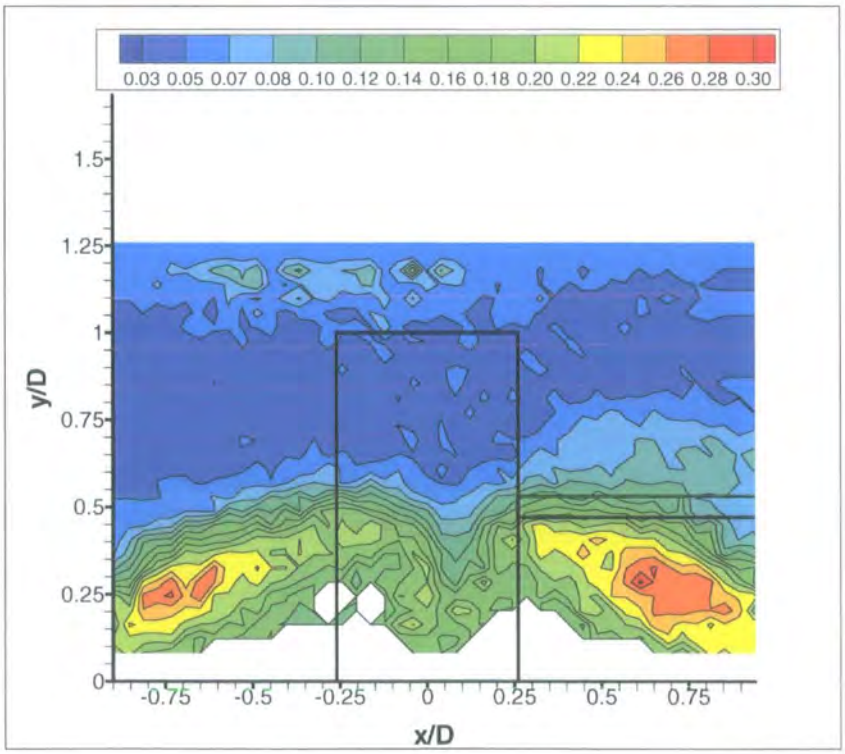


Figure 8.80: Time-Averaged Contours of Constant Standard Deviation for Dynamic Pressure Coefficient, Stationary, XY Plane @ Z = 1.5D.

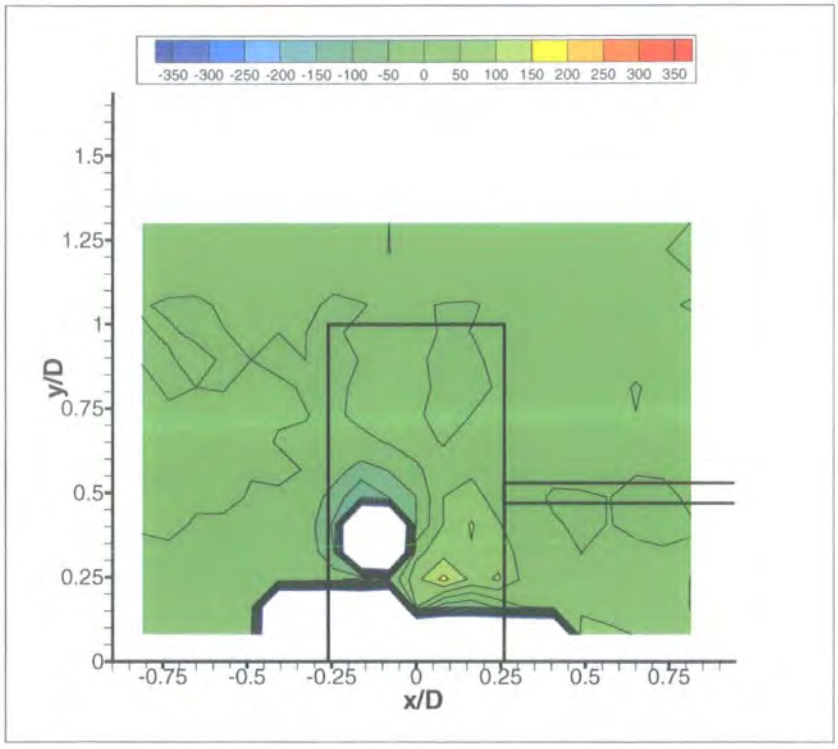


Figure 8.81: Time-Averaged Contours of Constant Streamwise Vorticity ($\xi$), Rotating, XY Plane @ Z = 1.5D.

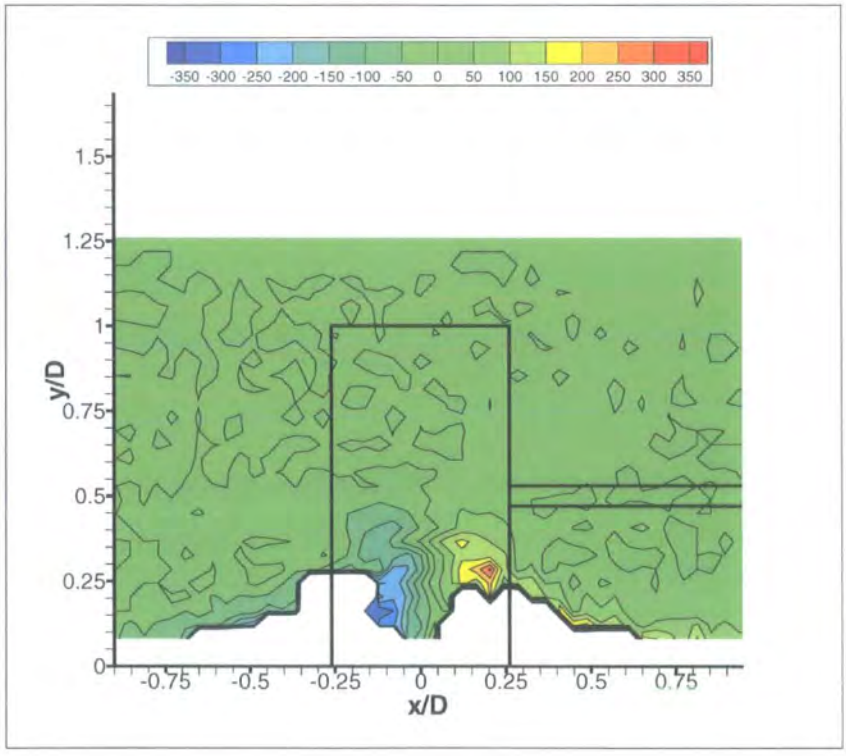


Figure 8.82: Time-Averaged Contours of Constant Streamwise Vorticity ($\xi$), Stationary, XY Plane @ Z = 1.5D.

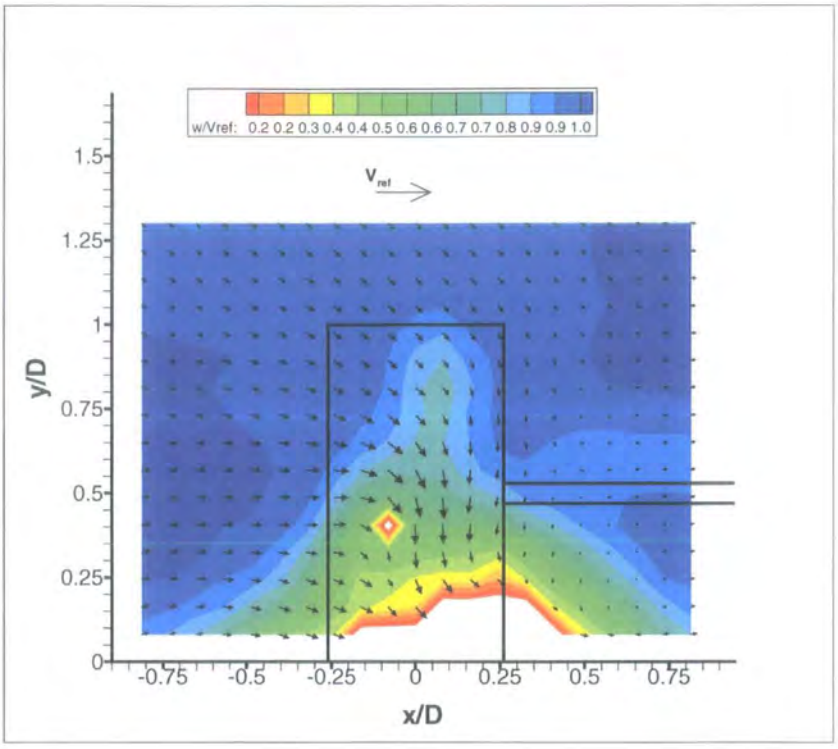


Figure 8.83: Time-Averaged Secondary Flow Velocity Vectors Coloured by Contours of $w/V_{ref}$ Velocity, Rotating, XY Plane @ Z = 1.5D.

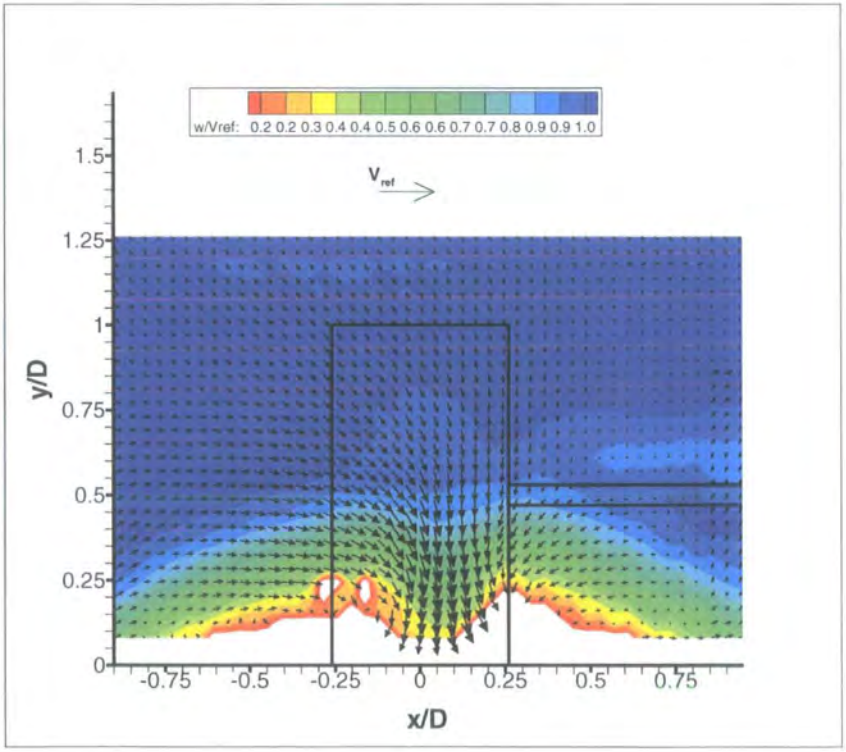


Figure 8.84: Time-Averaged Secondary Flow Velocity Vectors Coloured by Contours of $w/V_{ref}$ Velocity, Stationary, XY Plane @ Z = 1.5D.

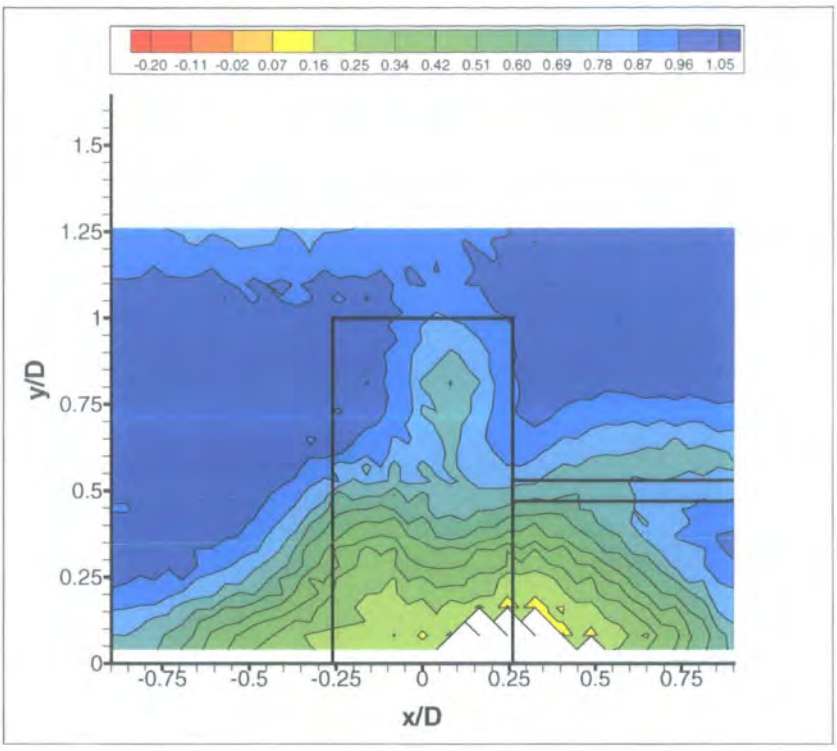


Figure 8.85: Time-Averaged Contours of Constant Total Pressure Coefficient, Rotating, XY Plane @ Z = 2.0D.

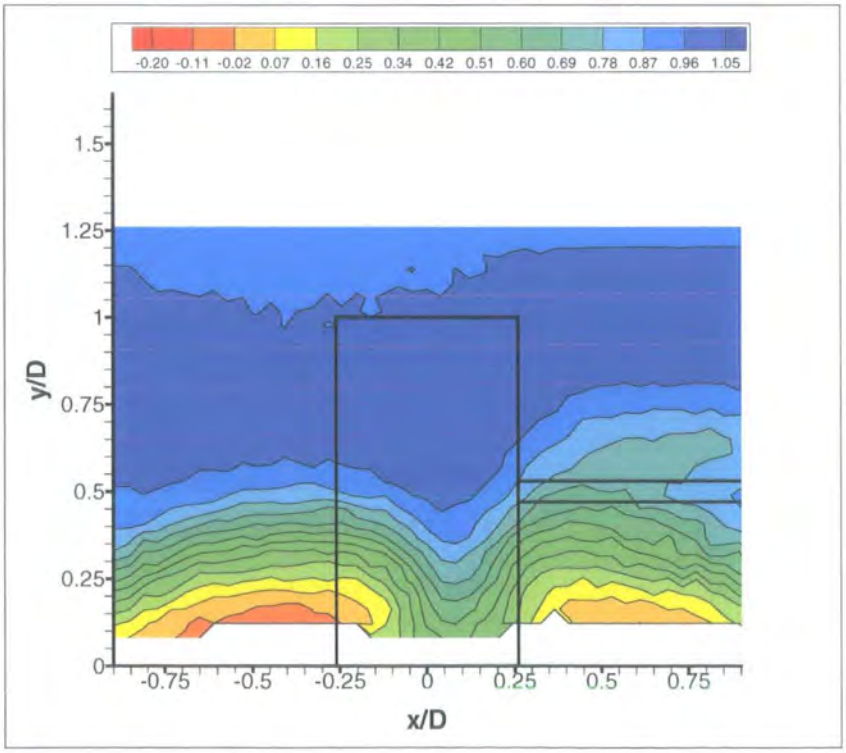


Figure 8.86: Time-Averaged Contours of Constant Total Pressure Coefficient, Stationary, XY Plane @ Z = 2.0D.

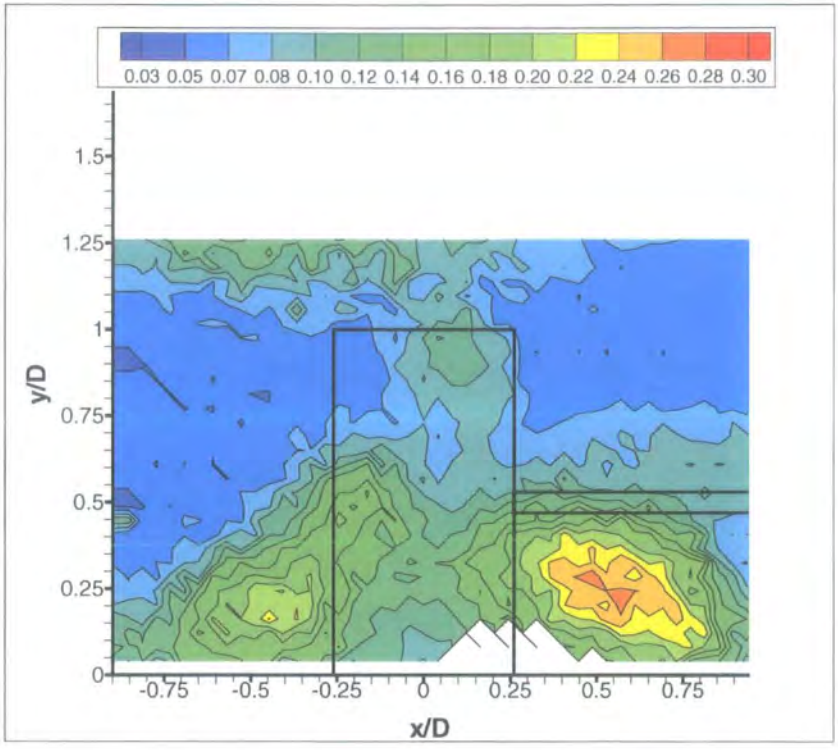


Figure 8.87: Time-Averaged Contours of Constant Standard Deviation for Dynamic Pressure Coefficient, Rotating, XY Plane @ Z = 2.0D.

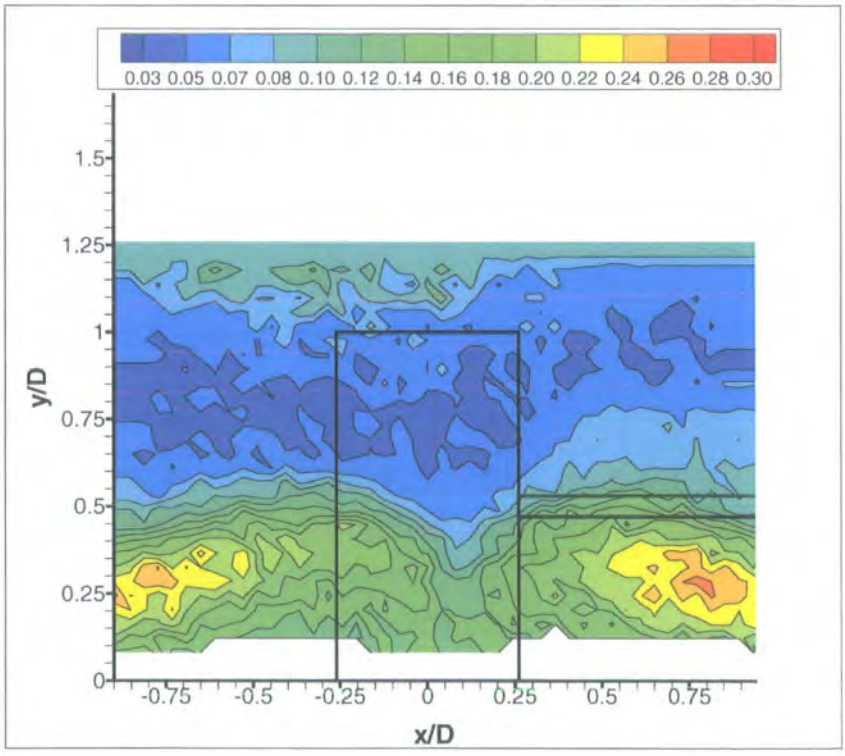


Figure 8.88: Time-Averaged Contours of Constant Standard Deviation for Dynamic Pressure Coefficient, Stationary, XY Plane @ Z = 2.0D.

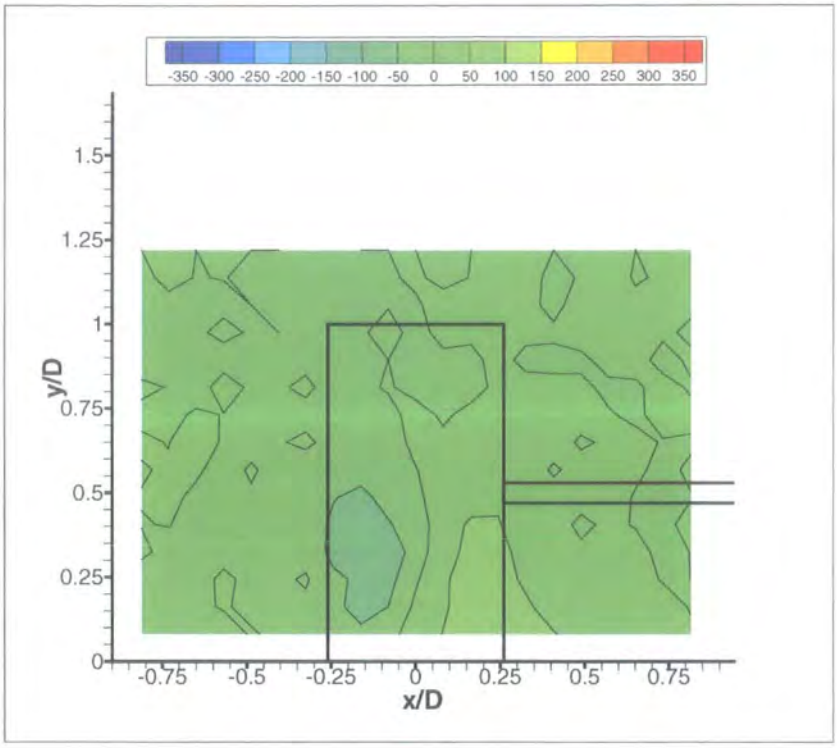


Figure 8.89: Time-Averaged Contours of Constant Streamwise Vorticity ($\xi$), Rotating, XY Plane @ Z = 2.0D.

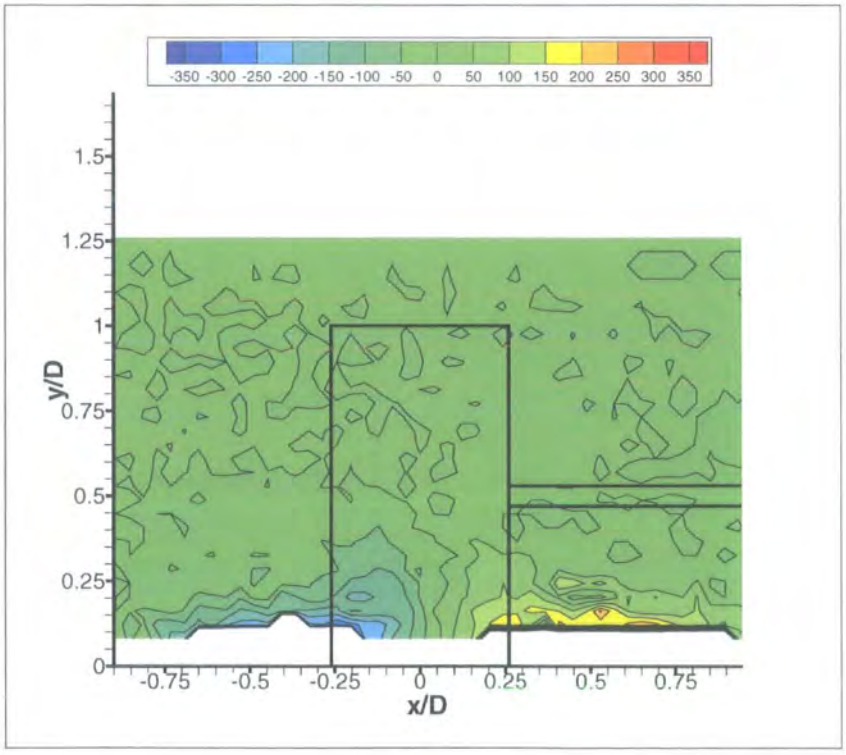


Figure 8.90: Time-Averaged Contours of Constant Streamwise Vorticity ($\xi$), Stationary, XY Plane @ Z = 2.0D.

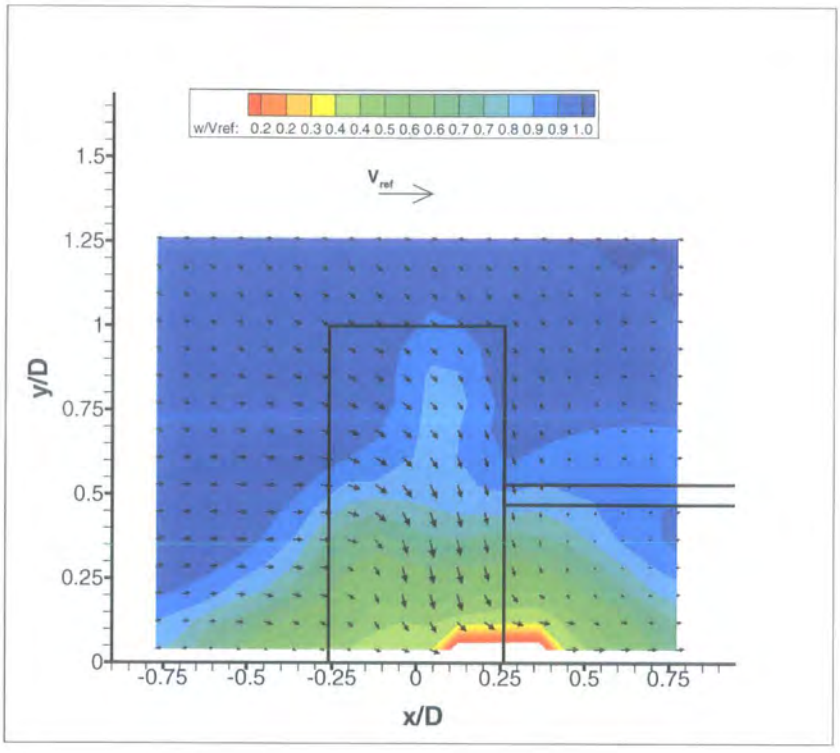


Figure 8.91: Time-Averaged Secondary Flow Velocity Vectors Coloured by Contours of $w/V_{ref}$ Velocity, Rotating, XY Plane @ Z = 2.0D.

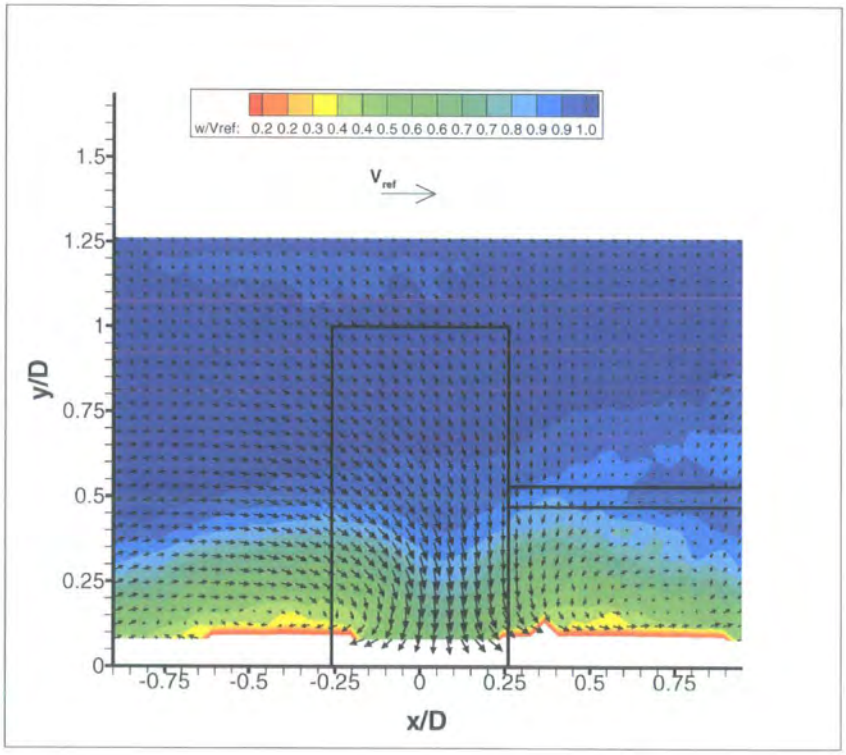


Figure 8.92: Time-Averaged Secondary Flow Velocity Vectors Coloured by Contours of $w/V_{ref}$ Velocity, Stationary, XY Plane @ Z = 2.0D.

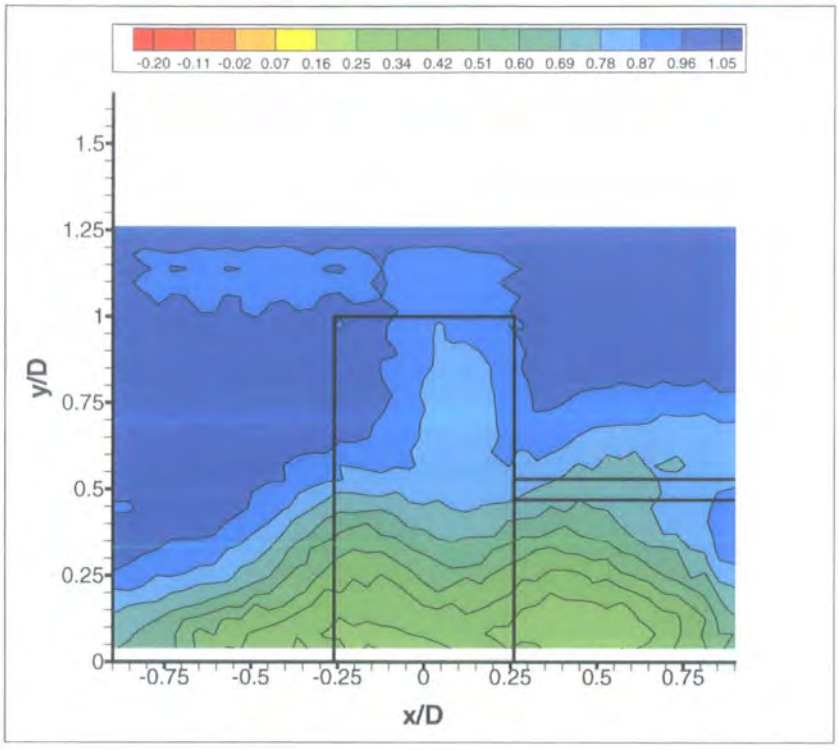


Figure 8.93: Time-Averaged Contours of Constant Total Pressure Coefficient, Rotating, XY Plane @ Z = 2.5D.

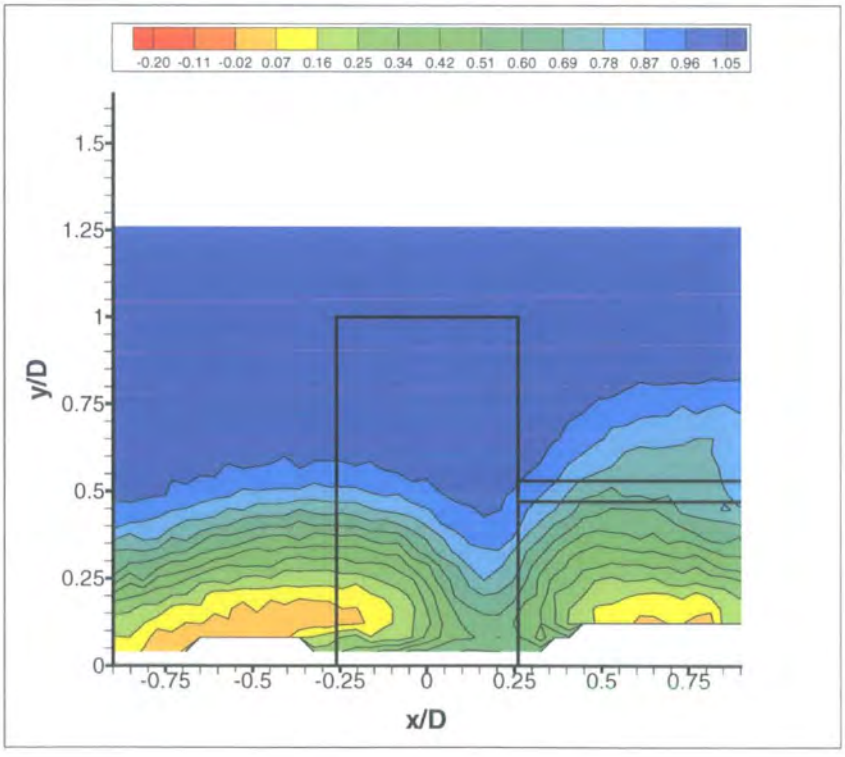


Figure 8.94: Time-Averaged Contours of Constant Total Pressure Coefficient, Stationary, XY Plane @ Z = 2.5D.

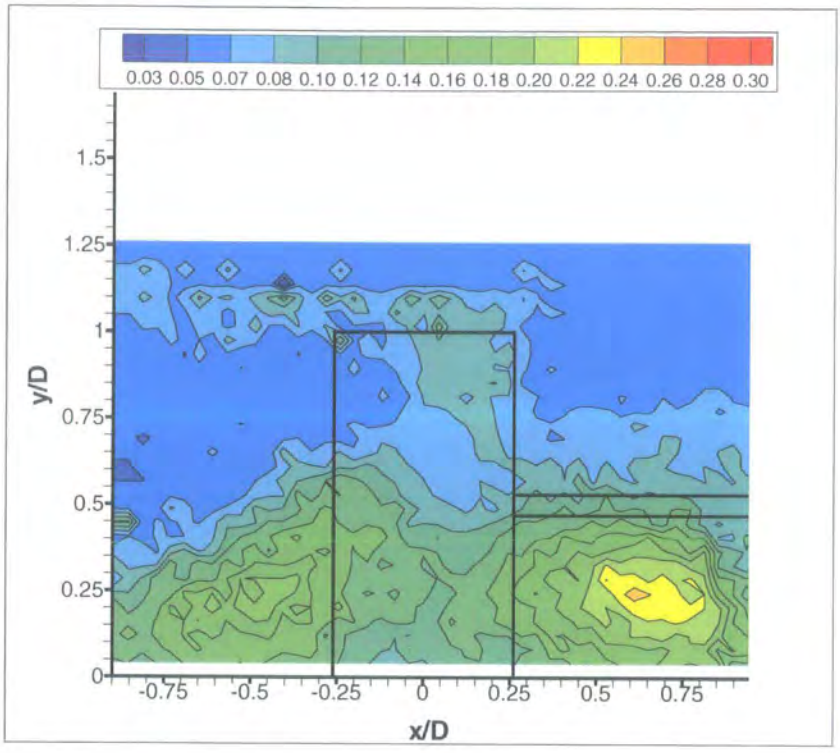


Figure 8.95: Time-Averaged Contours of Constant Standard Deviation for Dynamic Pressure Coefficient, Rotating, XY Plane @ Z = 2.5D.

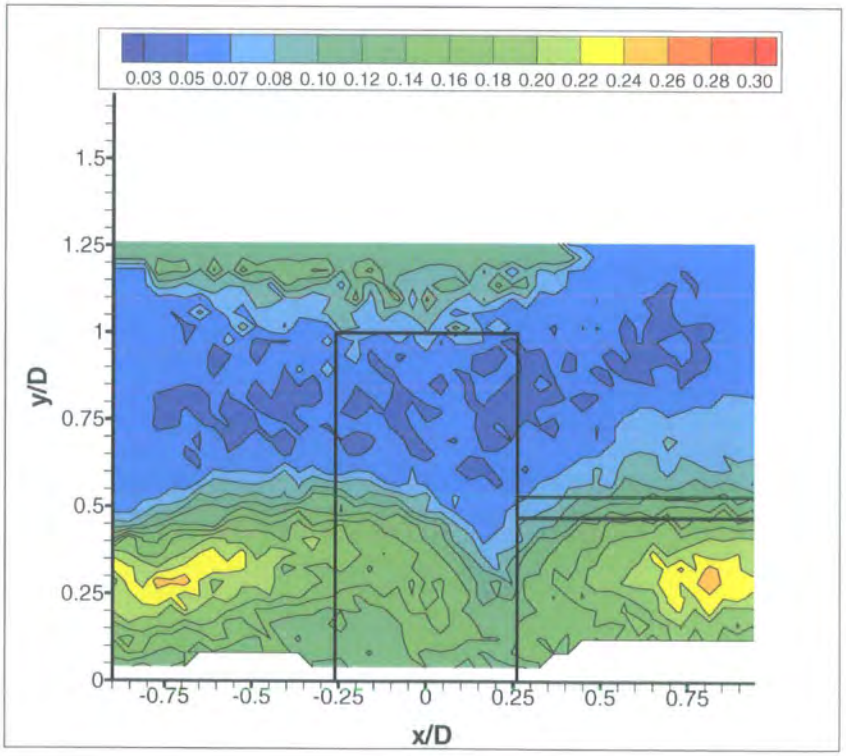


Figure 8.96: Time-Averaged Contours of Constant Standard Deviation for Dynamic Pressure Coefficient, Stationary, XY Plane @ Z = 2.5D.

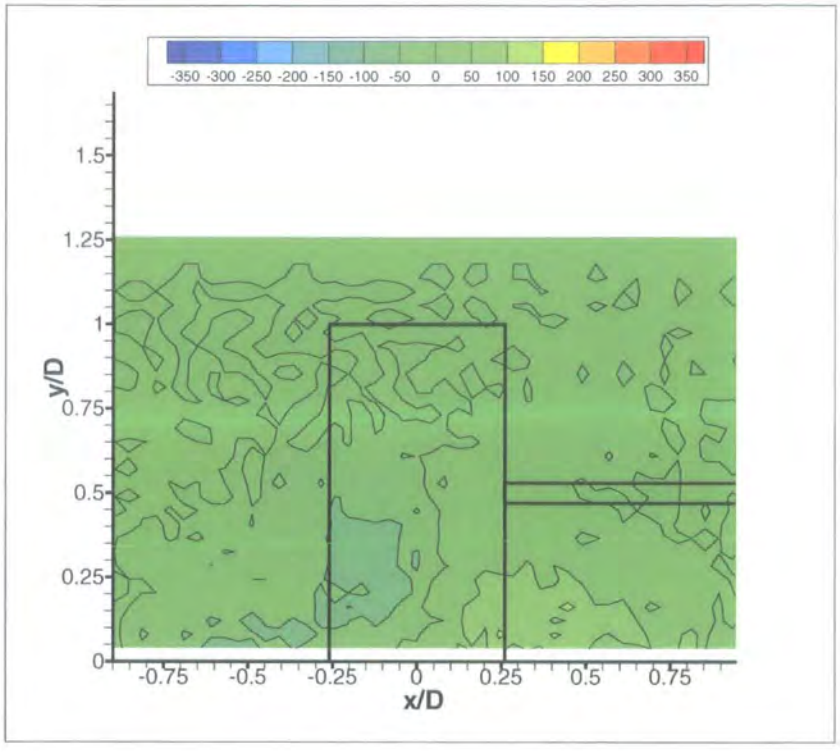


Figure 8.97: Time-Averaged Contours of Constant Streamwise Vorticity ($\xi$), Rotating, XY Plane @ Z = 2.5D.

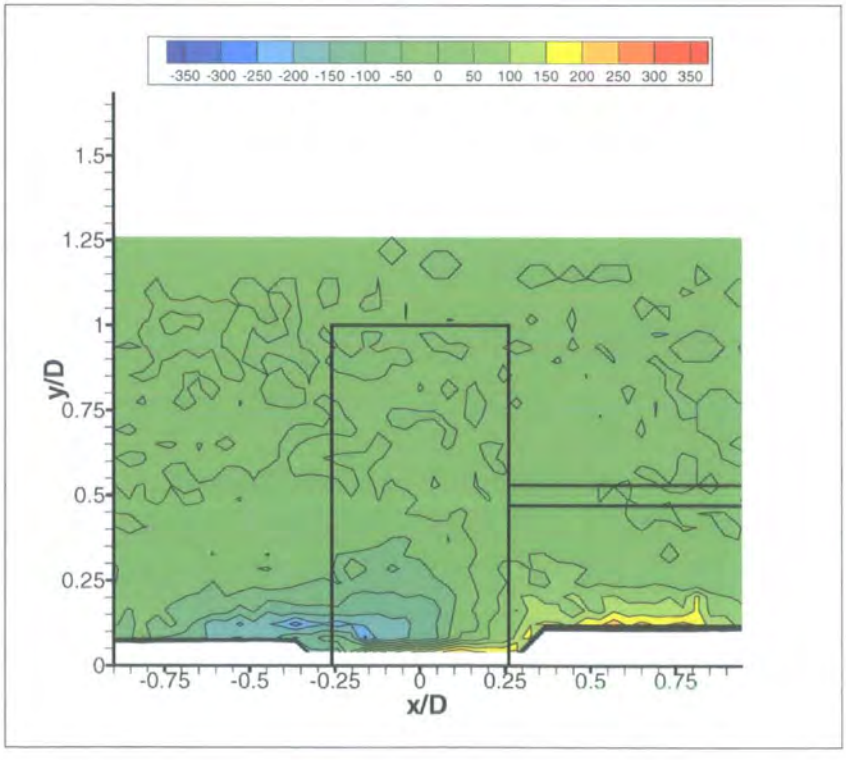


Figure 8.98: Time-Averaged Contours of Constant Streamwise Vorticity ($\xi$), Stationary, XY Plane @ Z = 2.5D.

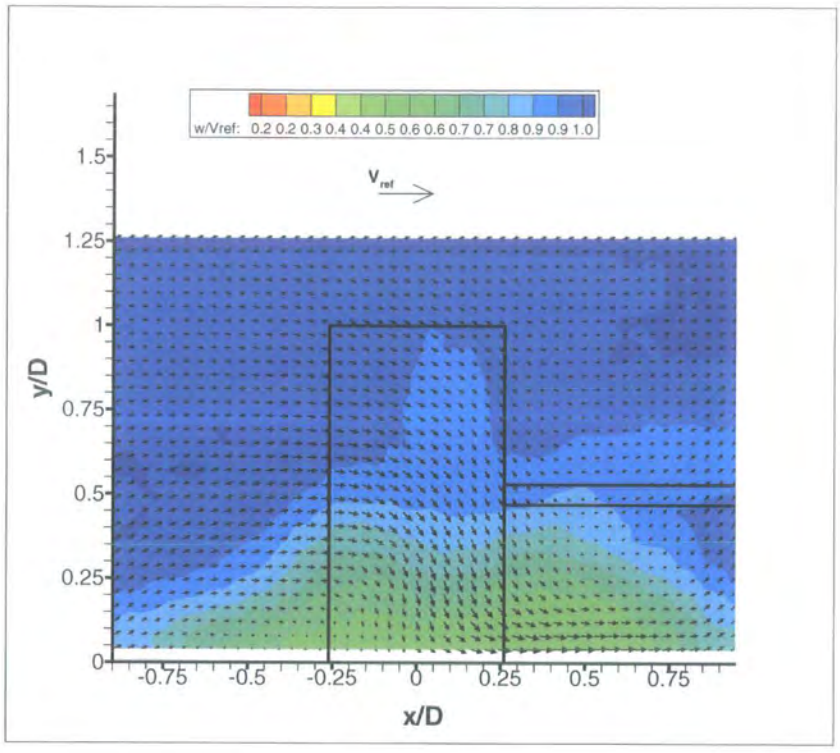


Figure 8.99: Time-Averaged Secondary Flow Velocity Vectors Coloured by Contours of $w/V_{ref}$ Velocity, Rotating, XY Plane @ Z = 2.5D.

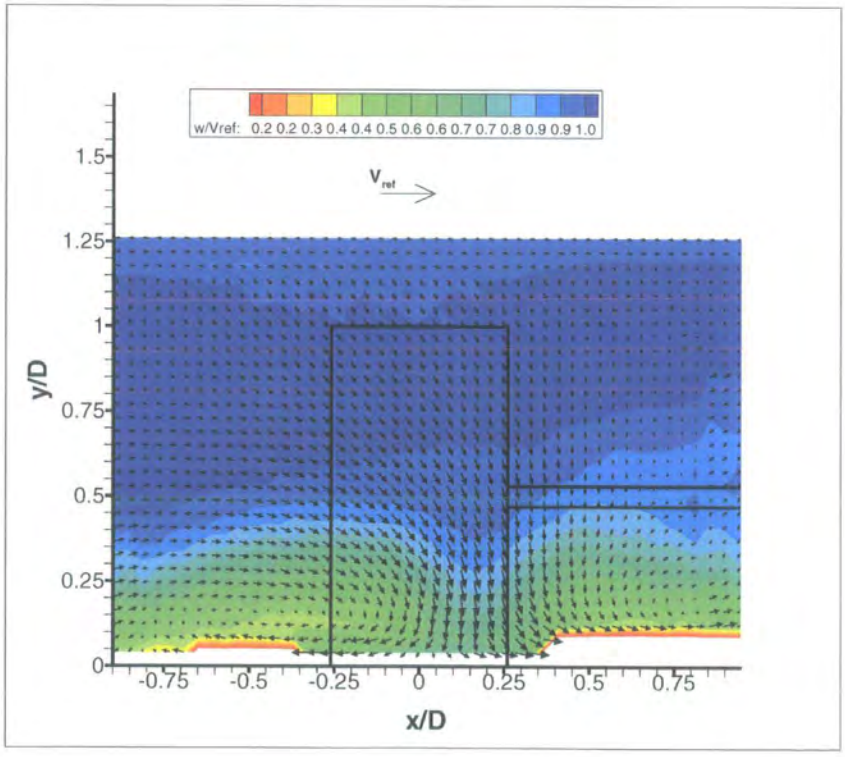


Figure 8.100: Time-Averaged Secondary Flow Velocity Vectors Coloured by Contours of $w/V_{ref}$ Velocity, Stationary, XY Plane @ Z = 2.5D.

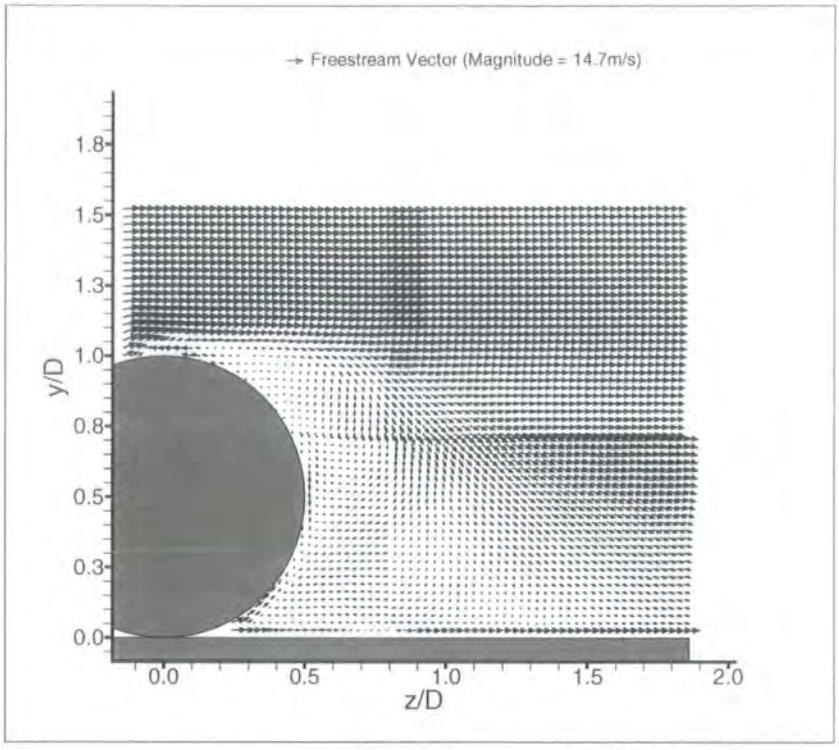


Figure 8.101: Ensemble Time-Averaged Velocity Vectors for Centreline (W/D = 0) YZ Plane (PosA-D), Rotating.

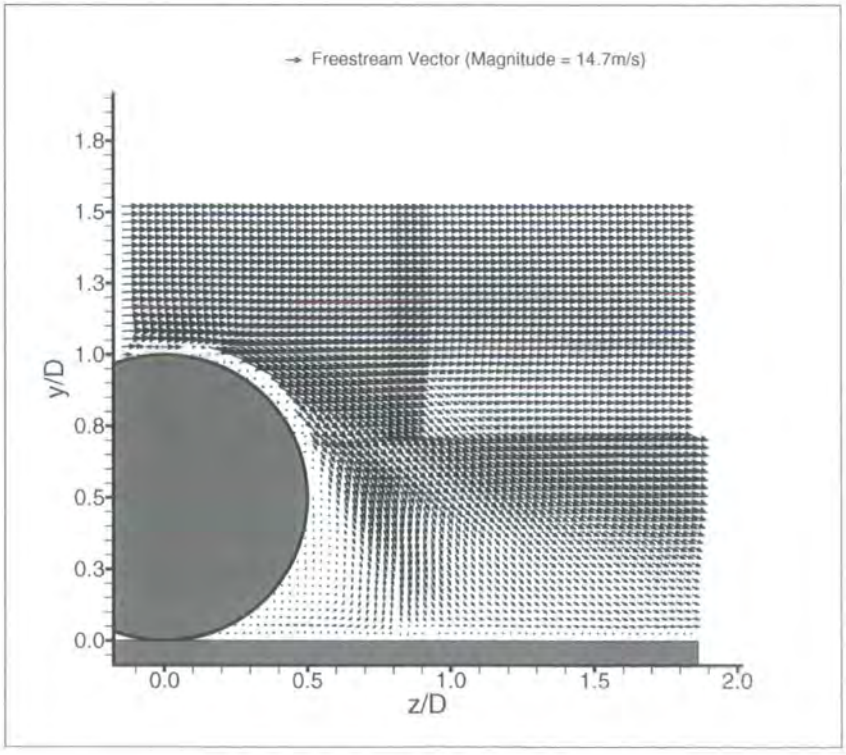


Figure 8.102: Ensemble Time-Averaged Velocity Vectors for Centreline (W/D = 0) YZ Plane (PosA-D), Stationary.

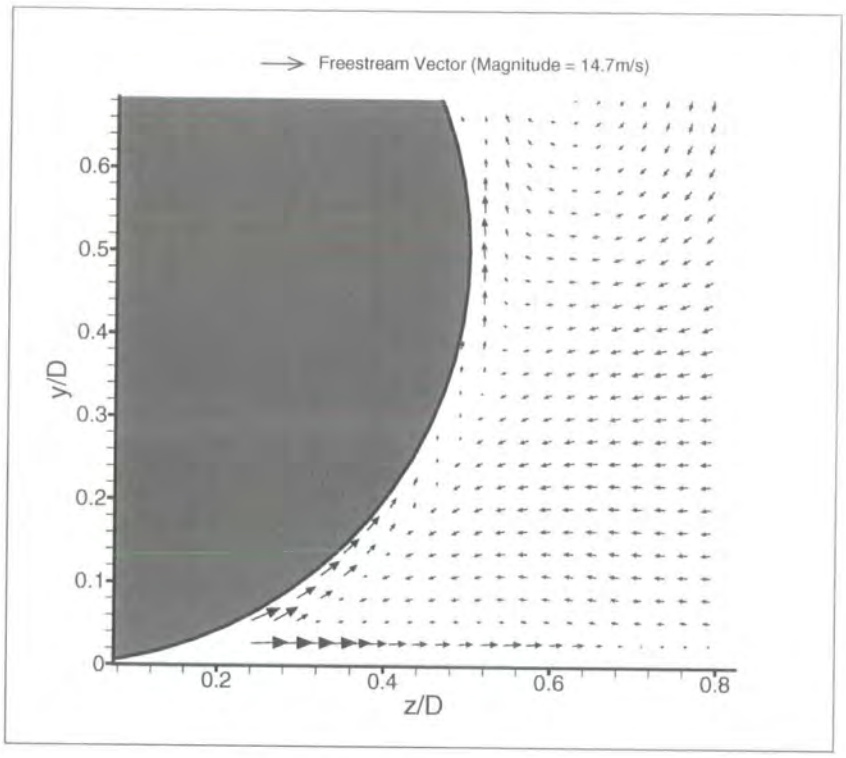


Figure 8.103: Ensemble Time-Averaged Velocity Vectors for Centreline (W/D = 0) YZ Plane (PosA), Rotating.

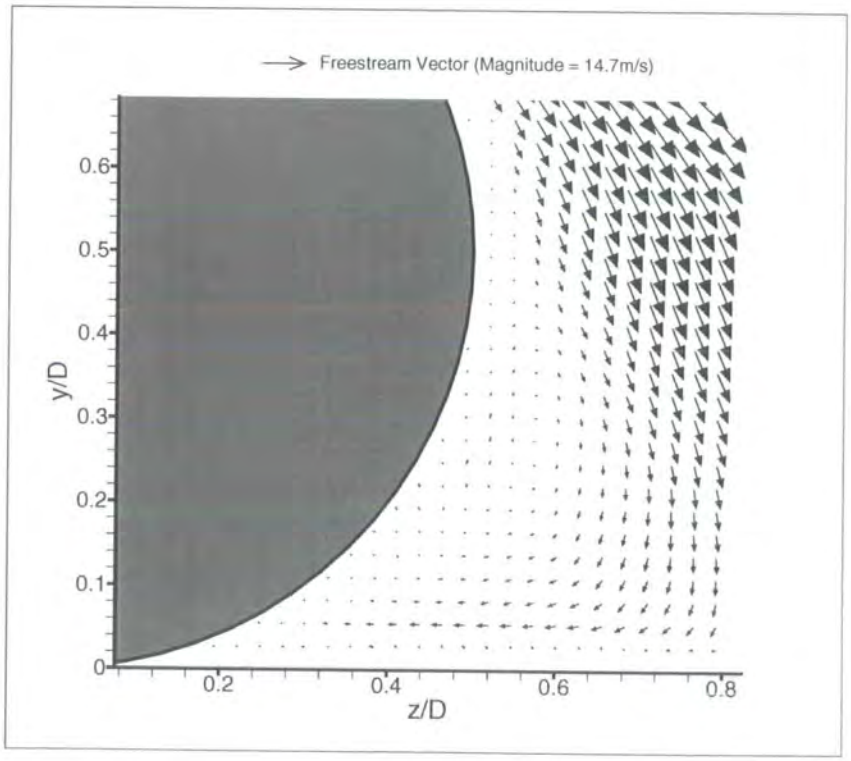


Figure 8.104: Ensemble Time-Averaged Velocity Vectors for Centreline (W/D = 0) YZ Plane (PosA), Stationary

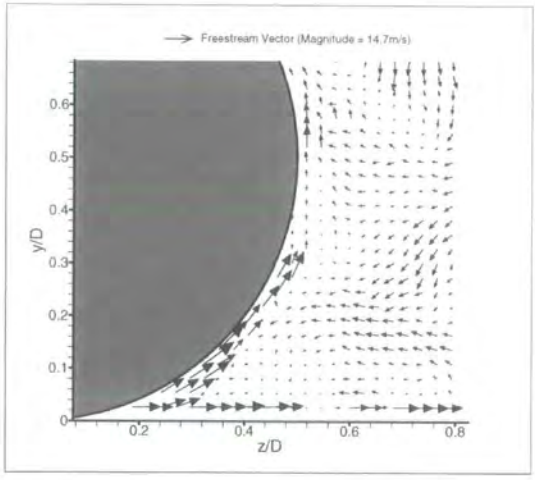


(a) t = 0.0s

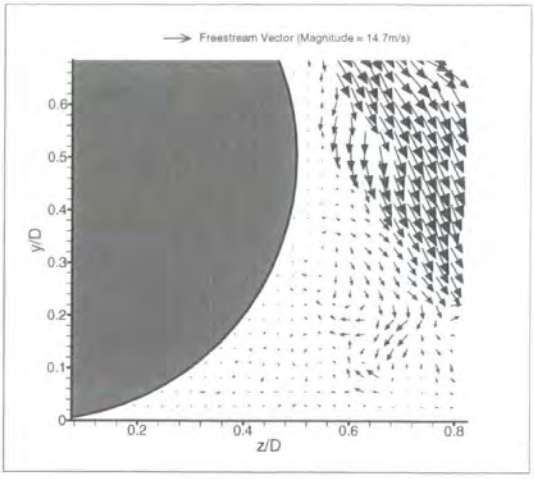


(d) t = 0.0s

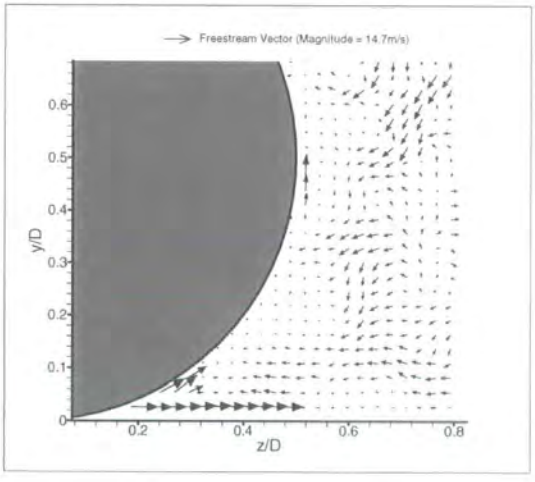


(b) t = 0.2s

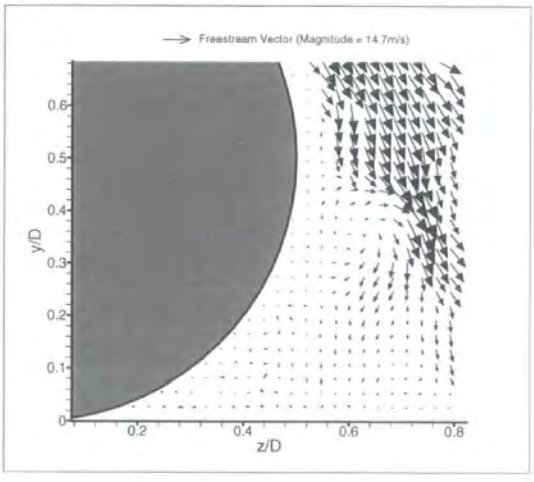


(e) t = 0.2s

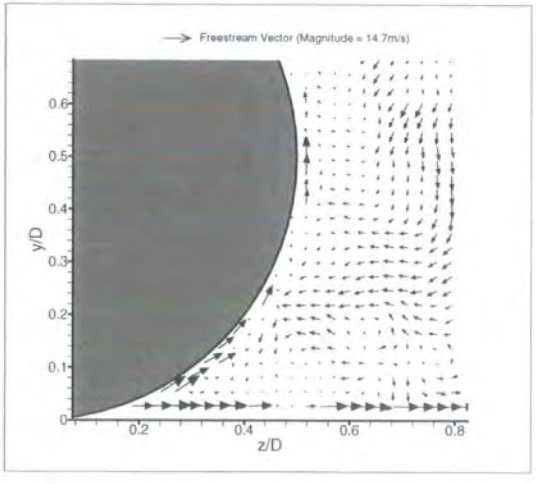


(c) t = 0.4s

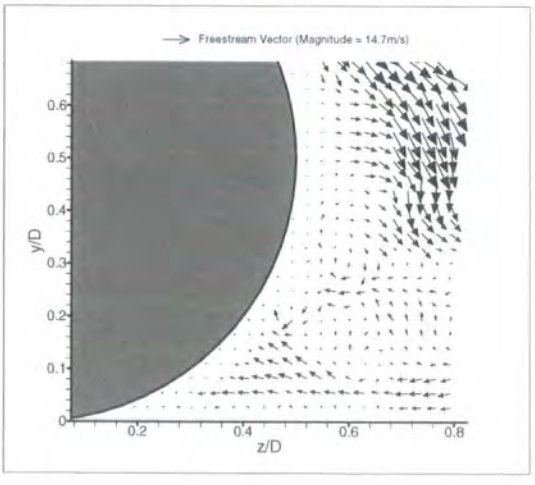


(f) t = 0.4s

Figure 8.105: Sequence Showing Velocity Vectors for PosA Centreline (W/D = 0) YZ Plane, Rotating (a-c) and Stationary (d-f).

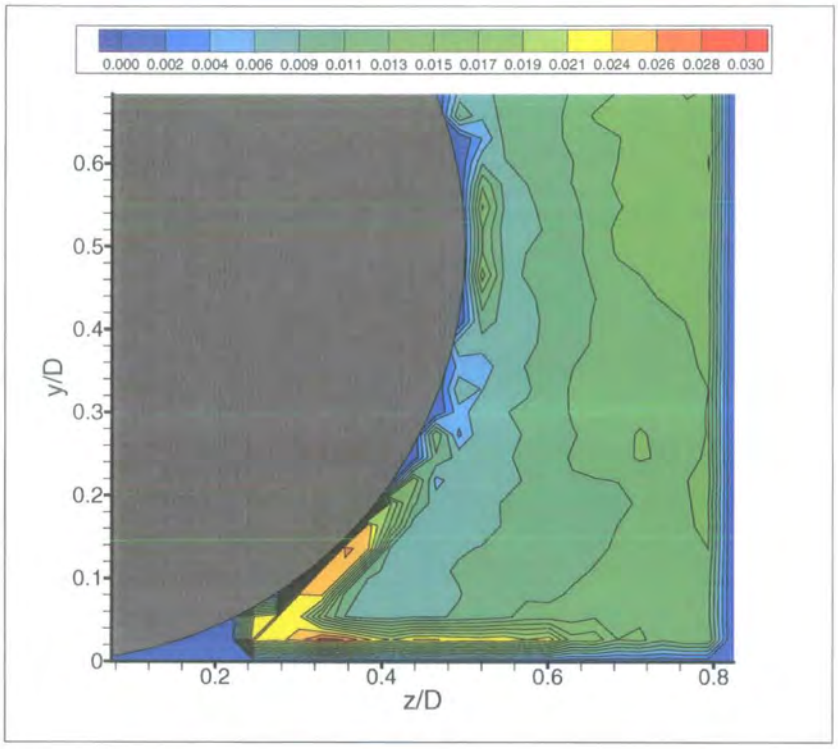


Figure 8.106: Velocity Vector Standard Deviation for Centreline (W/D = 0) YZ Plane (PosA), Rotating.

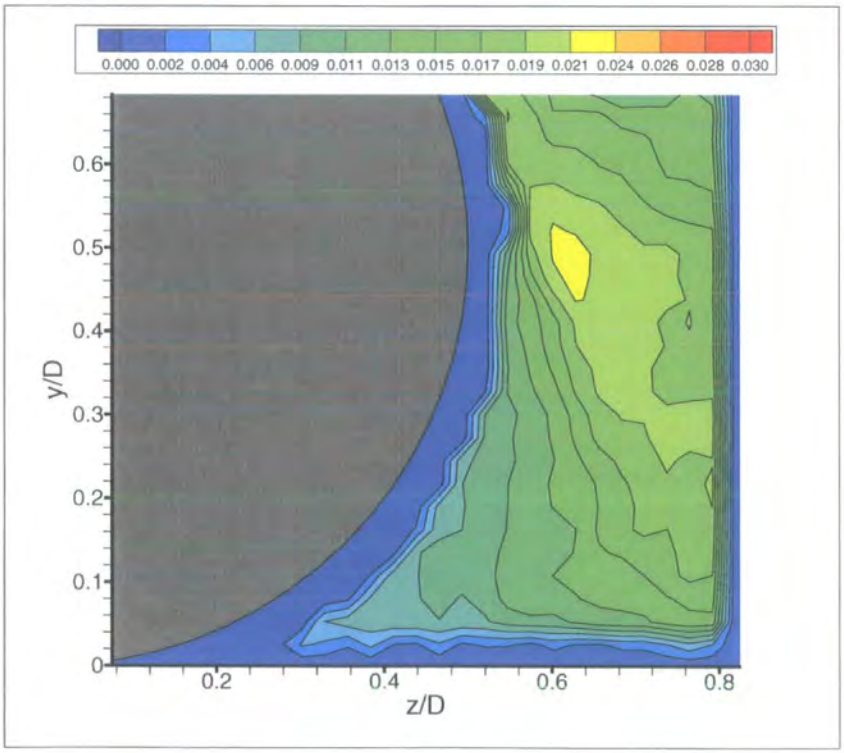


Figure 8.107: Velocity Vector Standard Deviation for Centreline (W/D = 0) YZ Plane (PosA), Stationary.

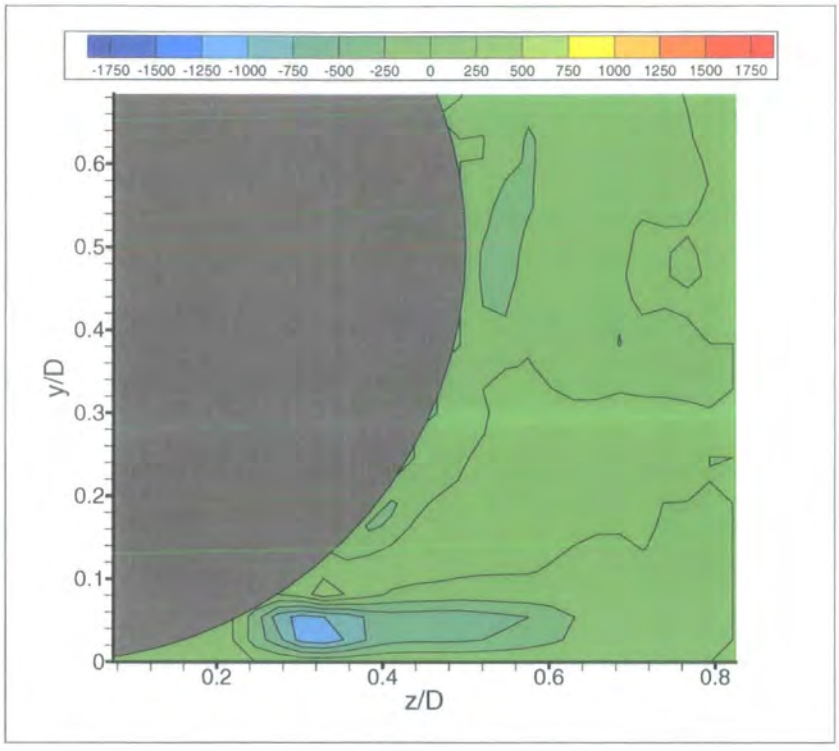


Figure 8.108: Ensemble Time-Averaged Contours of Constant Spanwise Vorticity ($\zeta$) for Centreline (W/D = 0) YZ Plane (PosA), Rotating.

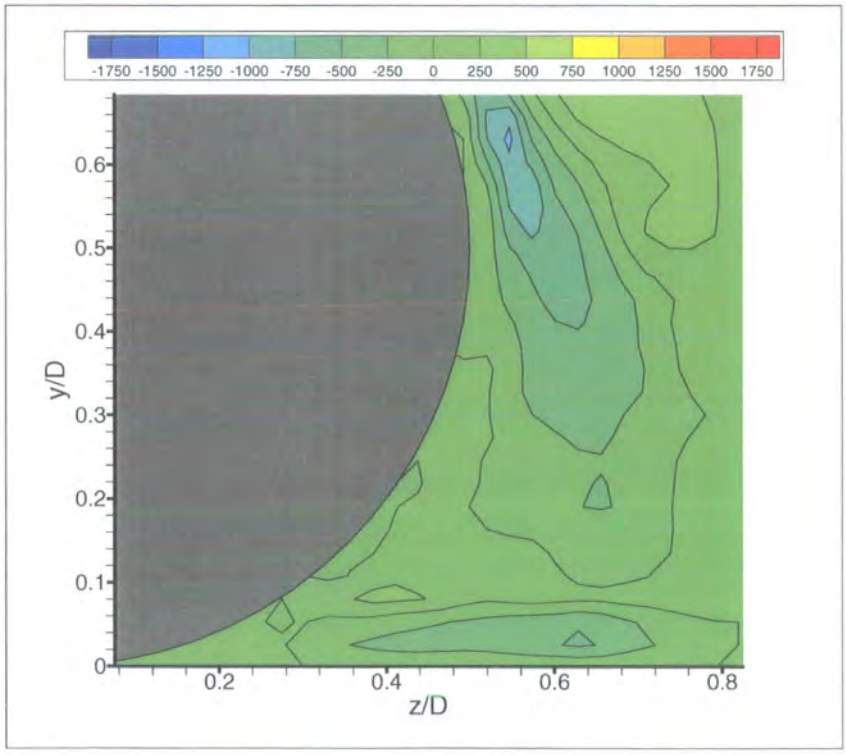


Figure 8.109: Ensemble Time-Averaged Contours of Constant Spanwise Vorticity ($\zeta$) for Centreline (W/D = 0) YZ Plane (PosA), Stationary.

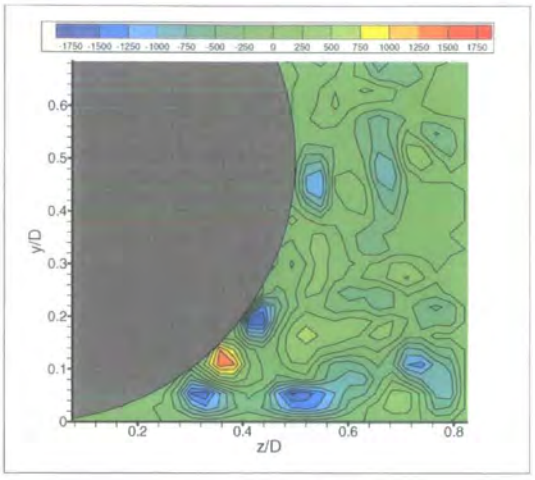


(a) t = 0.0s

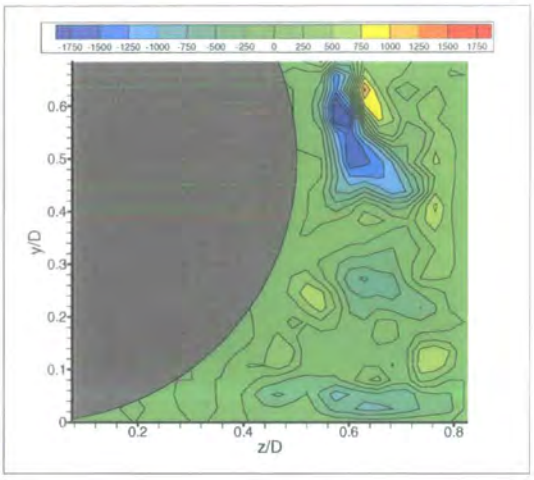


(d) t = 0.0s

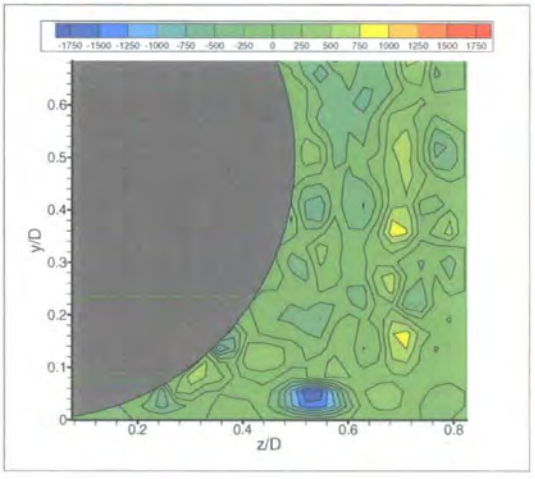


(b) t = 0.2s

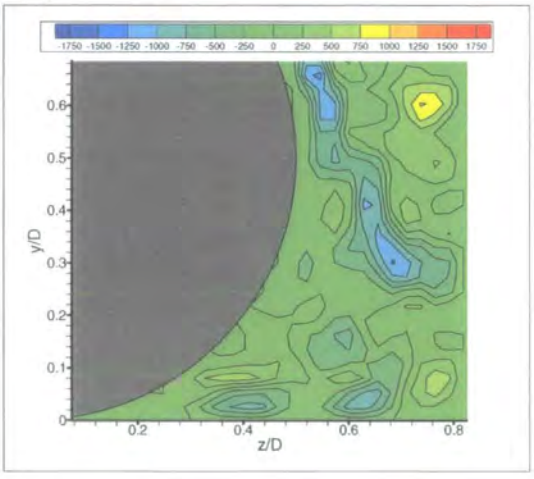


(e) t = 0.2s

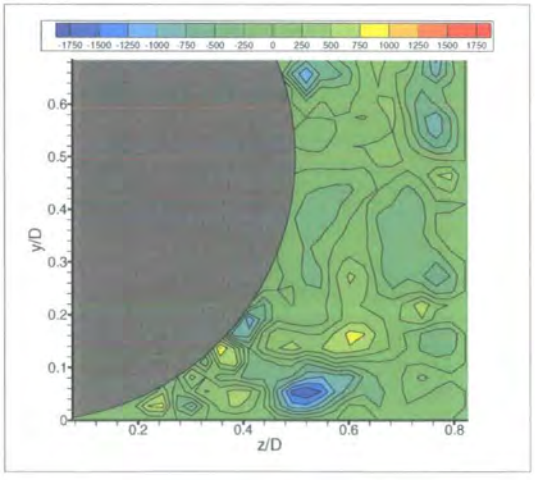


(c) t = 0.4s

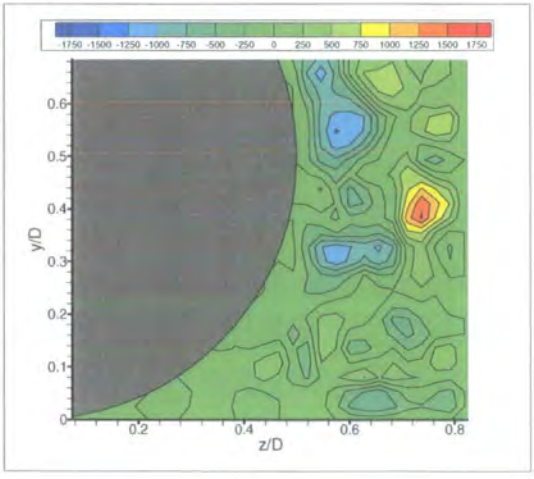


(f) t = 0.4s

Figure 8.110: Sequence Showing Contours of Constant Spanwise Vorticity ($\zeta$) for PosA Centreline (W/D = 0) YZ Plane, Rotating (a-c) and Stationary (d-f).

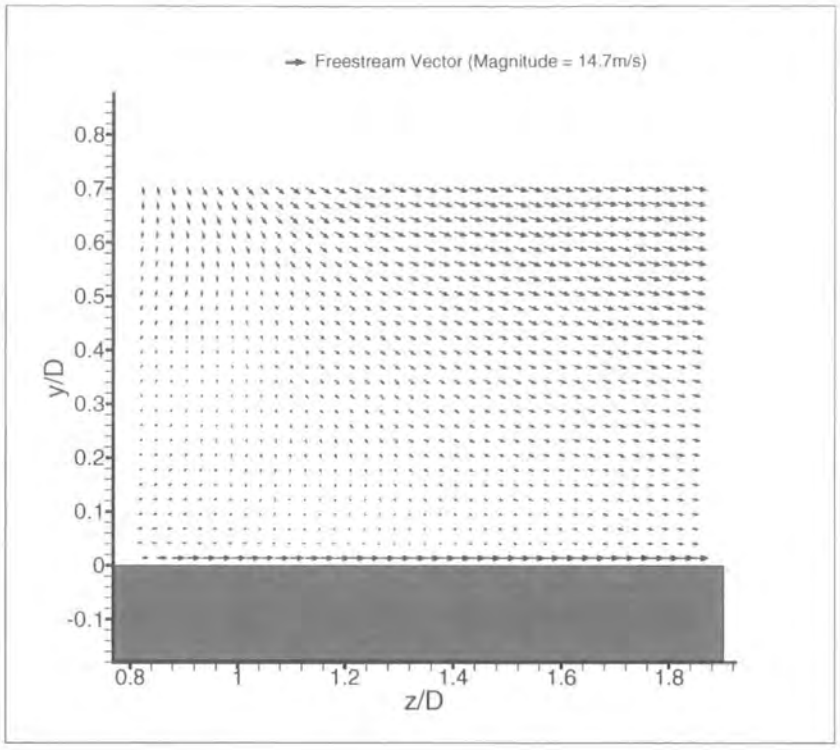


Figure 8.111: Ensemble Time-Averaged Velocity Vectors for Centreline (W/D = 0) YZ Plane (PosB), Rotating.

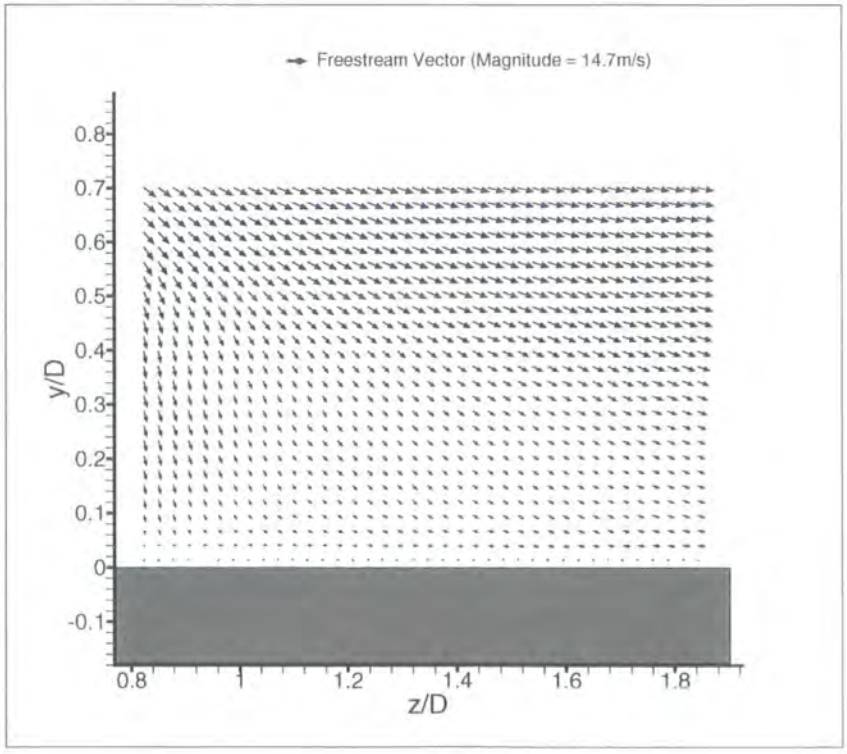


Figure 8.112: Ensemble Time-Averaged Velocity Vectors for Centreline (W/D = 0) YZ Plane (PosB), Stationary

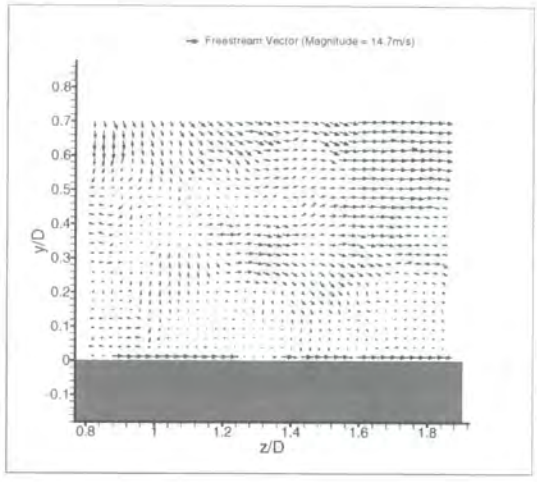


(a) t = 0.0s

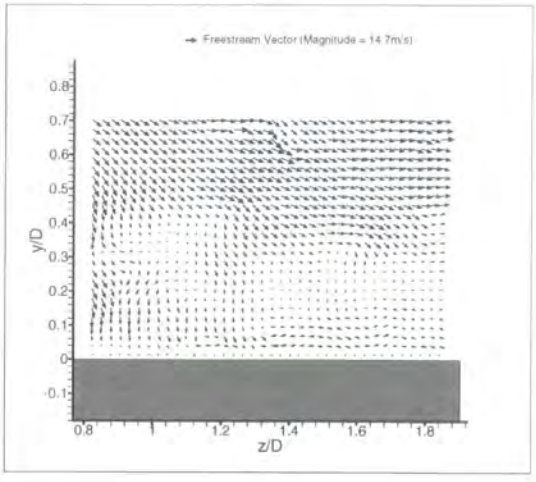


(d) t = 0.0s

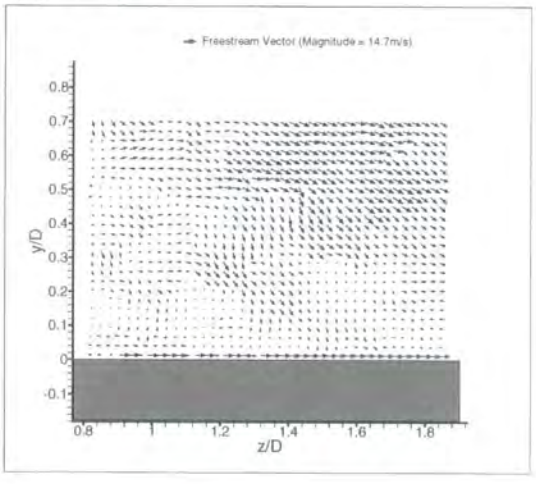


(b) t = 0.2s

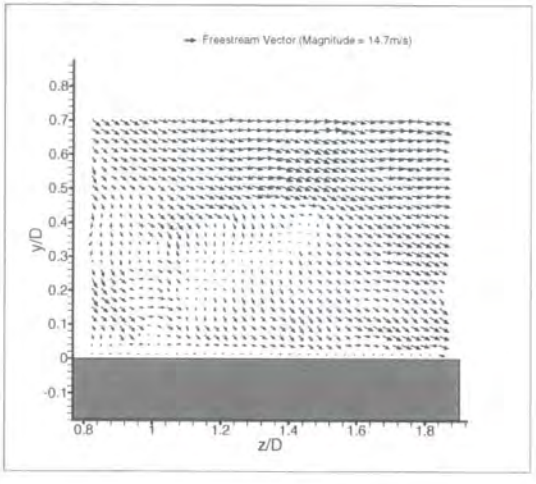


(e) t = 0.2s

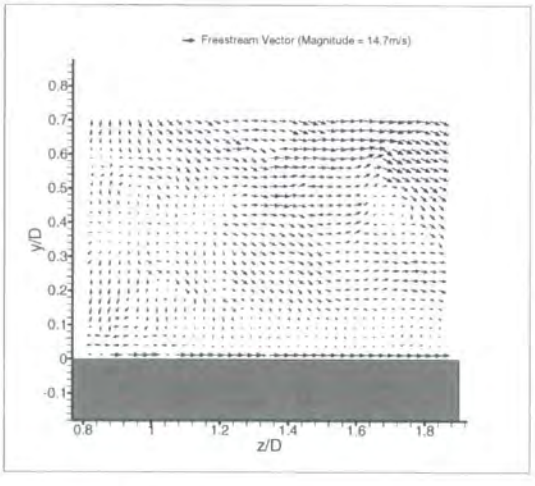


(c) t = 0.4s

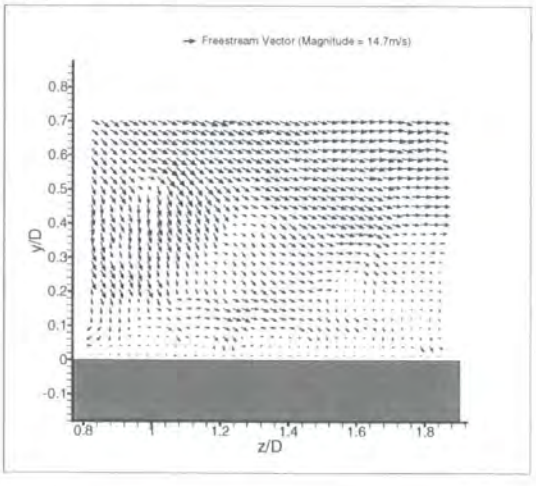


(f) t = 0.4s

Figure 8.113: Sequence Showing Velocity Vectors for PosB Centreline (W/D = 0) YZ Plane, Rotating (a-c) and Stationary (d-f).

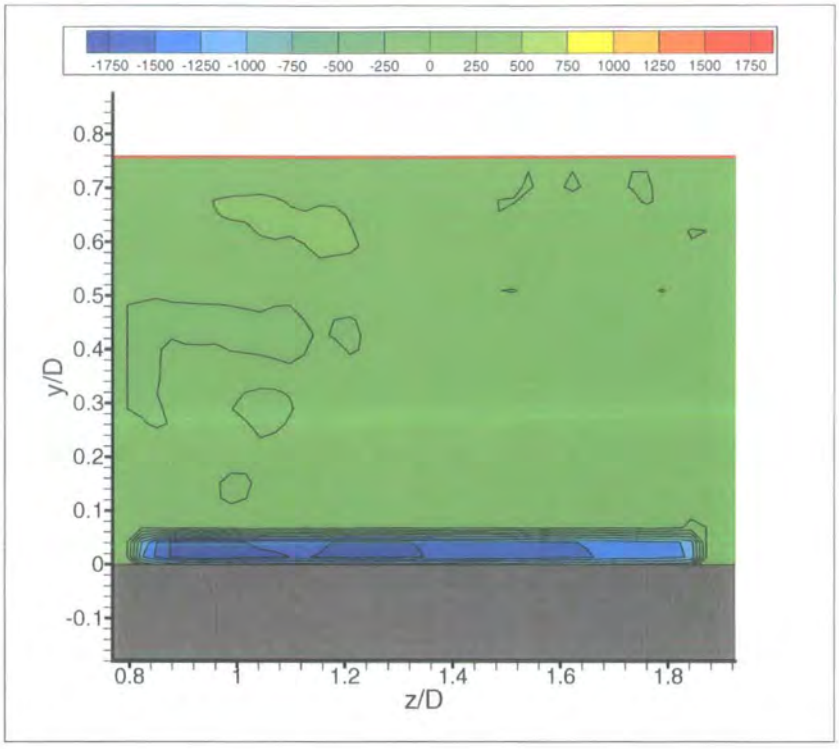


Figure 8.114: Ensemble Time-Averaged Contours of Constant Spanwise Vorticity ($\zeta$) for Centreline (W/D = 0) YZ Plane (PosB), Rotating.

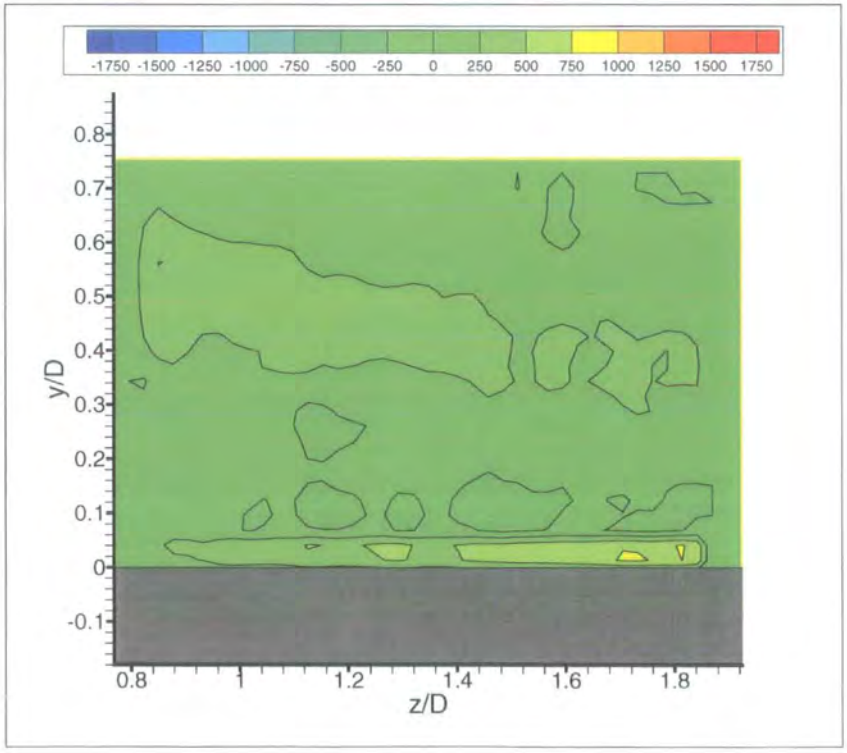


Figure 8.115: Ensemble Time-Averaged Contours of Constant Spanwise Vorticity ($\zeta$) for Centreline (W/D = 0) YZ Plane (PosB), Stationary.

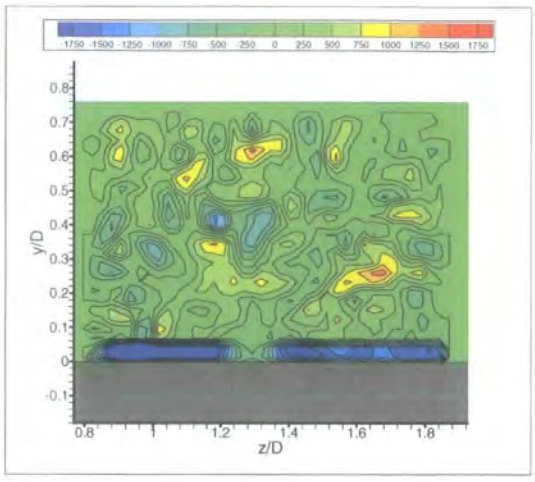


(a) t = 0.0s

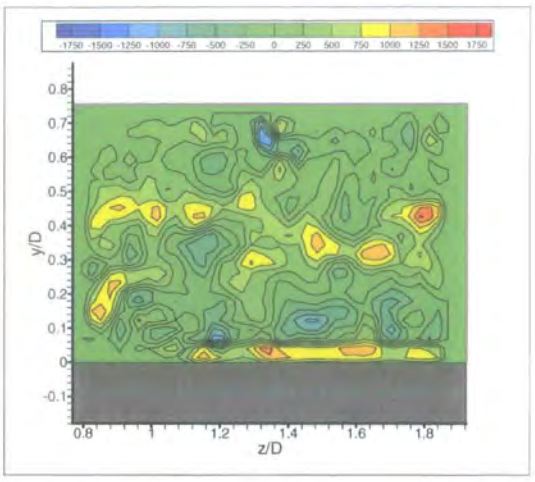


(d) t = 0.0s

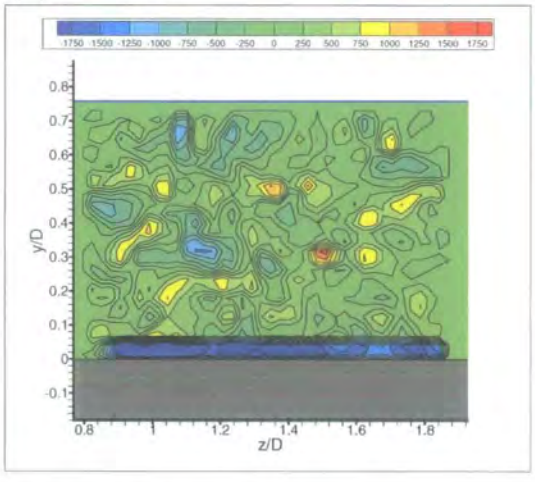


(b) t = 0.2s

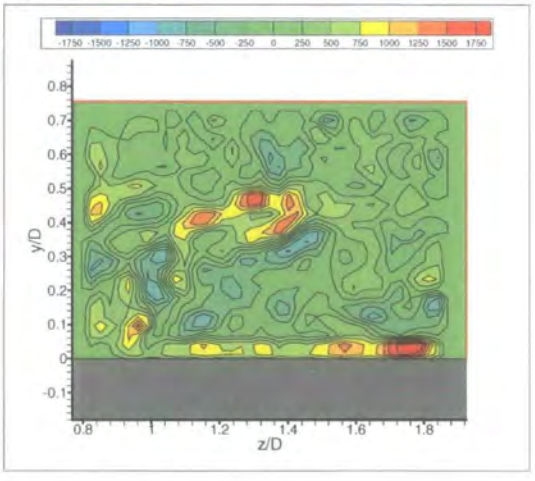


(e) t = 0.2s

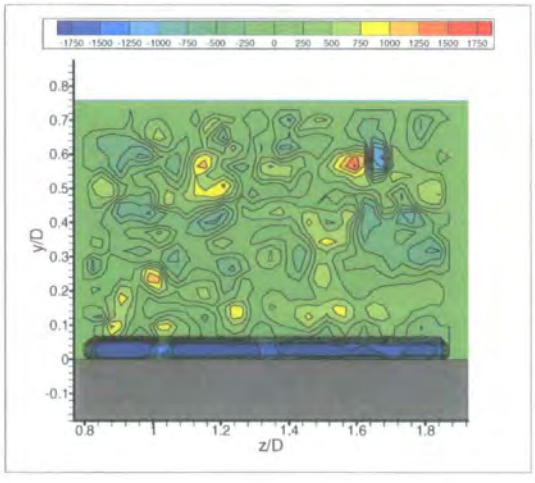


(c) t = 0.4s

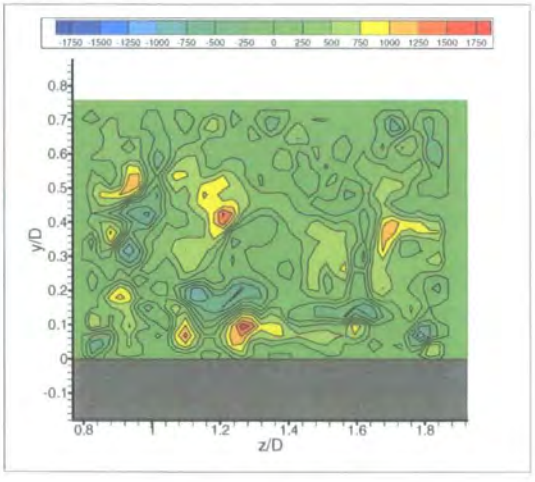


(f) t = 0.4s

Figure 8.116: Sequence Showing Contours of Constant Spanwise Vorticity ($\zeta$) for PosB Centreline (W/D = 0) YZ Plane, Rotating (a-c) and Stationary (d-f).

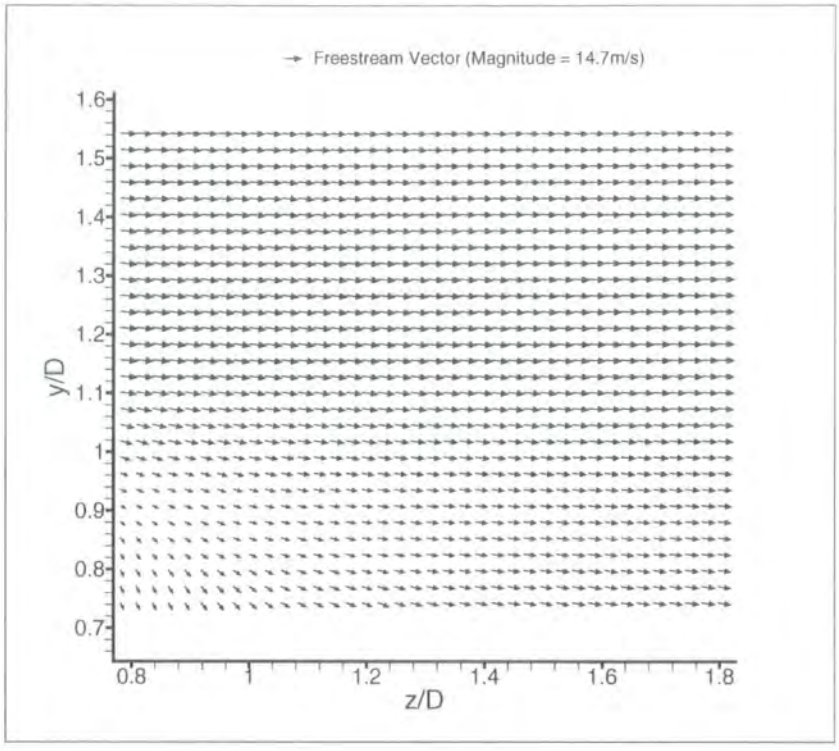


Figure 8.117: Ensemble Time-Averaged Velocity Vectors for Centreline (W/D = 0) YZ Plane (PosC), Rotating.

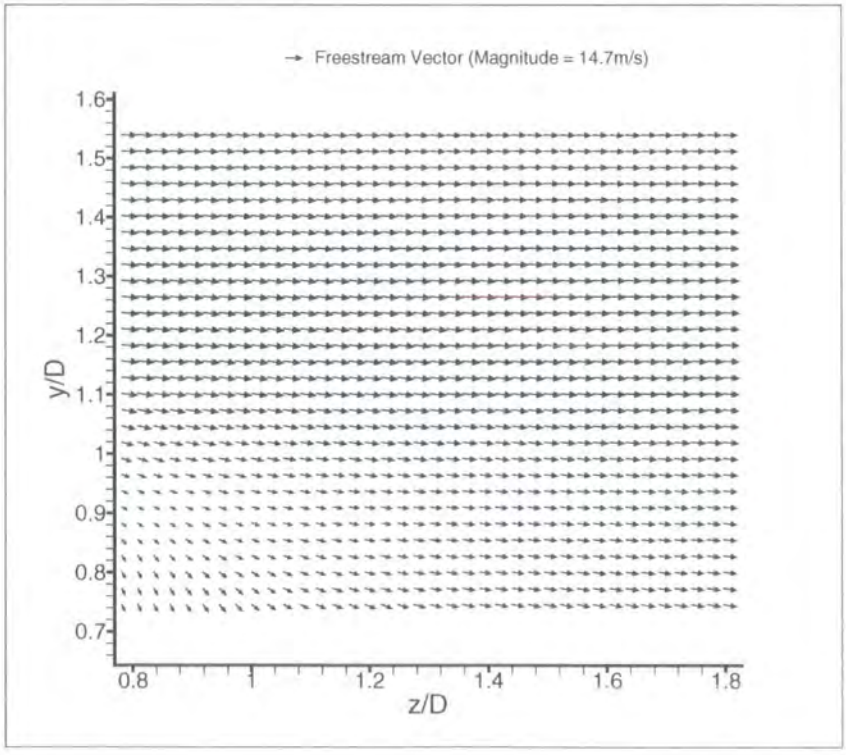


Figure 8.118: Ensemble Time-Averaged Velocity Vectors for Centreline (W/D = 0) YZ Plane (PosC), Stationary

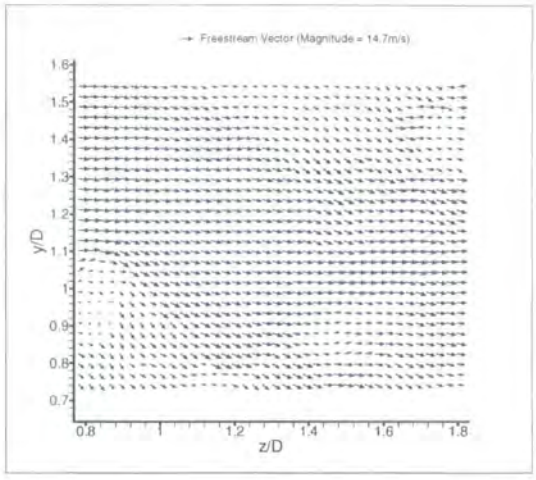


(a) t = 0.0s

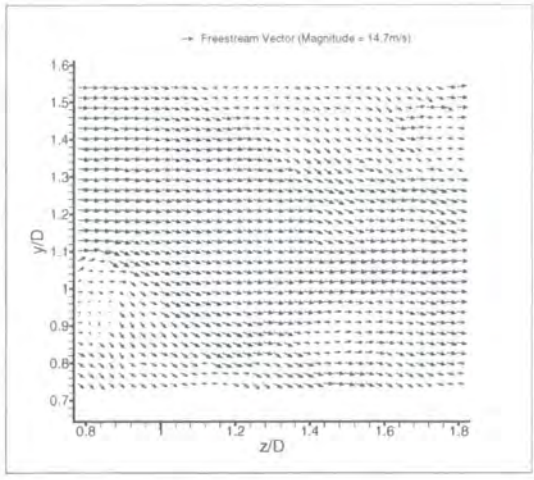


(d) t = 0.0s

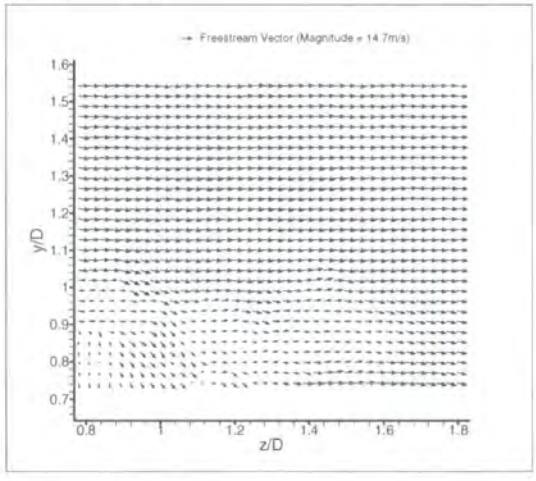


(b) t = 0.2s

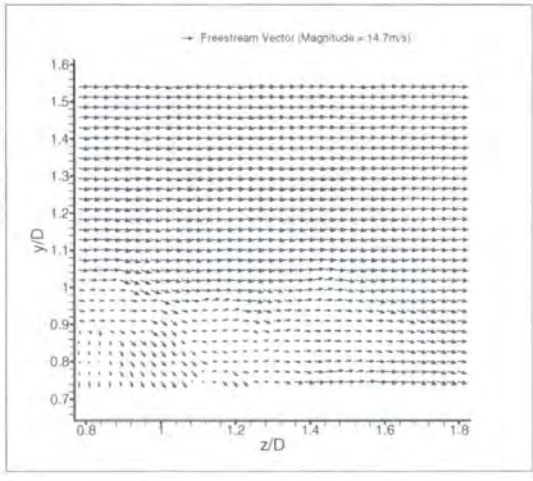


(e) t = 0.2s

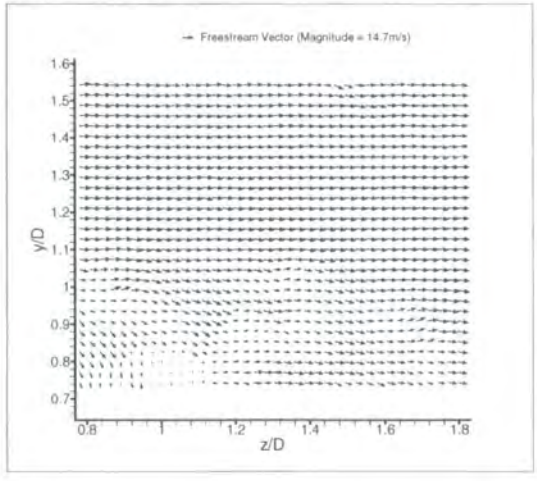


(c) t = 0.4s

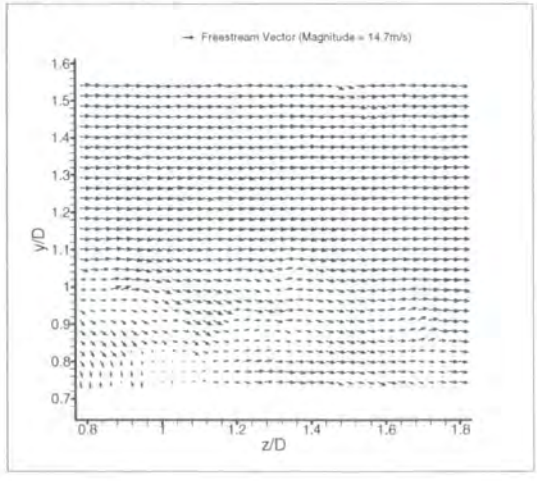


(f) t = 0.4s

Figure 8.119: Sequence Showing Velocity Vectors for PosC Centreline (W/D = 0) YZ Plane, Rotating (a-c) and Stationary (d-f).

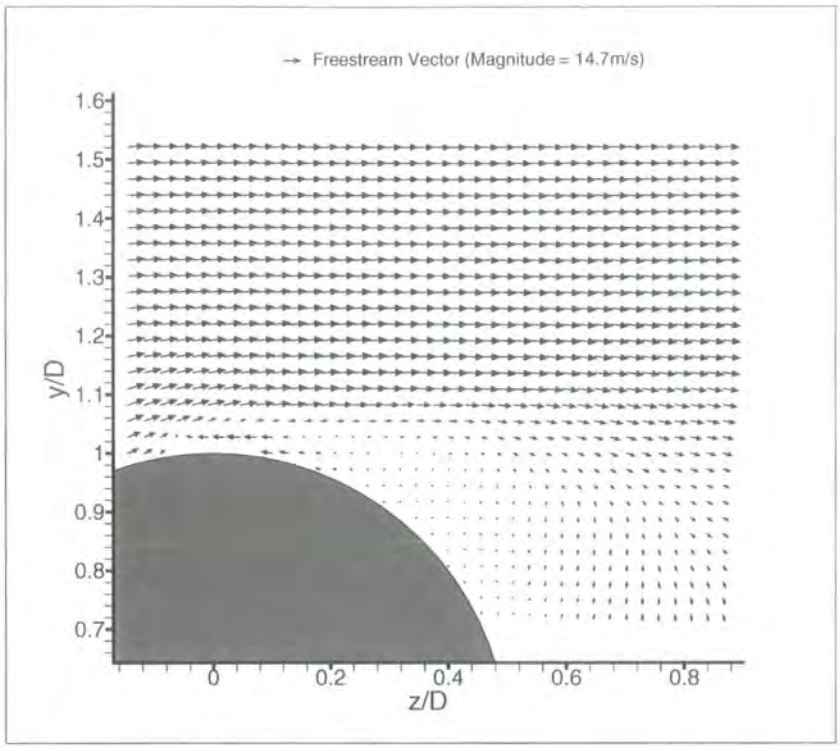


Figure 8.120: Ensemble Time-Averaged Velocity Vectors for Centreline (W/D = 0) YZ Plane (PosD), Rotating.

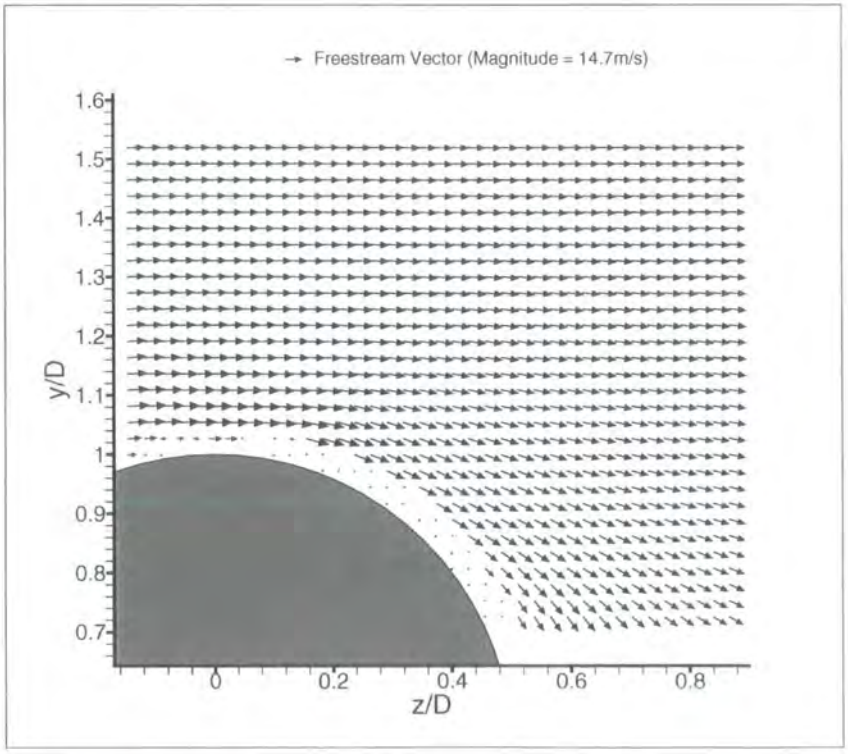


Figure 8.121: Ensemble Time-Averaged Velocity Vectors for Centreline (W/D = 0) YZ Plane (PosD), Stationary

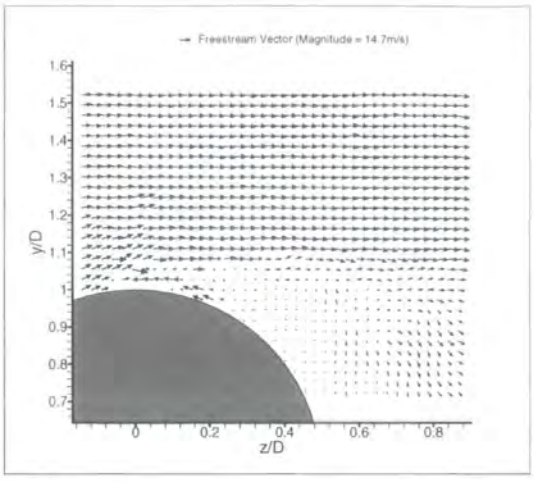


(a) t = 0.0s

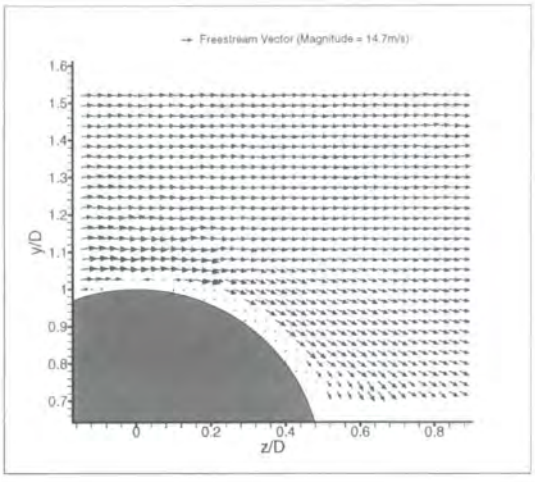


(d) t = 0.0s

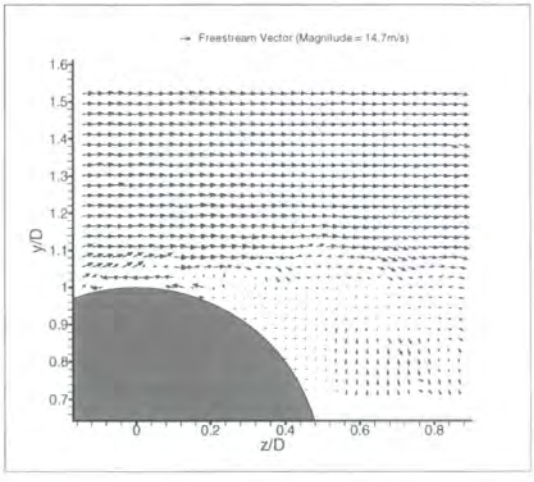


(b) t = 0.2s

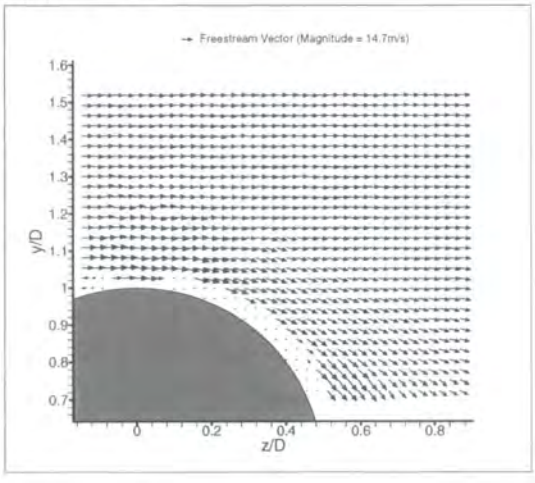


(e) t = 0.2s

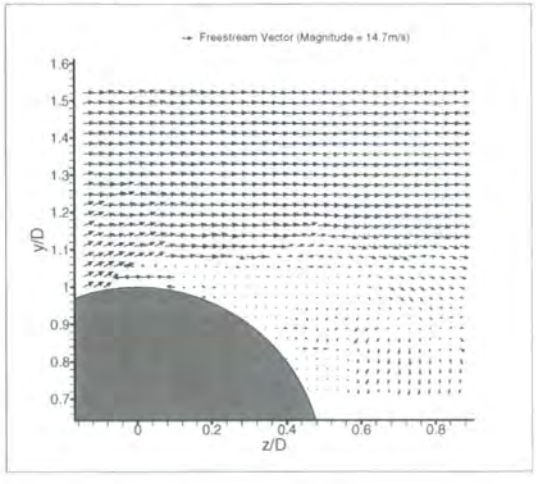


(c) t = 0.4s

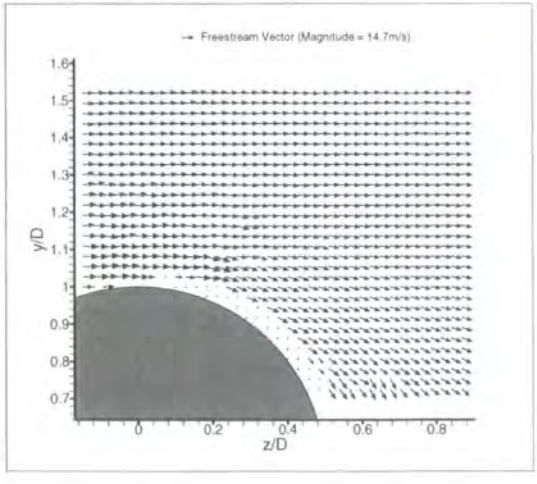


(f) t = 0.4s

Figure 8.122: Sequence Showing Velocity Vectors for PosD Centreline (W/D = 0) YZ Plane, Rotating (a-c) and Stationary (d-f).

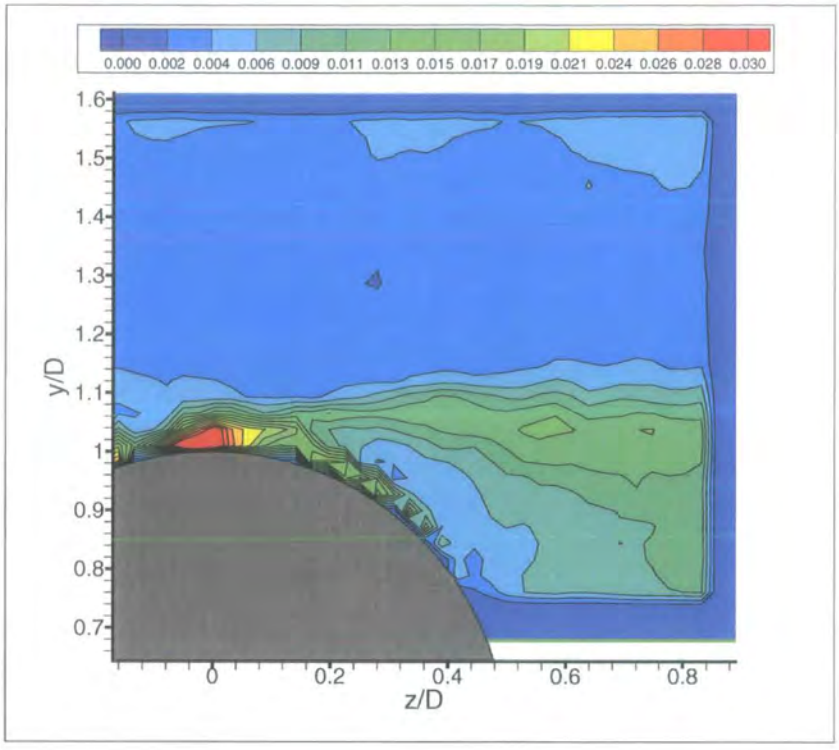


Figure 8.123: Velocity Vector Standard Deviation for Centreline (W/D = 0) YZ Plane (PosD), Rotating.

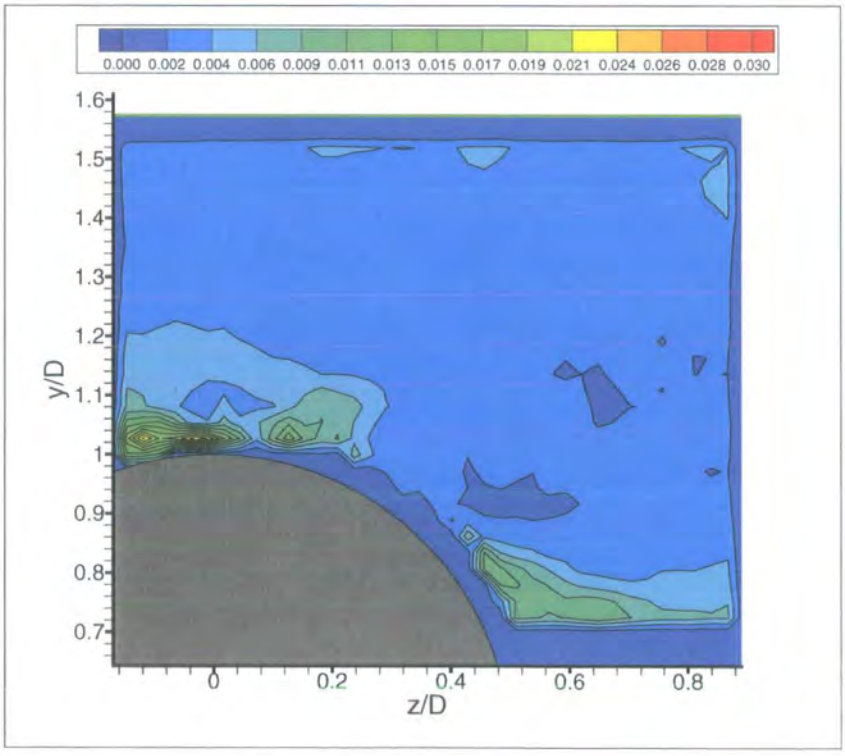


Figure 8.124: Velocity Vector Standard Deviation for Centreline (W/D = 0) YZ Plane (PosD), Stationary.

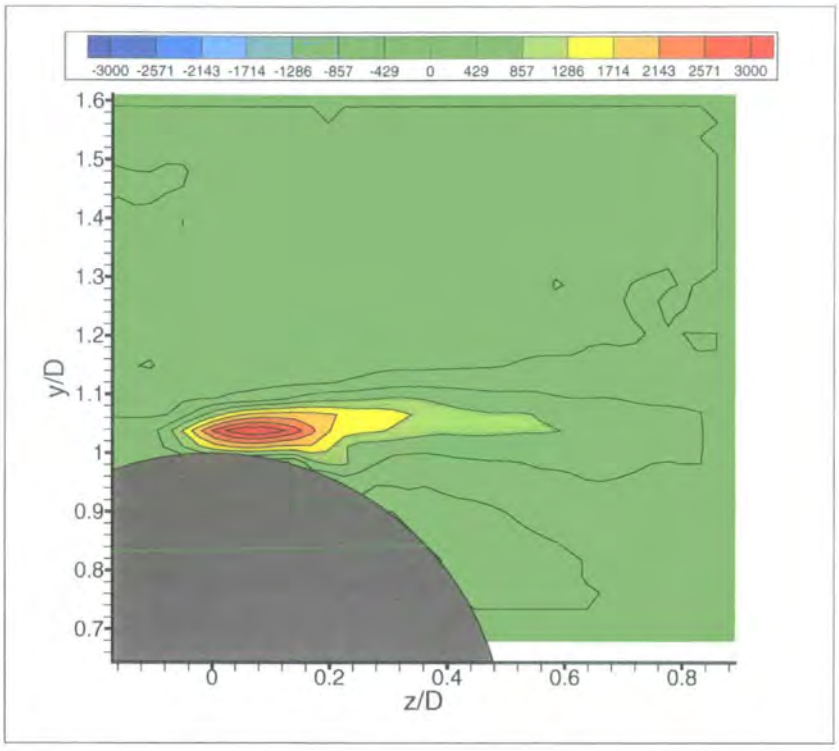


Figure 8.125: Ensemble Time-Averaged Contours of Constant Spanwise Vorticity ($\zeta$) for Centreline (W/D = 0) YZ Plane (PosD), Rotating.

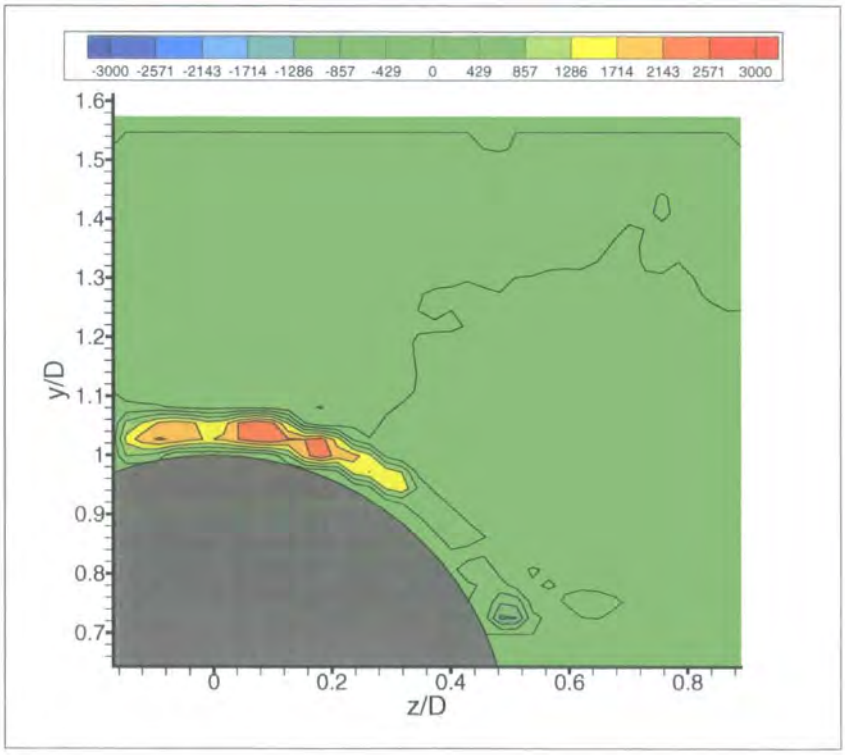


Figure 8.126: Ensemble Time-Averaged Contours of Constant Spanwise Vorticity ($\zeta$) for Centreline (W/D = 0) YZ Plane (PosD), Stationary.

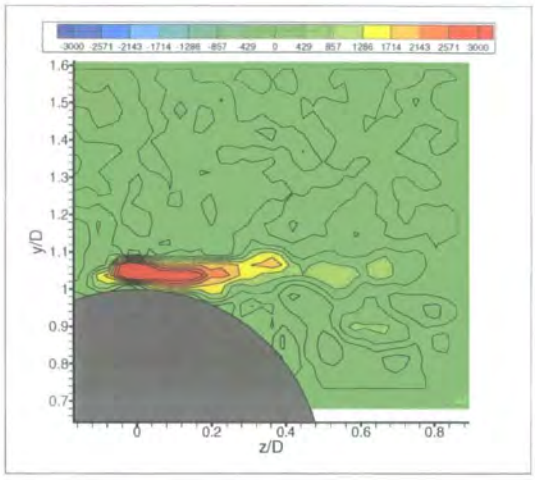


(a) t = 0.0s

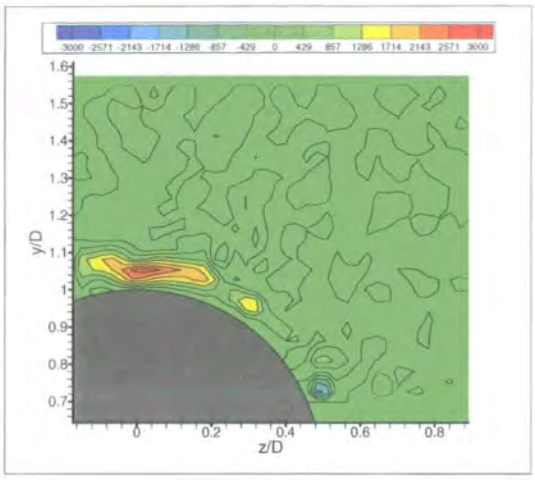


(d) t = 0.0s

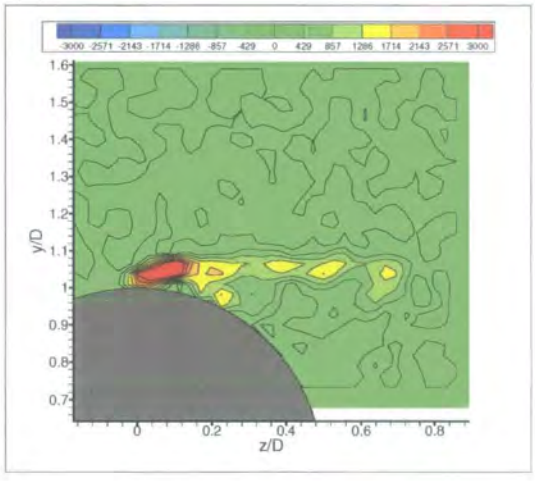


(b) t = 0.2s

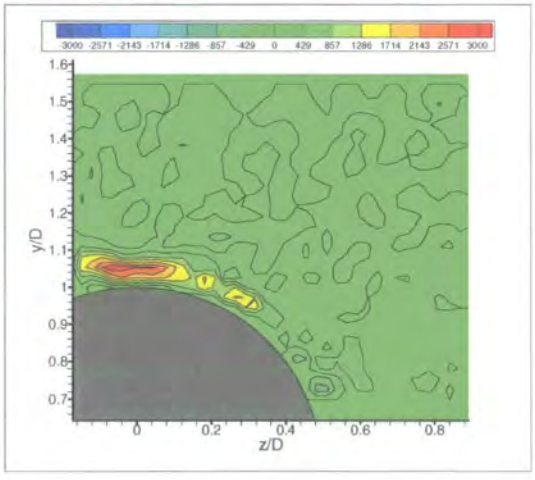


(e) t = 0.2s

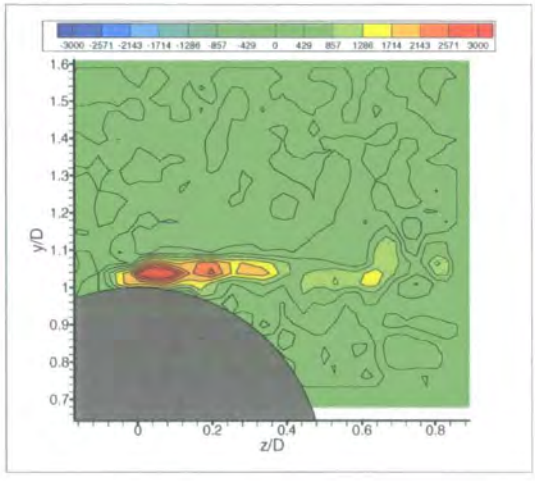


(c) t = 0.4s

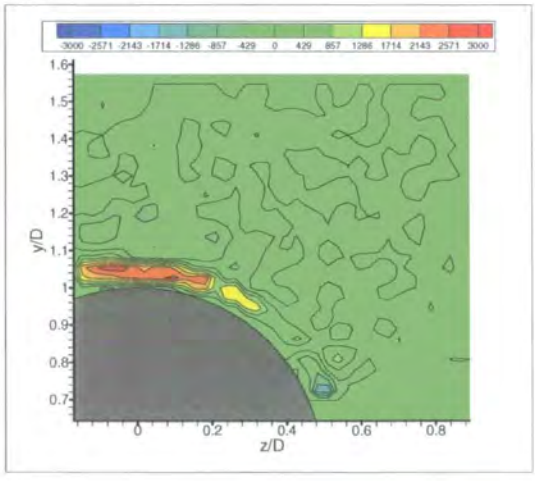


(f) t = 0.4s

Figure 8.127: Sequences Showing Contours of Constant Spanwise Vorticity ($\zeta$) for PosD Centreline (W/D = 0) YZ Plane, Rotating (a-c) and Stationary (d-f).

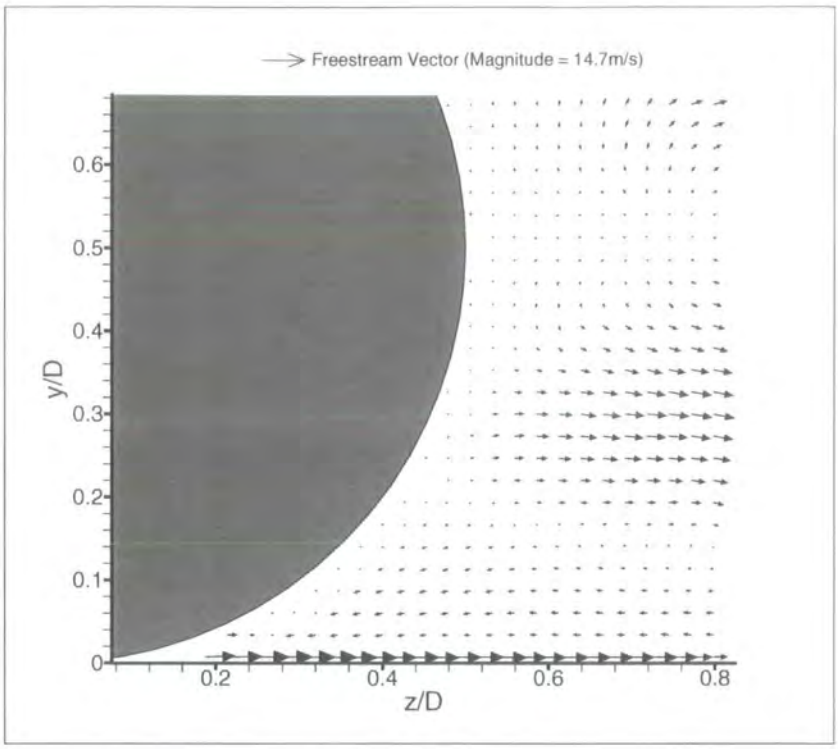


Figure 8.128: Ensemble Time-Averaged Velocity Vectors for Wheel Edge (W/D = +0.18) YZ Plane (PosA), Rotating.

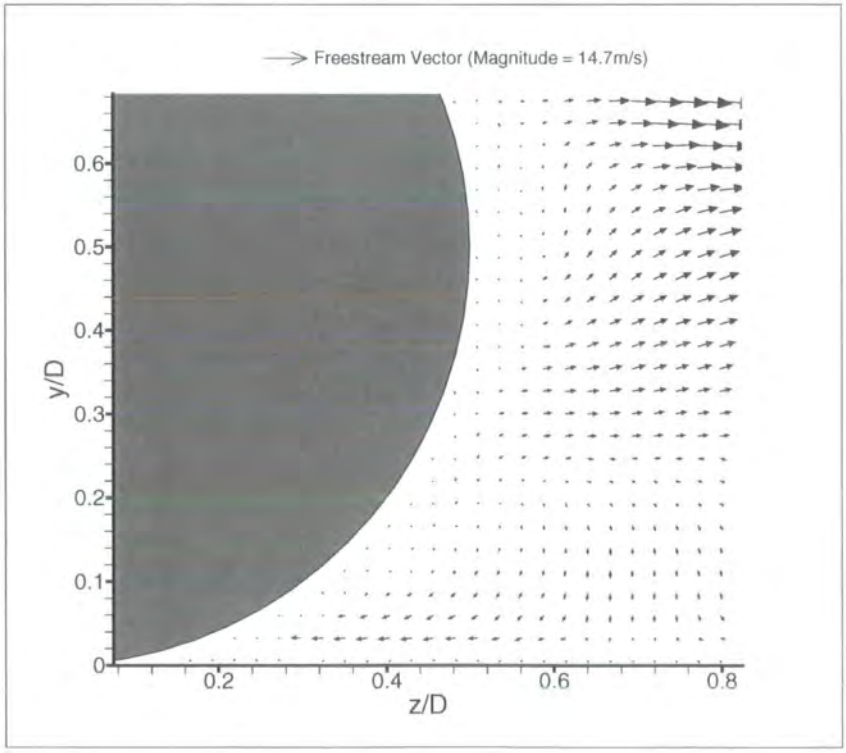


Figure 8.129: Ensemble Time-Averaged Velocity Vectors for Wheel Edge (W/D = +0.18) YZ Plane (PosA), Stationary.

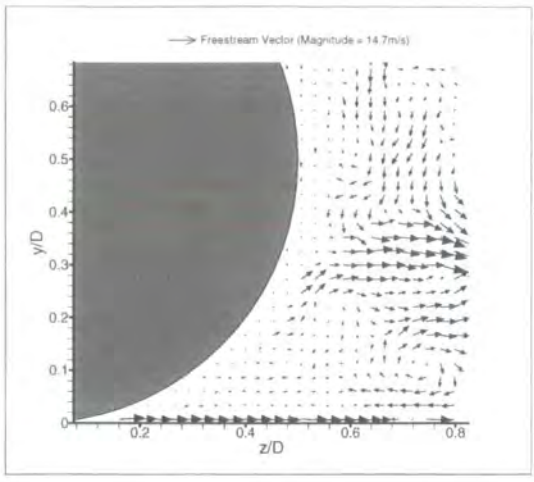


(a) t = 0.0s

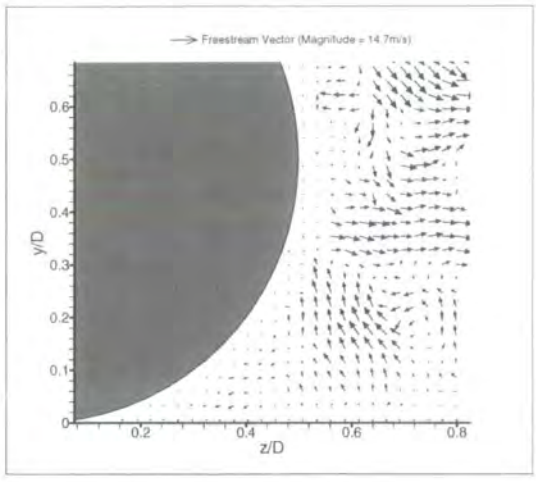


(d) t = 0.0s

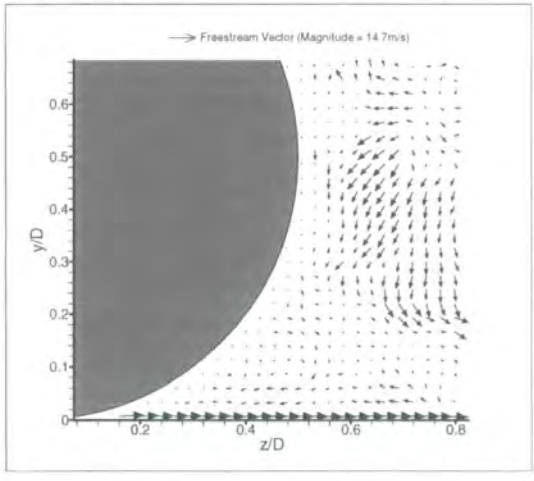


(b) t = 0.2s

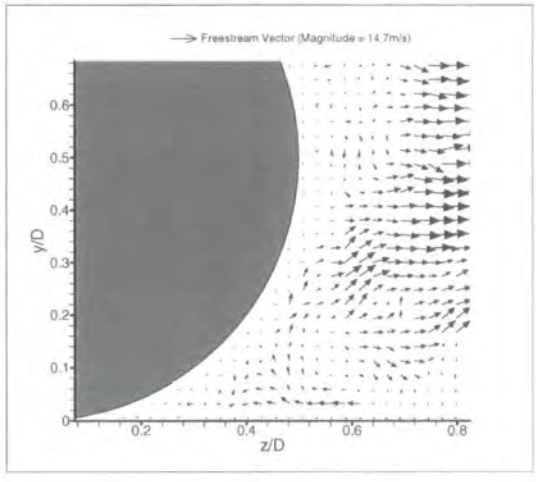


(e) t = 0.2s

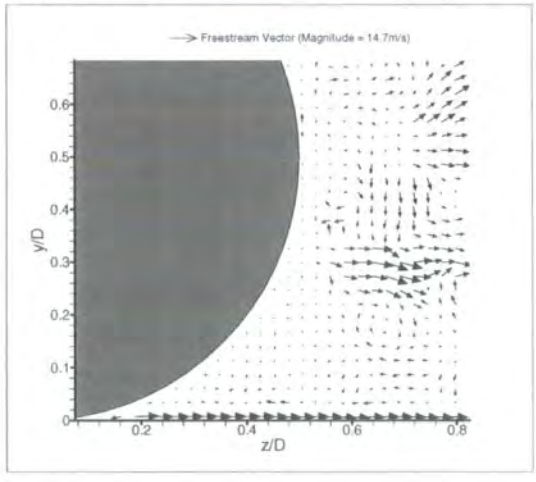


(c) t = 0.4s

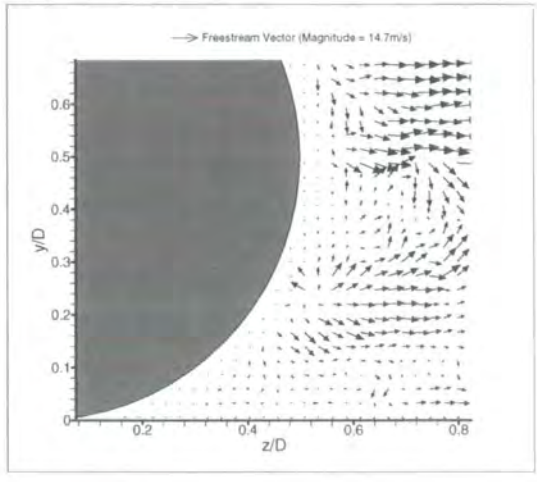


(f) t = 0.4s

Figure 8.130: Sequence Showing Velocity Vectors for PosA Wheel Edge (W/D = 0.18) YZ Plane, Rotating (a-c) and Stationary (d-f).

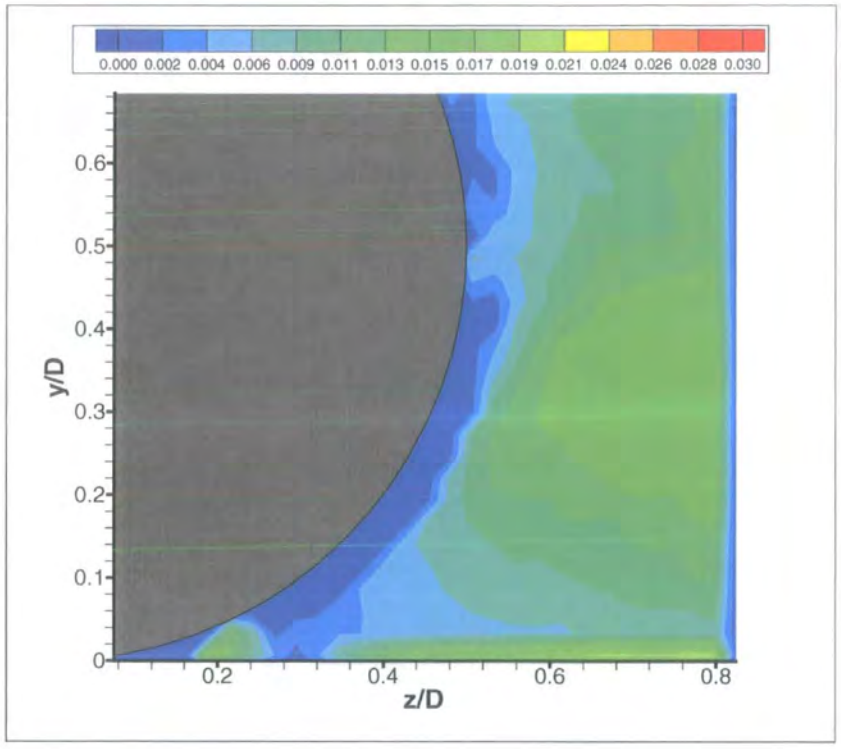


Figure 8.131: Velocity Vector Standard Deviation for Wheel Edge (W/D = +0.18) YZ Plane (PosA), Rotating.

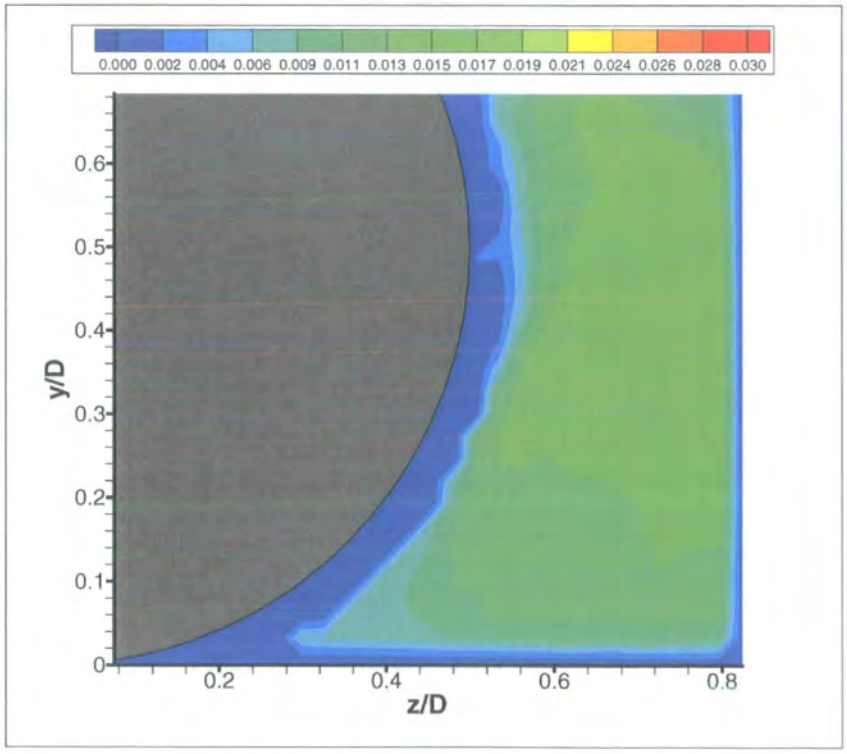


Figure 8.132: Velocity Vector Standard Deviation for Wheel Edge (W/D = +0.18) YZ Plane (PosA), Stationary.

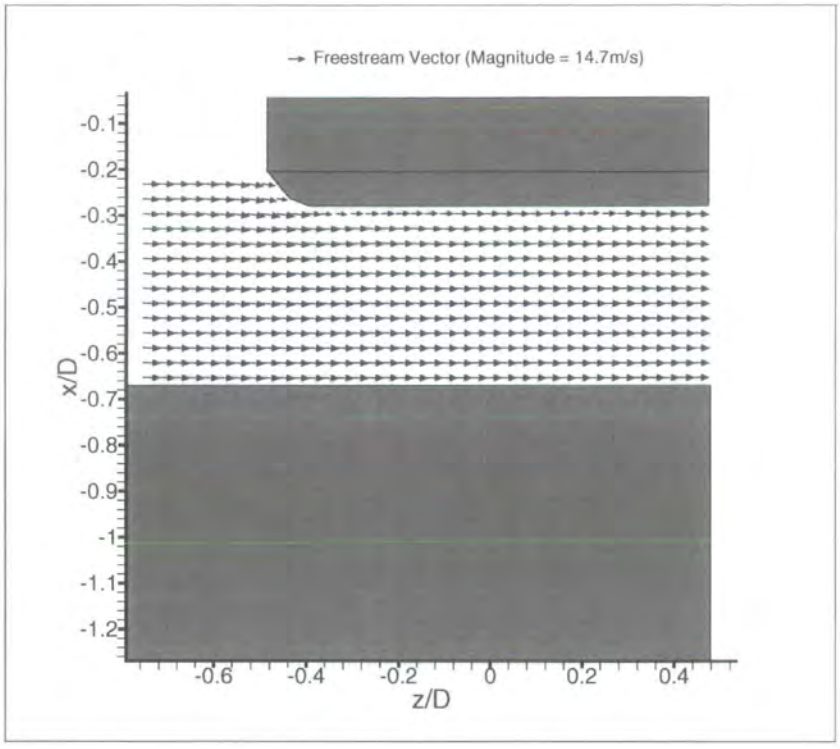


Figure 8.133: Ensemble Time-Averaged Velocity Vectors for Overhead (y/D = 0.26) XZ Plane (PosA), Rotating.

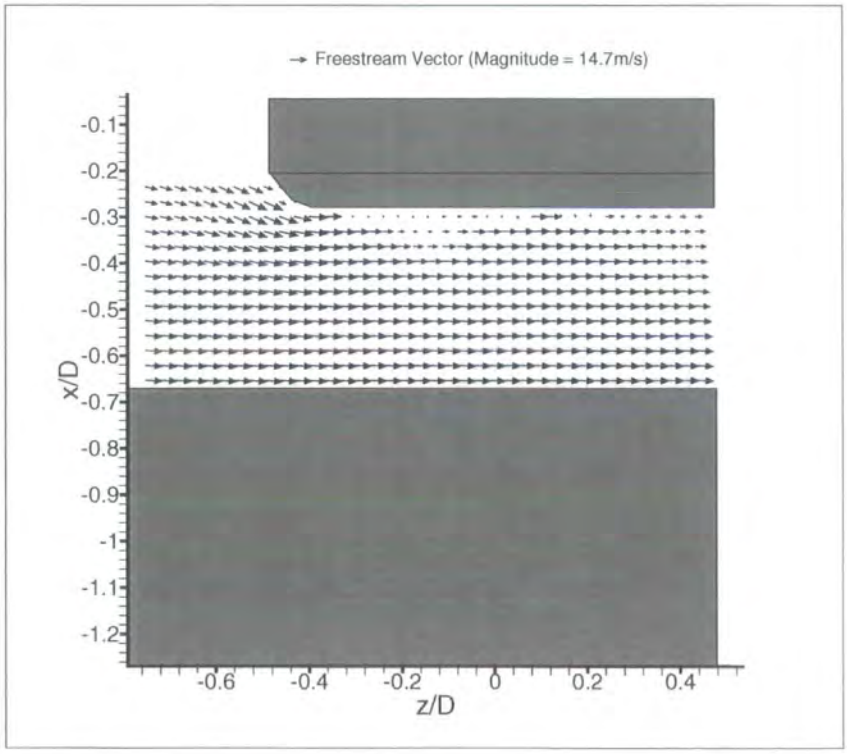


Figure 8.134: Ensemble Time-Averaged Velocity Vectors for Overhead (y/D = 0.26) XZ Plane (PosA), Stationary.

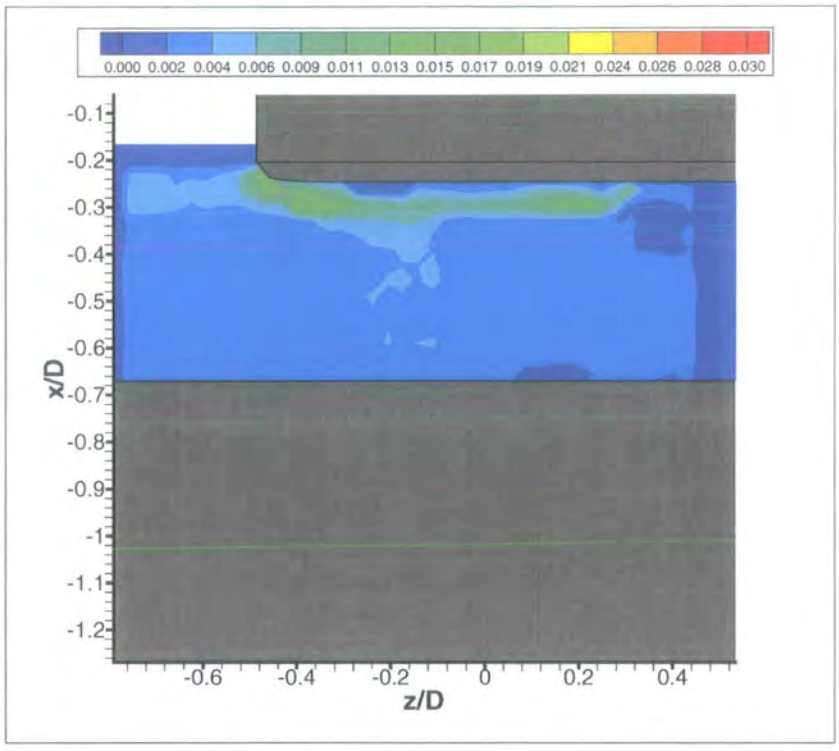


Figure 8.135: Velocity Vector Standard Deviation for Overhead (y/D = 0.26) XZ Plane (PosA), Rotating.

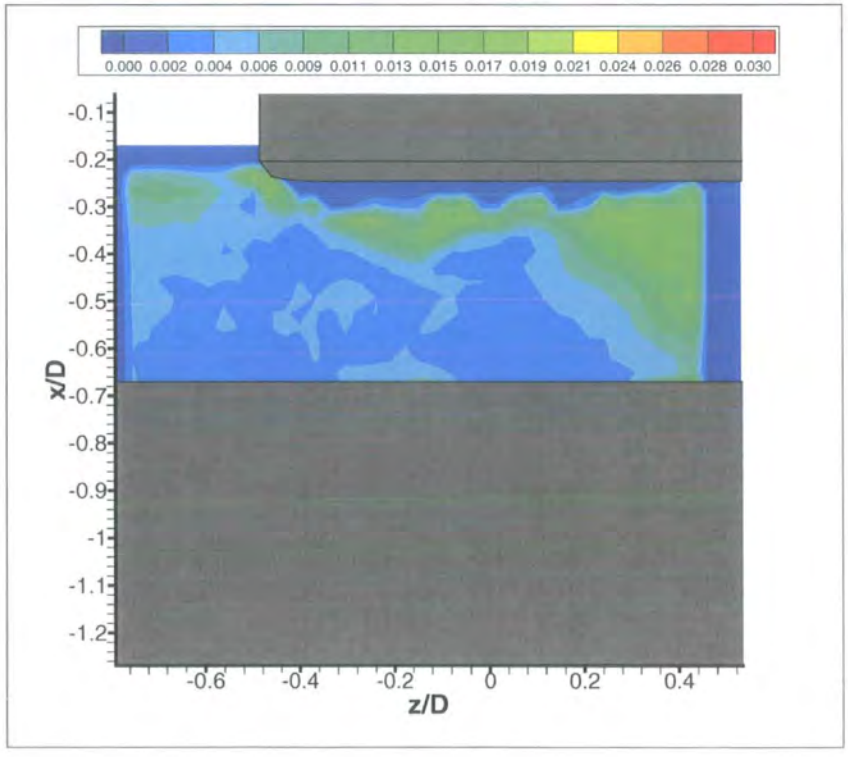


Figure 8.136: Velocity Vector Standard Deviation for Overhead (y/D = 0.26) XZ Plane (PosA), Stationary.

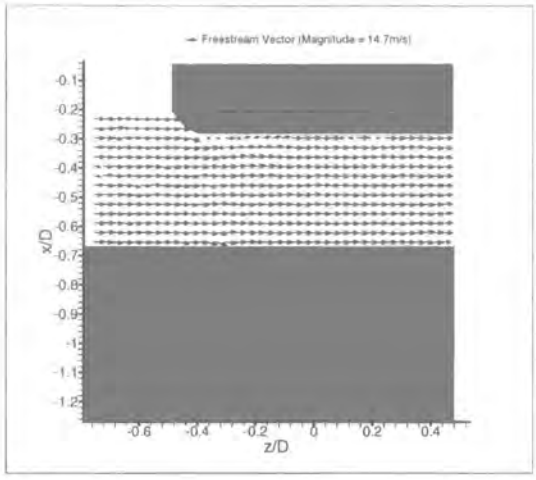


(a) t = 0.0s

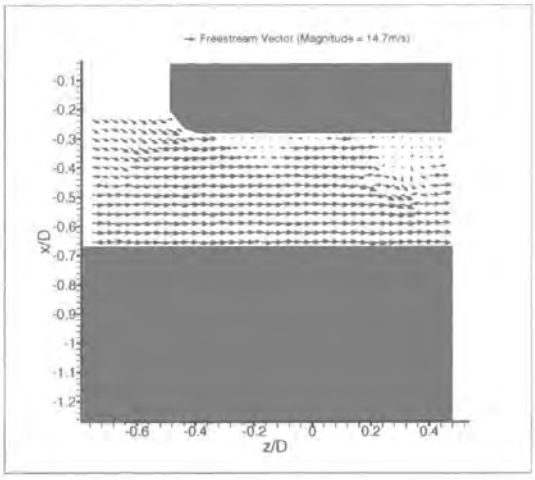


(d) t = 0.0s

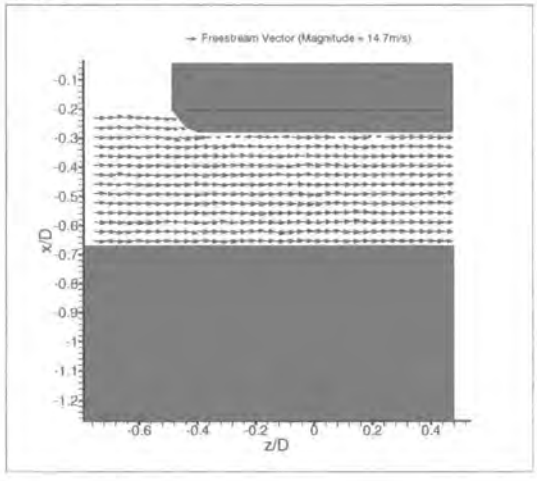


(b) t = 0.2s

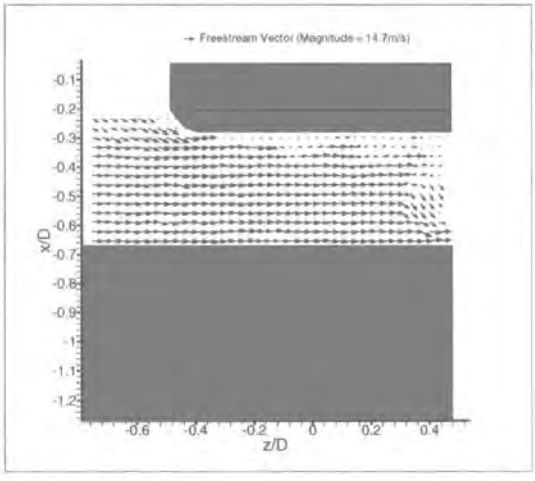


(e) t = 0.2s

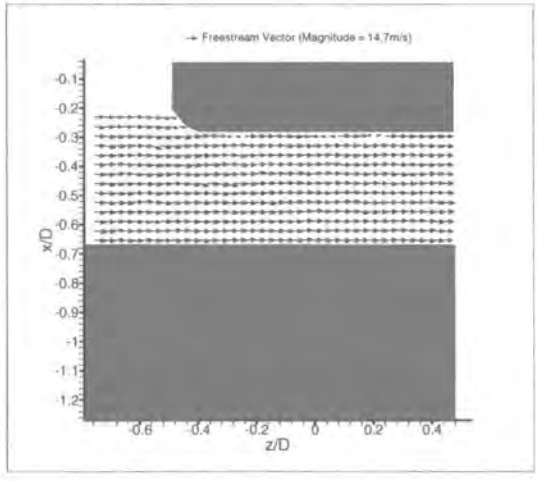


(c) t = 0.4s

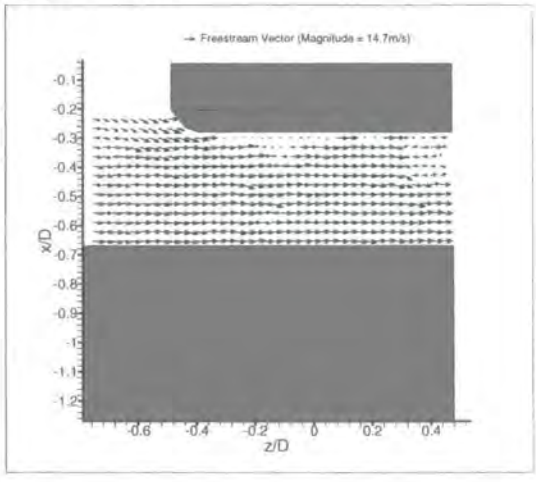


(f) t = 0.4s

Figure 8.137: Sequence Showing Velocity Vectors for PosA Overhead (y/D = 0.26) XZ Plane, Rotating (a-c) and Stationary (d-f).

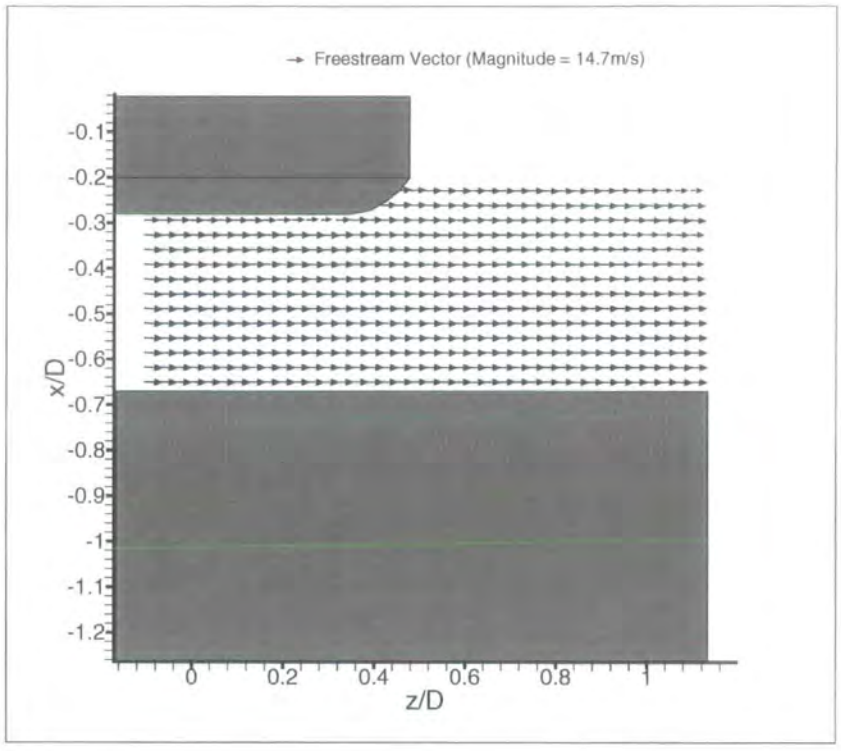


Figure 8.138: Ensemble Time-Averaged Velocity Vectors for Overhead (y/D = 0.26) XZ Plane (PosB), Rotating.

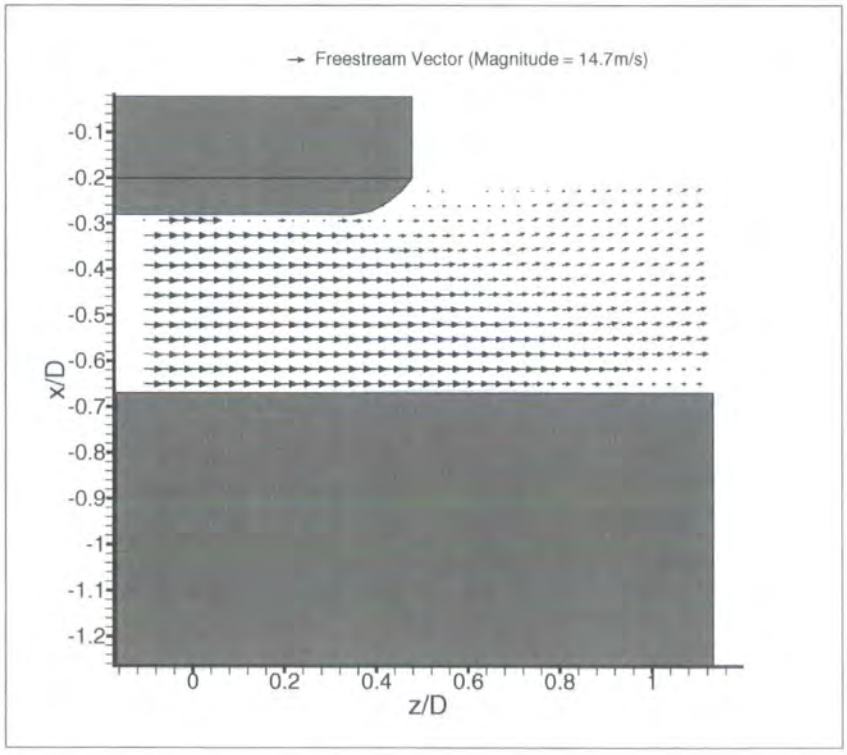


Figure 8.139: Ensemble Time-Averaged Velocity Vectors for Overhead (y/D = 0.26) XZ Plane (PosB), Stationary.

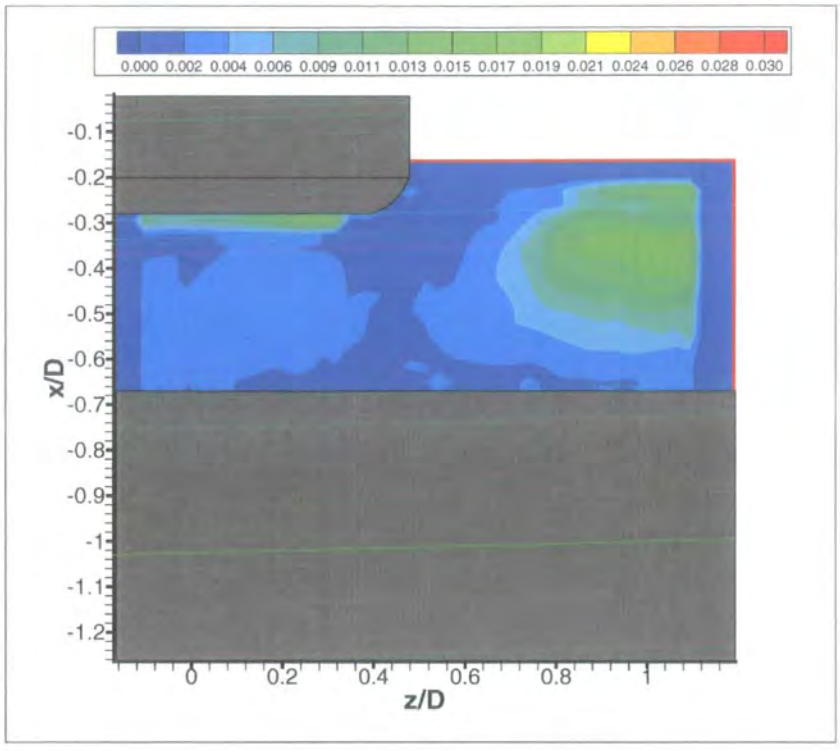


Figure 8.140: Velocity Vector Standard Deviation for Overhead (y/D = 0.26) XZ Plane (PosB), Rotating.

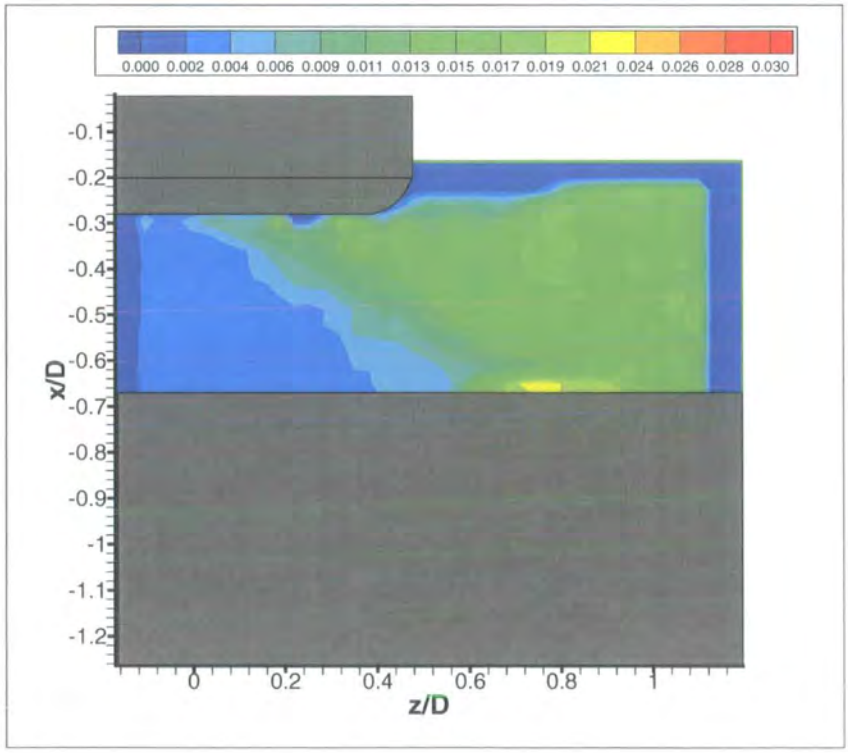


Figure 8.141: Velocity Vector Standard Deviation for Overhead (y/D = 0.26) XZ Plane (PosB), Stationary.

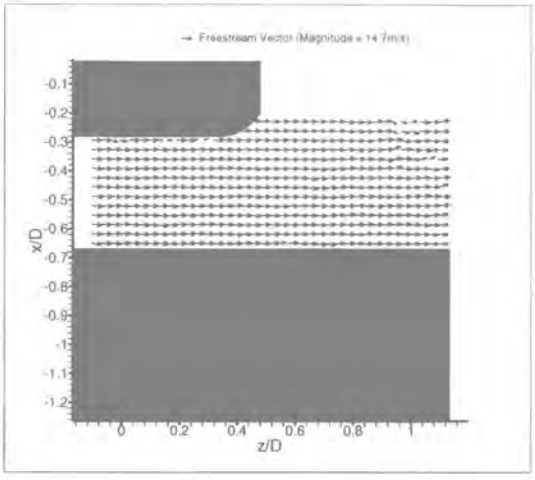


(a) t = 0.0s

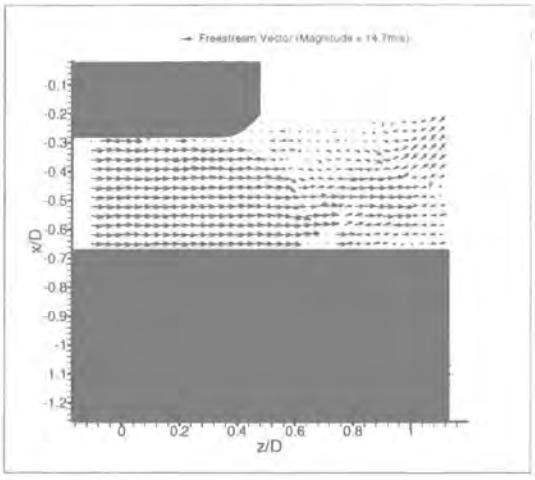


(d) t = 0.0s

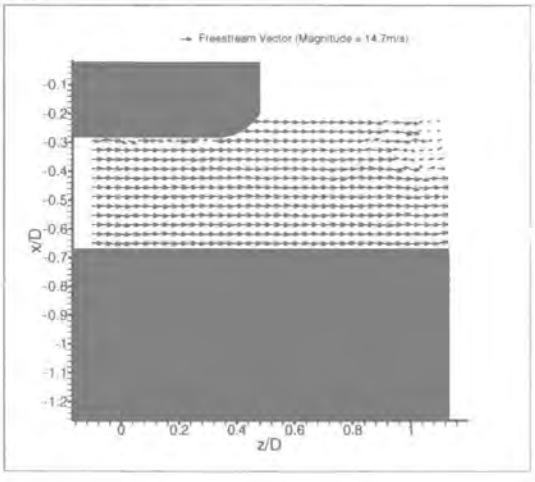


(b) t = 0.2s

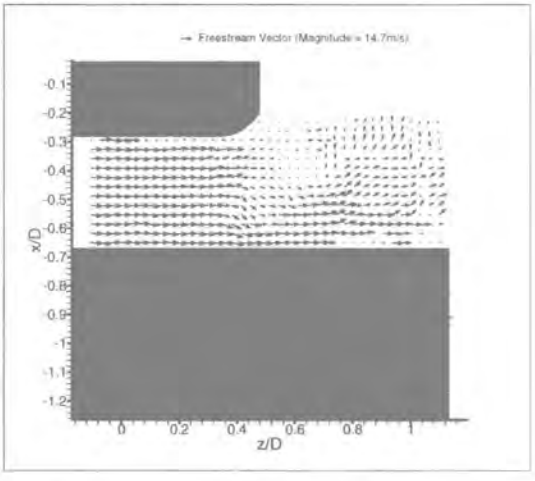


(e) t = 0.2s

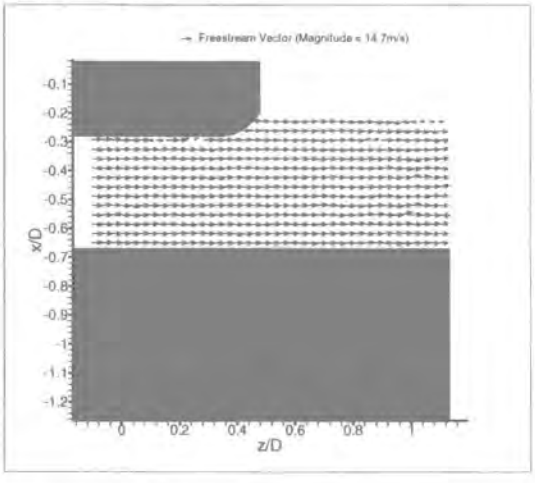


(c) t = 0.4s

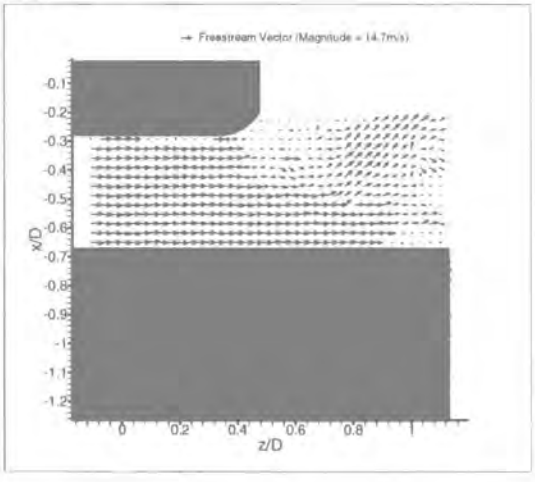


(f) t = 0.4s

Figure 8.142: Sequence Showing Velocity Vectors for PosB Overhead (y/D = 0.26) XZ Plane, Rotating (a-c) and Stationary (d-f).

# Chapter 9

# Computational Results

## 9.1 Introduction

This chapter presents the CFD results for the rotating and stationary wheel, acquired using the aforementioned computational techniques. The results are presented in identical format to the experimental results with the data in separate sections.

## 9.2 Predicted Static Pressure Distributions

The predicted static pressure distributions were obtained by exporting the static pressure data at regions corresponding to the experimental pressure tappings. Effectively 1mm slices of the wheel were exported, therefore due to the unstructured nature of topology some distributions presented have a lower number of data points at particular radial positions.

Figure 9.1 shows the steady-state surface static pressure distribution for the centreline of the rotating wheel compared to experiment. Figure 9.2 shows the steady-state surface static pressure distribution for tapping +2 (W/D=+0.037) on the rotating wheel compared to experiment. Figure 9.3 shows the steady-state surface static pressure distribution for tapping +3 (W/D=+0.073) on the rotating wheel compared to experiment. Figure 9.4 shows the steady-state surface static pressure distribu-

tion for tapping +4 (W/D=+0.110) on the rotating wheel compared to experiment. Figure 9.5 shows the steady-state surface static pressure distribution for tapping +5 (W/D=+0.146) on the rotating wheel compared to experiment. Figure 9.6 shows the steady-state surface static pressure distribution for tapping +6 (W/D=+0.183) on the rotating wheel compared to experiment. Figure 9.7 shows the steady-state surface static pressure distribution for tapping +7 (W/D=+0.220) on the rotating wheel compared to experiment. Figure 9.8 shows the steady-state surface static pressure distribution for tapping +8 (W/D=+0.244) on the rotating wheel compared to experiment. Figure 9.9 shows the steady-state surface static pressure distribution for tapping +9 (W/D=+0.268) on the rotating wheel compared to experiment. Figure 9.10 shows the steady-state surface static pressure distribution for tapping +10 (W/D=+0.280) on the rotating wheel compared to experiment. Figure 9.11 shows the steady-state surface static pressure distribution for tapping +11 (W/D=+0.272) on the rotating wheel compared to experiment.

## 9.3 Predicted XY Wake Planes

### 9.3.1 XY Spanwise Plane at Streamwise Station Z/D = 0

Figure 9.12 shows predicted steady-state contours of constant total pressure for the rotating wheel at the streamwise station z/D = 0. Predicted steady-state contours of constant streamwise vorticity for the rotating wheel at z/D = 0 are shown in Figure 9.13. Figure 9.14 shows predicted steady-state secondary flow velocity vectors at z/D = 0 for the rotating wheel.

### 9.3.2 XY Spanwise Plane at Streamwise Station Z/D = 0.25

Figure 9.15 shows predicted steady-state contours of constant total pressure for the rotating wheel at the streamwise station z/D = 0.25. Predicted steady-state contours of constant streamwise vorticity for the rotating wheel at z/D = 0.25 are shown in Figure 9.16. Figure 9.17 shows predicted steady-state secondary flow velocity vectors at z/D = 0.25 for the rotating wheel.

### 9.3.3 XY Spanwise Plane at Streamwise Station Z/D = 0.75

Figure 9.18 shows predicted steady-state contours of constant total pressure for the rotating wheel at the streamwise station z/D = 0.75. Predicted steady-state contours of constant streamwise vorticity for the rotating wheel at z/D = 0.75 are shown in Figure 9.19. Figure 9.20 shows predicted steady-state secondary flow velocity vectors at z/D = 0.75 for the rotating wheel.

### 9.3.4 XY Spanwise Plane at Streamwise Station Z/D = 1.0

Figure 9.21 shows predicted steady-state contours of constant total pressure for the rotating wheel at the streamwise station z/D = 1.0. Predicted steady-state contours of constant streamwise vorticity for the rotating wheel at z/D = 1.0 are shown in Figure 9.22. Figure 9.23 shows predicted steady-state secondary flow velocity vectors at z/D = 1.0 for the rotating wheel.

### 9.3.5 XY Spanwise Plane at Streamwise Station Z/D = 1.5

Figure 9.24 shows predicted steady-state contours of constant total pressure for the rotating wheel at the streamwise station z/D = 1.5. Predicted steady-state contours of constant streamwise vorticity for the rotating wheel at z/D = 1.5 are shown in Figure 9.25. Figure 9.26 shows predicted steady-state secondary flow velocity vectors at z/D = 1.5 for the rotating wheel.

### 9.3.6 XY Spanwise Plane at Streamwise Station Z/D = 2.0

Figure 9.27 shows predicted steady-state contours of constant total pressure for the rotating wheel at the streamwise station z/D = 2.0. Predicted steady-state contours of constant streamwise vorticity for the rotating wheel at z/D = 2.0 are shown in Figure 9.28. Figure 9.29 shows predicted steady-state secondary flow velocity vectors at z/D = 2.0 for the rotating wheel.

## 9.4 Predicted YZ Centreline Planes

Figure 9.30 shows predicted steady-state velocity vectors for the complete (PosA-D) analysis region on the rotating wheel centreline. Figure 9.31 shows the predicted velocity vectors for PosA on the centreline of the rotating wheel. Figure 9.32 shows the predicted velocity vectors for PosD on the centreline of the rotating wheel. The prediction of the rear jetting phenomenon is shown in Figure 9.33 for the centreline of the rotating wheel.

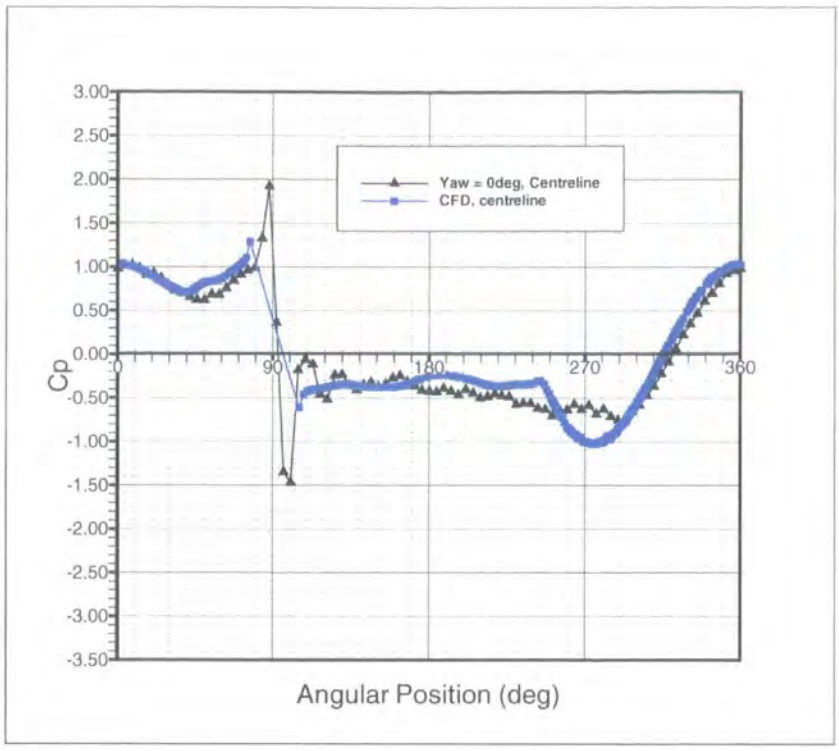


Figure 9.1: Predicted Steady State Surface Static Pressure Distribution for the Centreline (W/D = 0) of the Rotating Wheel compared to Experiment.

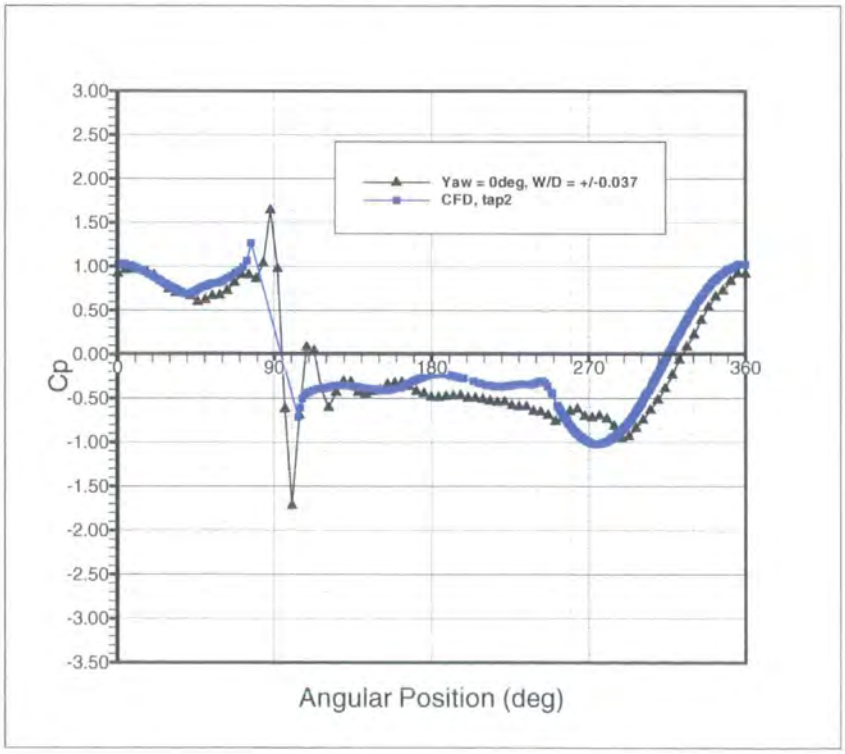


Figure 9.2: Predicted Steady State Surface Static Pressure Distributions for Tapping 2 (W/D=+0.037) of the Rotating Wheel compared to Experiment.

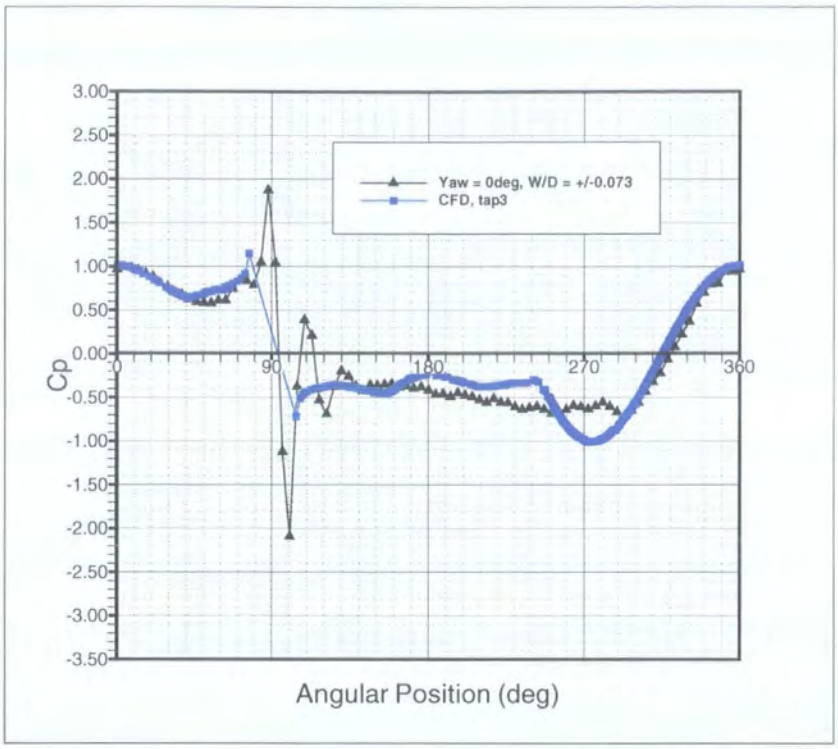


Figure 9.3: Predicted Steady State Surface Static Pressure Distributions for Tapping 3 (W/D=+0.073) of the Rotating Wheel compared to Experiment.

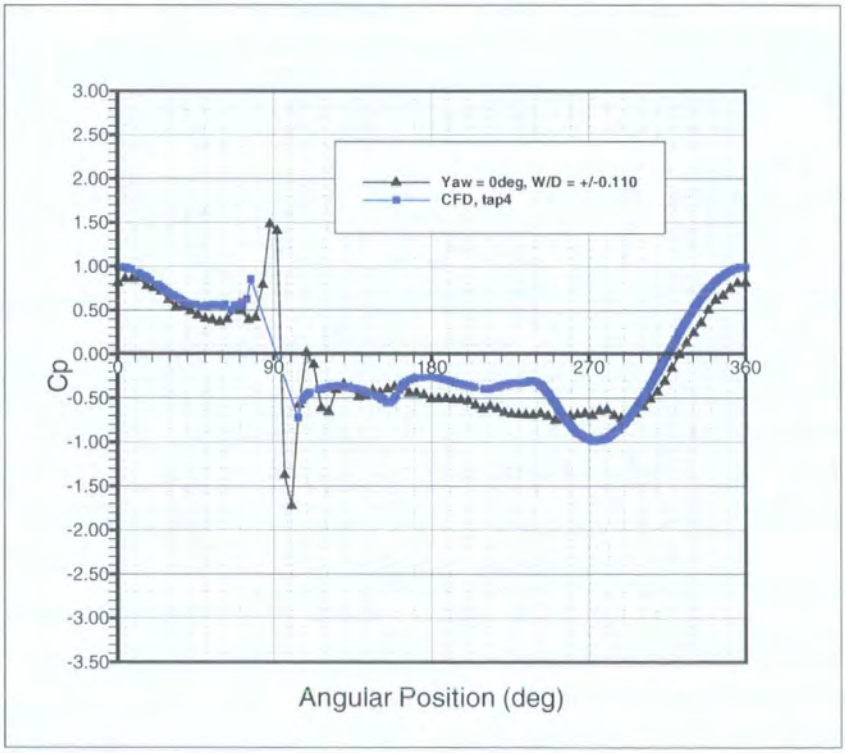


Figure 9.4: Predicted Steady State Surface Static Pressure Distributions for Tapping 4 (W/D=+0.110) of the Rotating Wheel compared to Experiment.

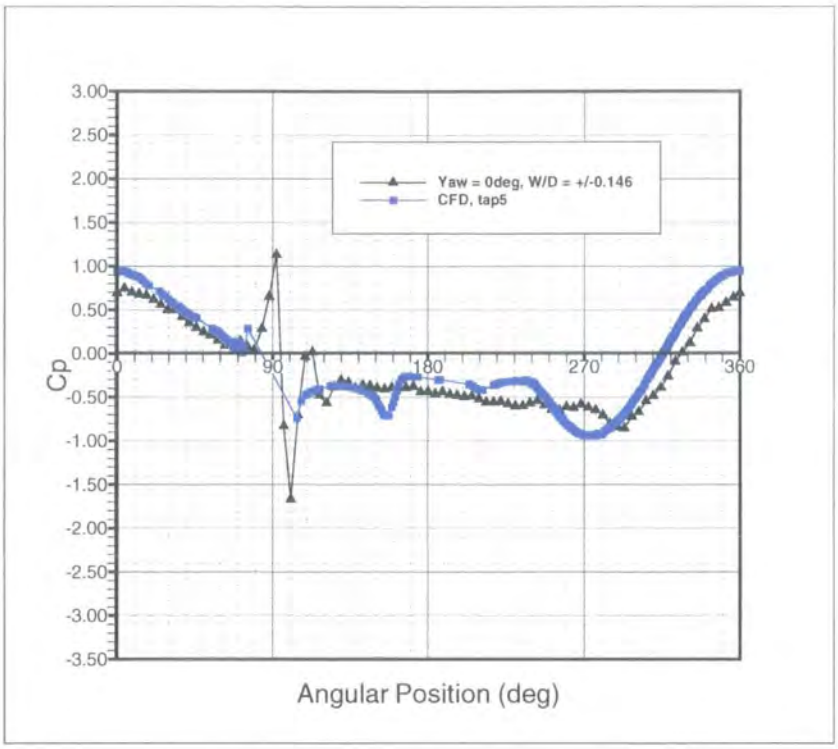


Figure 9.5: Predicted Steady State Surface Static Pressure Distributions for Tapping 5 (W/D=+0.146) of the Rotating Wheel compared to Experiment.

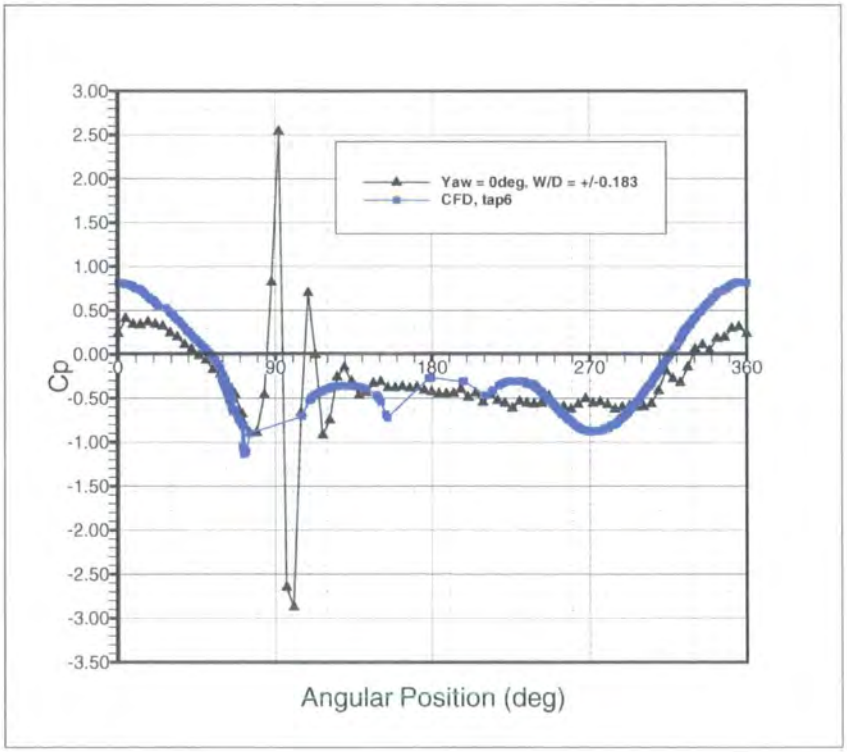


Figure 9.6: Predicted Steady State Surface Static Pressure Distributions for Tapping 6 (W/D=+0.183) of the Rotating Wheel compared to Experiment.

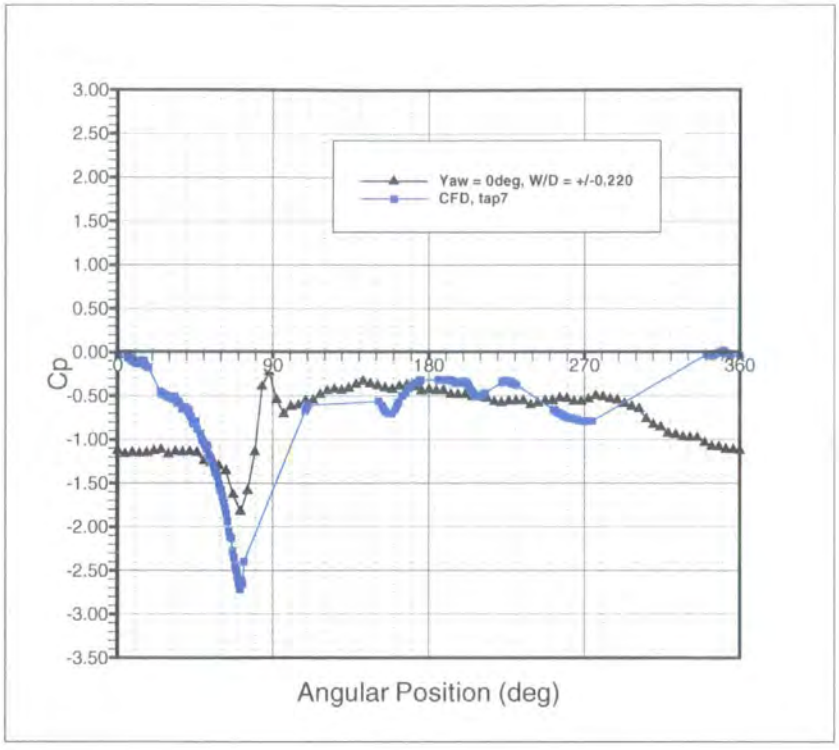


Figure 9.7: Predicted Steady State Surface Static Pressure Distributions for Tapping 7 (W/D=+0.220) of the Rotating Wheel compared to Experiment.

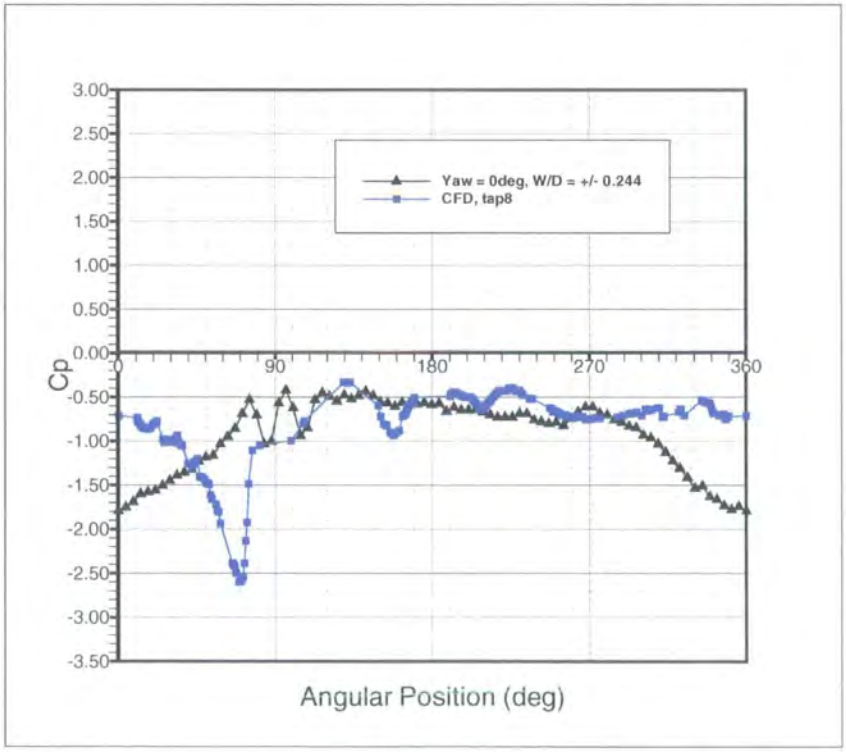


Figure 9.8: Predicted Steady State Surface Static Pressure Distributions for Tapping 8 (W/D=+0.244) of the Rotating Wheel compared to Experiment.

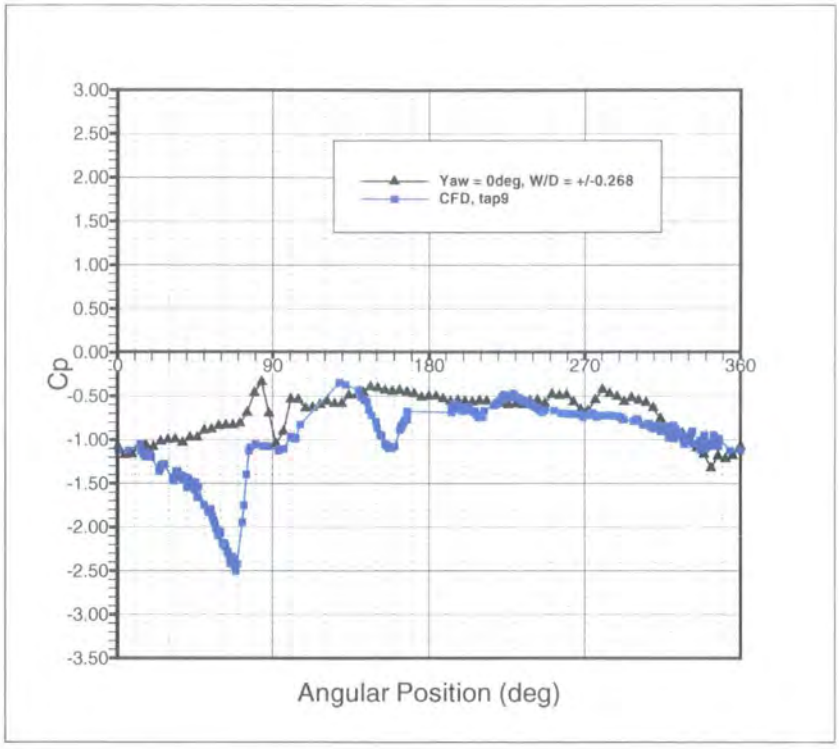


Figure 9.9: Predicted Steady State Surface Static Pressure Distributions for Tapping 9 (W/D=+0.268) of the Rotating Wheel compared to Experiment.

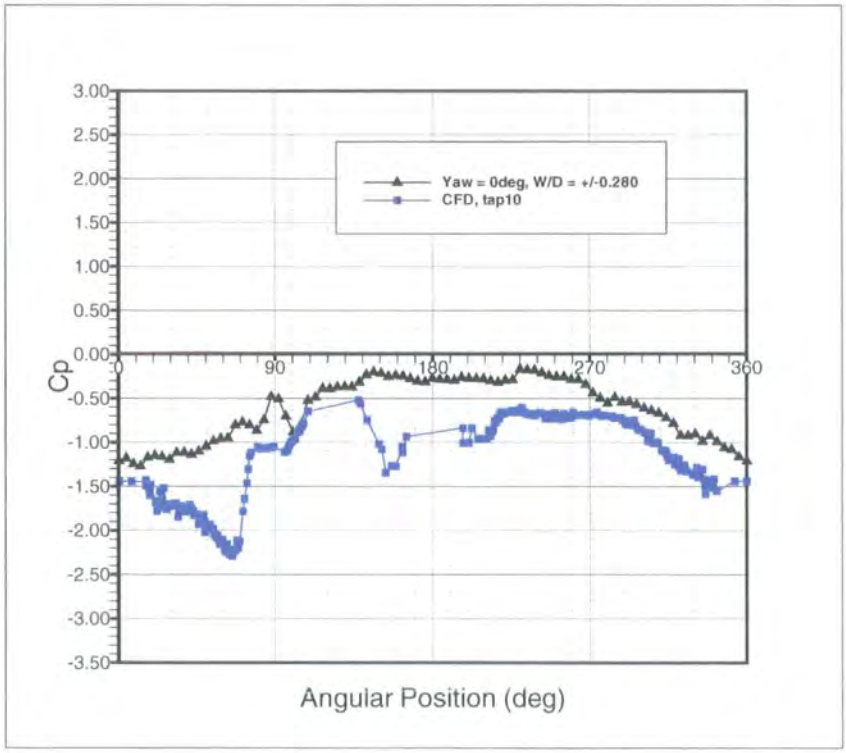


Figure 9.10: Predicted Steady State Surface Static Pressure Distributions for Tapping 10 (W/D=+0.280) of the Rotating Wheel compared to Experiment.

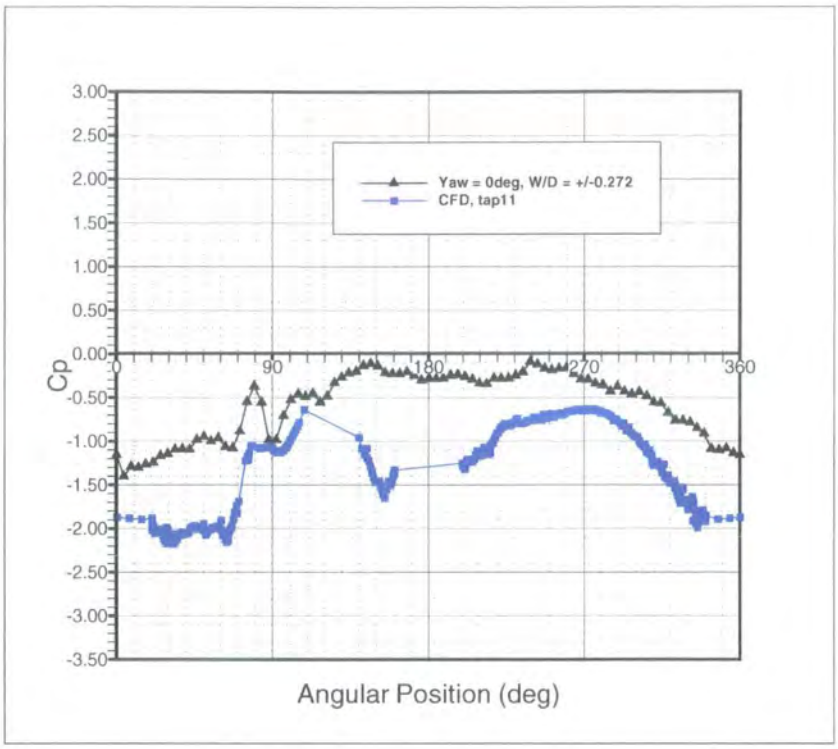


Figure 9.11: Predicted Steady State Surface Static Pressure Distributions for Tapping 11 (W/D=+0.272) of the Rotating Wheel compared to Experiment.

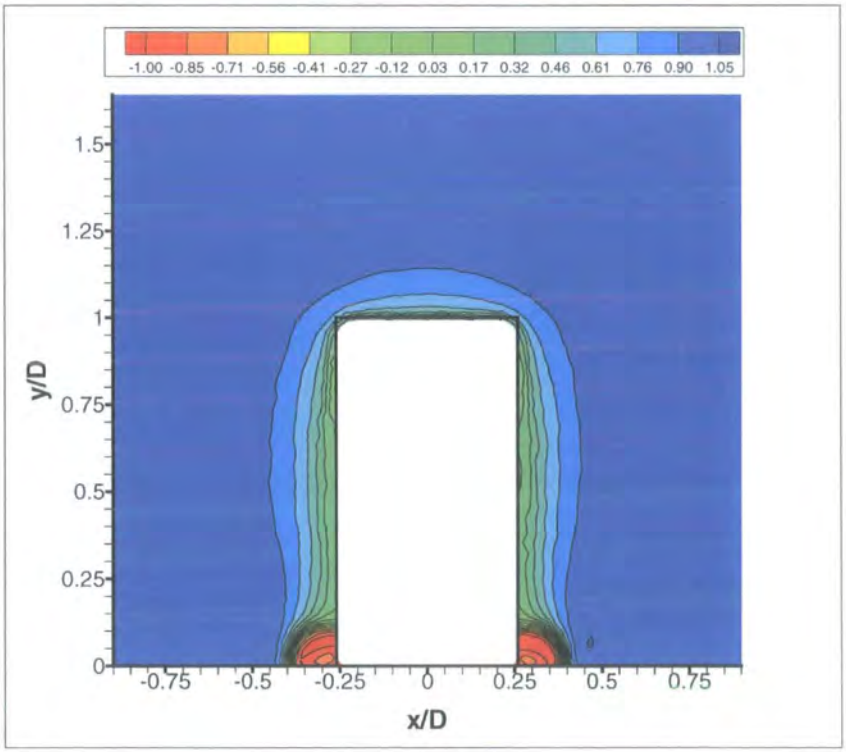


Figure 9.12: Predicted Steady State Contours of Constant Total Pressure Coefficient, Rotating, XY Plane @ Z/D = 0.

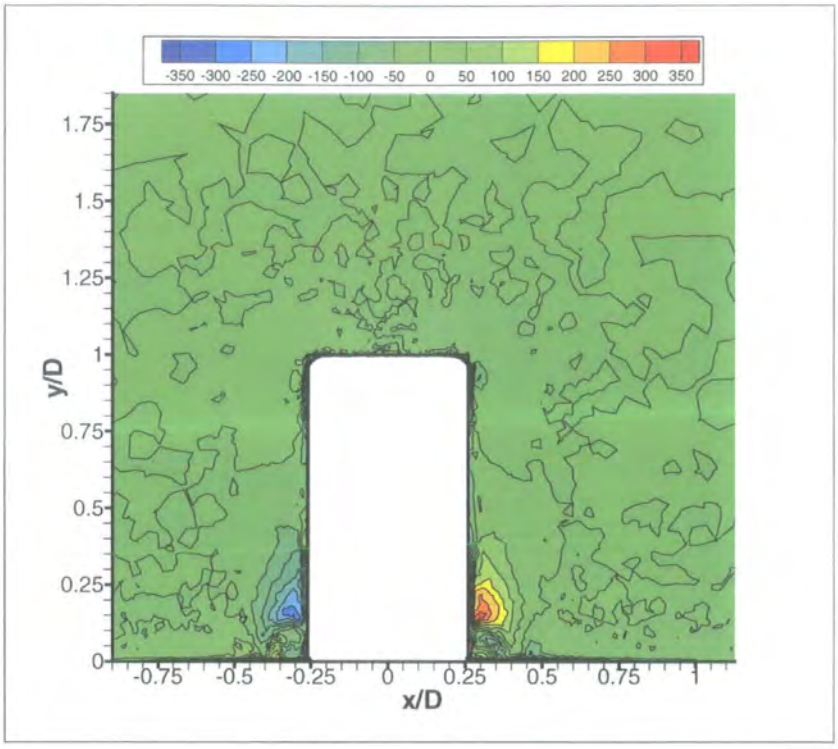


Figure 9.13: Predicted Steady State Contours of Constant Streamwise Vorticity ($\xi$), Rotating, XY Plane @ Z/D = 0.

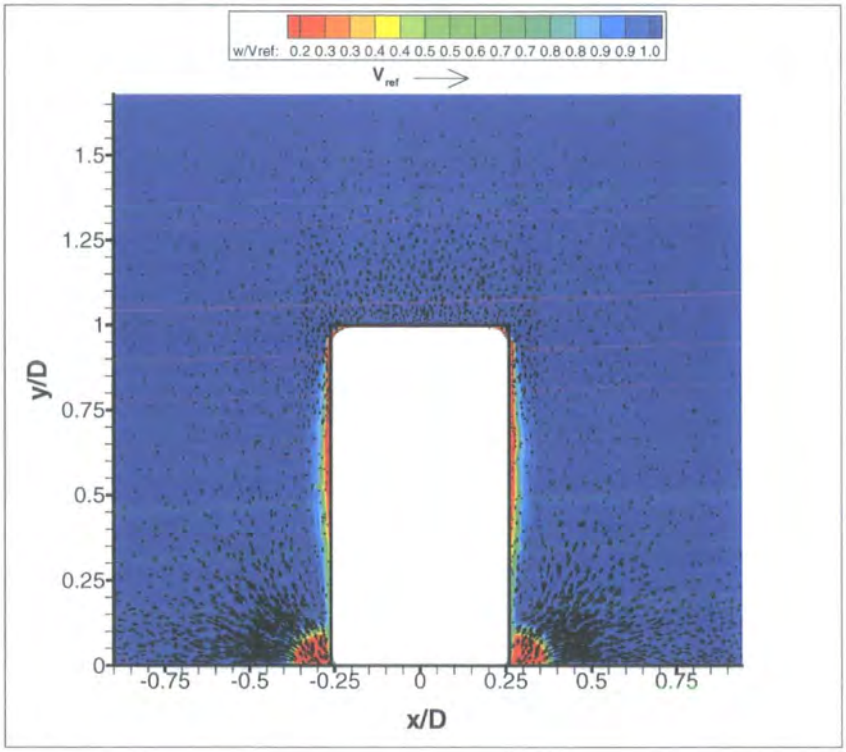


Figure 9.14: Predicted Steady State Secondary Flow Velocity Vectors, Rotating, XY Plane @ Z/D = 0.

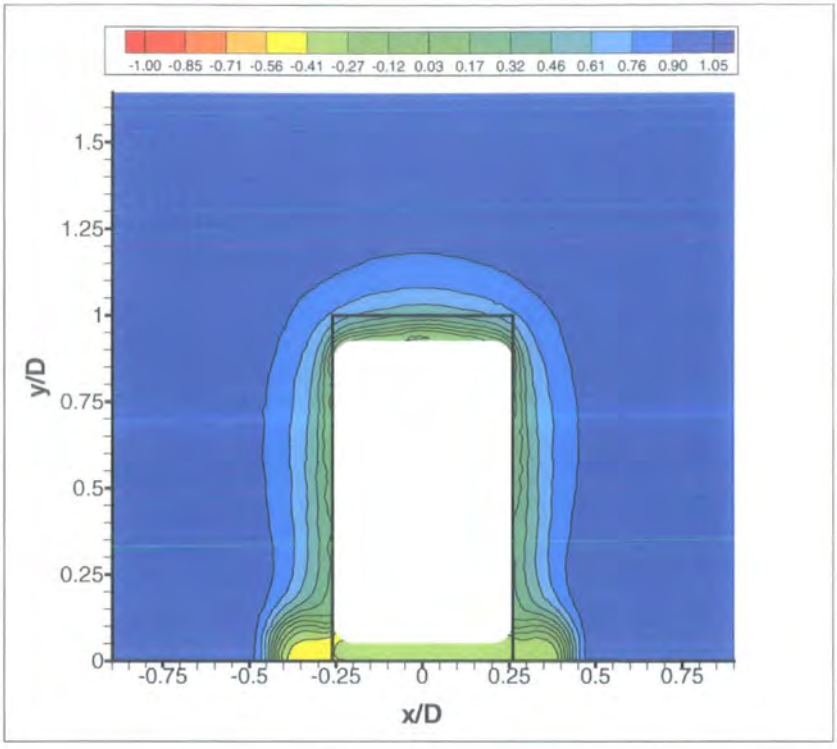


Figure 9.15: Predicted Steady State Contours of Constant Total Pressure Coefficient, Rotating, XY Plane @ Z/D = 0.25.

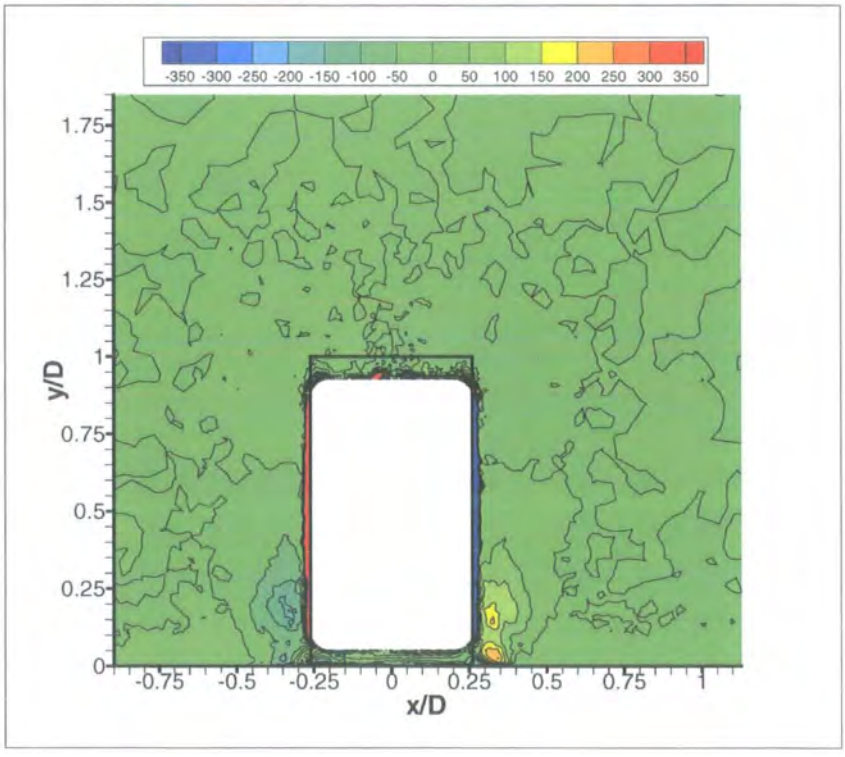


Figure 9.16: Predicted Steady State Contours of Constant Streamwise Vorticity ($\xi$), Rotating, XY Plane @ Z/D = 0.25.

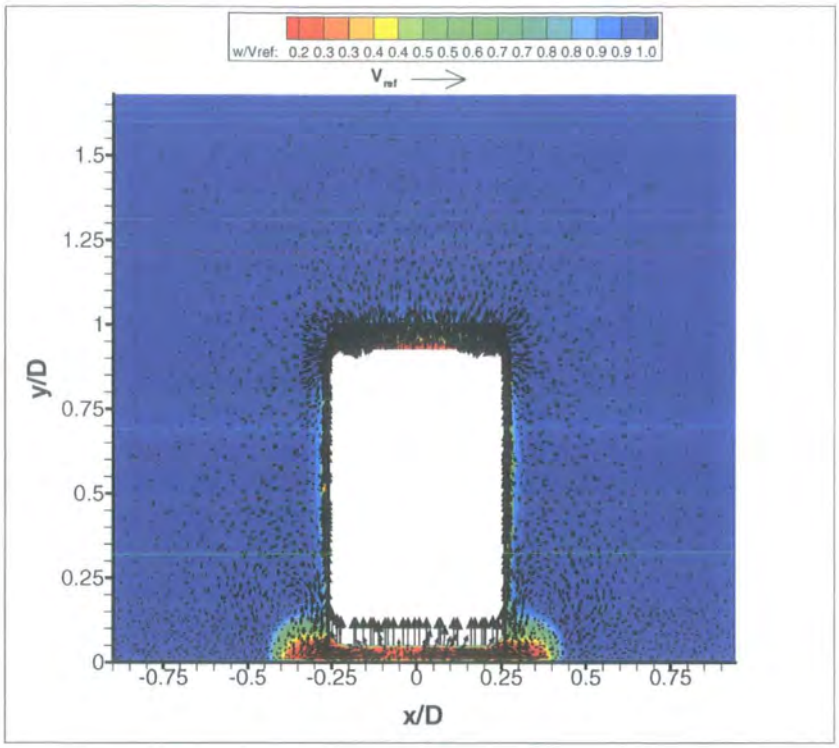


Figure 9.17: Predicted Steady State Secondary Flow Velocity Vectors, Rotating, XY Plane @ Z/D = 0.25.

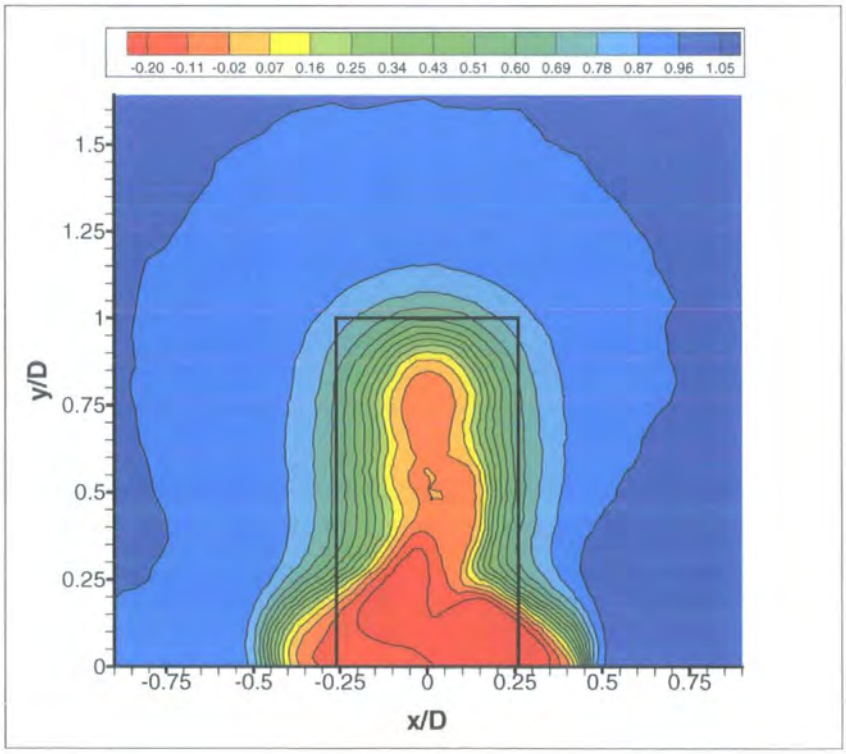


Figure 9.18: Predicted Steady State Contours of Constant Total Pressure Coefficient, Rotating, XY Plane @ Z/D = 0.75.

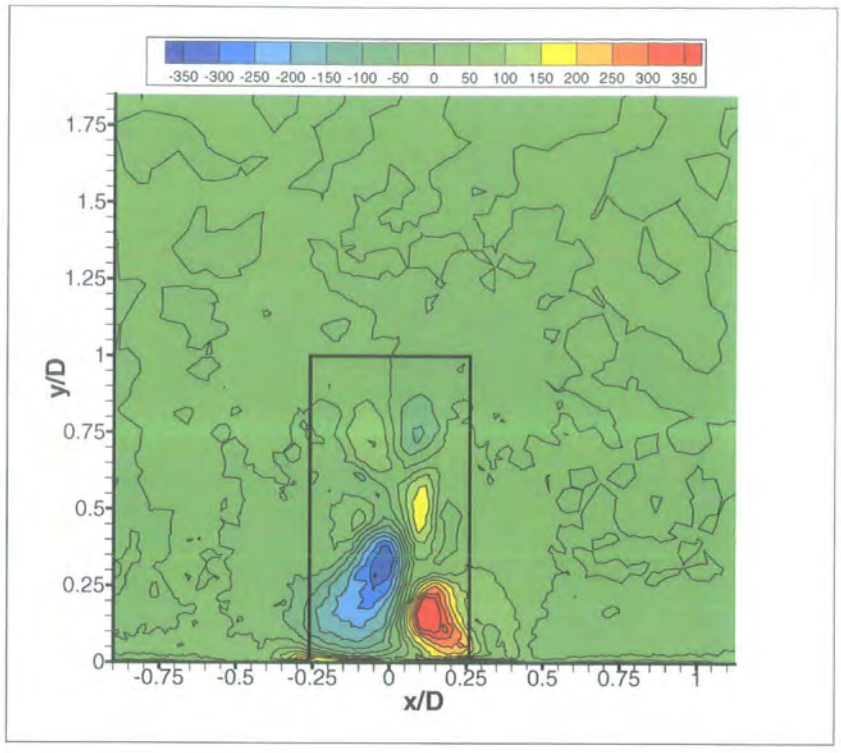


Figure 9.19: Predicted Steady State Contours of Constant Streamwise Vorticity ($\xi$), Rotating, XY Plane @ Z/D = 0.75.

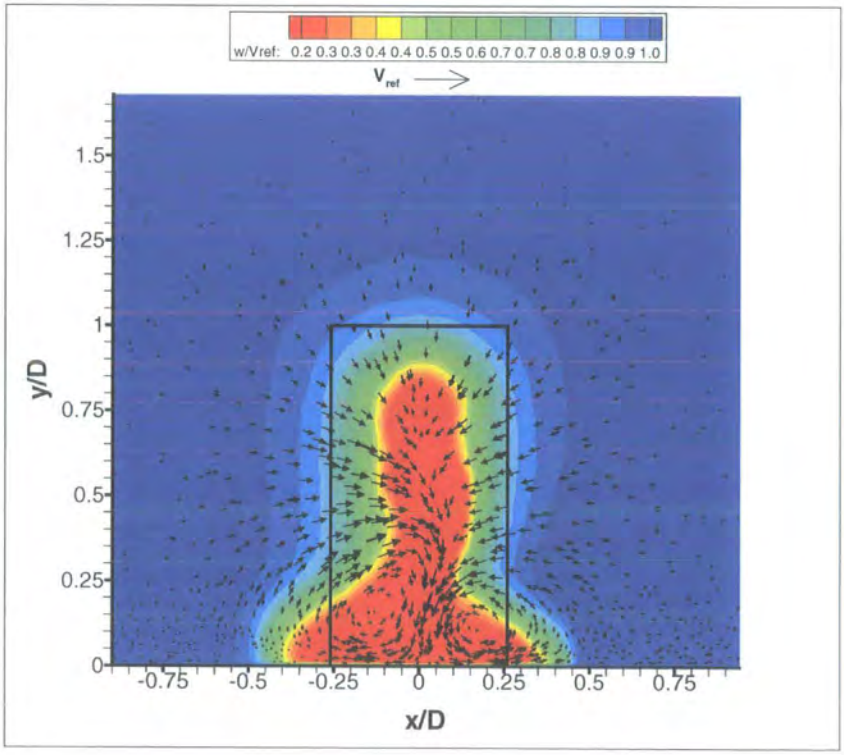


Figure 9.20: Predicted Steady State Secondary Flow Velocity Vectors, Rotating, XY Plane @ Z/D = 0.75.

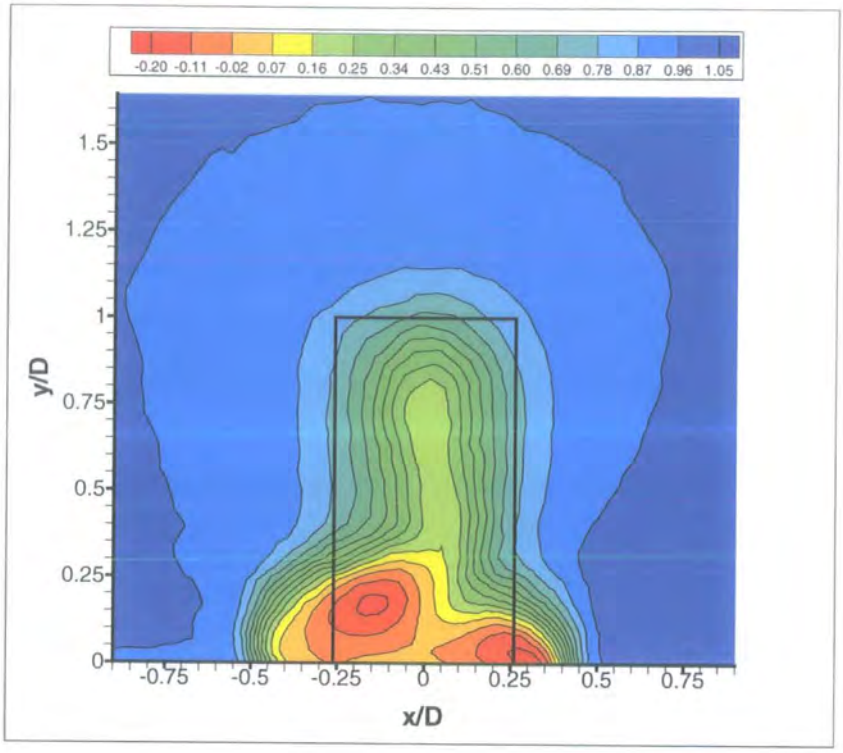


Figure 9.21: Predicted Steady State Contours of Constant Total Pressure Coefficient, Rotating, XY Plane @ Z/D = 1.0.

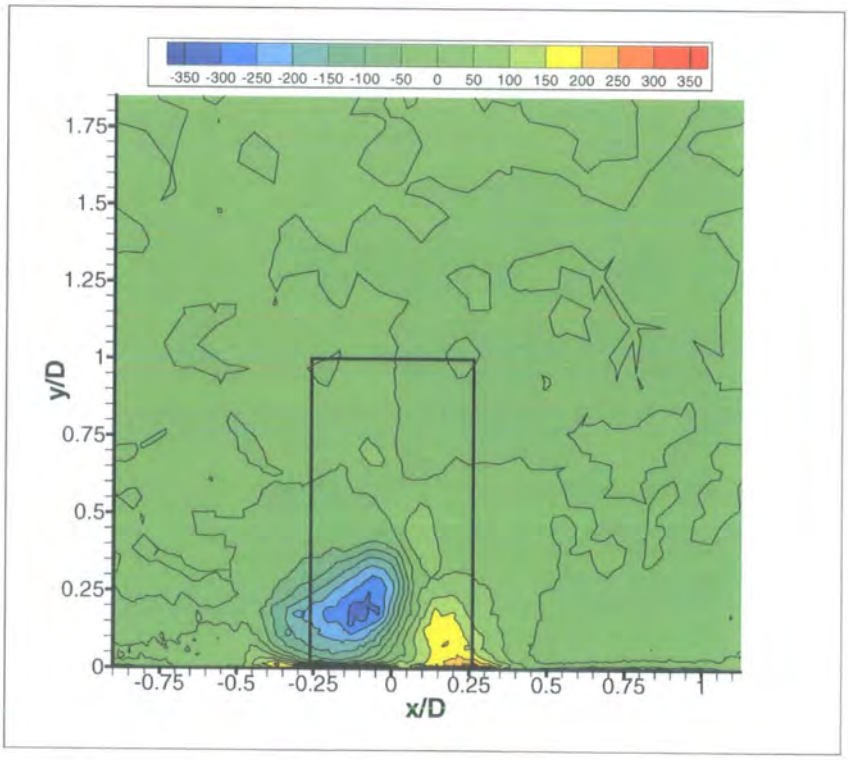


Figure 9.22: Predicted Steady State Contours of Constant Streamwise Vorticity ($\xi$), Rotating, XY Plane @ Z/D = 1.0.

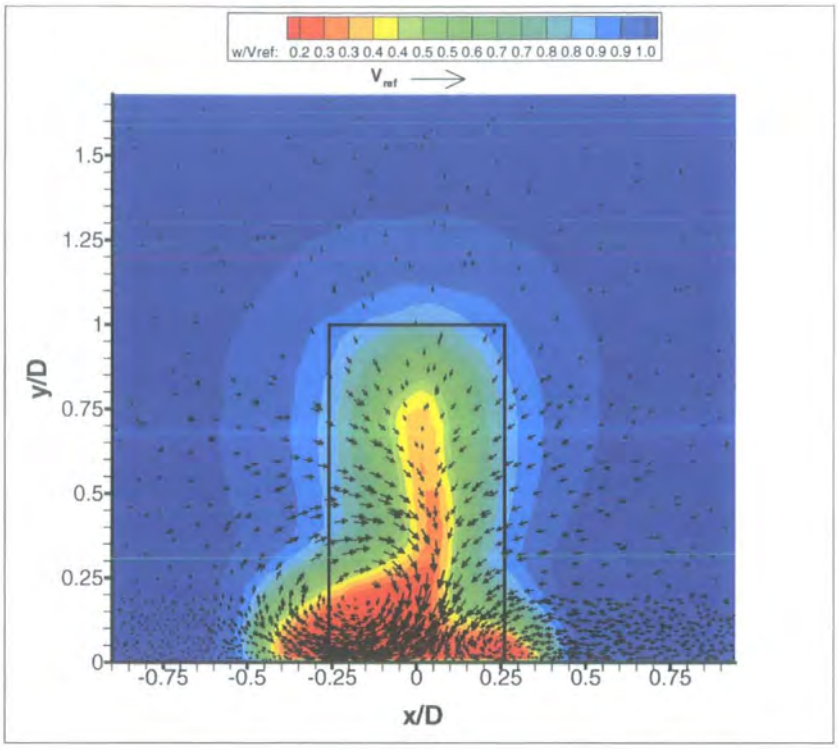


Figure 9.23: Predicted Steady State Secondary Flow Velocity Vectors, Rotating, XY Plane @ Z/D = 1.0.

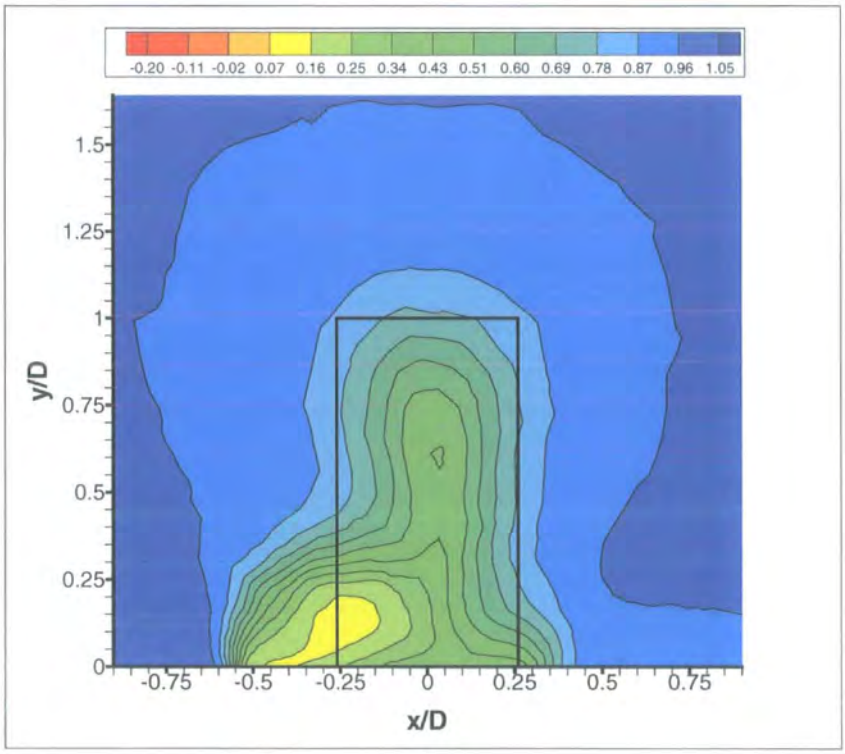


Figure 9.24: Predicted Steady State Contours of Constant Total Pressure Coefficient, Rotating, XY Plane @ Z/D = 1.5.

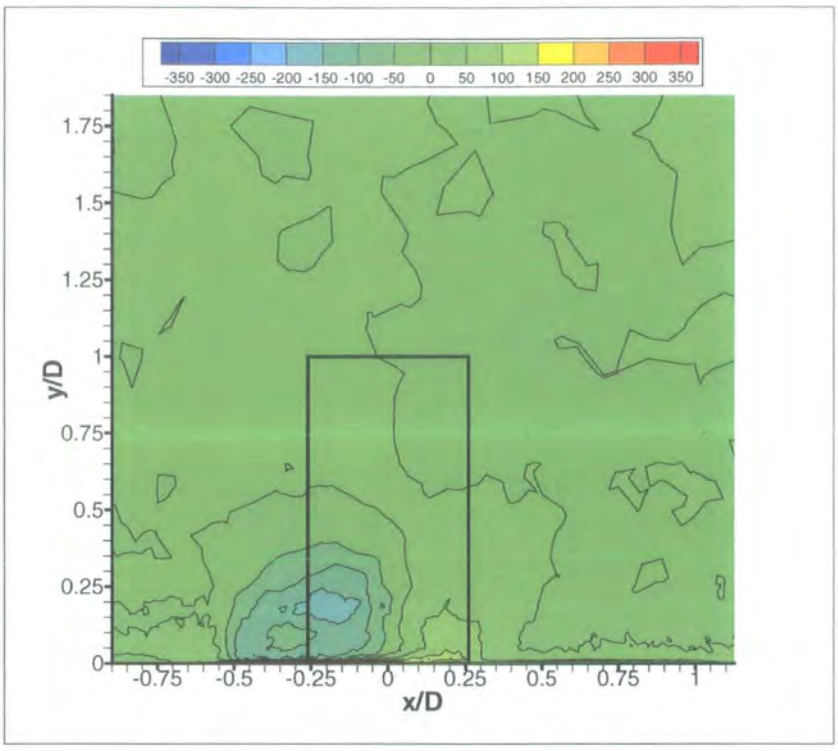


Figure 9.25: Predicted Steady State Contours of Constant Streamwise Vorticity ($\xi$), Rotating, XY Plane @ Z/D = 1.5.

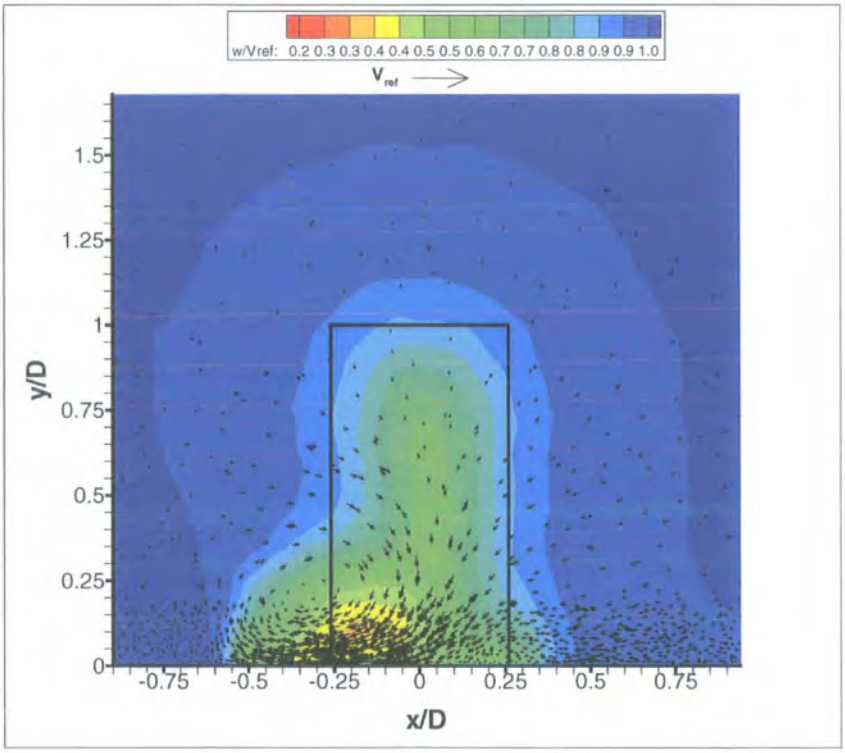


Figure 9.26: Predicted Steady State Secondary Flow Velocity Vectors, Rotating, XY Plane @ Z/D = 1.5.

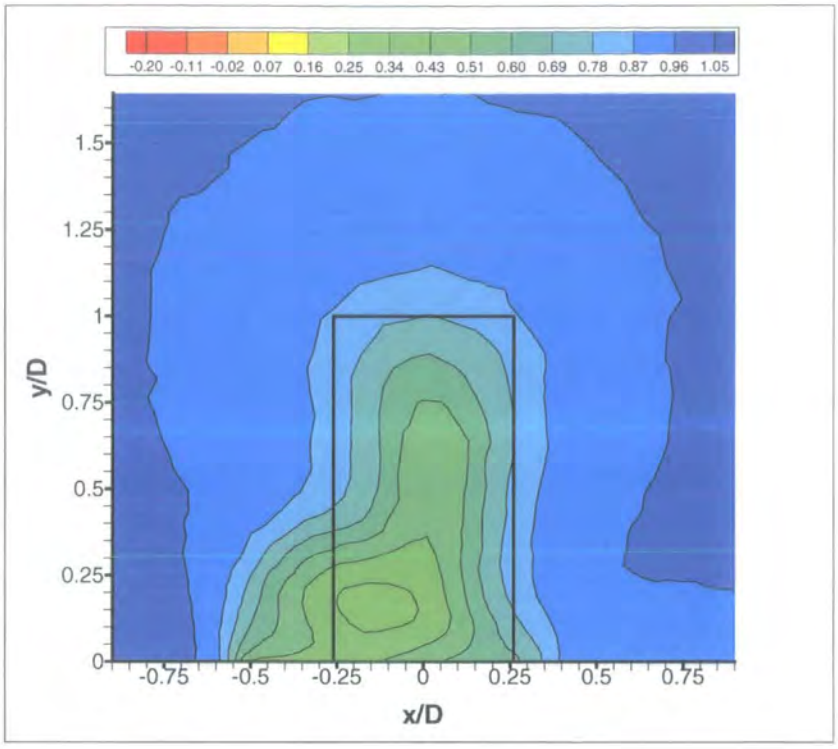


Figure 9.27: Predicted Steady State Contours of Constant Total Pressure Coefficient, Rotating, XY Plane @ Z/D = 2.

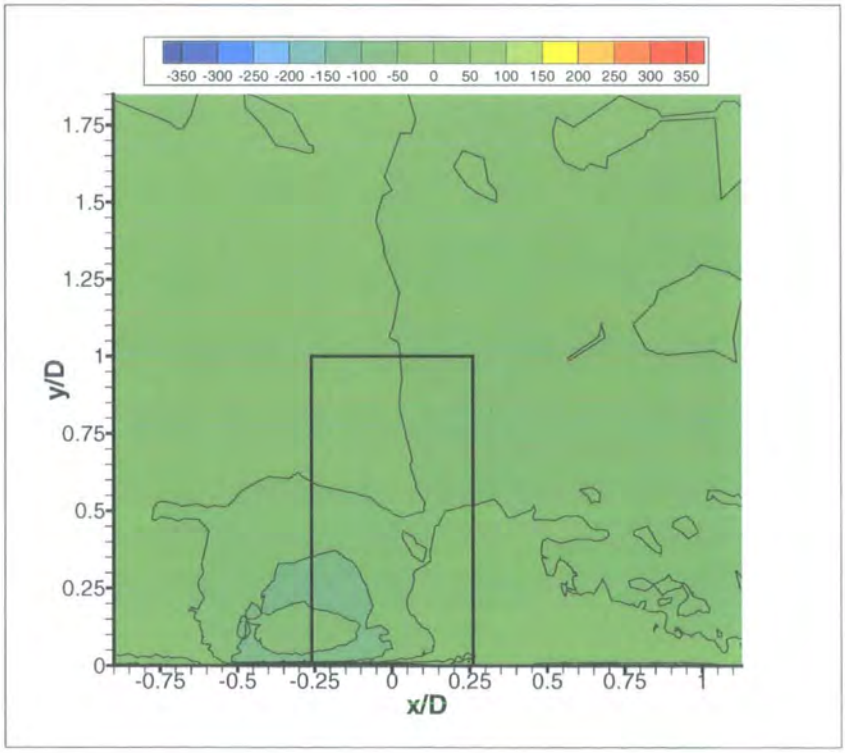


Figure 9.28: Predicted Steady State Contours of Constant Streamwise Vorticity ($\xi$), Rotating, XY Plane @ Z/D = 2.

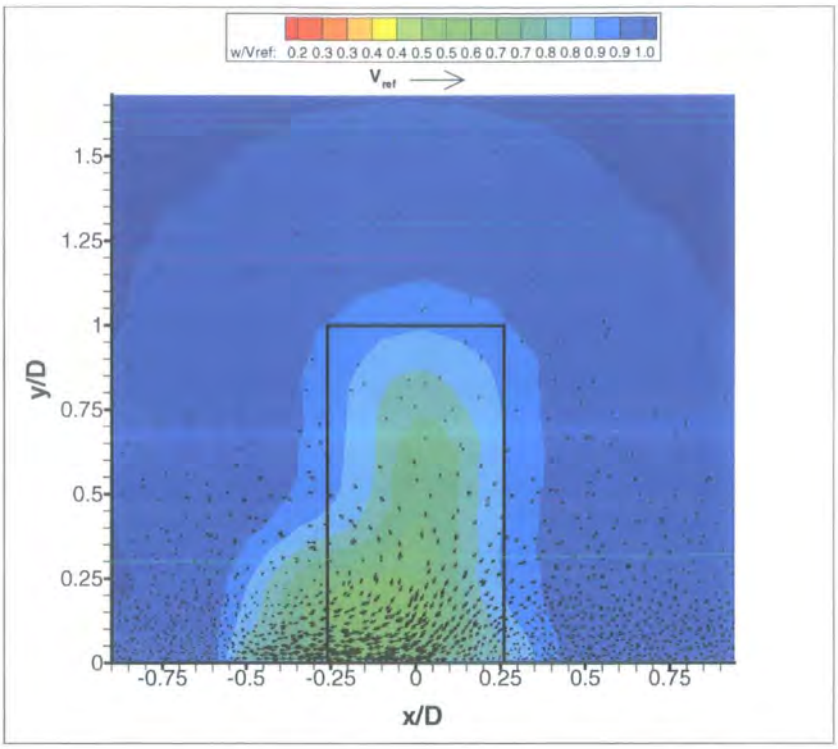


Figure 9.29: Predicted Steady State Secondary Flow Velocity Vectors, Rotating, XY Plane @ Z/D = 2.

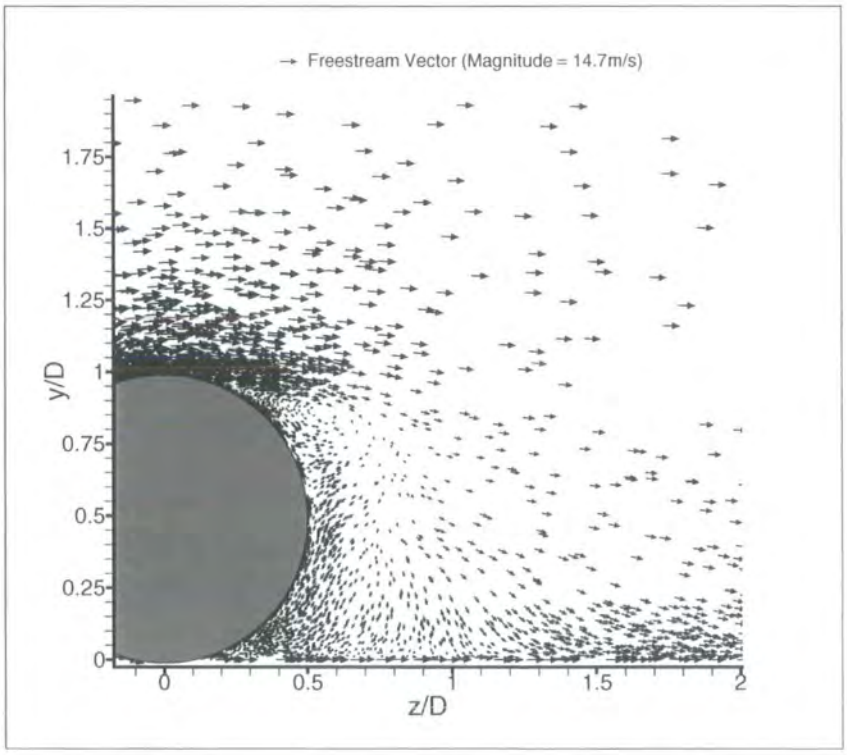


Figure 9.30: Predicted Steady State Velocity Vectors for Centreline (W/D = 0) YZ Plane (PosA-D), Rotating.

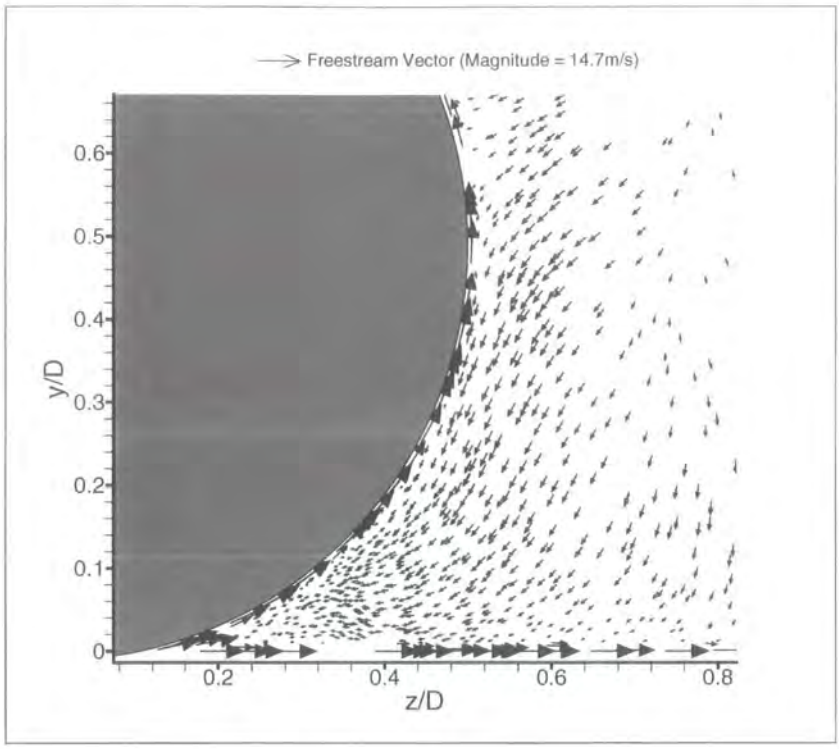


Figure 9.31: Predicted Steady State Velocity Vectors for Centreline (W/D = 0) YZ Plane (PosA), Rotating.

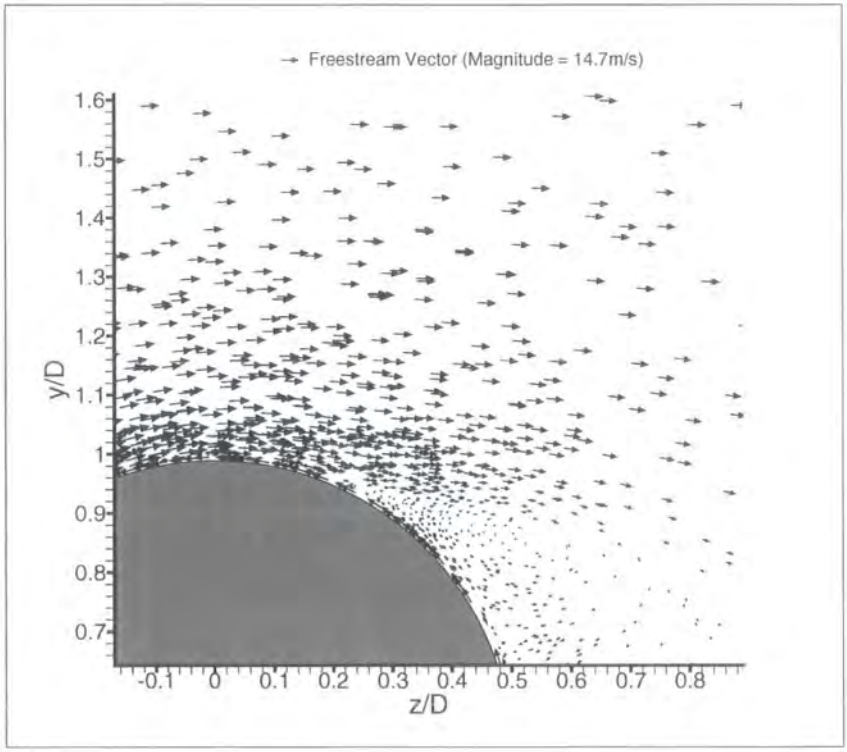


Figure 9.32: Predicted Steady State Velocity Vectors for Centreline (W/D = 0) YZ Plane (PosD), Rotating.

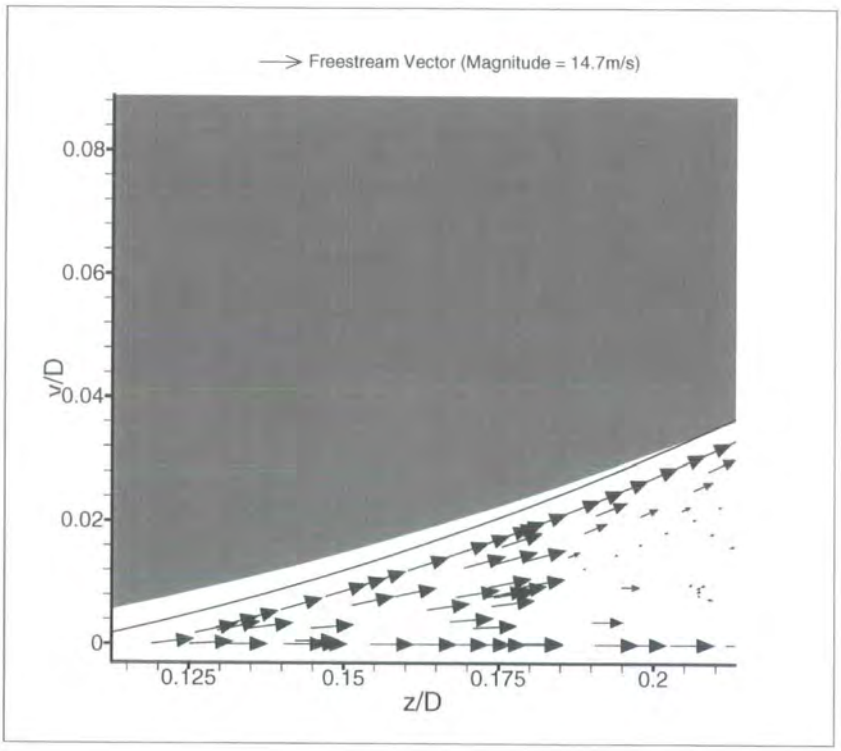


Figure 9.33: Prediction of the Rear Jetting Phenomenon.

# Chapter 10

# Discussion

## 10.1 Introduction

Chapter 2 gave a critical review and highlighted our current level of understanding of the aerodynamic characteristics of exposed/isolated wheels and summarised the important flow features highlighted during previous investigations. The purposes of this chapter are to describe in detail the experimental and computational results presented in Chapters 8 and 9 respectively, and to try and link together the results obtained during the course of this work and the work of other researchers, in order to explicitly state the major additions and extensions to our knowledge of exposed wheel flows as a result of this work.

## 10.2 Lift and Drag Coefficients

The time-averaged lift and drag force coefficients (see Table 8.1) show that wheel rotation causes both the lift and drag forces to decrease which is in agreement with all investigations from Stapleford and Carr [63] to present day. The reasons for such force reductions are explained in this chapter. The surface pressure distribution (SPD) data derived coefficients for the stationary and rotating P1 wheels are in very good agreement with the B2 wheels of Fackrell [19] with the exception of the stationary P1 wheel which shows a slightly reduced lift coefficient, $C_{Lw}$, of 0.60, although the two wheel geometries were different and were not expected to have the

same lift and drag coefficients. The load cell (LC) drag coefficient for the stationary P1 wheel is lower ($C_{Dw} = 0.70$) than the SPD derived drag coefficient ($C_{Dw} = 0.73$), which was a little surprising since the load cell measures the total drag force and not just the pressure drag. Conversely the load cell derived drag coefficient for the rotating P1 wheel is higher ($C_{Dw} = 0.63$) compared to the SPD derived drag coefficient ($C_{Dw} = 0.56$). The angular measurement resolution differed between the stationary (measurement taken every 10 degrees) and the rotating (measurement taken approximately every 5 degrees) cases, and the effects this had on the surface pressure derived force coefficients are discussed in Section 10.9.

The wake integral (WI) derived drag force coefficients were based on measurements taken at the streamwise station Z/D = 2.5 for the rotating and stationary cases, as these stations produced the minimum amount of out-of-range data since out-of-range data would introduce errors into the computed force coefficients. The sting wake was also combined into the computed force coefficients. No attempts were made to carry out a wake integral of the sting on its own in the working section in order establish the contribution to drag from the sting since, as will be shown in the wake contour plots, the sting affects the wake structure of the wheel and therefore eliminating its contribution to the overall drag force is not worthwhile due to the fact it has such an effect on the flow-field. The stationary P1 wheel WI derived drag coefficient ($C_{Dw} = 0.77$) is higher than the LC and SPD drag coefficients which was expected due to the measurements including both the wheel and sting. The rotating P1 wheel WI derived drag coefficient is the same as the load cell drag coefficient ($C_{Dw} = 0.63$). The spanwise measurement planes spanned -1.26<x/D<1.26 which are wider than the measurement planes shown in Table 7.4 in Chapter 7 for plane G (z/D = 2.5); the same $y/D$ range was used. Discrete measurements were taken every 10mm in both $x$ and $y$ directions and the planes were widened to try and capture the complete wake. However, the stationary wheel wake is much wider than the rotating wheel wake and it was not possible to capture the full wake. Moving further upstream would have been beneficial as the wake is not as diffuse and can be fully captured, although out-of-range data are prevalent further upstream and

would have more of a detrimental effect, in terms of error, on the computed forces.

The predicted CFD drag force coefficient is in good agreement with the experimentally derived coefficients. The predicted lift coefficient is under predicted and will be discussed further alongside the computational results.

The surface pressure distribution (SPD) derived force coefficients for the rotating P1 wheel at yaw (yaw = 5 degrees) are also shown in Table 8.1. The data show that the drag force coefficient increases from $C_{Dw} = 0.56$ (yaw = 0 degrees) to $C_{Dw} = 0.59$ for the yaw case. The lift force coefficient decreases from $C_{Lw} = 0.42$ for the yaw = 0 degrees case to $C_{Lw} = 0.35$ when the wheel is at yaw. These are discussed fully when the surface static pressure distributions at yaw are discussed in Section 10.3.2.

## 10.3 Surface Static Pressure Distributions

### 10.3.1 Yaw Angle ($\beta$) = 0 Degrees

As discussed earlier all pressure distributions are time-averaged. The rotating and stationary time-averaged centreline surface static pressure distributions are shown in pressure coefficient form in Figure 8.1. The wheel notation relating to the static pressure distributions is shown in Figure 3.9 of Chapter 3. The pressure tapping locations are shown in Figures 3.6 and 3.7 also of Chapter 3. The scale of the axes for the pressure distributions presented hereinafter were based on the minimum and maximum pressures recorded for all pressure tappings, hence some traces occupy only a small region of the whole plot area. On initial inspection of the two pressure traces significant differences exist between the rotating and stationary cases. With regard firstly to the stationary case, the flow stagnates at the front of the wheel at approximately 10 degrees which is to be expected on the wheel centreline at zero degrees yaw. The static pressure then decreases to a pressure coefficient value of approximately Cp = 0.6 at 45 degrees as the flow accelerates toward the contact region. The pressure then gradually increases to a value of unity (Cp = 1, i.e. stagnation)

at around 80 degrees. The slightly more deformed contact patch for the stationary case causes this earlier stagnation position. This "twin stagnation point" (e.g. at $\theta$ = 10 and 80 degrees) is a characteristic of wheel flows and is caused by ground contact as additionally the flow stagnates at the contact patch. Moreover, previous investigations have shown only the flow stagnating on the front of the wheel and not at the contact patch due to a gap under the wheel (such as Stapleford and Carr [63] (Figure 2.5)). At 270 degrees the boundary layer is attached and the flow accelerates over the top of the wheel causing a decrease in local static pressure and this is a contributory factor to the increased lift force for the stationary wheel. The flow separates at approximately 225 degrees due to the adverse pressure gradient, which is 50 degrees after the top of the wheel. The base pressure is relatively constant at an average, in terms of pressure coefficient, of Cp = -0.6.

The rotating time-averaged static pressure distribution shows a similar stagnation position on the front of the wheel at around 8 degrees. The two pressure traces (stationary and rotating) are almost contiguous up to the contact region at which point the local static pressure rapidly increases for the rotating case to a value of Cp = 1.9 (front jetting). The pressure cannot rise above the stagnation value unless extra energy is being injected into the flow and this is caused by the viscous actions as the two moving boundaries, namely the wheel and MGP, converge with one another and squeeze the air to a local static pressure in excess of unity. Another interesting feature is the negative pressure peak (Cp = -1.5) after the line of contact. Fackrell [19] expected to see this in his static pressure distributions on the wheel centreline, based on a theoretical solution for flow into and out of finite corners with moving boundaries, but did not observe this phenomenon experimentally. If the two converging boundaries at the front of the contact patch cause a rapid increase in local static pressure it is reasonable to postulate that two diverging boundaries (i.e. the wheel and belt behind the line of contact) should cause a rapid decrease in local static pressure. It may appear, from the distributions, that the negative pressure peak at the rear of the contact patch effectively cancels out the positive pressure peak at the front of the contact patch and that the net result is a negligible

contribution to the overall lift force from the contact patch region. A full and thorough examination of the front and rear jetting phenomena is given in Section 10.8 of this chapter. There is a slight oscillation after the low pressure peak and this was thought to be caused by the tubing since the pressure scanner natural frequency is in the kHz range. However, as discussed in the pressure measurement instrumentation chapter (Chapter 4) a tubing transfer function correction method was applied to the pressure data but the oscillatory behaviour remained. It is therefore probably caused by the tyre deflecting slightly in the low pressure region behind the line of contact and then oscillating slightly. Fackrell [19] in fact observed a similar oscillatory behaviour for his A and C wheels although the amplitude was reduced compared to here. Fackrell put this down to the moving belt lifting and touching the wheel and therefore pressure tapping since his wheels were non-deformable. The reason why his B wheels did not show this behaviour is probably due to the reduced angular position measurement resolution employed by Fackrell for this particular wheel. Here the contact patch was indeed observed to check that the belt was not lifting and it was concluded that the belt did not lift. Moreover, it would be unlikely that the oscillations would span some 30 degrees around the rear of the wheel if the belt had lifted, therefore it is a possibility that the deformable tyre indeed flexed and caused the fluctuating pressure picked up by the pressure tapping; suffice to say that the oscillations may not be an intrinsic aerodynamic flow mechanism. However, it could also be related to the aerodynamic unsteadiness shown in Figure 8.105 (rotating case (a-c)) which shows an apparent attachment / detachment of the jet entrainment at the tyre surface. In particular Figure 8.105a seems to indicate that at its most persistent case the jet extends to around 45 degrees from the contact patch. A time-resolved pressure measurement system would aid the analysis of this to determine whether this is a genuine aerodynamic flow structure. Flow separation occurs over the top of the wheel for the rotating case at around 290 degrees, which is before the top of the wheel. Therefore, somewhat paradoxically a later boundary layer separation (such is the case with the stationary wheel) results in higher drag which goes against normal bluff body flows such as cylinders and spheres. For example, the dimples on golf balls (spheres) provoke boundary layer transition to a fully

turbulent boundary layer which is more capable (compared to a laminar layer) of sustaining a greater adverse pressure gradient and therefore delays separation. This later separation causes a reduction in drag force due to a smaller wake. The base pressure is reasonably constant at around Cp = -0.4, and of course this is higher compared to the stationary case which corresponds to the reduced drag force acting on the rotating case.

Figure 8.2 shows the rotating time-averaged static pressure distribution compared to that obtained by Fackrell [19]. On initial inspection the two static pressure distributions are in excellent agreement with the exception of the aforementioned rear jetting low pressure peak after the line of contact. This particular pressure distribution gave confidence in the pressure measurement instrumentation for analysing the aerodynamics of rotating wheels. Moreover, this pressure distribution confirmed that the flow regime was in fact supercritical since Fackrell's was supercritical (this is discussed in more detail in Section 10.10). The time-averaged flow separation positions are in very good agreement at around 290 degrees (both before the top of the wheel). It is worth noting that the two geometries of the wheels were different so the comparisons are general observations and the distributions were not expected to be identical.

Figure 8.3 shows the stationary static pressure distribution for the wheel centreline compared to Fackrell [19]. Again, the pressure distributions are in very good agreement. Both show that boundary layer separation occurs at around 210 degrees in an adverse pressure gradient. The flow reaches stagnation pressure at the contact patch at an angular position of 80 degrees and to reiterate this is due to the slight tyre deformation for the stationary wheel. Of course the wheel of Fackrell [19] was non-deformable. Both pressure distributions show a relatively constant base pressure.

Figure 8.4 shows the time-averaged static pressure distributions for the rotating and stationary cases for pressure tapping 2 located at W/D = +0.037. All of the static

pressure distributions for the pressure tappings that contact the groundplane (tread tappings) have a similar form. The two pressure traces are very similar to those on the wheel centreline although this is not surprising since geometrically the pressure tapping is only 9mm from the centreline. At this tapping location the effects of crossflow are minimal but do exist due to the stagnation streamline being on the wheel centreline when the wheel is at zero degrees yaw. The stationary pressure trace almost reaches stagnation value (Cp = 0.9) at the front of the contact patch (80 degrees) so the crossflow component of velocity combined with the flow accelerating towards the contact region reduce the local static pressure there. The front and rear jetting phenomena are still present but with slightly reduced magnitude for the front jetting (Cp = 1.65) and marginally increased magnitude for the rear jetting low pressure peak (Cp = -1.7). The amplitude of the oscillation after the line of contact has increased and will be a consequence of the increased negative pressure peak (rear jetting). The base pressure for both the rotating and stationary traces is relatively constant and similar to the centreline as it should be in the separated region. The boundary layer separates at around 290 degrees for the rotating case and around 225 degrees for the stationary case. The attached flow around the top of the stationary wheel causes low local static pressure at 270 degrees.

Figure 8.5 shows the time-averaged static pressure distributions for the rotating and stationary cases for pressure tapping 3 located at W/D=+0.073. Again, these pressure distributions are very similar to the centreline for both the stationary and rotating cases. The front and rear jetting can be clearly seen at the contact patch ($\theta$ = 90 degrees). The flow accelerates from the front of the wheel ($\theta$ = 360 degrees) to the point at which the boundary layer separates (rotating case) at around 290 degrees, and to the top of the wheel for the stationary case. The base pressure is relatively constant, although more so in the rotating case. The flow does not reach stagnation pressure (Cp = 0.8) for the stationary case at the contact patch ($\theta$ = 80 degrees) due to the crossflow component of velocity and the accelerating flow towards the contact region.

The rotating and stationary time-averaged static pressure distributions for pressure tapping 4, located at W/D=+0.110, are shown in Figure 8.6. At this spanwise position the local static pressure, in terms of Cp, reaches around Cp = 0.85 on the front of the wheel. The pressure will not reach the stagnation value all the way across the front of the wheel as would be the case if it were infinitely long. The stationary pressure trace reaches a pressure of Cp = 0.7 at the contact patch ($\theta$ = 80 degrees) again due to the spanwise position of the measuring hole. The jetting can be seen and the oscillation after the line of contact. The accelerated flow around the top of the stationary wheel has diminished in terms of a reduction in local static pressure; this being due to the end effects playing an increasing role as the three-dimensional effects are accentuated towards the sides (ends) of the wheel. Again, the base pressure is relatively constant.

Figure 8.7 shows the time-averaged static pressure distributions for the rotating and stationary cases for pressure tapping 5 located at W/D=+0.146. Again, the flow does not stagnate on the front of the wheel at $\theta$ = 0 degrees for this pressure tapping. The flow accelerates towards the contact patch and the stationary trace shows a pressure of Cp = 0.5 at $\theta$ = 80 degrees. The front and rear jetting pressure peaks can be seen clearly but with reduced magnitude. The base pressure is relatively constant; more so for the rotating case.

The rotating and stationary time-averaged static pressure distributions for pressure tapping 6, located at W/D=+0.183, are shown in Figure 8.8. This is the last pressure tapping that contacts the groundplane. At this location the stationary pressure distribution has significantly altered from the centreline. The flow still accelerates around the top of the stationary wheel but the static pressure has reduced significantly compared to the centreline pressure distribution. At $\theta$ = 220 degrees the stationary trace shows a reduction in static pressure and this is due to this pressure tapping being located both spanwise and angularly in proximity to the trailing vortical structure (later distributions shows this more clearly). The point of interest for the rotating pressure trace is the front and rear jetting pressure peaks which are

of increased magnitude (Cp = 2.55 front, Cp = -2.85 rear) compared to previous distributions. Initially this was thought to be caused by the flow across the front of the wheel interacting with the flow around the edge profile, although one would expect the front jetting magnitude to be decreased at the edge of the tread region due to "leakage" around the side of the wheel. The rear jetting may not be as affected since this is in the separated region and therefore the air flow at the side of the wheel may in fact decrease the local static pressure at this location due to entrainment into the wake (the overhead PIV investigation was in fact set-up to investigate this). The oscillation after the line of contact has increased amplitude at the same frequency of oscillation as the other distributions and this is not surprising since the low pressure peak has increased magnitude. There would therefore appear to be a strong correlation between the rear jetting pressure peak magnitude and the amplitude of oscillation. A number of, what appear to be, spurious data points exist in the rotating trace between $310 < \theta < 340$ degrees and should be treated with suspicion.

Figure 8.9 shows the time-averaged static pressure distributions for the rotating and stationary cases for pressure tapping 7 located at W/D=+0.220. These pressure distributions have changed form from those of the tread region; at no angular position does the pressure become positive. The most remarkable feature of the rotating pressure trace is the rapid increase in local static pressure between $70 < \theta < 90$ degrees. It is worth noting that this tapping does not come into contact with the groundplane during any part of the rotational cycle of the wheel. This observation means that the jet of air produced by the viscous actions at the front of the contact patch must pass down by the side of the wheel as it is convected downstream into the wake region. Another interesting point to note, this time for the stationary pressure trace, is the low pressure region at $\theta = 210$ degrees. This was briefly mentioned earlier and is caused by proximity of the pressure tapping to the trailing vortex on the hub side of the wheel. The existence of trailing vortical structures in the wheel wake were confirmed through preliminary flow visualisation experiments using a wool tuft and smoke flow. The trailing vortices are formed when the axial flow at the side of

the wheel turns around the wheel edge profile due to the low pressure region at the rear of the wheel. More in depth investigations involved the wake traversing using the pneumatic pressure probe, the results of which are discussed in this chapter.

The rotating and stationary time-averaged static pressure distributions for pressure tapping 8, located at W/D=+0.244, are shown in Figure 8.10. The stationary pressure trace shows the low pressure region at $\theta = 225$ degrees has increased magnitude. At this angular position the measuring hole is close to the core of the vortical structure. The jetting effects can, again, be seen at the contact region.

The rotating and stationary time-averaged static pressure distributions for pressure tapping 9, located at W/D=+0.268, are shown in Figure 8.11. At this location the trailing vortex has less effect on the surface pressure field with a reduction in magnitude of the low pressure region at $\theta = 210$ degrees; this pressure tapping being located on the sidewall of the tyre. The jetting effects are also visible for the rotating case at the contact region.

The rotating and stationary time-averaged static pressure distributions for pressure tapping 10, located at W/D=+0.280, are shown in Figure 8.12. The stationary wheel trailing vortex structure has no effect on the surface pressure field at this pressure tapping location due to the tapping being located too far away from the tread region. The jetting effects can be seen at the contact region, although the effects have decreased due to the spatial separation between the tapping and the contact region.

The rotating and stationary time-averaged static pressure distributions for pressure tapping 11, located at W/D=+0.272, are shown in Figure 8.13. The jetting effects can be seen also in the rotating pressure distribution.

### 10.3.2 Yaw Angle ($\beta$) = 5 Degrees

The results discussed here refer to the rotating case only at a yaw angle of 0 and 5 degrees.

Figure 8.14 shows the centreline time-averaged static pressure distributions for the rotating wheel at yaw angles of 0 and 5 degrees. For the purposes of this discussion the yaw = 5 degrees pressure trace will be called the "yaw" trace. As expected the pressure trace at yaw does not show the flow stagnating on the front of the wheel on the centreline due to the stagnation streamline being located towards the windward side of the wheel. Up to the contact patch ($\theta$ = 0 to 80 degrees) the pressure traces are contiguous with the yawed condition showing reduced magnitude due to the crossflow component of velocity reducing the local static pressure. The rapid rise in pressure at the front of the contact patch are quantitatively almost identical (Cp = 1.9 at $\theta$ = 90 degrees). The rear jetting low pressure peak has increased in magnitude for the yawed case (Cp = -2.6). Again, the amplitude of the oscillations after the contact region is increased due to the more negative pressure behind the line of contact. The base pressure is lower for the yawed condition and helps explain the increased drag force acting on the yawed wheel.

Figures 8.15 and 8.16 show the time-averaged static pressure distributions for tapping -2 and +2 located at W/D = -0.037 and W/D = +0.037, respectively, for the rotating wheel at yaw angles of 0 and 5 degrees. The -ve data refers to the leeward side of the wheel. The same zero degree yaw trace is shown in both figures due to the tapping only being logged on one side of the wheel (the side opposite the sting side); therefore the effects the sting and cavity have on the surface pressure distribution at zero yaw cannot be quantified. The flow does not stagnate on the windward side of the wheel at this tapping position (Cp = 0.9 at $\theta$ = 0 degrees) and the leeward side shows a lower local static pressure (Cp = 0.85) at the same angular position caused by the flow accelerating across the tread region of the tyre and hence reducing the static pressure from the windward to leeward side. The magnitude of the front and rear jetting pressure peaks is increased on the leeward side of the wheel and decreased

on the windward side. The base pressure is relatively constant for all pressure traces.

Figures 8.17 and 8.18 show the time-averaged static pressure distributions for tapping -3 and +3 located at W/D = -0.073 and W/D = +0.073, respectively, for the rotating wheel at yaw angles of 0 and 5 degrees. Again, the front and rear jetting has reduced magnitude for the windward side of the wheel. The rest of the traces resemble the tapping ± 2 traces.

Figures 8.19 and 8.20 show the time-averaged static pressure distributions for tapping -4 and +4 located at W/D = -0.110 and W/D = +0.110, respectively, for the rotating wheel at yaw angles of 0 and 5 degrees. At this pressure tapping location the flow stagnates on the front of the wheel at $\theta = 0$ degrees on the windward side. On the leeward side the pressure is below that observed for the zero degrees yaw condition as expected. The magnitude of the rear jetting negative pressure peak is reduced for the windward side compared to the leeward side. The general trends for all of the pressure distributions are similar.

The time-averaged static pressure distributions for tapping -5 and +5 located at W/D = -0.146 and W/D = +0.146 are shown in figures 8.21 and 8.22 respectively, for the rotating wheel at yaw angles of 0 and 5 degrees. The static pressure at the front of the wheel is, as expected, greater on the windward side of the wheel. The base pressure is reasonably constant.

Figures 8.23 and 8.24 show the time-averaged static pressure distributions for tapping -6 and +6 located at W/D = -0.183 and W/D = +0.183, respectively, for the rotating wheel at yaw angles of 0 and 5 degrees. Once again, the pressure at $\theta = 0$ degrees is greater for the windward side compared to the leeward side. Also, the front and rear jetting pressures are greater in magnitude for the leeward side of the wheel. The oscillations are still present. The base pressure is lower for the leeward side of the wheel at yaw, and is relatively constant for all conditions.

The time-averaged static pressure distributions for tapping -7 and +7 located at W/D = -0.220 and W/D = +0.220 are shown in figures 8.25 and 8.26 respectively, for the rotating wheel at yaw angles of 0 and 5 degrees. This pressure tapping is the first of the sidewall tappings and does not come into contact with the groundplane at any time during a rotational cycle of the wheel. Fairly predictable the static pressures are lower on the leeward side of the yawed wheel, although the difference in base pressure is small compared to frontal regions of the wheel. The jetting can be clearly seen at the contact patch on both sidewalls.

Figures 8.27 and 8.28 show the time-averaged static pressure distributions for tapping -8 and +8 located at W/D = -0.244 and W/D = +0.244, respectively, for the rotating wheel at yaw angles of 0 and 5 degrees. The pressure distributions are similar on both sides of the wheel at yaw. The jetting can be seen at the contact patch.

Figures 8.29 and 8.30 show the time-averaged static pressure distributions for tapping -9 and +9 located at W/D = -0.268 and W/D = +0.268, respectively, for the rotating wheel at yaw angles of 0 and 5 degrees. The zero degrees yaw and leeward yawed condition pressure distributions are almost contiguous with the jetting clearly visible at the contact patch. The windward pressure trace shows no signs of jetting and this is probably due to the location of the pressure tapping; any jetting will be washed across the wheel towards the leeward side of the wheel and also down by the windward side but not in close proximity to this tapping.

The time-averaged static pressure distributions for tapping -10 and +10 located at W/D = -0.280 and W/D = +0.280 are shown in figures 8.31 and 8.32 respectively, for the rotating wheel at yaw angles of 0 and 5 degrees. These pressure distributions also show the jetting effects on the leeward side with no signs of jetting on the windward side. The static pressure is generally higher on the windward side of the wheel.

Figures 8.33 and 8.34 show the time-averaged static pressure distributions for tap-

ping -11 and +11 located at W/D = -0.272 and W/D = +0.272, respectively, for the rotating wheel at yaw angles of 0 and 5 degrees. Once again, as was the case with similarly located tappings, the jetting effects can be seen on the leeward side of the wheel.

## 10.4 Flow Visualisation

The strong downwash can be seen in the wake of the stationary wheel (see Figure 8.35) with the Aerotech smoke probe positioned on the centreline of the wheel at an angular position of around 200 degrees. Axon [7] discusses this feature of the flow about a stationary wheel and suggested this could prove difficult to measure experimentally using a conventional pressure probe due to the air flowing vertically down towards the groundplane.

The same image but with the wheel rotating is shown for direct comparison in Figure 8.36. The smoke output from the probe is more diffuse this time and the strong downwash is no longer present as the smoke spreads into the separated region.

The next two smoke images (see Figures 8.37 and 8.38) show the stationary and rotating images, respectively, with the smoke probe positioned in the wake at approximately 225 degrees on the centreline. Again, the stationary wheel image shows the downwash in the wake. The rotating smoke image shows the early flow separation just before the top of the wheel with flow reversal as the smoke flows back to the top of the wheel. The smoke flow from the probe is more diffuse as the taller, unsteady separated region is filled with smoke. Since the flow separates later for the stationary wheel there is no air flowing back to the top of the wheel. The early boundary layer separation for the rotating wheel results in a taller wake structure, which is visible in this image.

Smoke visualisation images are shown in Figures 8.39 and 8.40 for the stationary and rotating case, respectively, with the smoke probe positioned at approximately

250 degrees on the centreline. The stationary wheel shows the flow following the curvature of the wheel and the rotating case shows, again, the early boundary layer separation before the top of the wheel. These particular images will be compared qualitatively with the PIV results later in this chapter.

The smoke visualisation images with the probe positioned at around 340 degrees on the centreline are shown in Figures 8.41 and 8.42 for the stationary and rotating wheels, respectively. The attached flow over the top of the stationary wheel can be seen clearly, and the early flow separation with taller wake can be clearly seen for the rotating wheel.

During the pressure probe traverse investigations a number of regions where out-of-range data were prevalent were discovered. Now, reversed flow could be measured using the pressure probe and the near-wake was expected to, and indeed did, exhibit large regions of reversed flow. Another region where reversed flow was measured was at the side of the contact patch. Figures 8.43 and 8.44 show this reversed flow clearly for the stationary and rotating cases, respectively. The flow separates from the edge of the tread region at it turns around the sidewall profile to the axial flow direction. This is discussed further with the pressure probe results.

## 10.5 Wake Surveys (XY planes)

### 10.5.1 Z = 0D plane

The time-averaged contours of constant total pressure coefficient for the XY plane at Z = 0D are shown for the rotating and stationary cases in Figures 8.45 and 8.46, respectively. A wool tuft was positioned at this station in the flow and a clockwise vortical structure was observed. Both plots show little useful information due to the out of range data present, which is coloured white. Indeed the smoke flow photographs at this position (Figures 8.43 and 8.44) show reversed flow which resulted in out of range data being acquired. Moreover, the probe was rotated about the pitch axis but did not result in any additional data, possibly due to the flow field

being affected by the presence of the probe at this position in the flow-field.

As an indication into the unsteadiness in the wake the standard deviation of the dynamic pressure was computed. Figures 8.47 and 8.48 show contours of standard deviation for the dynamic pressure coefficient for the rotating and stationary cases, respectively, for the streamwise station Z = 0D. Again, both figures show the out of range data along with small regions of unsteady flow (standard deviation (SD) = 0.16) at y/D = 0.1, x/D = -0.3, although the stationary case shows a slightly larger region of fluctuating dynamic pressure.

Contours of constant streamwise vorticity at the Z = 0D station are shown in Figures 8.49 and 8.50 for the rotating and stationary cases, respectively. There appears to be slight clockwise vorticity (y/D = 0.1, x/D = -0.4) in both figures which agrees with the wool tuft investigation, although the out of range data makes the vorticity almost indiscernible.

Figures 8.51 and 8.52 show time-averaged secondary flow vectors at Z = 0D for the rotating and stationary cases, respectively. The air is flowing from the contact patch in an outwards and upwards direction away from the wheel for both cases with the magnitude of the velocity being greater for the stationary case ($V/V_{ref}$ = 0.4).

### 10.5.2 Z = 0.25D plane

The development of the flow by the side of the wheel is shown in Figures 8.53 and 8.54, which show contours of constant total pressure coefficient for the rotating and stationary cases, respectively, at Z = 0.25D. Larger regions of low total pressure exist at this station for both cases and the out of range data remain prevalent. The region of low total pressure is larger for the stationary wheel.

Due to the larger region of lower total pressure for the stationary wheel a corresponding region of localised unsteadiness was measured and shown in Figures 8.55 and 8.56, which show contours of constant standard deviation of the dynamic pres-

sure coefficient for the rotating and stationary cases respectively, at Z = 0.25D.

Once again, as was the case with the vorticity plots at Z = 0D, the vorticity fields for the rotating and stationary cases (Figures 8.57 (rotating) and 8.58 (stationary)) show slight clockwise vortical structures that are difficult to analyse because of the out of range data.

Figures 8.59 and 8.60 show time-averaged velocity vectors at Z = 0.25D for the rotating and stationary cases, respectively. There is reduced secondary flow for both cases relative to the planes presented for Z = 0D. The rotating case shows the most reduction in secondary flow and this may be due to the jet of air passing down the side of the wheel as a result of the front jetting phenomenon.

### 10.5.3 Z = 0.75D plane

The first spanwise plane in the near-wake of the wheel was stationed at Z = 0.75D. Time-averaged contours of total pressure coefficient for the XY plane at Z = 0.75D are shown in Figures 8.61 and 8.62 for the rotating and stationary cases, respectively. Both plots show a large region of out of range data. This region of the flow-field is dominated by reversed flow and the pressure probe was rotated about the pitch axis to maximise the quantity of valid data which did indeed yield additional data. It is thought that the probe was out of range in terms of yaw angle flow inclination relative to the probe head since the pitch angle envelope spanned 360 degrees.

The rotating case confirms the early flow separation (discussed in Section 10.3), with a small region of total pressure loss (at y/D = 1.05, x/D = 0.0) just above the wheel, and therefore results in a taller wake structure compared to the stationary case. The stationary wake structure is reasonably symmetrical about the centreline of the wheel if the sting wake is ignored, since the sting wake can be clearly seen at $0.6<y/D<0.7$, $0.3<x/D<0.9$ in both contour plots. The rotating wheel wake shows slight asymmetry with the wake being larger on the sting side of the wheel, which could be due to the hub cavity although one would expect it to have an effect on

the stationary wake also. The stationary wheel wake is wider and this is most likely due to interaction with the slower moving fluid in the boundary layer on the fixed groundplane. There are regions of low total pressure in both the stationary and rotating wakes but these regions are adjacent to out of range data and are therefore difficult to analyse. The pressure gradient across the wake is marginally greater for the stationary case and this will be discussed further at a streamwise station further downstream where more valid data exist.

Figures 8.63 and 8.64 shows contours of constant standard deviation for the dynamic pressure coefficient for the XY plane at Z = 0.75D for the rotating and stationary cases, respectively. Again, the regions of out of range data are present. Fluctuating dynamic pressures are exhibited in the wake of the rotating and stationary wheels with regions of increased unsteadiness. Increased flow unsteadiness (standard deviation = 0.3) can be seen at y/D = 0.3, x/D = 0.4 for the sting side of the rotating wake with a similar flow feature on the opposite side of the wheel, although it is difficult to see this due to the out of range data. The asymmetry in the rotating wake can be seen. There are slight pressure fluctuations in the sting wake but these are small compared to the wheel wake, as would be expected from a slender streamlined body compared to a bluff body such as the wheel. The stationary wheel wake shows regions of increased flow unsteadiness at y/D = 0.18, x/D = $\pm$ 0.62. Although the flow unsteadiness has been highlighted no spectral analysis of the pressure data was conducted, hence it remains unknown at this stage whether any periodic structures exist. It seems unlikely that any strong periodic structures will be present due to the low aspect ratio of the wheel and the presence of ground contact. Bearman and Zdravkovich [10] (discussed in Chapter 2) showed that the spanwise coherent vortex shedding disappeared due to ground contact, and Park and Lee [47] showed that vortex shedding diminished when the aspect ratio was reduced to 6.0. However, further work is needed to ascertain if any periodic structures are present.

Figures 8.65 and 8.66 show time-averaged contours of constant streamwise vorticity for the rotating and stationary cases, respectively at Z = 0.75D. No signs of vorticity

are present due to large regions of out of range data. Other measurement techniques may have yielded more data at this streamwise station such as 3D LDA or 3D PIV.

The time-averaged secondary flow velocity vectors coloured by contours of $w/V_{ref}$ velocity for the XY plane at Z = 0.75D are shown in Figures 8.67 and 8.68 for the rotating and stationary wakes, respectively. Note the different measurement resolution for these plots; the rotating case has lower resolution and this was adopted due to a potential MGP overheating problem whereby the measurement grid was coarsened to prevent damage to the belt. The same measurement resolution was used for the planes used for the wake integration and this was achieved by conducting several runs and then concatenating the data. The different measurement resolution employed here was not considered detrimental to direct measurement comparisons since a number of planes exhibited large regions of out of range data and hence no flow structures in such regions of the flow.

Both the rotating and stationary secondary flow vector plots show fluid being entrained into the wake, although the entrainment is more towards the top of the wake (0.65<y/D<1.0, -0.25<x/D<0.25) with a maximum velocity magnitude of $V/V_{ref}$ = 0.4 for the rotating case. The flow entrainment into the stationary wake is in a lower position (0.5<y/D<0.95, -0.3<x/D<0.3), but with similar magnitude, by comparison but as will be shown in the measurement stations further downstream the trailing vortices are nearer to the MGP than their rotating wheel wake counterparts so this was expected. The contours of constant w-velocity show the outlines of the wakes.

### 10.5.4 Z = 1.0D plane

The rotating and stationary wheel time-averaged contours of constant total pressure coefficient for the streamwise station Z = 1.0D are shown in Figures 8.69 and 8.70, respectively. The rotating wheel wake at this station shows a slight decrease in overall wake height and the wake structure resembles that at Z = 0.75D. Both wakes are marginally more diffuse at this station with the pressure gradient across both

wakes being slightly reduced. The stationary wake also has a decrease in height. It is difficult to comment in more detail on the differences between the rotating and stationary wake structures due to the out of range data.

Figures 8.71 and 8.72 show contours of constant standard deviation of the dynamic pressure at Z = 1.0D for the rotating and stationary cases, respectively. On initial inspection the two figures look very similar to those at Z = 0.75D, although regions of increased unsteadiness can be seen in comparison. The rotating case shows a large region of high unsteadiness (SD = 0.3) at y/D = 0.3, x/D = 0.4. Out of range data dominate both the rotating and stationary plots. The stationary wake shows larger regions of high unsteadiness at y/D = 0.18, x/D = ± 0.62.

Figures 8.73 and 8.74 show contours of constant time-averaged streamwise vorticity for the rotating and stationary wheels, respectively at Z = 1.0D. Due to out of range velocity data no signs of vorticity are present in either the rotating or stationary contour plots.

The time-averaged secondary flow velocity vectors are shown in Figures 8.75 and 8.76 for the rotating and stationary cases, respectively at Z = 1.0D. Flow entrainment into the wake is in a lower position at this station for both cases due to the reduced height of the wake. The rotating case shows fluid being entrained at the lower region of 0.5<y/D<0.85, -0.25<x/D<0.25 with a maximum secondary flow velocity of $V/V_{ref}$ = 0.4. The stationary case shows entrainment into the wake at 0.3<y/D<0.85, -0.3<x/D<0.3. The stationary wheel wake being lower in height due to the later boundary layer separation. Again, the maximum flow velocity into the wake is $V/V_{ref}$ = 0.4.

### 10.5.5 Z = 1.5D plane

This is the first streamwise station where it is possible to compare both rotating and stationary data since the out of range data are significantly reduced. Figures 8.77 and 8.78 show time-averaged contours of constant total pressure coefficient for the

rotating and stationary cases, respectively at Z = 1.5D. The rotating wheel wake is tall and narrow in comparison to the stationary wake which is short in height and wide. There are two regions of low total pressure in the stationary wake (Cpo = -0.18) that can be seen at y/D = 0.15, x/D = -0.35 for the left (hub) side of the wake, and y/D = 0.15, x/D = 0.45 for the right (sting) side of the wake, which correspond to higher drag for the stationary wheel. The wake is offset towards the sting from the centreline and this asymmetry is most likely due to interactions with the sting wake and hub cavity. By comparison the rotating wheel shows two regions of low total pressure (Cpo = -0.01) at y/D = 0.25, x/D = -0.1 for the hub side and y/D = 0.25, x/D = 0.25 for the sting side of the wake. However, when compared to the stationary wheel wake the total pressure deficit is not as great, corresponding to lower drag for the rotating wheel. The pressure gradient across the wake structure is greater for the stationary case, and when compared to the upstream station (Z = 1.0D) the pressure gradients across the rotating and stationary wheel wakes have decreased as the wake diffuses downstream.

Figures 8.79 and 8.80 show contours of constant standard deviation of the dynamic pressure coefficient for the rotating and stationary wheels, respectively at Z = 1.5D. There is unsteadiness at the top of the plots (y/D = 1.2, -0.9<x/D<0.25) caused by one of the PIV seeding tubes that was fitted to the top of the wind tunnel nozzle. Not all plots show this due to different times when the data were acquired. The rotating case shows a large region of high unsteadiness (SD = 0.3) on the sting side of the wake (y/D = 0.3, x/D = 0.45) compared to the hub side of the wake where there exists a similar region but of lower unsteadiness (SD = 0.23). The hub cavity and sting seeming to increase the unsteadiness on that side of the wake, although this does not seem to be the case for the stationary wheel where the regions of increased unsteadiness are reasonably symmetrical (in terms of magnitude) about the wheel centreline (y/D = 0.25, x/D = ± 0.7) with a standard deviation (SD) of 0.26, although the sting side of the wake does show a larger region of unsteadiness.

The streamwise vorticity data were presented in Figures 8.81 and 8.82 for the rotat-

ing and stationary cases, respectively. The two plots show the trailing vortices that are formed when the axial flow turns and rotates onto the low pressure rear surface of the wheel and induces vortical structures. The rotating wheel trailing vortices can be seen to be higher and near to the centreline of the wheel in comparison to the stationary wheel vortices that are lower and much more spread out. The left (hub) side vortex rotates in a clockwise direction (although the out of range data mask this) and the right (sting) side vortex rotates in a counter-clockwise direction for both cases. There is a strong downwash behind the stationary wheel (discussed in the PIV results) which drives the trailing vortices down towards the groundplane. The vortices are spread out at the groundplane and this is most likely due to interaction with the groundplane boundary layer. The vortices are weaker for the rotating case (lower drag). The remainder of the field shows no vorticity as expected.

The time-averaged secondary flow velocity vectors are shown in Figures 8.83 and 8.84 for the rotating and stationary cases, respectively at Z = 1.5D. The strong downward component of velocity ($V/V_{ref}$ = 0.46) can be seen in the stationary wheel wake compared to the rotating case, which drives and strengthens the vortical structures.

### 10.5.6 Z = 2.0D plane

The number of out of range data at this streamwise station are minimal. Figures 8.85 and 8.86 show time-averaged contours of constant total pressure for the rotating and stationary cases, respectively at Z = 2.0D. The progression downstream shows that both wake structures have decreased in height and are more spread out. The upper region of the wake corresponding to early flow separation for the rotating wheel can be clearly seen. The pressure gradients across the wakes have decreased due to the structures being more diffuse relative to the streamwise station Z = 1.5D. Asymmetry is present in both rotating and stationary contour plots due to the sting and hub cavity. The two regions of lower total pressure for the stationary wheel wake can be seen at y/D = 0.1, x/D = -0.4 for the hub side of the wake and y/D = 0.1, x/D = 0.6 which have moved away from the wheel relative to the upstream

station Z = 1.5D. The total pressure is slightly higher for the stationary case (Cpo ≈ -0.1) compared to around Cpo ≈ -0.18 for the stationary Z = 1.5D station, although the overall wake is larger for this station (Z = 2.0D) and therefore a similar drag force should be computed from both stations based on the wake integral method.

Figures 8.87 and 8.88 show contours of constant standard deviation of the dynamic pressure coefficient for the rotating and stationary cases, respectively at Z = 2.0D. The PIV tubing effects can also be seen in these plots. As a result of the wake structures spreading out the regions of high unsteadiness have moved outwards relative to the centreline of the wheel. The stationary wheel wake shows the two regions of increased unsteadiness (SD = 0.24) at y/D = 0.3, x/D = ± 0.75, and the rotating wheel wake shows the region of high unsteadiness (SD = 0.28) on the sting side of the wake (y/D = 0.25, x/D = 0.55). In line with the upstream rotating wake structures the unsteady region on the hub side of the wake (y/D = 0.2, x/D = -0.45) has reduced levels of unsteadiness (SD = 0.2) relative to the sting side of the wake.

The time-averaged contours of constant streamwise vorticity are shown for the rotating and stationary cases in Figures 8.89 and 8.90, respectively for the Z = 2.0D station. The rotating wheel wake shows the two trailing vortices, although it is difficult to see the sting side vortical structure due to the contour levels chosen (to allow direct comparison between data) since the trailing vortices are relatively weak for the rotating case at this streamwise station. The positions of these time-averaged structures are relatively high and close to the centreline of the wheel (y/D = 0.35, x/D = -0.15 (hub side, rotating clockwise), y/D = 0.25, x/D = 0.2 (sting side, rotating counter-clockwise)) when compared to the stationary wheel wake where the trailing vortices are strong and close to the fixed groundplane (y/D = 0.1, x/D = -0.4 (hub side, rotating clockwise), y/D = 0.1, x/D = 0.55 (sting side, rotating counter-clockwise)).

The time-averaged secondary flow vectors for the rotating and stationary cases are shown in Figures 8.91 and 8.92, respectively for the station Z = 2.0D. The contours

of $w/V_{ref}$ velocity show the outline of the wheel wakes. There is slight downwash ($V/V_{ref}$ = 0.28 (max.)) for the rotating wheel around the centreline of the wheel. The stationary wheel wake shows stronger downwash with a maximum downward component of velocity relative to the freestream axial flow of $V/V_{ref}$ = 0.34 and the two counter rotating trailing vortices can be seen at y/D = 0.15, x/D = -0.4 (hub side, rotating clockwise) and y/D = 0.15, x/D = 0.7 (sting side, rotating counter-clockwise).

### 10.5.7 Z = 2.5D plane

The data for this plane were used for the wake integral method with a wider analysis region to capture the complete wake structure. The measurement resolution for the rotating and stationary cases was identical for these measurement planes whereby measurements were taken every 10mm in both $x$ and $y$ directions. Time-averaged contours of constant total pressure coefficient for the rotating and stationary cases are shown in Figures 8.93 and 8.94, respectively for the station Z = 2.5D. Both wake structures are more diffuse compared to upstream measurement stations with decreased pressure gradients across the wakes. The stationary wheel wake shows the two regions of lower total pressure (y/D = 0.12, x/D = -0.5 (hub side) and y/D = 0.12, x/D = 0.65 (sting side)) compared to the rotating wake, which helps to explain the higher drag for the stationary wheel computed using the wake integral method of Ryan [53]. The wake asymmetry can be clearly seen in both cases. A small region of out of range data exists for the stationary case with no out of range data present for the rotating case.

The contours of standard deviation of the dynamic pressure coefficient are shown in Figures 8.95 and 8.96 for the rotating and stationary cases, respectively for the Z = 2.5D station. These plots show a similar trend to the stations upstream whereby the levels of unsteadiness have decreased and the regions of increased unsteadiness relative to the rest of the wake have moved away from the centreline of the wheel due to the wake being more diffuse at it progresses downstream. In fact the wakes are generally more unsteady in the near-wake than at this station. The rotating

wheel wake shows more unsteadiness on the sting side (y/D = 0.25, x/D = 0.65) of the wake which agrees with the upstream stations. The stationary wheel wake shows the two regions of increased unsteadiness at the wider positions of y/D = 0.3, x/D = ± 0.8.

The time-averaged contours of constant streamwise vorticity are shown in Figures 8.97 and 8.98 for the rotating and stationary cases, respectively for the streamwise station Z = 2.5D. Once again, the rotating wheel wake shows only weak streamwise vorticity at y/D = 0.3, x/D = -0.15 (hub side) and y/D = 0.15, x/D = 0.35. The stationary case shows larger, stronger regions of vorticity in comparison, again closer to the groundplane, although the wake asymmetry has moved these vortices towards the sting.

Figures 8.99 and 8.100 show time-averaged secondary flow vectors for the rotating and stationary cases, respectively for the station Z = 2.5D. The stationary wheel wake shows the stronger downward component of velocity ($V/V_{ref}$ = 0.28 max.) compared to the rotating case ($V/V_{ref}$ = 0.2 max.).

## 10.6 PIV

The complete (PosA-D) ensemble time-averaged velocity fields on the centreline (W/D = 0) YZ plane for the rotating and stationary wheels are shown in Figures 8.101 and 8.102, respectively. The reference freestream velocity vector is shown. A velocity vector scaling factor (SF) of 1.0 was used for these vector maps. The individual regions (e.g. PosA) are discussed individually so only general observations will be made here. On initial inspection the two flow-fields are significantly different. The early flow separation is clearly visible for the rotating case at y/D = 1.0, z/D = -0.05. Reversed flow can be seen after the separation point. The most remarkable feature of the rotating case is the rear jetting after the line of contact, and this is discussed fully when PosA is discussed later. The stationary case shows the strong downwash in the near-wake, which of course was mentioned in the flow visualisation

images. There is reversed flow evident in both cases.

Now to focus on PosA on the centreline of the wheel (YZ plane). Figures 8.103 and 8.104 show ensemble time-averaged velocity vectors for the centreline (W/D = 0) YZ plane for PosA for the rotating and stationary cases, respectively. The velocity scaling factor for these plots was set to SF = 2.7. Again, the two flow-fields are vastly different due to wheel rotation. With regard firstly to the rotating case (Figure 8.103) the rear jetting phenomenon can be seen at y/D = 0.05, z/D = 0.3. It is worth remembering that the wheel rotates counter-clockwise and the groundplane linear motion is from left to right. Recalling the surface static pressure data for the centreline of the rotating wheel (Figure 8.1) the rapid decrease to low pressure after the line of contact was caused by the two diverging boundaries drawing air out of the contact region. This PIV velocity field data confirms the existence of the rear jetting phenomenon. This is unique aerodynamic data and proves beyond doubt that this flow mechanism exists. The effect and influence it has on the wake mechanics are postulated in the Section 10.8. The majority of the flow in the lower half of the near-wake is flowing into the contact region, which should be the case for continuity since a localised region of strong negative pressure exists at the contact region. However, this represents a time-average of the velocity field and the instantaneous velocity fields are discussed later. The flow is being swept back around the wheel towards the top of the wheel in the upper region of the near-wake (0.4<y/D<0.7, 0.5<z/D<0.8) due to wheel rotation.

The stationary vector field (Figure 8.104) shows in more detail the strong downwash behind the wheel with a velocity magnitude of 14.85ms$^{-1}$ ($V/V_{ref}$ = 1.03) due to the attached flow around the top of the wheel. The strong downwash on the centreline will drive and strengthen the trailing vortices and push the vortical structure cores down towards the groundplane. Reversed flow is prevalent at y/D = 0.6, 0.4<z/D<0.7.

Figure 8.105 shows a sequence of instantaneous velocity vector plots for PosA on

the centreline (W/D = 0) YZ plane for the rotating (a-c) and stationary (d-f) cases. Immediately apparent in both the rotating and stationary plots is the unsteadiness in the near-wake of the wheel. It is worth reiterating that these measurements are not time-resolved and therefore a time of 0.0s represents the start of sampling only (not in-phase). At t = 0.0s the magnitude of the rear jetting is greater ($V/V_{ref} = 1$) compared to the time-averaged jetting ($V/V_{ref} = 0.6$), although this is not surprising since the rear jetting phenomenon is unsteady. This can be seen by looking at the rear jetting at t = 0.2s where the jetting "quantity" and magnitude have reduced compared to t = 0.0s. The jetting at t = 0.4s shows a slight increase in jetting compared to t = 0.2s. The animations provided on the CD that accompanies this thesis show this phenomenon more clearly. The animations can be run on either Windows Media Player or QuickTime Player. In particular "InstCLyzPosAStat.avi" shows an animation of instantaneous velocity vectors for the centreline of PosA for the stationary wheel on the YZ plane, and "InstCLyzPosARot.avi" shows an animation of instantaneous velocity vectors for the centreline of PosA for the rotating wheel on the YZ plane. It is recommended that the Media Player is operated in "loop" mode. The animations show the velocity field at 2 frames per second for clarity. The rotating PosA animation on the centreline YZ plane shows the unsteadiness in the wheel wake and highlights the unsteady rear jetting phenomenon. It was initially thought that there must be an inflow into the rear contact region around the side of the wheel although, as will be shown later, this is probably not the case. From continuity if there is a mass flow out of the contact region then there must be a mass flow into the region. Further discussion of the rear jetting phenomenon is given in Section 10.8 when all of the results obtained during this work and the contributions of others are brought together to form a more complete picture and therefore argument.

The stationary instantaneous velocity vector plots (Figure 8.105) show the strong downwash at $0.4<y/D<0.7$, $0.5<z/D<0.8$ with a local velocity as a fraction of the reference freestream velocity of $V/V_{ref} = 1.03$. At t = 0.2s there is a vortical structure (rotating clockwise) at y/D = 0.36, z/D = 0.63. The flow-field about racing car wheels is highly complex and three-dimensional, however the flow-field is more

likely to exhibit some two-dimensionality on the centreline of the wheel so it is not surprising to observe such a flow feature. This particular vortex will be formed when the boundary layer separates from the surface of the wheel and the resulting separated shear layer will roll up into a discrete vortical structure. Recall that the boundary layer separates later for the stationary case (in an adverse pressure gradient) at $\theta = 225$ degrees. This vortex is then convected downstream. It would have been beneficial to increase the temporal resolution of the PIV vector fields to observe the formation of this flow feature. Moreover, to observe any interesting flow feature associated with the wheel flows in general, and to observe these structures as they are washed downstream. This was not possible however as the CCD camera limited the temporal resolution of the PIV apparatus. The lower region of the wake at $0.0<y/D<0.3$, $0.2<z/D<0.8$ next to the groundplane shows reversed flow and the wake structure is highly unsteady. The animation (InstCLyzPosAStat.avi) shows the above in animated form.

The sequence highlights the unsteadiness in the near-wake and Figures 8.106 and 8.107 show contours of standard deviation of the velocity field for the rotating and stationary cases, respectively. Both plots show the unsteadiness in the near-wake and the rotating case shows increased unsteadiness at $0<y/D<0.2$, $0.2<z/D<0.4$ where the unsteady rear jetting phenomenon was observed. The stationary case shows increased unsteadiness at around the position of the separated shear layer rolling up into a discrete vortex ($y/D = 0.48$, $z/D = 0.61$).

Ensemble time-averaged contours of constant spanwise vorticity ($\zeta$) for PosA on the centreline ($W/D = 0$) YZ plane are shown in Figures 8.108 and 8.109 for the rotating and stationary cases, respectively. The rotating case (Figure 8.108) shows the time-averaged vorticity field has no significant spanwise vorticity with the exception of a vortex at the contact region ($y/D = 0.05$, $z/D = 0.3$). This vortical structure is present due to the rear jetting flow acting on fluid in the contact region and inducing rotational flow. The stationary case (Figure 8.109), again, shows no significant spanwise vorticity with the exception of one region of the flow-field at

this station. There is a vortex at y/D = 0.6, z/D = 0.55, caused by the separated shear layer that has rolled up into a discrete vortex. This represents a time-average of the vorticity field.

Figure 8.110 shows a sequence of instantaneous vorticity plots on the centreline YZ plane of PosA for the rotating (a-c) and stationary (d-f) wheels. Both sequences show the unsteadiness in the wake. The rotating case shows small regions of instantaneous vorticity that when averaged over a long enough time period (as was the case in Figure 8.108) effectively reduce to zero vorticity in a large proportion of the flow-field. This also happens in the stationary case. An interesting region in the instantaneous stationary vorticity plots is the roll up of the separated shear layer (y/D = 0.55, z/D = 0.6). Figure 8.110d (t = 0.0s) shows a strong vortical structure concentrated at y/D = 0.55, z/D = 0.6. Figure 8.110e (t = 0.2s) shows an elongated vortical structure which appears to be splitting into two separate vortices. By t = 0.4s (Figure 8.110f) the original vortex has separated into two discrete vortices with reduced vorticity. This flow structure appears to behave two-dimensionally based on these plots, although 3D measurements would be more conclusive. As previously mentioned, increasing the temporal resolution of these plots would show the formation and diffusion of these structures.

Ensemble time-averaged velocity vector plots on the centreline (W/D = 0) YZ plane for PosB are shown in Figures 8.111 and 8.112 for the rotating and stationary wheels, respectively. The velocity scaling factor (SF) was set to 1.0 for these plots. The two wake structures are significantly different at this station downstream of the wheel. The stationary case shows the strong downward component of velocity of $V/V_{ref}$ = 0.7 at 0.2<y/D<0.7, 0.85<z/D<0.9. The rotating case at this location shows reversed flow with a velocity magnitude of $V/V_{ref}$ = -0.19. The downward component of velocity for the stationary case helps to drive and strengthen the trailing vortices. The fluid adjacent to the MGP for the rotating case has the same velocity as the groundplane ($V/V_{ref}$ = 1.0). The local velocity at 0.55<y/D<0.7, 1.7<z/D<1.9 has almost reached the freestream velocity for the stationary wheel ($V/V_{ref}$ = 0.98) due

to the lower wake structure compared to the taller wake structure associated with the rotating wheel where the local velocity is $V/V_{ref} = 0.84$.

The instantaneous velocity vector plots for the centreline YZ plane of PosB are shown for the rotating (a-c) and stationary (d-f) in Figure 8.113. The strong downwash can be seen for the stationary wheel (d-f) and the unsteadiness in the wake can be clearly seen for both the stationary and rotating cases.

Time-averaged contours of constant spanwise vorticity for PosB on the centreline of the wheel are shown in Figures 8.114 and 8.115 for the rotating and stationary cases, respectively. The majority of the field shows no signs of any time-averaged spanwise vorticity for either case. The VidPiv4.0 PIV analysis software has computed strong vorticity at the MGP for the rotating case and slight vorticity for the stationary case at the fixed groundplane. This is due to the velocity change in the direction normal to the groundplane ($\partial w/\partial y$) and can be seen in Figures 8.111 and 8.112 for the rotating and stationary wheels, respectively.

A short sequence of instantaneous spanwise vorticity contour plots are shown in Figure 8.116 for PosB on the centreline YZ plane. All of the plots show small packets of spanwise vorticity that when averaged over time show no spanwise vorticity worthy of note. Again, as was the case with the ensemble time-averaged data for this position, the vorticity at the MGP can be clearly observed.

The time-averaged velocity vectors for PosC on the YZ centreline plane for the rotating and stationary cases are shown in Figures 8.117 and 8.118, respectively. Most of the flow in these two plots is the freestream axial flow apart from the lower left side of the plots where both vector fields show similar data due to the position of the measurement station in the flow-field.

The sequence of vector fields for PosC are shown in Figure 8.119. There is flow unsteadiness at the lower left region ($0.7<y/D<1.1$, $0.8<z/D<1.8$) of the field for

both cases.

The ensemble time-averaged velocity fields for the centreline YZ plane for PosD at the top of the wheel are shown in Figures 8.120 and 8.121 for the rotating and stationary cases, respectively. The velocity vector scaling factor (SF) was set to 1.0 for both plots. The upper region of both figures (1.2<y/D<1.5, -1.5<z/D<0.85) shows the freestream axial flow ($V/V_{ref}$ = 1.0). The most remarkable flow feature in these two plots is the early flow separation that has been successfully captured using PIV at y/D = 1.0, z/D = -0.05. From the static pressure measurements acquired using the radio telemetry system the boundary layer separated at around 290 degrees (before the top of the wheel). This can be seen clearly in Figure 8.120. This agrees favourably with the smoke visualisation image (Figure 8.40). There is reversed flow ($V/V_{ref}$ = -0.7) just after the separation position which is of course expected. The stationary case (Figure 8.121) shows attached flow around the top of the wheel. A short time sequence at this station in the flow-field is shown in Figure 8.122. The stationary (d-f) case shows the flow to be relatively steady and attached around the top of the wheel compared to the rotating case (a-c) where the flow after separation is unsteady. The separation position is not at a fixed angular position and will vary angular position slightly as a function of time, due to the unsteady nature of separation. Unsteady boundary layer separation can be seen when analysing the regular vortex shedding of "infinite" circular cylinders. This moving separation position can be seen in the rotating instantaneous plots where Figure 8.122b shows that boundary layer separation has moved forwards toward the front of the wheel. This is shown in animated form in "InstCLyzPosDRot.avi". The static pressure distribution over the surface of the wheel represents a time-average of the surface pressure field only. Acquiring the instantaneous static pressure on the centreline of the wheel would be more indicative of the separation position at any instant in time, although this data would be highly dependent on the temporal resolution of the instrumentation system (i.e. the radio telemetry system) and is beyond the scope of this work. Moreover, this type of system would be useful to analyse the effects of the rear jetting phenomenon.

For the stationary case (Figures 8.122d-f) the velocity data adjacent to the wheel surface is thought to be spurious due to poor quality data. Obviously the no-slip condition is present at the wheel surface and a boundary layer will have grown along the curved surface of the wheel. However, the stationary case seemed particularly prone to laser light reflections compared to rotating case. It is thought that these reflections resulted in small regions of poor data and Lawson et al [33] comment on the use of a fluorescent seeding material named Rhodamine to counter this reflective problem, although this was not tested here. With the spatial resolution used (10mm in both $x$ and $y$ directions) it would not be possible to capture the velocity profile in the boundary layer at any streamwise station in the layer. These vector fields can be seen in animated form in "InstCLyzPosDStat.avi".

The contours of standard deviation of the vector field are shown in Figures 8.123 and 8.124 for the rotating and stationary cases, respectively at PosD on the centreline YZ plane. Both plots show that the upper region of the vector field is relatively steady with minimal velocity fluctuations as expected. The rotating wheel wake can be clearly seen due to the increased unsteadiness in the near-wake. The early flow separation can be seen, which results in a taller wake structure with increased unsteadiness present at separation. The stationary case shows similar flow unsteadiness at the top of the wheel but, as mentioned above, the stationary wheel was extremely prone to laser reflections and this particular region of the flow-field yielded invalid vectors, therefore they were interpolated using the VidPiv4.0 analysis software. Suffice to say this region should be treat with caution. Another region of the flow exhibiting unsteadiness for the stationary wheel is located at approximately y/D = 0.75, z/D = 0.55, which is most likely due to the later boundary layer separation for the stationary wheel at around $\theta = 225$ degrees.

The ensemble time-averaged spanwise vorticity contours for PosD on the centreline YZ plane of the wheel are shown for the rotating and stationary cases in Figures 8.125 and 8.126, respectively. The instantaneous vorticity contour plots for this

flow-field station are shown in Figure 8.127. A vortex is formed at separation which extends downstream for the rotating case as the separated shear layer rolls up into a vortical structure. The rotating instantaneous plots (Figures 8.127a-c) show the unsteadiness in the near-wake, which of course has been discussed already. The instantaneous vorticity plots show pockets of vorticity being shed from the top of the wheel. The remainder of the vorticity field has little vorticity as expected. One anomaly that exists for the stationary case, which again is a direct consequence of the spurious velocity field near the wheel surface, is the relatively strong vorticity adjacent to the wall. It would be unlikely that any vorticity in the boundary layer would extend this far normal from the tyre surface. Additionally, the PIV velocity spatial resolution was not sufficient to resolve the layer.

The time-averaged velocity vectors for PosA on the wheel edge (W/D = +0.18) are shown in Figures 8.128 and 8.129 for the rotating and stationary cases, respectively. Care should be taken when analysing these vector fields and trying to draw any meaningful conclusions from them due to the three-dimensional nature of the flow at this station and the methods of acquisition. Namely, only the in-plane character of the flow was acquired using 2D PIV. The rotating vector field shows no sign of any rear jetting and this is most likely due to the 3D flow effects, with the through plane component of velocity not measured. There is a region of the flow-field ($0.2<y/D<0.3$, $0.55<z/D<0.8$) where the flow appears to be in-plane, although this vector field is of limited use in further understanding the wake structures and therefore 3D PIV would certainly be necessary at this station. For the stationary case it appears there is flow being entrained into the hub side trailing vortex, but for the reasons already discussed 3D measurements are needed.

A sequence showing the vector fields on the wheel edge (W/D = 0.18) are shown in Figure 8.130. The flow unsteadiness can be seen but, again, not many conclusions can be drawn from these vector fields. The flow unsteadiness is also seen in the standard deviation contours shown in Figures 8.131 and 8.132 for the rotating and stationary cases, respectively on the wheel edge (W/D = 0.18).

The overhead (y/D = 0.26) time-averaged PIV data for PosA on the XZ plane are shown in Figures 8.133 and 8.134 for the rotating and stationary cases, respectively. The direction of airflow is from left to right. The purpose of investigating the flow-field at this position was to establish whether the front jetting could be observed flowing around the side of the wheel into the main axial flow and hence see what influence it has on the flow structure for the rotating case. The data were also acquired for the stationary case at this station to allow direct comparisons to be made. Additionally, data were acquired downstream of PosA (discussed shortly) to try and establish where the inflow into the rear of the contact region is, in order that continuity is satisfied.

On initial inspection of the two vector plots at PosA they appear very similar. Only minor differences exist between the two plots, these being at the front of the wheel at x/D = -0.25, z/D = -0.5. The stationary case shows the flow turning around the sidewall profile of the wheel, whereas the rotating case does not show any signs of the flow turning around the sidewall as would have been expected although this is probably due to the flow accelerating towards the contact region. There are no signs of reversed flow in this region of the flow-field, although the measurement plane was stationed 0.26 diameters vertically from the MGP and the reversed flow shown in Figure 8.44 is limited to a region extending approximately 0.125 diameters vertically from the MGP.

Contours of standard deviation of the velocity field for PosA of the overhead (y/D = 0.26) XZ plane are shown in Figures 8.135 and 8.136 for the rotating and stationary cases, respectively. The rotating case shows minimal flow unsteadiness since most of the flow is the freestream axial flow. A small region of unsteady flow exists at x/D = -0.3, z/D = -0.4 for the rotating wheel and could be due to out of plane vectors caused by the wheel rotating and creating a forced vortex. The stationary wheel plot shows unsteady flow at the side of the wheel extending to the rear of the wheel as the freestream axial flow interacts with the wake. This is seen more clearly in

the overhead position PosB.

The instantaneous velocity vector plots for the overhead XZ plane for PosA are shown in Figure 8.137 for the rotating (a-c) and stationary (d-f) cases. The rotating plots (Figures 8.137a-c) show the flow-field at this station is relatively steady. The stationary plots (Figures 8.137d-f) show flow unsteadiness towards the rear of the wheel at -0.7<x/D<-0.2, 0.0<z/D<0.45.

The time-averaged velocity vector plots for the overhead (y/D = 0.26) XZ plane PosB (downstream of PosA) are shown in Figures 8.138 and 8.139 for the rotating and stationary cases, respectively. Paying attention to the rotating case first, there is little interaction with the axial flow and the wake at this station compared to the stationary case where fluid is being entrained with a relative velocity magnitude of $V/V_{ref}$ = 0.31 into the wake at -0.7<x/D<-0.25, 0.7<z/D<1.1, although from the pressure probe wake surveys the wake structure of the rotating wheel is not as wide as that of the stationary case, however looking at Figures 8.61 and 8.62 it is surprising to see such a lack of interaction between the axial flow and the wake at this station. The majority of the velocity field at this location is the freestream flow.

Contours of standard deviation of the velocity field for PosB of the overhead (y/D = 0.26) XZ plane are shown in Figures 8.140 and 8.141 for the rotating and stationary cases, respectively. Again, the rotating case shows flow unsteadiness adjacent to the wheel. A more narrow region of unsteady flow is present at Z = 0.75D compared to the stationary wheel where the unsteady flow extends from approximately the axis of wheel rotation (Z = 0D) to Z = 1.25D (in this plot) and gets progressively wider.

The instantaneous velocity vector plots for the overhead XZ planes of PosB are shown in Figure 8.142. There is a minimal level of unsteadiness in the rotating case and significant levels of unsteadiness for the stationary case. Figure 8.142f in particular shows fluid being entrained ($V/V_{ref}$ = 0.88) into the stationary wheel wake. There are no signs of an inflow into the rear contact region, which is not

surprising based on the vertical position of the laser sheet.

## 10.7 CFD

### 10.7.1 Predicted Surface Pressure Distributions

The predicted steady-state centreline surface static pressure distribution is shown in Figure 9.1 compared to experiment. The contact patch modelled was located between approximately 80 degrees and 100 degrees, and is similar to the stationary wheel contact patch, and therefore differs slightly from the rotating experiment. The same notation and axes scales were used for all CFD data as per experiment. The general shape of the predicted pressure trace is good with the exception of specific regions. Both traces show the flow stagnating at around 6 degrees and are almost contiguous up to the contact patch showing the same decrease in static pressure at $\theta$ = 40 degrees. At the contact patch the predicted static pressure increases in excess of unity to Cp = 1.32 (front jetting) compared to Cp = 1.9 for the experiment (a reduced y-axis scale would show the pressure peak more clearly). After the line of contact there is a low pressure peak of reduced magnitude (Cp = -0.6) compared to that observed experimentally (Cp = -1.5), which corresponds to predicted rear jetting. There are no predicted oscillations after the low pressure peak suggesting that the oscillations observed experimentally are not an intrinsic aerodynamic flow feature and must be a feature associated with the pneumatic tyre. Obviously there is no compliance in the CFD model of the wheel/tyre assembly compared to that of a rubber tyre. The base pressure for both traces are in good agreement and relatively constant. Between $\theta$ = 360 degrees and 290 degrees the flow is accelerating towards the top of the wheel and both traces are in excellent agreement. The discrepancy between the traces begins at $\theta$ = 290 degrees where the experimental pressure trace shows flow separation, compared to the predicted separation some 25 degrees after the top of the wheel in an adverse pressure gradient. Therefore the CFD model predicts accelerated flow over the top of the wheel which agrees well with the work of Knowles et al [31] where their predicted separation was 22 degrees after the top of the wheel. Bearing in mind the accelerated flow over the top of the wheel it is

difficult to explain the under predicted lift force coefficient ($C_{Lw}$ = 0.29), as can be seen from the predicted pressure trace the accelerated flow causes a localised reduction in static pressure at the top of the wheel which actually increases the lift. The predicted drag force coefficient ($C_{Dw}$ = 0.61) is in good agreement with the experimentally derived coefficients.

The predicted surface pressure distribution corresponding to pressure tapping 2 is shown in Figure 9.2. The general form of this distribution is similar to the centre-line, as are all tread region pressure tappings. At $\theta$ = 0 degrees the predicted static pressure is marginally over predicted at Cp = 1.0 compared to Cp = 0.9 for the experiment. Up to the contact region (10< $\theta$ <80 degrees) the predicted pressure traces are in good agreement. The static pressure at the front of the contact patch is Cp = 1.25, which is lower than the centreline value (Cp = 1.32) and this trend is also shown in the experimental data (Cp = 1.9 centreline c.f. Cp = 1.65 for tapping 2). The predicted low pressure peak after the line of contact is of lower pressure compared to the centreline predicted value, and this is also the case for the experimental data. The base pressure is fairly constant although over predicted. As was the case with the centreline, the predicted separation is after the top of the wheel.

Figure 9.3 shows the predicted surface pressure distribution corresponding to pressure tapping 3. Once again the predicted static pressure distribution is in good general agreement with the experiment with the exception of the separation position, which is predicted after the top of the wheel. The predicted static pressure between $\theta$ = 0 and 80 degrees is excellent and the front and rear jetting phenomena can be seen at the contact patch. The base pressure is relatively constant but again over predicted.

The predicted surface pressure distribution corresponding to pressure tapping 4 is shown in Figure 9.4. The static pressure is over predicted at the front of the wheel (0< $\theta$ <80 degrees and 290< $\theta$ <360 degrees) although the form of the traces are in good agreement. The front jetting high pressure peak and rear jetting low pressure

peak were predicted but with reduced magnitude, which is similar to other distributions. The base pressure is over predicted and is not as constant as the experimental pressure trace. The predicted separation position is again after the top of the wheel.

Figure 9.5 shows the predicted surface pressure distribution corresponding to pressure tapping 5. The static pressure is over predicted at the front of the wheel ($0< \theta <80$ degrees and $290< \theta <360$ degrees) but the shape of the traces are in good agreement. There is a slight increase in static pressure at the front of the contact patch (front jetting) and a slight decrease in pressure after the line of contact (rear jetting). There are several missing data points between $\theta = 180$ and 200 degrees. This is due to the data that were extracted within a width of 1mm across the wheel width in order to acquire the predicted static pressures at the same locations as the pressure tappings. The predicted base pressure is fairly constant with the exception of a low pressure region at $\theta = 155$ degrees, which is difficult to explain. Once again the separation position is poorly predicted.

The predicted surface pressure distribution corresponding to pressure tapping 6 is shown in Figure 9.6. The static pressure is again over predicted at the front of the wheel ($0< \theta <60$ degrees and $300< \theta <360$ degrees) although the general profiles at these regions of the wheel are in good agreement with the experimental data. No front or rear jetting was predicted compared to large jetting observed experimentally. The separation position is once again predicted poorly. The accelerated flow over the top of the wheel has reduced due to the end effects of the wheel resulting in an increase in static pressure at $\theta = 270$ degrees. Some missing data are present at around 180 degrees due to the data extraction method employed and the mesh topology.

Figure 9.7 shows the predicted surface pressure distribution corresponding to pressure tapping 7. The form of the distributions changes here from the tread region distributions as was seen in the experimental work. The general form of the static pressure traces are similar here with the exception of the region between $\theta = 280$

and 360 degrees, although for this region there are a number of missing data points. The static pressures are over predicted at the front of the wheel ($\theta = 0$ degrees) and under predicted at the contact patch ($\theta = 80$ degrees). The pressure traces between $\theta = 110$ and 270 degrees are similar, although the CFD predicts a varying pressure compared to a relatively constant measured static pressure. Several missing data points are notable between $\theta = 110$ and 150 degrees. Again a small decrease in pressure was predicted at $\theta = 155$ degrees.

The predicted surface pressure distribution corresponding to pressure tapping 8 is shown in Figure 9.8. Between $\theta = 0$ and 70 degrees the experimental data show increasing static pressure whereas CFD predicts the opposite to this with the static pressure decreasing. The static pressure is also over predicted at the front upper region of the wheel ($290 < \theta < 360$ degrees). The predicted static pressure between $\theta = 110$ and 270 degrees shows varying pressure with the same decrease in static pressure at $\theta = 155$ degrees as was predicted for tapping 7.

Figure 9.9 shows the predicted surface pressure distribution corresponding to pressure tapping 9. The static pressure for both traces is the same at $\theta = 0$ degrees, then the experimental data show an increase in pressure towards the contact patch and the predicted data show an opposite trend with a decrease in static pressure. Just before the contact patch the predicted pressure trace rapidly increases. The remainder of the traces show good agreement with the exception of the low pressure peak at $\theta = 155$ degrees. A number of data points appear bunched together at around $\theta = 330$ degrees and this is due to the data extraction method and mesh topology. There is a small region of missing data at around $\theta = 180$ degrees.

The predicted surface pressure distribution corresponding to pressure tapping 10 is shown in Figure 9.10. The trend for the predicted static pressure trace between $\theta = 270$ and 360 degrees is in good agreement with the experiment, although the pressures are under predicted. Prediction is poor between $\theta = 100$ and 270 degrees compared to other predicted tappings such as tapping 9. A number of missing data

points are present between $\theta$ = 110 and 200 degrees. The static pressure at $\theta$ = 0 degrees is under predicted and shows a decrease in static pressure towards the contact patch.

Figure 9.11 shows the predicted surface pressure distribution corresponding to pressure tapping 11. At this tapping location similar trends can be seen for the regions 0< $\theta$ <90 degrees and 220< $\theta$ <360 degrees, although the static pressures are under predicted. Several missing data points can be seen at 110< $\theta$ <200 degrees.

The CFD predicted static pressure distributions were generally over predicted at the front of the wheel, which helps explain why the drag force coefficient was over predicted at $C_{Dw}$ = 0.61. The predicted delayed separation will also have an increasing contribution to drag as $cos\theta$ becomes increasingly greater than zero further around the rear of the wheel.

### 10.7.2 Predicted XY Wake Planes

The predicted wake structures are generally in reasonable agreement with the five-hole probe measured wake structures but the out of range experimental data make the comparisons extremely difficult at stations close to the wheel.

Figure 9.12 shows the predicted contours of constant total pressure coefficient for the XY plane at Z = 0D. This figure can be compared to the experimental measurement plane (Figure 8.45). Two regions of predicted low total pressure (Cpo = -0.95) can be seen at y/D = 0.05, x/D = $\pm$ 0.3. At the top of the wheel it appears that the wake is tall possibly due to early flow separation, however the predicted surface pressure distributions and centreline YZ plane velocity field show that the flow separates some 25 degrees after the top of the wheel. It is difficult to say whether these data compare well with the experiment due to the out of range data.

Contours of constant streamwise vorticity for the XY plane at Z = 0D are shown in Figure 9.13. This figure can be compared with the experimental data (Figure

8.49). Two predicted counter rotating vortices can be seen at y/D = 0.2, x/D = ± 0.3. The vortex at y/D = 0.2, x/D = -0.3 is rotating in a clockwise direction and the vortex at y/D = 0.2, x/D = 0.3 is rotating in a counter clockwise direction. These vortices are observed and noted by Knowles et al [30] as the jetting vortices because they originate at the viscous regions of the contact patch. The position of the vortex cores appear slightly high compared to the positions of the predicted low total pressure regions and the experimental data which shows vorticity near to the MGP although a small pocket of clockwise vorticity exists at a similar position experimentally. The remainder of the field show no signs of any vorticity as expected.

The predicted secondary flow velocity vectors for the XY plane at Z = 0D are shown in Figure 9.14, which can be compared experimentally with Figure 8.51. A vector index skip of 10 was used in the vector/contour plotting software to reduce the number of visible vectors for reasons of clarity. The predicted flow can be seen to flow upwards and outwards from the contact region at 0<y/D<0.25, -0.5<x/D<-0.25 with a maximum velocity of $V/V_{ref}$ = 0.28, which is similar to that observed in the experimental data ($V/V_{ref}$ = 0.26 max.). The remainder of the predicted velocity field shows the primary axial flow.

Figure 9.15 shows predicted contours of constant total pressure coefficient for the XY plane at Z = 0.25D, which can be compared to the experimental data shown in Figure 8.53. The progression downstream shows that the two regions of low total pressure, at y/D = 0.05, x/D = ± 0.35, have increased in width, which agrees with the experimental observations. The general shape of these predicted regions look similar to the experimental regions.

The predicted streamwise vorticity contours for the XY plane at Z = 0.25D are shown in Figure 9.16, which can be compared to the experimental vorticity contours (Figure 8.57). The predicted vorticity has decreased compared to the predicted Z = 0D station with the vortex cores at the same position. The rest of the field shows no signs of vorticity.

Figure 9.17 shows the predicted secondary flow velocity vectors for the XY plane at Z = 0.25D, which can be compared to Figure 8.59. The vertical vectors at the top and bottom of the wheel correspond to the vertical component of the rotational velocity (boundary condition) as this condition is applied to the nodes at the surface of the wheel. The outward flow from the contact region is not as prominent at this station which corroborates well with the experimental observations.

The predicted contours of total pressure coefficient for the XY plane at Z = 0.75D are shown in Figure 9.18, which can be directly compared with the experimental data (Figure 8.61). The general wake shape is in reasonable agreement with the experiment and the pressure gradient across the wake is predicted well for the hub (left) side of the wake. It is again difficult to compare the CFD and experimental data due to regions of out of range data. Again the wake is reasonably tall considering the late predicted boundary layer separation. A large region of low total pressure exists at $0<y/D<0.3$, $-0.25<x/D<0.25$ corresponding to the two vortical structures. The predicted streamwise vorticity contours are shown in Figure 9.19, which can be compared with the experimental data (Figure 8.65). Two predicted counter rotating vortical structures can be seen in the same position as the low total pressure region of Figure 9.18. Initially these vortices were thought to be the jetting vortices that had strengthened and moved inboard as they were convected downstream. However, due to the size and position of these structures, and the fact that subsequent vorticity plots show only these two vortices, they must be the two trailing vortices. There relatively low position will be a direct consequence of the later predicted flow separation that will push the vortices down towards the groundplane. Unfortunately the experimental data cannot reinforce this. Knowles et al [30] in fact made 3D LDA measurements at a similar streamwise station (50mm downstream from the "trailing edge" of the wheel) and noted that the upper trailing vortices had higher peak vorticity than the jetting vortices. The positions of the trailing vortices observed by Knowles at al were slightly higher compared to these CFD predictions with the vortex cores located in line with the support sting. As

a result of these observations these predicted vortices will be referred to as trailing vortices.

The predicted secondary flow velocity vectors for the same XY plane at Z = 0.75D are shown in Figure 9.20, which can be compared to experiment (Figure 8.67). The predicted entrainment is in a lower position (0.25<y/D<0.75) in comparison to the experimental data and will be due to the later predicted flow separation. Entrainment into the two vortical structures can be clearly seen.

Figure 9.21 shows contours of constant total pressure coefficient for the XY plane at Z = 1.0D, which can be compared to the experimental data (Figure 8.69). The wake structure shows signs of asymmetry at this station. There are two regions of low total pressure at y/D = 0.15, x/D = -0.15 (left (hub) side) and y/D = 0.05, x/D = 0.25 (right (sting) side). The experimental wake is wider than the predicted wake although the predicted magnitudes of total pressure are in good agreement with experiment. The pressure gradient across the wake is also well predicted. The predicted wake structure is wider at this station than the predicted Z = 0.75D station, which shows the same trend as the experiments where the wake spreads out (diffusion).

The predicted streamwise vorticity contours for this XY plane at Z = 1.0D are shown in Figure 9.22, which can be compared to the experimental data (Figure 8.73). The trailing vortices can be seen in a lower position relative to the Z = 0.75D plane with reduced vorticity. The rest of the field shows no signs of vorticity. The predicted secondary flow velocity vectors for this plane (Z = 1.0D) are shown in Figure 9.23, which can be compared to the experimental data (Figure 8.75). The entrainment into the vortices (particularly the left (hub side) trailing vortex) can be seen at 0.25<y/D<0.60, -0.5<z/D<0. The asymmetry is more noticeable in this plot.

The predicted contours of total pressure coefficient for the XY plane at Z = 1.5D are shown in Figure 9.24, which can be compared to the experiment (Figure 8.77).

The asymmetry in the wake has increased and the right side of the wake structure seems to be poorly predicted. The main criteria for establishing whether the CFD results were grid independent were the surface pressure distributions and the YZ centreline planes. These showed grid independence when the centreline static pressure distribution or rear jetting flow out of the contact region did not change when grid adaptation had been performed. Obviously during initial flow solutions these data changed between successive grid adaptations. Despite this the wake asymmetry seems excessive especially when the grid topology was checked to ensure the cells did not grow by more than 50% (this figure recommended by Fluent [26]) and higher order discretisation of the convective terms was used. The predicted magnitudes of the total pressure do however seem to be well predicted as is the pressure gradient across the wake structure.

The streamwise vorticity contour plot for the XY plane at Z = 1.5D is shown in Figure 9.25, which can be compared to Figure 8.81. The predicted vorticity field shows slight vorticity at y/D = 0.15, x/D -0.25 and y/D = 0.1, x/D = 0.2 which is of reduced magnitude compared to that of the experiment. The right (sting side) vortex is almost indiscernible. Predicted secondary flow vectors at this plane are shown in Figure 9.26 and show the asymmetry in the wake. These should be viewed with caution.

The predicted total pressure coefficient contours for the XY plane at Z = 2.0D are shown in Figure 9.27 which shows the asymmetry once again. The magnitudes of total pressure are well predicted as is the pressure gradient across the wake. The streamwise vorticity contours for this plane are shown in Figure 9.28 and show no significant signs of vorticity compared to experiment (Figure 8.89). The secondary flow vectors for this station (Figure 9.29) show the asymmetry in the wake once again.

### 10.7.3 Predicted YZ Wake Planes

The predicted steady-state velocity field for the YZ plane on the centreline of the wheel is shown in Figure 9.30 which shows the complete PosA-D regions and can be directly compared with the PIV analysis regions shown in Figure 8.101. The vector scaling factor (SF) is 1 for both plots. The predicted field is in reasonable agreement with the PIV data and the later boundary layer separation is clearly visible at 245 degrees. Figure 9.31 shows the predicted velocity field for PosA and experimentally this was seen in Figure 8.103. These plots have a scaling factor of 2.7 due to some small magnitudes exhibited. The majority of the fields are in agreement in terms of velocity magnitude. The rear jetting can be seen at y/D = 0.02, z/D = 0.2 and this will be highlighted shortly. Air can be seen flowing towards the contact region (i.e. at y/D = 0.1, z/D = 0.4) which agrees with the prediction of Fackrell [19] (this is discussed in Section 10.8).

The later boundary layer separation can be seen more clearly in Figure 9.32 which can be compared with the PIV velocity field shown in Figure 8.120. The predicted flow clearly separates at approximately 245 degrees which is of course 25 degrees after the top of the wheel compared to the experimental flow where separation occurs before the top of the wheel at 290 degrees. Despite this inaccurate predicted separation the two velocity fields are in good agreement. Incidentally it was noticed during initial runs using the k-$\epsilon$ RNG turbulence model that the flow separation was nearer the top of the wheel using the same differencing scheme and other numerical parameters as per standard k-$\epsilon$ model. However, as mentioned previously the RNG model exhibited numerical instabilities and was not pursued due to time constraints. Whilst monitoring the separation position for the non-converged k-$\epsilon$ RNG solution it was found that the surface pressure distribution on the wheel centreline was poorly predicted, although the solution had not converged.

The prediction of the rear jetting phenomenon is shown in Figure 9.33. The rear jetting can be clearly seen and confirms that CFD, using the k-$\epsilon$ STD turbulence model, can predict this flow mechanism. It was discovered during this work that the

prediction of the rear jetting is highly dependant on the cell distribution at the contact patch. Moreover, a number of grid adaptations, based on y+, were conducted to ensure the y+ values were in the correct range, whilst ensuring that the domain was not refined beyond what was necessary to ensure the solution converged within an acceptable timescale. The predicted surface pressure distributions therefore corroborate this flow feature by showing the characteristic low pressure peak after the line of contact. The effects this flow mechanism has on the wake mechanics are discussed in Section 10.8.

## 10.8 Examination of the "Jetting" Phenomena

The front jetting phenomenon, as postulated and experimentally observed by Fackrell [19], has been experimentally observed in terms of a measured increase in local static pressure at the front of the contact patch. As discussed earlier the static pressure cannot rise above the value of stagnation pressure (for steady flow) unless extra energy is injected into the flow. This is achieved by the air being effectively squeezed between the wheel and MGP as the two moving boundaries converge with one another. Conversely it was postulated that if this is the case with two converging boundaries then two diverging boundaries (i.e. at the rear of the contact patch) should create a low local static pressure in proximity to the line of contact as air is drawn out of the region by the boundaries due to viscous effects. CFD methods, using tetrahedral volume cells and a $2^{nd}$ order differencing scheme, have predicted the rise in static pressure at the front of the contact region, although with reduced magnitude; nevertheless it has predicted this phenomenon. The jet of air that is produced at the contact patch will pass down by the sides of the wheel since the wheel is of low aspect ratio. These end effects reduce the lift force (in terms of front jetting) acting on the wheel compared to if the wheel were infinitely long. The PIV apparatus was in fact set up to try and observe this and to see what effect the jet has on the wake structure and indeed the forces acting on the wheel. However, due to experimental limitations, whereby the PIV laser arm could not be positioned nearer than 65mm from the MGP, it was not possible to observe such flow down by the side

of the wheel. However, the surface static pressure distributions for the sidewall of the wheel actually showed signs of the jetting phenomenon even when the pressure tappings did not contact the MGP at any part of the rotational cycle of the wheel, although it remains unknown exactly what (if any) effect the front jetting has on the lift and drag forces.

Fackrell showed, through a theoretical solution, that essentially the opposite of the front jetting phenomenon should exist after the line of contact (i.e. a negative pressure peak), and this has in fact been confirmed here using a number of different techniques. Fackrell did expect to observe experimentally the rear jetting flow mechanism but failed to observe it. The surface static pressure measurements obtained using the radio telemetry system show a negative pressure peak after the line of contact which confirms the prediction of Fackrell. A number of other investigators have measured this but have chosen to overlook it, mainly due to the experimental methods employed. For example, Skea et al [62] observed this phenomenon but put it down to experimental effects and not aerodynamic effects (as discussed in the literature review (Chapter 2)). Skea et al probably chose to ignore the experimentally measured rapid increase and decrease in static pressure at the contact patch as a result of their CFD prediction that did not show any significant front jetting. It would therefore appear they thought the data of Fackrell [19] were not conclusive in terms of the front jetting. Hinson [22] correctly stated that her experimentally observed low pressure peak could be a similar aerodynamic flow feature to that predicted by Fackrell, but due to excessive front jetting, caused by the experimental technique, chose to use the contact patch data of Fackrell in her pressure distributions. Other experimental observations have shown neither the front or rear jetting and this has usually been due to incorrect experimental set-up or the use of static pressure probes, or a combination of both of these, such as the investigations by Stapleford and Carr [63] and Imaizumi and Yoshida [24]. Recently several CFD investigations have been conducted and many show no signs of the jetting phenomena. A somewhat puzzling aspect of the work of Axon [7] was that the front jetting phenomenon was well predicted (Cp = 1.9) but the rear jetting phenomenon was

not resolved; not even a small reduction in local static pressure after the contact patch was predicted. The contact patch modelling appeared identical both front and rear and a structured hexahedral volume mesh was used. Therefore it is difficult to explain why no rear jetting was predicted since one would expect either both the front and rear jetting to be predicted (as was the case for this work) or no front or rear jetting, not just front jetting. If the viscous actions can be resolved at the front of the contact region then the viscous actions should also be resolved at the rear, although this will be highly dependent on the mesh topology. Indeed the work of Skea et al [61] and Knowles et al [31] showed minimal signs of front or rear jetting and both investigators opted to use hexahedral volume cells at the contact patch where viscous effects dominate. As mentioned earlier a basic study was carried out whereby hexahedral volume cells were used at the contact region for the P1 wheel geometry and they resulted in highly skewed cells when compared to tetrahedral volume cells. There seems to be a trend in the limited number of published data regarding the prediction of the jetting phenomena. The predictions of Axon [7] showed well the front jetting but not the rear jetting using hexahedral volume cells and a slightly modified contact patch geometry, whereas Skea et al [61] and Knowles et al [31] used hexahedral volume cells with an unmodified contact patch and did not predict the jetting phenomenon. This work has successfully predicted the front and rear jetting phenomena using an unstructured tetrahedral volume mesh. Tetrahedral volume cells therefore seem to be a better choice for discretising the contact region, based on the findings of this research, since they can predict these flow phenomena. However, a number of grid adaptations were necessary to resolve the viscous actions which resulted in a relatively large number of nodes distributed in the contact region in order to satisfy the y+ requirements for the wall treatment employed. Failure to adhere to these requirements would result in poor prediction of the front and rear jetting. Indeed the predicted flow structure on the centreline YZ plane (Figure 9.33) showed the rear jetting, which was slightly more confined to a small region at the contact patch, although the data correlate well with the PIV velocity field (Figure 8.103).

The rear jetting is thought to be of fundamental importance in understanding the wake mechanics of the rotating wheel, as well as being of practical importance in understanding entrainment and spray dispersal characteristics. It is unknown whether the small outflow (jetting) from the contact patch could work like base bleed which could increase the base pressure and hence decrease the drag force acting on the wheel. In order that continuity is satisfied there must be an inflow into the contact region since there is an outflow, however during experimentation using the smoke probe and wool tufts it seemed that there was no inflow to the rear of the contact region from the side of the wheel. It therefore seems more likely that the rear jetting essentially breathes in and out of the wake. This hypothesis is strengthened slightly but not conclusively by looking at Figure 8.105 which shows the instantaneous velocity fields for PosA on the wheel centreline. Figure 8.105b shows slight rear jetting and the fluid adjacent to this region is flowing back into the contact patch, whereas Figures 8.105a and 8.105c show increased rear jetting with the fluid adjacent to this region not flowing into the contact patch, although this may not be the case and requires further supporting evidence either computationally or experimentally. It does however provide the most likely of explanations currently available. A transient CFD solution could be useful here to establish whether there is a strong correlation between rear jetting and base pressure. The reasons for the reduced drag force acting on the rotating wheel are likely to be more complicated with more than just one mechanism responsible. The accelerated flow over the top of the stationary wheel causes a reduction in static pressure (increased lift) and the resulting downwash behind the wheel helps to strengthen the trailing vortices as these vortices entrain fluid from the base region of the wheel and results in lower base pressure and high drag compared to the rotating wheel. It has been discussed that the rear jetting flow is unsteady, although the data described were acquired using 2D PIV and the flow-field is three-dimensional. It was thought during analysis that the PIV data therefore could exhibit an unsteady nature due to the air flowing in three-dimensions and therefore some instantaneous velocity fields may show out of plane data. However, this by no means invalidates the two-dimensional velocity data, and this is certainly not the case, since the number of valid data were high

for this acquisition region (93% valid vectors) in comparison to the data acquired for the wheel edge where the out of plane character of the flow produced a large number of invalid data as the seeding flowed through the laser sheet. The data resulted in poor cross-correlation which was expected at this station. Also the centreline of the wheel is the region of the flow-field most likely to exhibit some two-dimensionality and therefore the rear jetting observed using the PIV apparatus is a genuine unsteady aerodynamic flow feature intrinsic to the flow-field of rotating wheels. Fackrell's prediction of a low pressure peak after the line of contact has been confirmed although the rear jetting effects on the flow-field remain speculative and purely hypothetical. Suffice to say this needs future investigation. However, based on the data available it seems possible that this mechanism could be the agent, or a contributory agent, causing wheel drag reduction for the rotating wheel. It may appear from the surface pressure distributions that the front and rear jetting static pressure peaks effectively cancel each other out in terms of the contribution to the overall lift force since they act at the contact patch at 90 degrees (sin 90 degrees = 1). This may be the case in terms of contribution to the integral lift force, however it is the effect the jetting phenomena have on the overall static pressure distribution that is more important since these effects are not likely to be confined to a small localised region of the contact patch. Further suggested data analysis techniques for the rear jetting flow effects are described in the recommendations for future work (Chapter 11). The oscillations after the rear jetting low pressure peak observed in the surface pressure distributions (Figure 8.1) may not be an intrinsic flow feature associated with the flow about racing car wheels, and therefore the oscillations could have a slight erroneous effect on the integral forces if they were not an genuine flow feature. This would be more so in the case of the computed lift force due to the angular position at which the oscillations occur (close to sin 90 degrees).

## 10.9 The Influence of Angular Measurement Resolution on the Integral Lift and Drag Forces

A reading was acquired every 10 degrees for the stationary surface pressure data and approximately every 5 degrees for the rotating data. To estimate the influence this had on the integral lift and drag forces the rotating data were modified whereby every odd numbered data point was removed resulting in a reading approximately every 10 degrees. The integral lift and drag forces were then computed in the same way as normal (discussed in Chapter 4). Table 10.1 shows the effects the decreased angular position measurement resolution has on the time-averaged integral lift and drag coefficients. The data presented are for the rotating case since one would expect this case to be more sensitive to these effects due to the increased pressure gradients at the contact region. Looking at the force coefficients the drag force appears little affected by the decreased resolution compared to the lift force coefficient. This is due to the decreased resolution effects having a pronounced effect at the contact region due to the large pressure gradients present there. The major reason it has such a small effect on the drag coefficient is due to the cosine of 90 degrees being zero at the contact region. The lift coefficient is more affected due to the sine of 90 degrees being equal to one and therefore any missing data points either increases or decreases the lift force. In this case the lift force is increased due to the rear jetting low pressure peak being removed for this test. Depending on the data sampling and wheel rotational frequencies the front jetting peak could have been removed instead, resulting in a decrease in lift force. The drag force would still be relatively little affected. During telemetry system development data were acquired at a sampling frequency of 3200Hz which resulted in a reading being taken approximately every 2.5 degrees. The centreline static pressure distribution was almost identical to that sampled at 1600Hz which gave confidence that the lift and drag forces were reasonably accurate. In addition the lift and drag forces compare favourably with Fackrell's data.

| Resolution | $C_{Dw}$ | $C_{Lw}$ |
|---|---|---|
| 5 degrees | 0.56 | 0.42 |
| 10 degrees | 0.54 | 0.54 |

Table 10.1: The Influence of Angular Measurement Resolution on the Lift and Drag Coefficients for the Rotating Wheel.

## 10.10 Notes on Reynolds Number

According to Cogotti [14] the operating Reynolds number for the present work ($Re = 2.5 \times 10^5$) is within the critical range. This required careful consideration when designing the wheel flow experiments. Operating at, or near to, the critical $Re$ number can exhibit significant hysteretic effects dependant on whether the velocity is being increased or decreased (Zdravkovich [69]). The air velocity, however, was fixed for these experiments. For example, Schewe [54] discusses that the drag force acting on a circular cylinder at the critical $Re$ number can experience a discontinuous decrease in drag with considerable hysteresis effects; these effects are long established and well documented in the field of fluid mechanics for nominally disturbance free flows. The repeatability of the lift and drag measurements could be indicative of being in the critical $Re$ number range, although for tests conducted with identical conditions (i.e. air velocity) this will probably not be the case. Other factors such as freestream turbulence and surface roughness can influence the effective Re number. The repeatability of the surface static pressure distributions was conducted and the centreline pressure distribution was found to be within 1.5% between different experiments conducted on different days. But this still does not, by itself, indicate a supercritical flow regime. The freestream turbulence was relatively high at 5% (longitudinal component) compared to other wind tunnels of less than 0.2%. Fundamental fluid mechanics texts (such as Massey [37]) show that the effective $Re$ number can be increased above the critical flow regime by increasing the freestream turbulence. The fact that the stationary wheel surface static pressure distributions agreed favourably with those of Fackrell [19] (see Figure 8.3 for stationary wheel centreline) suggests the flow regimes were the same i.e. supercritical.

If the flow regimes were not the same and these experiments had been conducted in the critical or sub-critical regime the pressure distributions would have differed in terms of the boundary layer separation position. Boundary layer separation would have occurred earlier for the stationary wheel (i.e. closer to the top of the wheel, for example at $\theta = 255$ degrees compared to 210 degrees shown in Figure 8.3) due to a fully turbulent boundary layer being more able to sustain more of an adverse pressure gradient since it has higher kinetic energy. It is therefore concluded that the higher freestream turbulence has changed the effective flow regime to supercritical. Therefore the effective Reynolds number for these experiments was not in the critical regime.

## 10.11 The CFD Modelling Approach

The front and rear jetting phenomena were successfully predicted using the standard k-$\epsilon$ turbulence model with enhanced wall treatment. However, this model is usually considered to be poor at predicting the correct position of boundary layer separation (Axon [7]) and this work is no exception with separation predicted some 25 degrees (delayed separation) after the top of the wheel. Knowles et al [31] also showed a similar predicted separation position (22 degrees after the top of the wheel) using the k-$\omega$ model, which Knowles et al deemed to be the most accurate of all Fluent turbulence models. Additionally, no significant jetting were predicted by Knowles et al [31]. The k-$\epsilon$ RNG model of Skea et al [61] using the QUICK differencing scheme provided the most accurate (to date) prediction of the flow separation from the rotating wheel, although again no significant front or rear jetting were predicted. Fluent actually conducted an investigation into automobile wheel flows (Fluent [25]) using hexahedral volume cells and the k-$\epsilon$ RNG model with standard wall functions. The wheel modelled was that used experimentally by Skea et al [61]. The results for the rotating wheel showed no signs of the front or rear jetting phenomena and boundary layer separation was predicted 32 degrees after the top of the wheel. The benefits of using the k-$\epsilon$ RNG model not being seen. Here early flow solutions using the k-$\epsilon$ RNG model showed signs of earlier flow separation but the solutions became

unstable and were abandoned due to time constraints. If the under-relaxation factors had been modified from the default settings to something less aggressive then maybe the solutions would have converged as some flow solutions became very unstable during the first few iterations. Therefore if the solution had not been allowed to excessively diverge numerically this may have resolved this particular problem. The predicted drag force was in good agreement with the experimental data but the lift force was under predicted. One would expect the later predicted boundary layer separation to cause an over predicted lift force due to accelerated flow over the top of the wheel (i.e. increased lift (recall the stationary wheel)), and makes explaining the under predicted lift force extremely difficult. The lift force coefficient does however agree favourably with Wäschle et al [67].

It appears that between this work and the work of Axon [7], Skea et al [61] and Wäschle et al [67] all the flow structures associated with the rotating wheel flows have been predicted well (i.e. the front jetting (Axon [7], this work), rear jetting (this work), early flow separation (Skea et al [61]), velocity field in the wheel wake (Wäschle et al [67], Knowles et al [31] and this work)). The modelling strategy adopted here utilised these other investigations but the k-$\epsilon$ RNG model was not used. It is believed that if future work used this turbulence model and an unstructured tetrahedral volume mesh then all flow structures associated with the wheel flows could be more accurately predicted.

## 10.12 Extensions to Our Understanding of the Time-Averaged Aerodynamics of Exposed Wheels

The most remarkable addition to the knowledge of exposed/isolated wheel flows is the rear jetting phenomenon, which was observed using the surface pressure measurement instrumentation and 2D PIV techniques. The PIV measurements were limited in the sense that only two components of velocity were acquired. Some measurement

stations in the flow-field, such as the wheel edge, showed out of plane characteristics due to three dimensional flow effects and caused poor cross-correlation of the image pairs. The rear jetting observed on the wheel centreline YZ plane did not suffer during data post-processing from poor cross correlation and the out of plane flow are thought to be minimal. Despite this, quantification would be more conclusive using a stereoscopic PIV system. The PIV instantaneous velocity field data also highlighted the unsteady nature of the rear jetting mechanism. Indeed the flow unsteadiness in the complete wheel wake has been shown.

The rear jetting was also predicted using CFD. These experimental observations and CFD prediction confirm the theoretical prediction of Fackrell [19]. The effects the rear jetting has on the wake mechanics and hence forces needs further investigation. This work has confirmed, through the experimental acquisition and CFD prediction of unique aerodynamic data, the existence of the rear jetting flow mechanism. Future work should focus on this phenomenon and develop techniques to understand it fully. Chapter 11 discusses such future strategies.

Prior to this work the flow structures in the wake were not known to any degree. Fackrell [19] showed the outline of the wake, which is of limited use. Axon [7] presented predictions of the wake outline validated against those of Fackrell; again of limited use. Bearman et al [9] measured the wake structures using a seven-hole pressure probe at one station in the wheel wake. Their results showed stronger trailing vortices and increased total pressure loss for the stationary wheel. Here the pneumatic pressure probe wake surveys showed the strong streamwise vorticity present in the wake of the stationary wheel. The downwash behind the stationary wheel drives these trailing vortices which result in higher drag compared to the rotating wheel where the trailing vortices are weaker in strength. Regions of low total pressure were observed as a result of the vortical flows in the wake. The major limitations of the wake surveys using the five-hole probe were the large regions of out of range data acquired. The probe was rotated about the pitch axis through 360 degrees, which did show the strong downwash behind the stationary wheel, and it is thought that the

probe was out of range in terms of flow yaw angle relative to the probe head. Alternative methods of data acquisition would be beneficial for regions of the near-wake such as 3D PIV or 3D LDV. The wake integral derived drag coefficients do compare favourably with other experimentally derived drag force coefficients even though the stationary wake was not fully measured i.e. the drag force should be larger than the one tabulated in Table 8.1. However, it is the flow structures that were considered the most useful in further understanding the aerodynamics of wheels rather than the precise quantification of the body forces. Moreover, the lift and drag coefficients do agree favourably between each method employed and those of Fackrell [19]. Where there are discrepancies they are usually easily justifiable, for example the load cell measuring a higher rotating wheel drag coefficient ($C_{Dw} = 0.63$) compared to the surface pressure distribution derived coefficient ($C_{Dw} = 0.56$) due to the load cell measuring the hub cavity drag and skin friction.

The major additions to CFD have been discussed in Section 10.11. This includes the use of tetrahedral unstructured volume cells to correctly discretise the contact region for predicting the front and rear jetting. However, even using grid adaptation based on y+ the flow separation position was incorrectly predicted using the standard k-$\epsilon$ turbulence model. The suggestions above for using the k-$\epsilon$ RNG model are discussed in the recommendations of future work (Chapter 11).

## 10.13 Summary

This chapter has discussed the experimental and computational results obtained throughout this research. The important results and flow phenomena have been discussed, and how the data acquired and presented in this thesis have increased our knowledge of wheel aerodynamics. This work provides a significant step towards fully understanding the wheel flows, although there is still research needed in order to achieve this ultimate goal. Recommendations and suggestions for future work and methods of achieving more detailed analyses of the wheel flows are given in the

next chapter (Chapter 11).

# Chapter 11

# Conclusions and Recommendations for Future Work

## 11.1 Conclusions

A pneumatic tyre/wheel assembly has been used in wind tunnel experiments to analyse the aerodynamic characteristics of exposed racing car wheels. A number of experimental techniques have been employed to analyse particular aspects associated with the wheel flows, which included using a purpose designed radio telemetry system to acquire surface pressure data from both rotating and stationary wheels. Time-averaged lift and drag forces were computed from the static pressure data obtained. Particle image velocimetry was also used to analyse the velocity field about the wheel, and a pneumatic pressure probe was used to make single-point pressure measurements in the wake of the wheel. Finally, the rotating wheel flows were analysed using a steady state 3D CFD model and compared with the experimental data.

From this research it can be concluded that:

1. The front jetting phenomenon, as postulated and experimentally observed by Fackrell [19], has been observed from wheel surface pressure measurements. The experimental surface pressure distributions agreed well with those of Fack-

rell for both stationary and rotating wheels, as indeed did the lift and drag coefficients. The wheel surface pressure measurements were made using a radio telemetry system that was designed, constructed and commissioned during the course of this study.

2. The rear jetting phenomenon has been experimentally observed using the surface pressure and PIV measurements. The data obtained corroborate the theoretical prediction of Fackrell [19]. This flow mechanism was found to be unsteady and therefore further development of the instrumentation is needed to further understand it. The effects this flow mechanism has on the wake mechanics have been postulated. As a result of this work the jetting phenomenon as postulated by Fackrell [19], which focused on the front jetting phenomenon, has been revised to include the rear jetting phenomenon.

3. The CFD predictions for the rotating wheel have successfully predicted the front and rear jetting phenomena. It was found that this success is highly dependant on the accurate setting of the y+ values for the wall boundaries. This was achieved using grid adaptation based on the y+ range. Moreover the prediction of the jetting phenomena seems to be highly dependant on the choice of volume cells with tetrahedral unstructured volume cells showing the most accurate results.

4. The flow separation position was accurately measured using the PIV techniques, which agreed well qualitatively with the smoke flow investigation images. Good quantitative agreement was had between the separation position acquired from the surface static pressure measurements and that of PIV. CFD predictions showed delayed boundary layer separation for the rotating wheel and is inaccurate compared with the experimental methods.

5. The PIV measurements highlighted the unsteadiness exhibited in the wheel wake. The majority of the data in this thesis were time-averaged.

6. The time-averaged lift and drag coefficients obtained using different methods of analysis were generally in good agreement. The lift force derived from CFD

was under predicted but agreed well with Wäschle et al [67].

7. The wake surveys showed the flow structures in the wake of the wheel. Two counter rotating trailing vortices were observed. The stationary wheel showed higher strength trailing vortices due to the downwash behind the wheel which drives and strengthens them. Two regions of low total pressure were present at the vortex cores. This corresponds to an increased drag force acting on the stationary wheel.

## 11.2 Recommendations for Future Work

This research programme represents a significant step towards fully understanding the aerodynamic characteristics of racing car wheels. The following points form suggested recommendations, both for the direction of potential future work, and in the application of experimental and computational techniques.

1. The surface pressure measurement instrumentation was developed to acquire / analyse the time-averaged static pressure distributions and subsequently compute the time-averaged lift and drag forces acting on the wheel. The forces acting on the wheel are however unsteady and hence the pressure measurement system needs further development. Knowing the instantaneous forces acting on the wheel is far more useful to racing car engineers since, for example, the instantaneous lift force into the suspension system would be quantifiable which could lead to improved vehicle dynamics. To achieve this multiple pressure tappings could be installed all around the wheel periphery and across the wheel width. Multiple pressure scanners could then be installed and multiplexed simultaneously. This would effectively give quasi-simultaneous pressure data since each scanner has to be operated sequentially, but at a sampling frequency of 20kHz the readings would be quasi-simultaneous. The data for all pressure tappings could then be integrated for a given instant in time to yield the instantaneous lift and drag forces. The electronics circuitry would however require major redevelopment. Obtaining an angular position measurement

resolution of 5 degrees would require a number of pressure scanners, which could be difficult to install in a model wheel and therefore a full-scale wheel may be more appropriate.

2. One of the disadvantages of the PIV system was the low temporal resolution. To gain more insight into the unsteady nature of the flow-field higher temporal resolution would be of benefit. An alternative would be to obtain phase-averaged velocity and vorticity data. It is unknown whether there are any coherent flow structures in the wake of the wheel. If there is any moderately periodic unsteadiness in the wake then the PIV system could be configured to acquire phase-averaged velocity data. A similar system to that of Leder and Geropp [34] could be adopted whereby a single hot-wire is placed in the wake and the signal used to trigger the acquisition of PIV data. This system would phase-lock the PIV system. Additionally the Oxford Lasers PIV system has a phase offset facility to delay acquisition after the trigger. This particular setup may be more applicable to quasi-periodic flows and the wheel wake is unlikely to be of this nature. Therefore an alternative method of triggering may be needed, or a method of simultaneously logging the PIV image pairs and the hot wire signal. If the latter is possible an unsteady velocity field reconstruction method similar to that of Sims-Williams [56] could be used. The first step to achieving this is to establish whether the flow exhibits any periodicity.

3. Establishing whether correlations exist between the rear jetting phenomenon and the drag force acting on the wheel could be the next step. The relation between rear jetting and base pressure fluctuations would be extremely beneficial in further understanding this mechanism. The pressure measurement instrumentation could be adapted to acquire the instantaneous centreline static pressure distribution by fitting radial pressure tappings all around the wheel periphery on the centreline. The pressure data could be logged quasi-simultaneous to get the instantaneous centreline pressure distribution. A surface pressure distribution time history could show the effects the rear

jetting has on the base pressure. Additionally a hot-wire could be placed at the position of the rear jetting flow and logged simultaneously with the pressure data. Correlation of these data would determine whether the rear jetting causes an increase in base pressure as was postulated in this thesis.

4. The unsteady wake could be analysed using a pneumatic pressure probe and the unsteady wake reconstruction method of Sims-Williams [56]. This does require the flow to exhibit some periodicity. The out of range data would still pose problems using this technique.

5. Stereoscopic PIV measurements are needed, especially when used for the XY spanwise planes, which would give further details of the flow structures in the wake. This technique has distinct advantages over the methods used in this thesis such as the pneumatic pressure probe methods which resulted in large regions of out of range data in the near-wake.

6. A transient 3D CFD solution is one of the next steps from a computational point of view. However, developing a modelling strategy for predicting all of the steady state flow structures is probably the next sensible choice. The transient flow solution would however give additional information regarding the unsteady forces acting on the wheel and the rear jetting phenomenon, and its effect on the base pressure.

7. Further analysis is needed to establish whether the tubing between the pressure scanner and tappings has an effect on the time-averaged surface static pressure distribution. Namely, to confirm that the oscillations behind the contact patch are an intrinsic aerodynamic flow mechanism and are not tubing related.

# References


[1] D. Alley. Ac inverter drives electrical noise and rfi. MCE Technical Publication, 1999.

[2] Amplicon. User manual for pc-30pgl and pc-30pgh cards.

[3] J. D. Anderson. *Computational Fluid Dynamics: the basics with applications.* McGraw-Hill Inc., New York, 1995.

[4] Atmel. 89c2051 datasheet. Atmel, year unknown.

[5] L. Axon. *The Aerodynamic Characteristics of Automobile Wheels - CFD Prediction and Wind Tunnel Experiment.* PhD thesis, Cranfield University: College of Aeronautics, 1999.

[6] L. Axon, K. Garry, and J. Howell. An evaluation of cfd for modelling the flow around stationary and rotating isolated wheels. *SAE980032*, pages 65–75, 1998.

[7] L. Axon, K. Garry, and J. Howell. The influence of ground condition on the flow around a wheel located within a wheelhouse cavity. *SAE1999-01-0806*, pages 149–158, 1999.

[8] P. W. Bearman. Review - bluff body flows applicable to vehicle aerodynamics. *Journal of Fluids Engineering*, 102:265–274, 1980.

[9] P. W. Bearman, D. De Beer, E. Hamidy, and J. K. Harvey. The effects of a moving floor on wind-tunnel simulation of road vehicles. *SAE880245*, pages 1–15, 1988.

[10] P. W. Bearman and M. M. Zdravkovich. Flow around a circular cylinder near a plane boundary. *Journal of Fluid Mechanics*, 89:33–47, 1978.

[11] D. W. Bryer and R. C. Pankhurst. *Pressure-Probe Methods for Determining Wind Speed and Flow Direction.* Her Majesty's Stationary Office, St. Albans, 1971.

[12] Chell. Wheel pressure measurement system wsms. Chell, year unknown.

[13] H. C. Child. A new telemetry system for the transmission of signals from rotating machines. Technical report, Durham University: Undergraduate Project Report, School of Engineering and Applied Science, 1992.

[14] A. Cogotti. Aerodynamic characteristics of car wheels. *Int. J. of Vehicle Design*, pages 173–196, 1983. Special Publication SP3.

[15] Burr-Brown Corporation. 12-bit 10$\mu$s serial cmos sampling analog-to-digital converter. USA: Burr-Brown Corporation, 1997.

[16] R. G. Dominy. Aerodynamics of grand prix cars. *Proc. Instn. Mech. Engrs.*, 206D:267–274, 1992. Part D.

[17] R. G. Dominy and H. P. Hodson. An investigation of factors influencing the calibration of 5-hole probes for 3-d flow measurements. *ASME International Gas Turbine and Aeroengine Congress and Exposition*, 1992. Cologne, Germany.

[18] C. Dyer. Simpson's rule. URL: http://pathfinder.scar.utoronto.ca/ dyer/csca 57/node42.html. Date accessed: 8/5/2002.

[19] J. E. Fackrell. *The Aerodynamics of an Isolated Wheel Rotating in Contact with the Ground.* PhD thesis, University of London, 1974.

[20] J. E. Fackrell and J. K. Harvey. The flow-field and pressure distribution of an isolated road wheel. 1973. In H. S. Stephens; Editor: Advances in Road Vehicle Aerodynamics. BHRA Fluid Engineering.

[21] J. E. Fackrell and J. K. Harvey. The aerodynamics of an isolated road wheel. *In Pershing, B., editor, Proceedings of the Second AIAA Symposium of Aerodynamics of Sports and Competition Automobiles*, 1975.

[22] M. Hinson. Measurement of the lift produced by an isolated, rotating formula one wheel using a new pressure measurement system. Master's thesis, Cranfield University: College of Aeronautics, 1999.

[23] J. D. Hooper and A. R. Musgrove. Reynolds stress, mean velocity, and dynamic static pressure measurement by a four-hole pressure probe. *Experimental Thermal and Fluid Science*, 15:375–383, 1997.

[24] T. Imaizumi and Y. Yoshida. The aerodynamic effect of rotating wheels. *JSAE Review*, 12(4):64–66, 1991.

[25] Fluent Inc. Flow around an automobile wheel. *Application Briefs from Fluent*, (EX193), 2002.

[26] Fluent Inc. Fluent user's manual, 2003.

[27] Pressure Systems Inc. Esp - miniature pressure scanners: User's manual. Pressure Systems Inc. Virginia: Pressure Systems Inc.2000.

[28] W. P. Kellar, S. R. Pearse, and A. M. Savill. Formula one car wheel aerodynamics. *Sports Engineering*, 2:203–212, 1999.

[29] T. Kim, B. Lee, D. Lee, J. Hwang, and D. Lee. A study on vortex shedding around a bluff body near the ground. *SAE2003-01-0652*, 2003.

[30] R. Knowles, A. Saddington, and K. Knowles. On the near-wake of rotating, 40-percent scale champ car wheels. *SAE02MSEC-27*, 2002.

[31] R. Knowles, A. Saddington, and K. Knowles. Simulation and experiments on an isolated racecar wheel rotating in ground contact. *4th MIRA International Conference on Vehicle Aerodynamics*, 2002.

[32] Oxford Lasers. User manual for piv system, 2002.

[33] N. J. Lawson, K. Knowles, R. J. E. Hart, J. N. Wray, and J. M. Eyles. An experimental investigation using piv of the underflow of a ga(w)-1 aerofoil section in ground effect. *4th MIRA International Conference on Vehicle Aerodynamics*, 2002.

[34] A. Leder and D. Geropp. Analysis of unsteady flows past bluff bodies. *Journal of Wind Engineering and Industrial Aerodynamics*, 49:329–338, 1993.

[35] C. Lei, L. Cheng, and K. Kavanagh. Re-examination of the effect of a plane boundary on force and vortex shedding of a circular cylinder. *Journal of Wind Engineering and Industrial Aerodynamics*, 80:263–286, 1999.

[36] L. M. Lourenço. *Particle Image Velocimetry.* Lecture Series 1996-03: Particle Image Velocimetry. Von Karman Institute for Fluid Dynamics, 1996.

[37] B. Massey and J. Ward-Smith. *Mechanics of Fluids.* Stanley Thornes (Publishers) Ltd, Cheltenham, seventh edition, 1998.

[38] A. P. Mears, S. C. Crossland, and R. G. Dominy. An investigation into the flow-field about an exposed racing wheel. *SAE2004-01-0446*, 2004.

[39] A. P. Mears, R. G. Dominy, and D. B. Sims-Williams. The air flow about an exposed racing wheel. *SAE2002-01-3290*, 2002.

[40] A. P. Mears, R. G. Dominy, and D. B. Sims-Williams. The flow about an isolated rotating wheel - effects of yaw on lift, drag and flow structure. *4th MIRA International Conference on Vehicle Aerodynamics*, 2002.

[41] J. Middendorf. Modeling of wind tunnel flow over a rotating cylinder. Project Report, 2003.

[42] A. Morelli. Aerodynamic effects on an automobile wheel. Technical report trans 47/69, MIRA, 1969.

[43] A. S. Morris. *The Essence of Measurement.* Prentice Hall Europe, Hertfordshire, 1996.

[44] P. Mowatt. A new telemetry system for the transmission of signals from rotating machines. Technical report, Durham University: Undergraduate Project Report, School of Engineering and Applied Science, 1993.

[45] C. Norberg. Fluctuating lift on a circular cylinder: review and new measurements. *Journal of Fluids and Structures*, 17:57–96, 2003.

[46] W. L. Oberkampf and T. G. Trucano. Verification and validation in computational fluid dynamics. *Progress in Aerospace Sciences*, 38:209–272, 2002.

[47] C.-W. Park and S.-J. Lee. Free end effects on the near wake flow structure behind a finite circular cylinder. *Journal of Wind Engineering and Industrial Aerodynamics*, 88:231–246, 2000.

[48] C.-W. Park and S.-J. Lee. Effects of free-end corner shape on flow structure around a finite cylinder. *Journal of Fluids and Structures*, 19:141–158, 2004.

[49] M. Predko. *Handbook of Microcontrollers*. McGraw-Hill, New Jersey, 1998.

[50] W. H. Press, S. A. Teukolsky, W. T. Vetterling, and B. P. Flannery. *Numerical Recipes in Fortran*. Cambridge University Press, second edition, 1992.

[51] Radiometrix. User manual for tx-2 and rx-2 radio transmitter/receiver, 2002.

[52] A. Roshko. Perspectives on bluff body aerodynamics. *Journal of Wind Engineering and Industrial Aerodynamics*, 49:79–100, 1993.

[53] A. Ryan. *The Simulation of Transient Cross-Wind Gusts and Their Aerodynamic Influence on Passenger Cars*. PhD thesis, University of Durham, 2000.

[54] G. Schewe. Reynolds-number effects in flow around more-or-less bluff bodies. *Journal of Wind Engineering and Industrial Aerodynamics*, 89:1267–1289, 2001.

[55] SensorTechnics. Pressure transducers and transmitters 94/95, 1994. SensorTechnics Manual.

[56] D. B. Sims-Williams. *Self-Excited Aerodynamic Unsteadiness Associated with Passenger Cars*. PhD thesis, University of Durham, 2001.

[57] D. B. Sims-Williams and R. G. Dominy. Experimental investigation into unsteadiness and instability in passenger car aerodynamics. *SAE 980391, SP-1318*, pages 169–189, 1998.

[58] D. B. Sims-Williams and R. G. Dominy. The validation and application of a 5-hole pressure probe with tubing transfer function correction for time-accurate measurements in unsteady flows. *2nd MIRA International Conference on Vehicle Aerodynamics*, 1998.

[59] D. B. Sims-Williams and B. D. Duncan. The ahmed model unsteady wake: Experimental and computational analyses. *SAE2003-01-1315*, 2003.

[60] R. Singh. Automated aerodynamic design optimisation process for automotive vehicle. *SAE2003-01-0993*, 2003.

[61] A. F. Skea, P. R. Bullen, and J. Qiao. The use of cfd to predict air flow around a rotating wheel. *2nd MIRA International Conference on Vehicle Aerodynamics*, 1998.

[62] A. F. Skea, P. R. Bullen, and J. Qiao. Cfd simulations and experimental measurements of the flow over a rotating wheel in a wheel arch. *SAE2000-01-0487*, pages 115–123, 2000.

[63] W. R. Stapleford and G. W. Carr. Aerodynamic characteristics of exposed rotating wheels. Technical report 1970/2, MIRA, 1970.

[64] J. W. Stewart. *The 8051 Microcontroller: Hardware, Software and Interfacing.* Regents/Prentice Hall, New Jersey, 1993.

[65] C. Uawithya. Aerodynamic measurements on rotating racing car wheels. Technical report, Durham University: Undergraduate Project Report, School of Engineering and Computer Science, 1994.

[66] P. P. Vlachos and M. R. Hajj. A time-resolved dpiv study of the unsteady character of the flow over a surface-mounted prism. *Journal of Wind Engineering and Industrial Aerodynamics*, 90:543–553, 2002.

[67] A. Wäschle, S. Cyr, T. Kuthada, and J. Wiedemann. Flow around an isolated wheel - experimental and numerical comparison of two cfd codes. *SAE2004-01-0445*, 2004.

[68] G. Wickern, K. Zwicker, and M. Pfadenhauer. Rotating wheels - their impact on wind tunnel test techniques and on vehicle drag results. *SAE970133*, pages 1–17, 1997.

[69] M. M .Zdravkovich. *Flow Around Circular Cylinders*, volume 1. Oxford University Press Inc., New York, 1997.

# Appendix A

# Publications

During the course of this research the following papers have been published.

1. A. P. Mears, R. G. Dominy, D. B. Sims-Williams.
   The Air Flow About an Exposed Racing Wheel.
   SAE 2002-01-3290. 2002.

2. A. P. Mears, R. G. Dominy, D. B. Sims-Williams.
   The Flow About an Isolated Rotating Wheel - Effects of Yaw on Lift, Drag and Flow Structure.
   4th MIRA International Vehicle Aerodynamics Conference. 2002.

3. A. P. Mears, S. C. Crossland, R. G. Dominy.
   An Investigation into the Flow-Field About an Exposed Racing Wheel.
   SAE 2004-01-0446. 2004.

4. A. P. Mears and R. G. Dominy.
   Racing Car Wheel Aerodynamics - Comparisons between Experimental and CFD derived Flow-Field Data.
   SAE 04MSEC-16. 2004.

# Appendix B

# Pressure Instrumentation

## B.1 Tubing Transfer Function Correction Data

Figures B.1 and B.2 show the transfer function data.

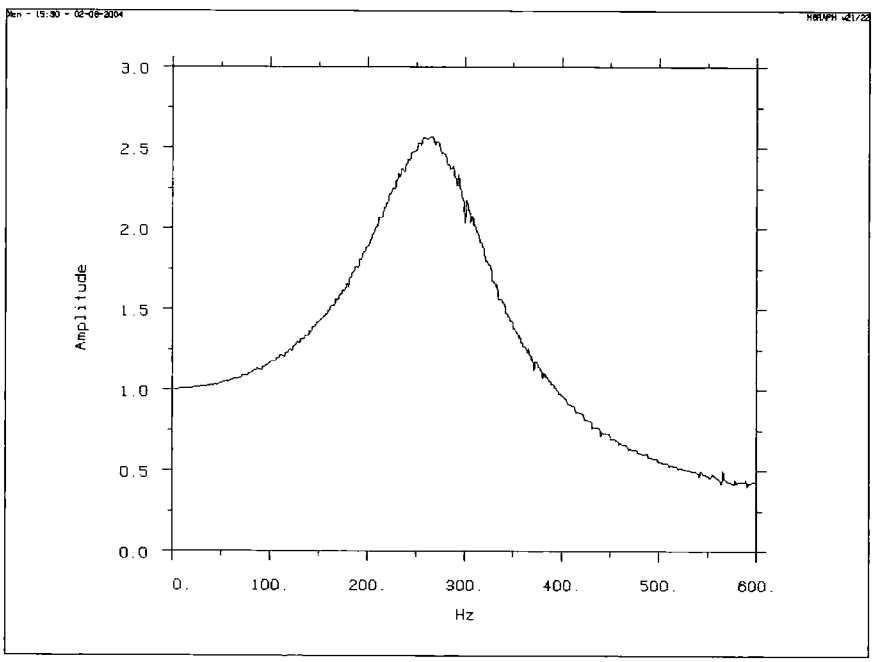


Figure B.1: Transfer Function of a Pressure Tapping and Tubing (120mm length) (Amplitude).

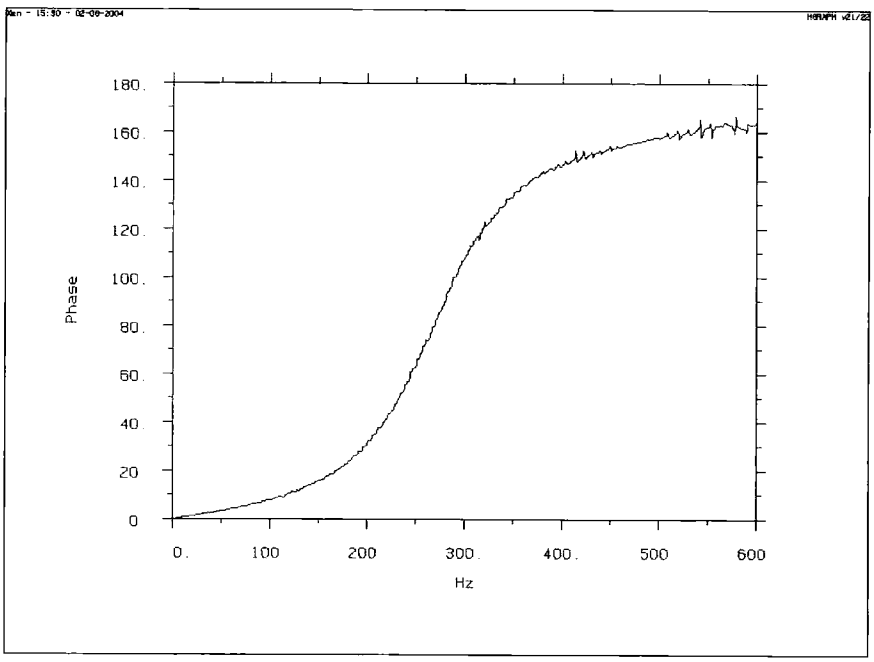


Figure B.2: Transfer Function of a Pressure Tapping and Tubing (120mm length) (Phase).

# Appendix C

# Five Hole Probe Details

## C.1 Five Hole Probe Calibration Coefficients

Eqs. (C.1.1 to C.1.4) are the calibration coefficients used to formulate the five hole probe calibration maps.

Yaw angle coefficient:

$$C_{Yaw} = \frac{P_2 - P_3}{P_1 - P_{Av}} \tag{C.1.1}$$

Pitch angle coefficient:

$$C_{Pitch} = \frac{P_4 - P_5}{P_1 - P_{Av}} \tag{C.1.2}$$

Total pressure coefficient:

$$C_T = \frac{P_1 - P_o}{P_1 - P_{Av}} \tag{C.1.3}$$

Static pressure coefficient:

$$C_S = \frac{P_{Av} - P_S}{P_1 - P_{Av}} \tag{C.1.4}$$

where:

$$P_{Av} = \frac{(P_2 + P_3 + P_4 + P_5)}{4} \tag{C.1.5}$$

and $P_{1-5}$ are the pressures at holes 1 through to 5.

# C.2 Five Hole Probe Calibration Maps

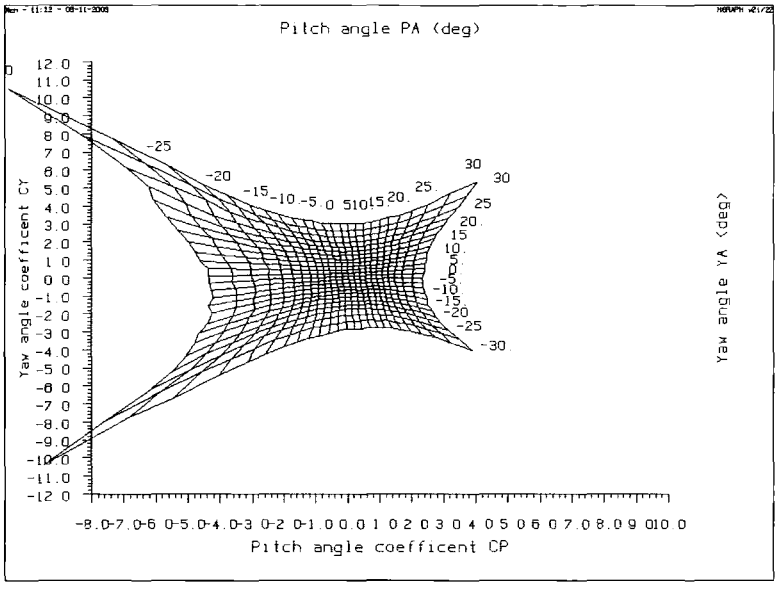


Figure C.1: Pitch/Yaw Coefficient Calibration Map.

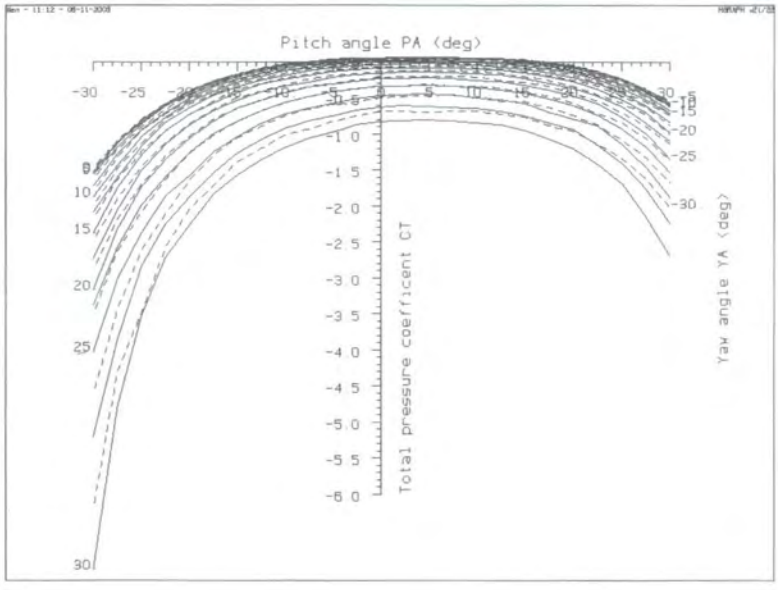


Figure C.2: Total Pressure Coefficient Calibration Map.


Figure C.3: Photograph of the Five-Hole Probe.